



DISSERTATION

FABRICATION OF TIN OXIDE NANOWIRE GAS SENSORS

ausgeführt zum Zwecke der Erlangung des akademischen Grades einer
Doktorin der technischen Wissenschaften unter der Leitung von

Ao.Univ.Prof. Dipl.-Ing. Dr.techn. Wolf-Dieter Schubert
Univ.Doiz. Mag.rer.nat. Dr.rer.nat. Anton Köck

eingereicht an der Technischen Universität Wien
Fakultät für Technische Chemie
Institut für Chemische Technologien und Analytik
von

Elise Brunet
Matrikelnummer: 0929532
Weimarerstraße 31/1, 1180 Wien

Wien, im März 2014

Abstract

The diversification of gas sensing applications is motivated by society issues, such as environmental monitoring in industrialized cities, safety devices to prevent CO intoxication and indoor air quality control. Metal oxide gas sensors, which measure changes of the electrical resistance of the metal oxide due to the adsorption/desorption reactions of gas molecules on its surface at high temperature, exhibit high sensitivity to a broad range of flammable and toxic gases. Their success can be further explained by their simplicity and their low cost fabrication. Still, commercial metal oxide sensors, which are mainly based on tin oxide (SnO_2) thick films, are rather bulky devices. The development of gas sensors based on metal oxide nanowires is promising regarding the improvement of the sensing performances, the miniaturization and the decrease of the power consumption of the devices. The aim of this thesis is to fabricate SnO_2 nanowire sensors and to address the technological issues related to their fabrication. Therefore, the synthesis of SnO_2 nanowires is developed based on a vapor growth method. Different materials (Al, Sn/Au, Cr/Au, Ti/Au and Au) are investigated to establish stable ohmic contacts with single SnO_2 nanowires. The sensing properties of single nanowire sensors are characterized upon exposure to CO, H_2 and H_2S in dry and humid synthetic air at temperatures in the range 150-350°C. Preliminary results of nanowire sensors based on a suspended network of SnO_2 nanowires, functionalized with metallic nanoparticles (Pd, Au or PdAu) or integrated on a suspended CMOS processed microhotplate are also presented.

Acknowledgements

The work within this thesis has been conducted at the AIT Austrian Institute of Technology GmbH in the business unit Molecular Diagnostic (Health & Environment department). This work has been partly funded by the European projects COCOA (CATRENE) and ESiP (ENIAC, FFG No. 824954) and by the WWTF Vienna Science and Technology Fund within the project “Mathematics and Nanosensors” (No. MA09-028).

I am first and foremost extremely grateful to my supervisor at AIT, Univ.Doiz. Mag. Dr. Anton Köck, who guided me during the whole thesis, encouraged me to participate to conferences and constantly supported me very positively with his inspiring energy and competent advice. I would like to express my gratitude to Ao.Univ.Prof. Dipl.-Ing. Dr.techn. Wolf-Dieter Schubert and to Ass.Prof. Dipl.-Ing. Dr.techn. Christian Edtmaier, who were my supervisors at the university, for their guidance, their precious advice and expertise, which largely contributed to the accomplishment of this thesis.

I would like to thank Dr. Giorgio C. Mutinati, from whom I have learnt a lot about methodology and problem solving, especially during the many hours spent in the lab “spray pyrolysing” and talking. Thank you to Dipl.-Ing. Stephan Steinhauer, who developed the lithography processes for nanowire contacting used in this thesis. It has been very cheerful to share the challenges of nanowire gas sensors with a friend. A special thank you goes to Dr. Thomas Maier for his patient help every time a technological issue emerged along my thesis. Thanks to Dr. Rudolf Heer for his support by any (IT) questions I had. Many thanks to all my colleagues at AIT for their moral support, the numerous great memories and the lots of fun I had with them.

Thank you to Gerhard Tulzer and Dr. Clemens Heitzinger for their work on modeling the reaction kinetics of gas molecules at the surface of the nanowires from experimental results partly presented in this thesis. Thank you to Dr. Lado Filipovic and Prof. Sigfried Selberherr from the Institute for Microelectronic at the TU Wien for modeling the spray pyrolysis deposition.

Thank you to Dr. Christian Gspan, Martina Dienstleder, Prof. Werner Grogger and Univ.Doiz. Peter Pölt from the FELMI-ZFE at the TU Graz for the preparation of the FIB cuts, the TEM and SEM EDS images shown in this thesis. Thanks to Dr. Alfred Neuhold and Prof. Roland Resel from the ISSP at the TU Graz for the XRD measurements shown in this thesis.

Many thanks to Dr. Olena Yurchenko from IMTEK-Sensors of the University of Freiburg for the functionalization of the nanowire sensors with nanoparticles within the project NanoSmart. Thank you to the partners at AIT, FOTEC Forschungs- und Technologietransfer GmbH and ams AG for the design and production of the microhotplate within the project COCOA.

I am very grateful to my parents and family, who always supported me in my choices, even though those choices implied moving away. Each visit to them is a concentrate of happiness and strengthens me to go on. My sincere gratitude goes to Herta and the whole Amsüss family for welcoming me so warmly and making me feel at home in Vienna.

I cannot thank my boyfriend, Sebastian, enough for being such a strong partner ever since I have known him. I would never have accomplished this work without his everyday caring and loving support.

Contents

Abstract	1
Acknowledgements	2
Introduction	7
1 Literature review	10
1.1 State-of-the-art of gas sensors	10
1.1.1 Types of gas sensors	10
1.1.2 Materials for conductometric gas sensors	12
1.1.3 Tin oxide gas sensors	13
1.2 Principle of SnO ₂ gas sensors	14
1.3 Tin oxide	19
1.3.1 Applications	19
1.3.2 Material properties	19
1.4 Methods reported for the growth of SnO ₂ nanowires	22
1.4.1 Vapor phase growth	24
1.4.2 Solution phase growth	27
2 Synthesis of SnO₂ nanowires	31
2.1 Spray pyrolysis development	31
2.1.1 Motivation	31
2.1.2 Theory	32
2.1.3 Methods	39
2.1.4 Results and discussion	42
2.2 Nanowire growth	48
2.2.1 Methods	48
2.2.2 Experimental approach	52
2.2.3 Results	54
2.2.4 Characterization of the SnO ₂ nanowires	77
2.2.5 Discussion	79
2.3 Summary	82
3 Fabrication of single nanowire gas sensors	84

3.1	Process flow	84
3.2	Choice of the metal used for the contacts	87
3.2.1	Methods	89
3.2.2	Results	90
3.2.3	Discussion	94
3.3	Electrical characterization of the SnO ₂ nanowires	98
3.3.1	Determination of the contact resistance	98
3.3.2	Measurement of conductivity	101
3.4	Investigation of the metal-nanowire interface	102
3.5	Summary	105
4	Characterization of gas sensing properties	108
4.1	Reaction mechanism of gas species on SnO ₂ surfaces	108
4.1.1	O ₂	108
4.1.2	H ₂ O	110
4.1.3	CO	112
4.1.4	H ₂	114
4.1.5	H ₂ S	114
4.2	Methods	115
4.2.1	Gas measurement setup	115
4.2.2	Analysis of the data	118
4.2.3	Description of the nanowire sensors	118
4.3	Results	121
4.3.1	Response to oxygen and water molecules	121
4.3.2	Response to CO	123
4.3.3	Response to H ₂	132
4.3.4	Response to H ₂ S	139
4.4	Discussion	142
4.4.1	Influence of the background atmosphere	143
4.4.2	Influence of humidity	146
4.4.3	Influence of the operating temperature	147
4.4.4	Influence of the size of the nanowire	147
4.4.5	Influence of the concentration of the test gas	150
4.4.6	Long-term stability	151

4.5	Summary	151
5	Towards stable, selective and CMOS integrated SnO₂ nanowire sensors	156
5.1	Towards stable nanowire sensors: the nanowire network configuration	156
5.2	Towards selective nanowire sensors: functionalization of SnO ₂ nanowires with metallic nanoparticles	158
5.3	Towards CMOS integrated nanowire sensors: processing of nanowire sensor on a microhotplate	159
	Conclusion and outlook	161
	Glossary	166
	Bibliography	167
	List of Figures	186
	List of Tables	190
	List of own publications	191
	Curriculum Vitae	194

Introduction

Gas sensors integrated as environmental monitors in smart phones, personal computers and wrist watches would enable a precise mapping of pollutant gases in industrialized cities in order to warn the population against local pollution peaks. The installation of safety devices in every household could be the solution to avoid fatal domestic accidents caused by carbon monoxide (CO), which is still the first cause of death by intoxication in many industrial countries [1]. The control of heating, ventilation and air conditioning (HVAC) systems via carbon dioxide (CO₂) sensors to ensure indoor air quality in buildings would result in energy saving of 40% in comparison with the traditional ventilation systems [2]. Those applications are just a few examples of how the commercialization of reliable, miniaturized and low cost gas sensors could respond to current society issues.

The success of metal oxide gas sensors can be explained by their high sensitivity to a broad range of flammable and toxic gas species and their rather simple detection principle, which facilitates their low cost fabrication. Traditionally, a metal oxide thick film is deposited on a substrate with embedded electrodes and heater in order to measure the changes of electrical resistance due to adsorption/desorption reactions of gas molecules on the metal oxide surface occurring at operating temperatures in the range 150-400°C. Tin oxide (SnO₂) is the most commonly used metal oxide sensing material. Since their first commercialization in 1968, the fabrication technology has largely remained unchanged. The devices are bulky and have high power consumption due to the required heater. Therefore, a considerable effort has been invested lately in integrating metal oxide gas sensors and the associated circuitry with complementary metal-oxide-semiconductor (CMOS) technology, which will potentially result in low cost miniaturized devices expandable to the consumer market and enabling the above mentioned applications [3].

Simultaneously, the interest for semiconducting nanowires has exponentially increased in the last fifteen years [4]. Among diverse potential applications, the use of semiconducting nanowires for gas sensing has been extensively investigated with high expectations regarding the improvement of the “3S” of gas sensing: sensitivity, selectivity and stability [5]. The electrical resistance of nanowires can be influenced by small amounts of gas due to their large surface-to-volume ratio, so higher sensitivity may be reached [6]. The selectivity may be tuned by controlling the gate potential of nanowire sensors operated in a field effect transistor (FET) configuration [7, 8]. The higher long-term stability of a sensor based on a 2-D network of SnO₂ nanowires in comparison with a sensor made of a porous 3-D network of SnO₂ nanoparticles has been attributed to the better thermal stability of the single crystalline nanowires [9]. Furthermore, the changes in electrical conductivity of the metal oxide are the direct consequence of charge transfers occurring dur-

ing the adsorption/desorption of the gas species at the surface of the metal oxide. A better theoretical understanding of the surface reactions may be gained by studying the charge transport in a single crystalline nanowire compared to a polycrystalline film. Another promising property of nanowire gas sensor is the self-heating effect of the nanowire, which may occur due to the power dissipation by the Joule heating effect from the electrical current applied to the nanowire during the conductometric measurement [10]. Using the self-heating effect of metal oxide nanowires offers a great advantage regarding the power consumption of the devices, because the heating supply implemented in the gas sensors could be removed. This may lead to technologically simplified, miniaturized and low power consuming devices. Recent studies also anticipated the integration of nanowire gas sensor with CMOS technology [11, 12]. However, no commercially viable fabrication method for nanowire gas sensors has been successfully implemented yet. The objective of this thesis is to fabricate gas sensors based on single crystalline SnO₂ nanowires and to address the related technological challenges. The feasibility of the integration of SnO₂ nanowire sensors on CMOS processed chips is shortly discussed as outlook.

The focus is set on the detection of three gas species: carbon monoxide (CO), hydrogen (H₂) and hydrogen sulfide (H₂S). The detection of CO and H₂S, which are both toxic gases, is of interest for safety devices in domestic environment and in industrial environment (petroleum/natural gas drilling and refining, wastewater treatment), respectively. Their permissible exposure limit (PEL), which is the maximum concentration of exposure for employees based on an 8-hour time weighted average exposure in US, is 35 ppm for CO and 10 ppm for H₂S. H₂ is an explosive gas with a lower explosive limit (LEL) of 4%. The demand for H₂ sensors able to detect much smaller concentrations for leak detection from hydrogen-powered cars and fueling stations is growing along with the interest of hydrogen fuel cells as alternative power source.

This thesis is divided in 5 chapters. Chapter 1 gives a literature review about SnO₂ conductometric gas sensors, presenting the state-of-the-art of commercial sensors, explaining the gas sensing principle, giving insight in the main material properties of SnO₂ and reviewing the different synthesis methods of SnO₂ nanowires. In Chapter 2, the experimental approach leading to a reproducible method for the synthesis of SnO₂ nanowires and to a better understanding of the nanowire growth mechanism is discussed. Chapter 3 focuses on the technological challenges of the fabrication of SnO₂ nanowire sensors. The issue regarding the establishment of ohmic electrical contacts with low contact resistance on single nanowires is investigated. The contribution of the contact resistance to the resistance measurement of the nanowire is calculated as well as the conductivity of the SnO₂ nanowires. In Chapter 4, the gas sensing performances of the SnO₂ single nanowire sensors

are measured. Three gas species are detected with concentration in different ranges: 10-100 ppm for CO and H₂, 0.1-1 ppm for H₂S. The background atmosphere (presence or absence of oxygen), the humidity level (dry or humid conditions) and the operating temperature (between 150°C and 350°C) are other variable parameters. Theoretical models from literature are used to interpret the obtained results and to explain the possible reactions taking place at the nanowire surface. Finally, Chapter 5 shows preliminary results how to improve the stability and selectivity of nanowire sensors based on a suspended network of SnO₂ nanowires and on single nanowire devices functionalized with metallic nanoparticles (Pd, Au or PdAu), respectively. As final outlook towards miniaturized and low power nanowire gas sensors, a viable method for integrating nanowires on a suspended CMOS processed microhotplate is presented.

1 Literature review

1.1 State-of-the-art of gas sensors

The first article reporting the use of metal oxide semiconductors as gas sensor based on the changes of their electrical conductivity due to the adsorption and desorption of the gas species present in the atmosphere was published by Seiyama et al. in 1962 [13]. The adsorption/desorption reactions between the gas species and the metal oxide occur at high temperatures in the range 200-400°C. From that experiment with ZnO thin films, great effort has been made to take advantage of this property and to employ metal oxides for gas sensors. In 1968, the FIGARO Engineering Inc., which was founded by Naoyoshi Taguchi, commercialized the first metal oxide conductometric gas sensors able to detect “low concentrations of combustible and reducing gases when used with a simple electrical circuit” [14].

The field of applications of gas sensors, which requires reliable, compact and efficient sensor systems, is very broad (see Table 1).

Table 1: Applications and corresponding target species of gas sensors.

Application	Target gas
Domestic safety (fire detection)	CO, H ₂ , NO ₂
Indoor air quality	O ₂ , CO ₂ , VOCs
Environmental monitoring (pollution)	CO ₂ , NO _x , O ₃
Automotive (exhaust emission control)	Hydrocarbons, CO, NO _x , SO ₂
Industry (monitoring of processes)	NH ₃ , Hydrocarbons, SO ₂
Medicine (breath analysis)	VOCs
Personal safety (detection of toxic gases)	CO, SO ₂ , H ₂ S

1.1.1 Types of gas sensors

The sensing principle of conductometric gas sensors relies on changes of the electrical resistance of the sensing material due to the adsorption of gas molecules on its surface. The sensing layer in the commercial devices is most commonly a semiconducting metal oxide thick film. A simple electrical circuit is built, as shown in Figure 1. A constant current is applied to the sensing layer, the voltage is measured and the resistance is calculated by Ohm’s law. At high temperature (typically in the range 200-400°C), the interaction between the metal oxide and the ambient gas may results in a charge transfer, which leads to band bending effects at the surface and thus to a direct influence on the sensing material resistance.

Conductometric gas sensors exhibit high sensitivity to a broad range of gas

species, their fabrication is relatively simple and low cost, and the devices can be miniaturized. Their selectivity can be improved by the use of filters, by adapting the operating temperature, by doping the sensing material or by functionalization with metallic nanoparticles.

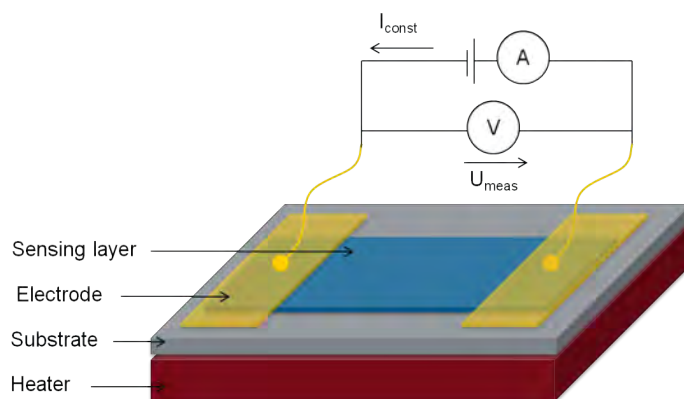


Figure 1: Schematic representation of a conductometric gas sensor. A constant current is applied to the semiconducting layer and the voltage is measured.

There are other kinds of gas sensors, which can be distinguished according to their detection principle [15, 16, 17].

The optical gas sensing method is mainly based on spectroscopic techniques, though ellipsometry and surface plasmon resonance (SPR) are other emerging techniques. The detection principle is based on the change of the optical properties (refractive index, reflection or absorption coefficient) of the sensing layer upon adsorption of gas species on its surface. Optical sensors exhibit high sensitivity, selectivity and stability with very long lifetime, but they are complex expensive devices, which can not be miniaturized.

The principle of mass-sensitive gas sensors relies on changes of the oscillation frequency of a piezoelectric material with the adsorption of gas species at the surface of the sensing layer. Quartz crystal microbalances (QCMs) are the most common mass-sensitive sensors. Surface acoustic wave (SAW) sensors detect changes in the velocity and attenuation in the propagating wave, which are caused by the adsorption of gas species on the sensing layer. Acoustic wave sensitive sensors have a high stability and a long lifetime, but they have a rather low selectivity and are influenced by environmental changes. Microcantilevers have also been developed to detect the downward bending of the cantilever upon adsorption of gas species on the sensing layer due to formation of surface stress [15].

Field-effect transistor (FET) gas sensors have been recently developed based on silicon or metal oxide nanowires [7]. The nanowire is deposited on a

SiO₂/Si substrate and plays the role of conduction channel between the source and drain electrodes. The bottom substrate (Si) serves as the gate electrode. The gas molecules adsorbed on the nanowire modulates its conductivity and act as an extra virtual gate voltage [5].

Electrochemical gas sensors are based on the change of current (amperometric sensors) or voltage (potentiometric sensors) between the working and the reference electrode due to a redox reaction at the working electrode [18]. Electrochemical sensors are rather cheap devices with a good reproducibility and accuracy, however, the cross-sensitivity with other gas species can be problematic and their lifetime is short.

Calorimetric sensors are of two kinds: catalytic and thermal conductivity. The catalytic sensors detect an increase of temperature induced by the oxidation of combustible gas species on the catalytic material. Thermal conductivity gas detectors detect the difference in thermal conductivity between the sample and a reference gas. Calorimetric sensors are low cost devices stable at ambient temperature, which are particularly sensitive to combustible gases, but they lack of selectivity and their sensibility to vibrations prevents their use in portable equipment.

Gas chromatography is another detection technique, which is very reliable, sensitive and selective, but it is mainly used as laboratory analytical tool because it is an expensive equipment, which can not be miniaturized to portable devices.

1.1.2 Materials for conductometric gas sensors

Conductometric gas sensors are usually based on metal oxide semiconductors, though new materials, like polymers or carbon nanotubes, are also investigated. Conducting polymers, such as polypyrrole, polyaniline and polythiophene, can be doped to become conductors or semiconductors and be used as conductometric gas sensors. Non-conductive polymers can also be used as sensitive layer coupled with other types of transducers (calorimetric, capacitive or mass-sensitive) [19]. Polymers present the advantage to be highly sensitive to a large variety of VOCs (e.g. alcohols, aromatic compounds, halogenated compounds) at room temperature with short response times [17]. The disadvantages are their long-time instability, irreversibility and poor selectivity.

Carbon nanotubes (CNTs) are also sensitive at room temperature [20]. The main target gases are alcohols, ammonia (NH₃), carbon dioxide (CO₂) and nitrogen oxide (NO_x). CNTs present high surface-to-volume ratios and can be decorated with other materials to increase their sensitivity [21]. Graphene is another very promising carbon-based material extensively investigated in the past few years [22, 23, 24].

Most of conductometric gas sensors are based on metal oxide semiconductors because of their high sensitivity to a broad range of gas species. A variety of n-type (CdO, MgO, SrO, BaO, In₂O₃, WO₃, TiO₂, V₂O₃, Fe₂O₃, GeO₂, Nb₂O₅, MoO₃, Ta₂O₅, La₂O₃, CeO₂, Nd₂O₃, SnO₂, ZnO) and p-type (Cr₂O₃, Mn₂O₃, Co₃O₄, NiO, CuO) semiconducting materials exhibits a change in the electrical conductance in response to combustible, reducing, or oxidizing gases [25]. The advantage of p-type over n-type semiconductors is their relatively lower operating temperature [17]. Among the most commonly used materials are TiO₂, SnO₂, ZnO and In₂O₃.

1.1.3 Tin oxide gas sensors

Commercial gas sensors currently on the market are mostly based on metal oxide thick films. The most commonly used metal oxide is tin dioxide (SnO₂). The advantage of metal oxide thick films is their porosity, which enables the diffusion of gas species inside the film so the surface area available for adsorption is increased and a higher sensitivity is obtained. However, the thick layers are obtained starting from powders by screen printing techniques, which are techniques lacking of reproducibility leading to slightly different initial characteristics for each sensor [15].

The second generation of gas sensors benefits from reproducible deposition techniques (physical vapor deposition (PDV) or chemical vapor deposition (CVD)) to produce metal oxide thin films with a nanocrystalline structure. However, the sensitivity of thin film sensors is lower than the sensitivity of thick film sensors due to the decrease of porosity. The main advantage of thin film sensors is their possible integration on microhotplates in order to miniaturize the devices and to reduce the heating power, which is necessary to reach the high operating temperatures required for gas sensing.

The synthesis of single crystalline metal oxide nanowires leads to the development of a third generation of gas sensors. Table 2 is a short review of the gas sensors based on a single SnO₂ nanowire or on a network of SnO₂ nanowires, which have been recently fabricated and the corresponding gas species detected.

SnO₂ nanowires present several advantages over the traditional thin- and thick film sensors:

- Higher sensitivity: Thanks to the large surface-to-volume ratio, a few gas molecules are sufficient to influence the electrical properties of the nanowire, especially if the diameter of the nanowire is comparable with the thickness of the depletion layer.
- Higher stability: The long-term stability of a sensor based on a 2-D network of SnO₂ nanowires is higher than a sensor made of a porous

3-D network of SnO₂ nanoparticles due to the better thermal stability of the single crystalline nanowires [9].

- Lower operating temperatures and power consumption: The bias current applied in conductometric measurements induces power dissipation at the nanowire, which is heated by the Joule effect (self-heating). The self-heating effect of nanowires enables to lower the consumption down to a few tens of μW [26].

Further, since the changes in electrical conductivity of the metal oxide are the direct consequence of charge transfers occurring during the adsorption/desorption of the gas species at the surface of the metal oxide, the theoretical understanding of the surface reactions will be facilitated by studying the charge transport in a single crystalline nanowire in comparison with a polycrystalline film.

Table 2: Summary of the gas species detected by SnO₂ nanowire and nanobelt sensors.

Configuration	Gas	Concentration (ppm)	Temperature (°C)	Reference
single	NH ₃	25-100	60-300	[27]
single	CO	5-1000	200-300	[28]
single	CO	25-100	60-300	[27]
single	CO	50-500	300	[29]
network	CO	250-500	400	[30]
network	CO	30	250-400	[31]
network	H ₂ S	4-20	300-500	[32]
network	NO ₂	0.2	250-400	[31]
network	NO ₂	0.5	400	[30]
network	ethanol	250	400	[30]
network	ethanol	10	250-400	[31]
network	ethanol	50	300	[33]
network	O ₃	0.28	400	[34]

1.2 Principle of SnO₂ gas sensors

A chemical sensor is composed of a receptor and a transducer. The receptor is a chemically reactive layer, which interacts with the target molecules. The transducer transforms the chemical interaction in a measurable signal. In case of a conductometric gas sensor, gas molecules interact with the surface of the sensing material (receptor). This interaction induces changes in the electrical properties of the bulk sensing material (transducer), which are measured as the sensor signal. It is assumed that the receptor component is

the same from one SnO₂ gas sensor to another, because the chemical reactions occurring at the surface of the SnO₂ material are the same. However, the transducer part is much influenced by the geometry and structure of the SnO₂ sensing layer [35, 36]. For compact thin films or for nanowires, the interactions with the gas species occur only at the surface of the SnO₂ layer. For porous layers, the gas species can penetrate into the sensing layer and react at the surface of the grains, so the active surface is much higher than for a compact layer [37]. Moreover, the conduction process occurs through the grain boundaries for porous layer as for nanocrystalline thin films. This differs from the conduction process in single crystalline nanowires.

The gas sensing principle of SnO₂ conductometric gas sensors is described in the literature by the combination of two models: the ionosorption model and the reduction-reoxidation model. The ionosorption model relates the sensor response to ionosorbed molecules at the surface of the sensing layer, which creates a space charge layer near the surface and induces changes in the electrical conductivity and work function. The reduction-reoxidation model explains the changes of conductivity by the variation of the number of oxygen vacancies in the surface region of the sensing layer.

The ionosorption model supports the assumption that oxygen molecules become ionosorbed at the surface of the sensing layer. First, the physisorption of an oxygen molecule at the surface occurs O_{2,phys}, followed by its chemisorption. The chemisorbed oxygen molecule can act as a surface state and trap an electron from the conduction band of the metal oxide, thus inducing a negative charged surface O_{β,S}^{-α}. Since the charge transfer involves free charge carriers, the term “ionosorption” is employed to describe the adsorption of oxygen molecules rather than the term “chemisorption”. As electrons flow from the conduction band of the semiconductor to the chemisorbed layer, a space charge is formed between the bulk and the surface. The negative space charge layer at the surface is compensated by a positive space charge layer, where the density of conduction electrons is reduced. This positive space charged layer is called “electron depleted layer” or “depletion layer”. An electric field induced by the negative charge present at the surface causes the upward bending of the energy bands in the solid. If the energy bands bend upward, it means that the Fermi level is pushed into the band gap of the solid, thus decreasing the conductivity. The band bending increases with the concentration of ionosorbed oxygen species at the surface until a steady state is reached [36]. The band bending effect caused by the ionosorption of oxygen at the surface of SnO₂ is schemed in Figure 2.

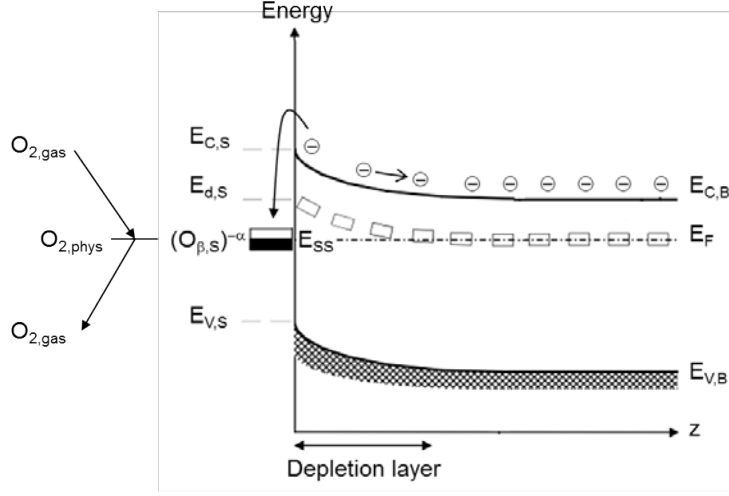


Figure 2: Schematic representation of the band bending effect caused by the ionosorption of oxygen at the surface of an n-type semiconductor. The chemisorbed oxygen may act as surface state and trap electrons from the conduction band of the semiconductor, which results in the formation of a depletion layer near the surface on one hand and in the upward bending of the energy bands on the other hand. $E_{C,s}$ and $E_{C,B}$ are the bottom of the conduction band at the surface and in the bulk, respectively; $E_{V,s}$ and $E_{V,B}$ the top of the valence band at the surface and in the bulk, respectively; $E_{d,s}$ is the donor level at the surface; E_F the Fermi level; E_{SS} the acceptor surface state; $O_{2,gas}$ is an oxygen molecule in the ambient atmosphere; $O_{2,phys}$ a physisorbed oxygen molecule; $O_{\beta,s}^{-\alpha}$ a ionosorbed oxygen ($\alpha=1$ and $\alpha=2$ for singly and doubly ionised forms, respectively; $\beta=1$ and $\beta=2$ for atomic and molecular forms, respectively). After [38, 36].

The thickness of the depletion layer is in the order of the Debye length L_D , which is defined as:

$$L_D = \sqrt{\frac{\varepsilon k_B T}{q^2 n_C}} \quad (1)$$

where ε is the dielectric constant, k_B the Boltzmann's constant, T the temperature in K, q the elementary charge and n_C is the density of charge carriers [39]. Different values of L_D for SnO_2 have been reported: 130 nm to 10 nm when temperature changes from 120°C to 420°C for SnO_2 single crystals [37], 13 nm at 250°C for single crystalline nanowires [40] and 3-12 nm in the temperature range 20°C-250°C for nanocrystalline SnO_2 thick films [39, 41].

It is generally accepted that the nature of the ionosorbed oxygen species at the surface of SnO_2 depends on the adsorption temperature: below 150°C, the molecular form O_2^- predominates, while above 150°C, the atomic form (O^- , O^{2-}) predominates. According to the ionosorption model, other species, such as physisorbed oxygen molecules and lattice oxygen ions, do not play any role in the gas sensing mechanism. Reducing gases, such as CO, react with the ionosorbed oxygen species, which results in the release

of electrons into the conduction band of the metal oxide, so the conductivity increases [42]. The overall gas sensing mechanism according to the ionosorption model is schemed in Figure 3.

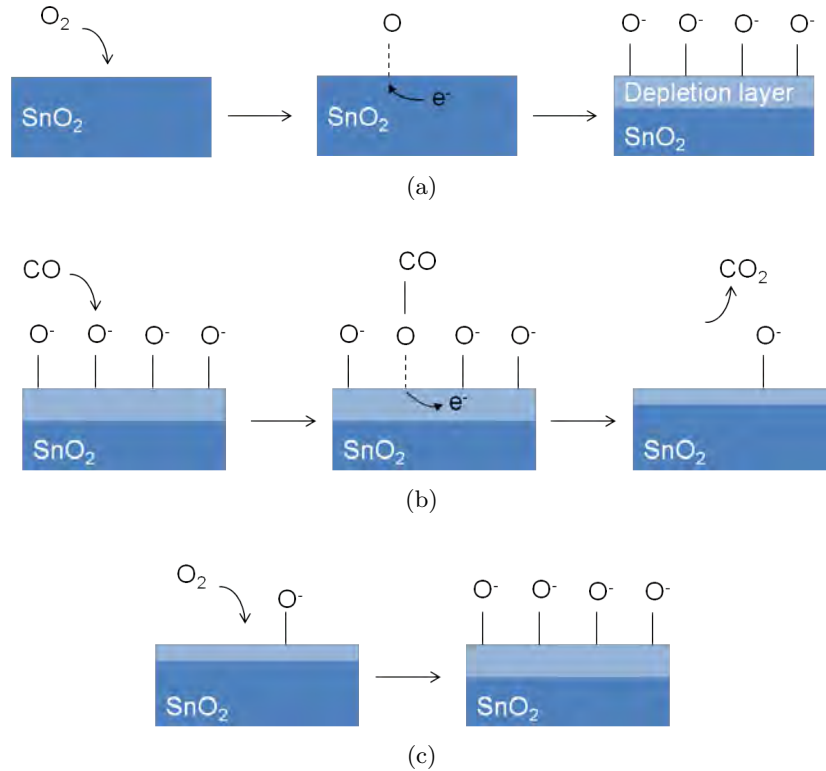


Figure 3: Schematic representation of the gas sensing principle of SnO₂ gas sensors according to the ionosorption model. (a) Ionosorption of oxygen species and creation of a depletion layer. (b) Reaction of CO molecules with the ionosorbed oxygen species and release of the trapped electrons into the conduction band of SnO₂ (diminution of the depletion layer). (c) Recovery of the sensor with the ionosorption of new oxygen species.

The reduction-reoxidation model is based on the variation of the number of oxygen vacancies in the surface region of the sensing layer. The conductivity of SnO₂ is controlled by the intrinsic oxygen vacancies, which act as electron donors. The reduction-reoxidation mechanism, which is schemed in Figure 4, occurs as follows: First, the gas molecule reacts with a lattice oxygen at the surface of the metal oxide, which creates an oxygen vacancy. Then, the vacancy becomes ionised and electrons are released in the conduction band, which means that the conductivity increases. In the presence of oxygen, the vacancy may be filled and electrons are removed from the conduction band, which results in the decrease of the conductivity.

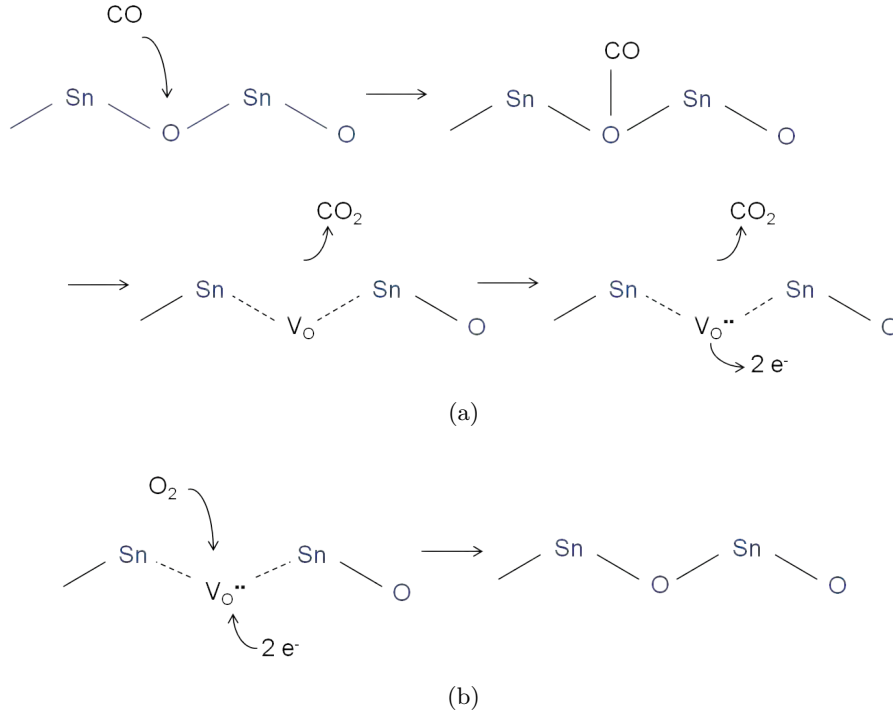


Figure 4: Schematic representation of the gas sensing principle of SnO₂ gas sensors according to the reduction-reoxidation model. (a) Reaction of the CO molecule with a lattice oxygen, creation of an oxygen vacancy, ionization of the oxygen vacancy and release of electrons in the conduction band of SnO₂. (b) Recovery of the sensor: in the presence of oxygen in the atmosphere, the oxygen vacancy can be filled.

The ionosorption model is generally accepted in the literature [43, 37, 25]. XPS studies of SnO₂ nanocrystalline thin films revealed an upward band bending after exposure to O₂ at 120°C and 250°C. Although no chemisorbed oxygen was detected, an inverted band bending was induced by exposure to CH₄, which proves the reaction of CH₄ with chemisorbed oxygen [44]. However, the existing spectroscopic analyses of the SnO₂ surface, which demonstrate the presence of ionosorbed oxygen species (O₂⁻, O⁻, O²⁻), have been recently questioned because the experiments were not conducted in the real working conditions of gas sensors [42]. On the contrary, the reactions with oxygen vacancies and their ionization, which are involved in the reduction-reoxidation model, have been proven by spectroscopy under the working conditions of the gas sensors. The limitation of this model lies in the lack of understanding, what leads to the recovery of the sensor conductivity in the absence of oxygen (e.g. alternating flows of CO in N₂ and pure N₂), where oxygen should be necessary to fill the vacancy, so the sensor conductivity recovers its initial value. However, no spectroscopic studies have investigated this particular case yet [36].

1.3 Tin oxide

1.3.1 Applications

SnO_2 is mainly used in applications as transparent conducting oxide (TCO), oxidation catalyst, and solid state gas sensing material. SnO_2 is a common TCO material used in binary systems as tin doped In_2O_3 (ITO), and antimony or fluorine doped SnO_2 . Thanks to its low electrical resistance and high optical transparency, SnO_2 is used as electrode materials in solar cells, light emitting diodes, or flat panel displays, among others. Additionally to its transparency in the visible range, SnO_2 is highly reflective for infrared light, which is used for coating windows in order to keep the heat out or in the building.

SnO_2 is also used as heterogeneous catalyst for CO oxidation or NO reduction following the Mars-van-Krevelen mechanism. In this mechanism, the gas molecule first adsorbs at the surface of the catalyst and is oxidized by the reaction with lattice oxygen. The oxidized molecule desorbs, creating an oxygen vacancy in the crystal lattice at the surface of the catalyst. This oxygen vacancy is filled again by gas-phase oxygen, thus regenerating the catalyst. The succession of reduction and re-oxidation processes is enabled thanks to the dual valency of tin atoms, which can be present at the surface in the oxidation states 2+ and 4+ according to the oxygen chemical potential.

1.3.2 Material properties

Tin oxide exists as stannic oxide (SnO_2) and stannous oxide (SnO), but stannic oxide is the thermodynamically most stable form of tin oxide. A natural source of the SnO_2 crystal is a mineral called cassiterite. SnO_2 crystallizes in the same rutile structure as many other metal oxides, such as TiO_2 , RuO_2 , GeO_2 , MnO_2 , VO_2 , IrO_2 , and CrO_2 [25]. The rutile structure has a tetragonal unit cell with a space-group symmetry of $P4_2/mnm$ (see Figure 5). In the bulk, the Sn atoms are sixfold coordinated to threefold coordinated oxygen atoms. The lattice constants are $a=b=4.7374 \text{ \AA}$, $c=3.1864 \text{ \AA}$ [25].

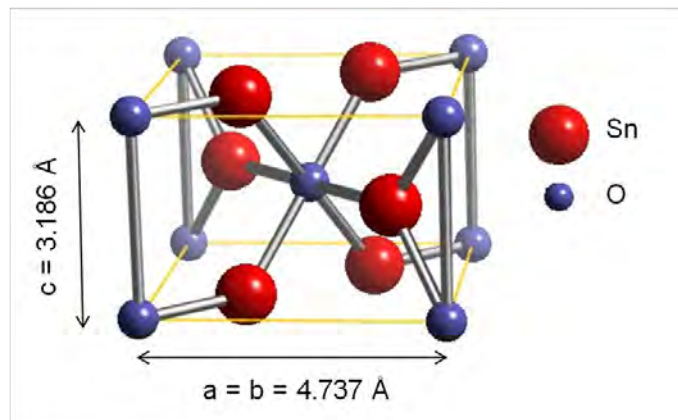


Figure 5: Crystal structure of the rutile SnO_2 .

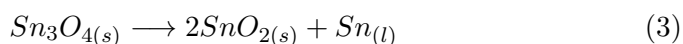
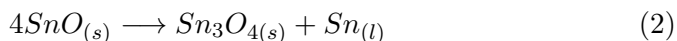
The low index SnO_2 surfaces with the lowest surface energy are (110), followed by the (100) and (101) surfaces. Those three low index SnO_2 surfaces experience loss of surface lattice oxygen under reducing conditions [25]. The (100) and (101) reduced surface are formed by removal of bridging oxygen atoms from the stoichiometric bulk termination. The most stable (110) reduced surface exhibits high defect concentrations. The variation of the lattice oxygen concentration at the surface plays an important role in the SnO_2 gas sensing properties.

Pure stoichiometric tin dioxide (SnO_2) is an insulator due to its wide band gap of 3.6 eV. However, the presence of intrinsic oxygen vacancies is responsible for the n-type semiconducting properties of non-stoichiometric SnO_{2-x} , because the oxygen vacancies may be singly or doubly ionized, creating two donor levels at energy of 30 meV and 150 meV below the conduction band, respectively [45].

Li-Zi et al. [46] observed a variation of the oxygen vacancy concentration in the bulk with the temperature and the oxygen partial pressure, when measured by coulometric titration. Values of 0.02 and 0.034 for x in SnO_{2-x} were reported at 420°C and 715°C, respectively, showing an increase of the oxygen vacancy concentration with increasing temperature. The oxygen vacancy concentration x also increases with decreasing oxygen partial pressure. The formation of tin vacancies has also been reported at temperatures above 800°C causing an increase of the lattice constants [47].

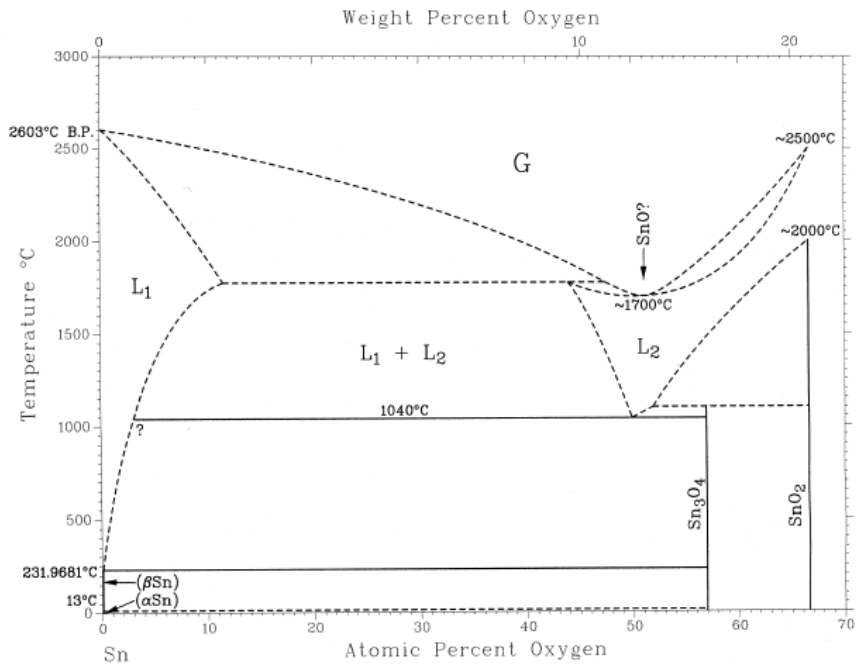
The Sn-O system is not completely understood and two different phase diagrams have been found in the literature [25, 48]. The first diagram (Figure 6a) considers the compounds Sn_3O_4 and SnO_2 , while the phase $\text{SnO}(s)$ is not described. This can be related to the work by Platteeuw et al. [49], who experimentally showed that $\text{SnO}(s)$ is unstable and decomposes into $\text{Sn}(l)$ and $\text{SnO}_2(s)$ at temperatures above 300°C, although gaseous SnO is stable.

The values reported in the literature for the melting points of SnO₂ and SnO are 1630°C and 1080°C, respectively, which is not quite in agreement with the phase diagram. The second diagram (Figure 6b) suggests the dissociation of SnO(s) to Sn₃O₄(s) and Sn(l) above 270°C and the coexistence of SnO₂(s) and Sn(l) at temperatures above 450°C [46]. The latter reactions have already been described by Lawson et al. [50]:

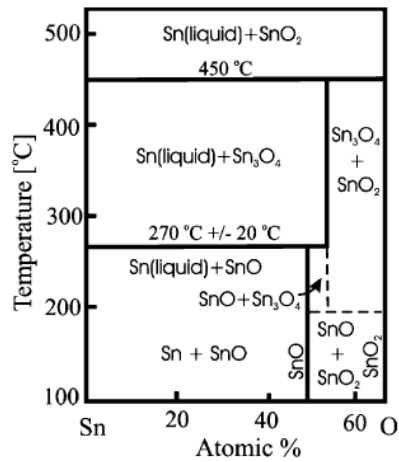


Both phase diagrams agree on the existence of the intermediate phase Sn₃O₄, which is composed of Sn in the oxidation states Sn(II) and Sn(IV). However, according to Platteeuw et al. [49]: “at least in the temperature range of 300-1127°C, liquid Sn, solid SnO₂ and gaseous SnO are the only stable phases”.

SnO₂ is only little volatile below 1500°C. The vapor pressure of SnO₂ is about 0.1 torr at 1350°C, 0.5 torr at 1450°C and increases to 2 torr at 1500°C [51]. For many oxides, the vapor pressure increases with the decrease of the oxidation state [52]. So the vapor pressure of SnO is expected to be higher than the vapor pressure of SnO₂.



(a)



(b)

Figure 6: Sn-O phase diagrams (a) from [48] (b) from [25].

1.4 Methods reported for the growth of SnO₂ nanowires

Several synthesis techniques have been developed to grow nanowires. They are divided in two categories: the bottom-up and the top-down approaches. The top-down approach is based on the patterning of a film until the reduc-

tion of the lateral dimensions to the nanoscale. The fabrication techniques rely on the standard micro fabrication methods, such as optical and X-ray lithography, e-beam and ion-beam lithography, printing and imprinting [6]. It enables the synthesis of well-ordered nanowires, which exhibit a high homogeneity in diameters and lengths, directly on site so no assembly step is necessary. Besides the high equipment costs and long preparation times, the top-down techniques are challenged by the technological difficulties to synthesise structures below 10 nm [4] or arbitrary three-dimensional objects [6]. Moreover, the nanowires synthesized with these techniques are in general not single crystalline [53].

The bottom-up approach relies on the assembly of individual atoms or molecules to build up the desired nanostructures by vapor phase transport, electrochemical deposition, solution-based techniques or template growth [53]. The main advantages of these techniques are: (1) the ability to generate structures with dimensions in the angstroms range, (2) the possibility to assemble the nanowires on nearly any type of surface (not necessarily CMOS compatible), (3) the high purity of the single crystalline nanowire produced, (4) the low cost of the experimental setups, and (5) the possibility to vary the doping of the nanowires. However, the main challenge faced by the bottom-up approach is the difficulty to integrate the nanowires on planar substrates: issue to transfer the nanowires on a substrate in an arranged manner on specific locations for the successive patterning.

It is expected that a combination of the top-down and the bottom-up approaches will eventually fulfil the requirements for the industrial production of metal oxide nanowires [6]. In the literature, no report on the synthesis of SnO₂ nanowires by the top-down approach has been found. The top-down approach has been used for the synthesis of Si nanowires [54, 55], Si/Ge heterostructures [54], and GaAs nanowires [56], among other materials. In this section, the synthesis of SnO₂ nanowires based on the bottom-up approach is presented.

The most important requirements to develop 1D nanocrystals are dimensions and morphology control, uniformity and crystalline properties. In order to obtain nanowires, a preferential growth direction with a faster growth rate must exist. There are different growth processes: catalyst-free and catalyst assisted processes, vapor and solution phase growth. In general, the catalyst assisted processes yield nanowires with uniform diameters [53] and the corresponding growth mechanisms are described by the vapor-liquid-solid (VLS) and the vapor-solid (VS) models.

1.4.1 Vapor phase growth

Thermal evaporation

The thermal evaporation is the process most used to grow SnO₂ nanowires. It occurs in a tube furnace, where the source material is first evaporated and then transported by a gas carrier towards the substrate. After nucleation, the nanowires grow by condensation of the evaporated source material on the seeds. Table 3 reviews the synthesis conditions reported in the literature for the growth of SnO₂ nanowires by vapor phase methods.

The source material (Sn, SnO or SnO₂ powder) is placed in an alumina crucible in the tube furnace. The substrate, where the SnO₂ nanowires grow, is usually a Si, alumina or quartz wafer, and may be coated with Au in order to induce a VLS growth mechanism. In most cases, the substrate is placed downstream a few centimetres away from the alumina crucible (typically 1-10 cm), though Hieu et al. [57] reported the growth of SnO₂ nanowires on substrates placed upstream from the source for a very low flow of carrier gas. The carrier gas (Ar or N₂, with possible addition of O₂) is introduced in the tube furnace with a precisely controlled flow (30-500 sccm). Many groups control also the pressure in the tube furnace. The temperature in the tube furnace is in the range 680-1550°C. The temperature depends mainly on the source material. Most authors report a process temperature in the range 700-900°C for Sn powder as source material, 900-1000°C for SnO powder and 1350-1550°C for SnO₂ powder. The dependence of the temperature with the source material can be linked with their melting point: 231.9°C for Sn, 1080°C for SnO and 1630°C for SnO₂. The duration of the heating phase is usually between 30 minutes and 2 hours.

PLD

Pulsed Laser Deposition (PLD) is also a process used for the synthesis of SnO₂ nanowires by vapor phase growth. The PLD technique consists in the ablation of a target material by a pulsed laser beam and the subsequent deposition of the vaporized material on a substrate. The process occurs under high vacuum or in a reactive environment, for instance in the presence of oxygen in order to deposit oxide materials. Tien et al. [58] reported the growth of SnO₂ nanorods by PLD from a target composed of SnO₂ on a single crystal silicon (100) substrate heated at 700-800°C. A dense array of SnO₂ nanorods is formed on the Si substrate. The as-grown single crystalline SnO₂ nanorods have diameters on the order of 50-90 nm and lengths of 1.5 μm. The growth mechanism is supposed to be a simple columnar growth mechanism. Yanagida et al. [59] also used the PLD technique to grow SnO₂ nanowires. The target material is pure Sn. The process occurs at an oxygen pressure of 10 Pa and a temperature of 800°C. SnO₂ nanowires were grown by a VLS growth mechanism on TiO₂ (001) substrate with the presence

of Au catalyst on the surface. Additionally to Au, the authors reported that the presence of a carbon layer (thickness of 2 nm) on the substrate improved the VLS growth. It is suggested that the carbon layer acts as a seed and/or catalyst, contributing to an initial nucleation stage within the metal catalysts. PLD is a versatile method, which enables the doping of the grown SnO₂ nanowires with other chemical elements, such as Sb [60] or Ta [61].

CVD

Instead of vaporizing a solid target material, another technique consists of introducing directly gaseous precursors in a CVD reactor for the recrystallization, as reported by Mathur et al. [62]. The alkoxide precursor [Sn(O^tBu)₄] is introduced into the reactor by applying a dynamic vacuum of 10⁻⁴ Torr and heating the precursor reservoir to a temperature in the range 20-45°C. The Si-substrate coated with Au particles is heated to 550-750°C. The as-grown single crystalline SnO₂ nanowires have diameters matching the size of the deposited Au particles (60-80 nm for particle size of 70 nm). The decomposition of the precursor is discussed in the original paper and leads to the formation of SnO₂ nanowires by a VLS growth mechanism. Müller et al. [63] used similar synthesis conditions but reported on the influence of the gaseous precursor [Sn(O^tBu)₄] or [Sn(O^tBu)₂]₂ on the surface properties of the SnO₂ nanowires.

Growth mechanism

The growth mechanism of the SnO₂ nanowires is also discussed in most of the publications referenced in Table 3. Three mechanisms are suggested to explain the vapor phase growth: the vapor-liquid-solid (VLS), the self-catalytic VLS and the vapor-solid (VS) mechanisms.

The VLS growth mechanism was first proposed in 1964 by Wagner and Ellis [91] for the growth of Si whiskers on Au particles. The VLS growth mechanism is named after the three phases involved in the growth process: the vapor phase precursor, the liquid catalyst droplet and the solid crystalline product. In 2001, Wu et al. [92] reported the real-time observation of semiconductor nanowire growth in an in situ high temperature transmission electron microscope (TEM), thus providing direct evidence of the VLS growth mechanism. The VLS growth mechanism involves a metal catalyst, which is deposited on the growth substrate and act as nucleation seeds. For the synthesis of SnO₂ nanowires, the metal catalyst is often a Au thin film (thickness below 10 nm) or Au nanoparticles, though Fort et al. [87] also reported the catalytic effect of Pt nanoparticles. The precursor material is evaporated and forms a liquid alloy droplet with the catalyst. The precipitation occurs when the liquid droplet becomes supersaturated with the precursor material, thus producing the nanowire. The diameter of the

Table 3: Synthesis conditions reported in the literature for the growth of SnO₂ nanowires by thermal evaporation.

Source material	Substrate	Carrier gas	Flow (sccm)	Temperature (°C)	Pressure (torr)	Time (min)	Growth mechanism	Reference
Sn	quartz	H ₂ /O ₂	200/5	850	0,7	30	Self-catalytic VLS	[64]
Sn	Si	Ar	50	900	ambient	60	-	[65]
Sn	Si + Au	N ₂ /O ₂	300/10	900	5	-	-	[66]
Sn	Si + Au	N ₂ /O ₂	(99%/1%)	800	-	120	-	[33]
Sn	Si + Au	N ₂	50	800	-	60	VLS	[67]
Sn	Si + Au	Ar	50	850-1000	-	60	VLS	[68]
Sn	Si + Au	Ar	500	900	-	60	VLS	[69]
Sn	Si + Au	Ar/O ₂	150/12.5	1080	6,4	60	VLS	[70]
Sn	Si + Au	Ar/O ₂	60/0.5	900	1	60	VLS	[71]
Sn	Si + Au	O ₂	0,5	750	-	25	-	[72]
Sn	Si + Au	O ₂	0,5	750	-	20	-	[73]
Sn	Si + Au	O ₂	0,3	800	2	15, 30, 60	VLS	[74]
Sn	Si + Au	O ₂	0,3	700, 750, 800	0.5-5	30	VLS	[57]
Sn	Al ₂ O ₃ boat	Ar/O ₂	(99%/1%)	900	-	60	VS	[75]
Sn	Al ₂ O ₃ boat	Ar	50	850-1000	-	60	VS	[68]
Sn	Al ₂ O ₃ boat	Ar	100	800	-	120	VS	[76]
SnO	Al ₂ O ₃ boat	Ar	15	680	200	480	Self-catalytic VLS	[77]
SnO	Al ₂ O ₃ boat	Ar	100	900	250	-	VS	[78]
SnO	Al ₂ O ₃	Ar	50	1000	300	120	VS	[79]
SnO	Si + Au	O ₂	0.3-0.5	980	2-5	30	VLS	[80]
SnO	stainless steel	N ₂ or Ar	100	1050-1150	200-800	-	-	[81]
SnO + Sn	Si	Ar	50	900	100	60	Self-catalytic VLS	[82]
SnO + graphite	Si + Au	Ar	400	880	-	20, 90	VLS	[83]
SnO ₂	Si	Ar	500	1380	-	120	-	[84]
SnO ₂	6H-SiC	Ar	200	1550	-	90	Self-catalytic VLS	[85]
SnO ₂	Al ₂ O ₃	Ar	50	1350	300	120	VS	[79]
SnO ₂	Al ₂ O ₃ + Au	Ar/O ₂	50/0.5	960	100-200	120	VLS	[86]
SnO ₂	Al ₂ O ₃ + Pt	Ar	75	1370	75	90	VLS	[87]
SnO ₂ + carbon	Si + Au	N ₂	100	700	200	240	VLS	[88]
SnO ₂ + carbon	Si + Au	N ₂	300	950	650	60	-	[89]
SnO ₂ + carbon	stainless steel + Au	Ar	30	900	0,3	30	-	[90]

nanowires is controlled by the size of the catalyst droplets. The VLS growth is epitaxial, so the nanowires obtained exhibit a high crystalline quality.

The self-catalytic VLS growth mechanism does not require the addition of a catalyst material, because the catalytic effect involved in that case is directly provided by liquid droplets formed after decomposition and precipitation of the source material on the growth substrate. Chen et al. [77] reported the growth of SnO₂ nanowires by a self-catalytic VLS growth mechanism. The SnO source material is first evaporated. SnO dissociates following a two-step reaction to Sn(l) and SnO₂(s) at temperatures in the range 300-500°C [49, 93]. The Sn liquid droplets condensed on the growth substrate can provide the energetically favoured sites for adsorption of oxygen and SnO vapor and subsequent formation of SnO₂. Finally, the authors assume that the continuous dissolution of SnO₂ in the Sn droplets leads to a super-saturated solution and the SnO₂ nanowires grow by precipitation, as in a conventional VLS growth mechanism described above. In their report, Li et al. [85] present the growth of SnO₂ nanowires by a self-catalytic VLS growth mechanism from SnO₂ powder. The authors suggest that SnO₂ is decomposed to vapor phase SnO_x and Sn at 1550°C, transported to the substrate in the low-temperature zone in order to enable the condensation of Sn liquid droplets, which act as nucleation sites for the further VLS growth mechanism.

The VS growth mechanism is a catalyst-free growth process, where the source material is evaporated, oxidized and directly condensed on the growth substrate. It is suggested that the VS mechanism is mainly governed by the minimization of the surface free energy. Therefore, the initially condensed molecules form seed crystals serving as nucleation sites and facilitating the directional growth to minimize the surface energy [53]. Sun et al. [76] reported the growth of SnO₂ nanobelts by a VS mechanism. They assumed that the Sn vapor generated from the Sn powder combines with oxygen to form SnO vapor. As SnO is metastable, it decomposes to Sn and SnO₂. The decomposition is followed by the condensation of SnO₂ nanoparticles on the substrate, which act as nucleation sites and initiate the growth of SnO₂ nanobelts via the VS mechanism. Furthermore, the authors suggest that the sharp tip observed at the end of the nanobelt acts as the energetically favourable site for absorbing the SnO₂ clusters from the vapor, eventually leading to the one-dimensional growth of the SnO₂ nanobelts.

1.4.2 Solution phase growth

The solution phase growth methods are usually conducted at low temperature, so complexity and cost are reduced. They lead in general to SnO₂ nanowires with an inferior crystalline quality in comparison with the vapor phase growth methods. They can be divided into the template-assisted and

template-free methods.

Template-assisted synthesis

Template-assisted synthesis has mainly been developed for the fabrication of SnO₂ nanotube or nanowire arrays. Sol-gel approaches have been used to deposit SnO₂ into the tubular pores of the template, such as cellulose fibers [94] or anodic aluminium oxide (AAO) [95], leading to the formation of polycrystalline SnO₂ nanotubes. Wang et al. [96] immersed the AAO template in a colloidal suspension of SnO₂ nanoparticles to enable the infiltration casting of the SnO₂ nanoparticles into the nanotubular channels of the template. The SnO₂ nanoparticles were chemically bound by thermal treatment and the AAO template was removed in a NaOH solution to form the nanotubes. Another strategy reported by Kolmakov et al. [97] consists in filling the AAO template with metallic Sn by electrodeposition and a successive oxidation step results in the formation of SnO₂ nanowires with controlled lengths and diameters, which can be used as gas sensors.

Another technique consists in using surfactant assisted micelles as soft template. This approach has been developed by several groups. N. Wang et al. [98] reported the synthesis of polycrystalline SnO₂ nanotubes, Y. Wang et al. [99] produced polycrystalline SnO₂ nanowires, and Ye et al. [100] synthesized single crystalline SnO₂ nanoribbons.

Template-free synthesis

There are three template-free synthesis methods reported in the literature to synthesize SnO₂ 1D nanostructures: the hydrothermal process, the electrospinning method and the molten-salt synthesis. Each method is developed in the following paragraphs.

The hydrothermal process is a method to grow single crystals based on the solubility of minerals in an aqueous solution at high temperature (usually above 100°C) and pressure (higher than 1 bar). The synthesis occurs in an autoclave, where a gradient of temperature enables the spatial separation of the dissolution of the precursors (formation of crystal seeds) and the crystal growth.

The synthesis of SnO₂ nanorods and nanowires based on the hydrothermal process has been developed by several research groups. The first reports demonstrating the synthesis of SnO₂ nanorods by the hydrothermal process are the one by Cheng et al. [101], who showed SnO₂ nanorods with a single crystalline structure and small dimensions (15-20 nm in length and 2.5-5 nm in diameter) and the one by Vayssieres et al. [102], who synthesized larger nanorods (500 nm in length and 50 nm in diameter) with a polycrystalline structure. Later on, Shi et al. [103] and Xi et al. [104] synthesized single crystalline SnO₂ nanorods and demonstrated the high sensitivity of the SnO₂ nanorods gas sensors upon exposure to ethanol. Qin et al. [105] and Lupan

et al. [106] reported the growth of single crystalline SnO₂ nanowires with high aspect ratio. Zhang et al. [107] chose a different solvent and conducted the reaction in a reverse microemulsion solution resulting in the synthesis of SnO₂ nanorods with diameters of about 8-15 nm and lengths in the range 150-200 nm.

Electrospinning is a simple, versatile and low-cost method for producing nanofibers of organic or inorganic materials. A sol-gel solution containing a polymer and inorganic precursors is electrospun on a substrate to form the fibers. Subsequently, the fibers are calcined in order to enable the decomposition of the organic components as well as the oxidation and crystallization of the fibers to obtain the desired composition and nanocrystalline structure. The electrospinning setup consists of a metallic needle, which is connected to the syringe containing the precursor solution, and an electrically conductive collector. When a high voltage is applied between the needle and the collector, the solution is ejected, continuously stretched and elongated by electrostatic repulsive forces, leading to the formation of a long, thin, and uniform thread [108]. The solvent rapidly evaporates during the spinning process, which results in decreasing the diameter of the thread, thus leading to the formation of an ultrathin fiber. Moreover, reactions such as hydrolysis, condensation and gelation of the precursors also influence the morphological and microstructural evolution of the fibers during electrospinning [108, 109]. In the end, the charged fiber is deposited on the grounded collector placed under the needle as a result of electrostatic attraction.

Electrospinning is a popular synthesis method to obtain SnO₂ nanofibers with diameters in the range 100-300 nm [109, 110], as well as Pd-doped [109, 111] or Pt-doped [32] SnO₂ nanofibers. Kim et al. [112] presented a slightly different approach than conventional electrospinning in order to synthesize SnO₂ nanotubes. First, polyacrylonitrile (PAN) fibers were electrospun. Subsequently, SnO₂ thin films were coated on the PAN nanofibers by plasma-enhanced atomic layer deposition (PEALD). Finally, the SnO₂ thin film-coated PAN nanofibers were annealed at 700°C to burn out the PAN template and crystallize the SnO₂ coating. The as-synthesized polycrystalline SnO₂ nanotubes have diameters of about 100 nm. The wall thickness of the nanotubes (ranging from 8 to 37 nm) was controlled by the number of ALD cycles.

The molten-salt method is a relatively low temperature synthesis technique for preparing single crystalline nanomaterials. The precursor material, the salt and the surfactant are ground to a fine powder, which is heated at temperatures in the range of 700-800°C for up to 2.5 h. After cooling down, the sample is washed with distilled water to dissolve and remove the salt. The molten-salt method has been reported in the literature for the synthesis of SnO₂ nanorods [113, 114, 115, 116, 117]. The as-prepared single crystalline SnO₂ nanorods are ca. 20-70 nm in diameter and up to several micrometers

in length. The salt-solution medium facilitates the dissolution of the reactants and enables a rapid diffusion of the species. The role of the surfactant is crucial, since it serves as microreactor to confine the crystal growth. The growth mechanism of the SnO₂ nanorods by molten-salt method is assumed to result from the dissolution of fine particles and the successive deposition of the components on larger particles.

2 Synthesis of SnO₂ nanowires

The synthesis of SnO₂ nanowires employed within this thesis is a two-step process: First, a SnO₂ thin film is deposited on a Si-substrate by spray pyrolysis. In the second step, the SnO₂ thin film is heated in a tube furnace to 900°C in argon atmosphere for 1.5 hour, which results in the growth of SnO₂ nanowires. Consequently, this chapter is composed of two main parts. The first part describes the principle of spray pyrolysis and how the process is developed for the deposition of a SnO₂ thin film with reproducible parameters. The second part details the experimental approach followed in order to find the optimal conditions for the growth of SnO₂ nanowires and to get a better understanding of the nanowire growth mechanism.

2.1 Spray pyrolysis development

2.1.1 Motivation

The hydrolysis of tin(IV) compounds, mostly SnCl₄, has already been reported in the 1950's as an industrial method to deposit SnO₂ layers [51]. The solvent is water or more often a solution of mixed water and alcohol (methanol or ethanol). The addition of alcohol, which has reducing properties at higher temperatures, results in the desired O-deficiency in the SnO₂ layer.

Spray pyrolysis was first reported in 1966 by Chamberlin and Sharkman [118], who demonstrated the growth of CdS thin films for solar cell applications. Since then, numerous materials have been deposited as thin films by spray pyrolysis, such as: ITO for photovoltaic devices [119], WO₃ for electrochromic applications [120], TiO₂ for antireflexion, transparent or self-cleaning coatings [121], Yttria-stabilized zirconia (YSZ) used in solid oxide fuel cells [122, 123], ZnO [124], In₂O₃ [125, 126] and SnO₂ [125, 127, 128, 129, 130, 131, 132] for gas sensors.

SnO₂ is a prominent material for gas sensing and the techniques used to deposit thin films are often based on physical vapor deposition (PVD) processes such as evaporation or sputtering. Spray pyrolysis offers an attractive alternative to those complex processes. It is based on very simple equipment and does not require vacuum, which results in low operational costs [133]. Spray pyrolysis is a chemical vapor deposition (CVD) process used to prepare various coatings, such as thin and thick films and powders. The advantages of spray pyrolysis encompass the recognised benefits of CVD over PVD processes: possibility to coat large surfaces with high aspect ratio structures, rapid film growth rates, control of stoichiometry and ability to fabricate abrupt junctions [134]. In addition, the spray pyrolysis process exhibits a few specific advantages [135]:

- The moderate temperatures required for the process (100-500°C) enable the coating of a large variety of substrates nearly without restrictions to the size and structure.
- The deposition rate and the thickness of the film can be controlled over a wide range by changing the spray parameters.
- The doping of the thin film is versatile and almost any chemical element can be added to the precursor solution in any proportion.

Considering its simplicity, spray pyrolysis is a method of choice for the deposition of SnO₂ thin films, which serve as precursor material in the SnO₂ nanowire growth. Besides, the potential for mass production of SnO₂ thin film gas sensors deposited on processed CMOS chip with this method is very attractive and motivates our interest to develop a reliable and reproducible spray pyrolysis process.

2.1.2 Theory

In this section, the principle of spray pyrolysis is introduced. Spray pyrolysis can be regarded as the succession of three processes, which are described in the following paragraphs. First the atomization of the precursor solution, second the transport of the atomized droplets, finally the decomposition of the droplets on the heated substrate.

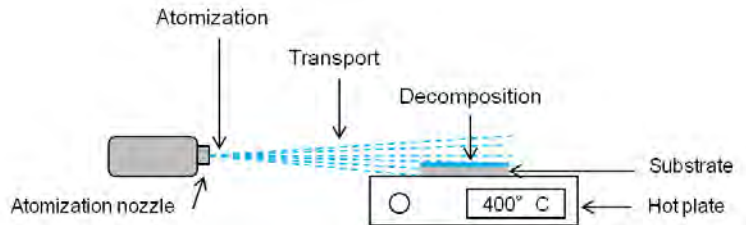


Figure 7: Schematic representation of the spray pyrolysis process as a succession of the atomization of the precursor solution, the transport of the precursor droplets, and the precursor decomposition on the heated substrate.

Atomization techniques

The simplest spray pyrolysis processes use the pressure atomization technique. This technique relies on the mixing of the precursor solution with the carrier gas both supplied to the atomizing nozzle with a defined pressure. There are several other atomization techniques enabling the formation of smaller droplets with a narrower size distribution [135].

- Ultrasonic spray pyrolysis: An ultrasonic atomizer is connected to an oscillator and the solution is vaporized using the ultrasonic waves [136].
- Corona spray pyrolysis: The droplets are charged in the electric field of a corona discharge, which enables the controlled transport of the droplets towards the substrate by electric forces [125].
- Improved spray pyrohydrolysis: The substrate is located above the spraying chamber and the droplets are sprayed upwards to the substrate with a 90° angle. This specific geometry enables to filter the larger droplets, which cannot be transported by the carrier gas due to the gravitational force and must return to the spraying chamber [124].
- Electrostatic spray pyrolysis: A positive high voltage is applied to the nozzle through which the precursor solution is forced to flow. The positively charged droplets undergo mainly the electrostatic force and tend to move towards the substrate [131, 137].

Aerosol transport of droplets

After atomization of the precursor solution, the droplets are transported to the heated substrate with an initial velocity determined by the atomizer and a horizontal trajectory following the carrier gas flow. However, the trajectory is also influenced by the forces applied to the droplet once leaving the atomizer [128]. The total force applied to the droplet is the sum of the gravitational, thermophoretic and Stokes forces:

$$F = F_g + F_t + F_S \quad (4)$$

The gravitational force F_g pulls the droplet downward. This force influences mainly the trajectory of larger droplets, because it depends on the mass of the droplet. The thermophoretic force F_t slows the droplets down, when they approach the heated substrate. It is caused by the thermal gradient in the immediate vicinity of the heated substrate (a few millimetres above). The Stokes force F_S is due to the friction of the droplets with the air molecules. It depends on the velocity and size of the droplet, so the influence is higher on the large droplets. In case of pressure atomization, gravity is the main driving force to consider. In case other atomization techniques are used, such as ultrasonic, corona or electrostatic spray pyrolysis, the electrical force, which depends on the field produced and on the droplet charge, is the main driving force and must be additionally considered.

Precursor decomposition

The principle of spray pyrolysis relies on the thermal decomposition of the precursor, followed by the oxidation of the decomposition products and the

formation of the desired thin film on the substrate. For the formation of SnO₂ thin films, the chemical reaction occurring directly on the surface of the heated substrate is described by the following reaction equation:



It is very important that the thermal decomposition occurs in the vicinity of the substrate and not before. Therefore the precursor is dissolved in a solvent, which cools the precursor to prevent the thermal decomposition from happening too soon. Then the solution is atomized to form small droplets directed to the hot substrate with the flow of an inert carrier gas. Ideally the solvent is vaporized just as the droplet approaches the substrate. Viguié and Spitz [138] and Siefert [125] described the precursor decomposition according to the temperature of the substrate and the initial droplet size, as illustrated in Figure 8.

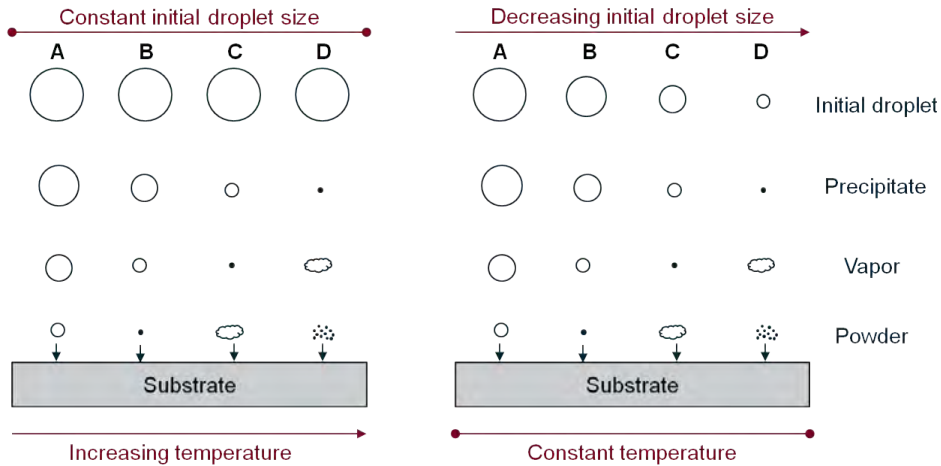


Figure 8: Mechanism of precursor decomposition depending on the substrate temperature and the initial droplet size, after [133].

For a low temperature or a large initial droplet size, the process A is obtained. The droplet is not entirely vaporized on the way to the substrate. The fully vaporization of the droplet occurs once in contact with the substrate, resulting in the deposition of a dry precipitate. The vaporization step goes along with a local cooling of the substrate, which slows down the kinetics of the reaction. The surface obtained is rough and the film produced exhibits weak sticking properties.

In the process B occurring at low to intermediate temperatures or for a medium-sized droplet, the hydrolysis reaction occurs in the liquid phase above the substrate, the droplet is completely vaporized at the contact to

the substrate, so a SnO_2 powder is formed and deposited on the surface [128].

In the case of intermediate to high temperatures or for small droplets (process C), the solvent is completely vaporized on the way to the substrate, which results in the formation of a precipitate. The precipitate sublimates in the vicinity of the substrate and the reactant molecules undergo a heterogeneous reaction: diffusion to the surface, adsorption, surface diffusion, chemical reaction and incorporation into the lattice, followed by desorption of the product molecules from the surface and diffusion away from the surface into the vapour phase. The process described is a classical CVD process, which leads to a thin film of high quality.

By further increasing of the temperature or decreasing of the initial droplet size, the process D is obtained. The precipitate is formed so fast and far from the surface that a homogeneous reaction occurs in the gas phase. The micro-crystallites formed condense as a powdery precipitate on the substrate without deposition reaction.

Brinzari et al. [139] estimated the temperature ranges corresponding to the different spray processes for SnO_2 thin films deposited from a 0.2 M aqueous solution of pentahydrate stannic chloride ($\text{SnCl}_4 \cdot 5\text{H}_2\text{O}$). They identified the beginning of the film growth at 270°C , which is in agreement with the temperature of 250°C reported in [140] for the same parameters (0.2 M $\text{SnCl}_4 \cdot 5\text{H}_2\text{O}$ water solution). Moreover, they observed two distinct changes in the film morphology as a function of the process temperature at 350°C and at 410°C . In the range $300\text{-}350^\circ\text{C}$, separate crystallites with a sphere-like shape are formed. The authors hypothesized that the atom mobility on the surface is very low and the coalescence of the crystallites is not possible due to the low temperature, which refers to process A. At temperatures $350\text{-}410^\circ\text{C}$, the sphere-like shaped crystallites agglomerate, which corresponds to the process B. Above 410°C , the growth of nanocrystals is reported, which goes along with the description of a heterogeneous reaction during a CVD process.

To sum up, a droplet may undergo a CVD process during spray pyrolysis if the vaporization of the solvent occurs on the way to the substrate and the precipitate formed sublimates in the vicinity of the substrate, so the reactant molecules contained in the vapour react heterogeneously at the surface of the substrate to form a thin film. Obviously, it is not possible to recreate those ideal conditions experimentally. However, it is possible to approach CVD conditions by studying the main experimental parameters influencing the spray pyrolysis deposition process and the properties of the deposited thin film.

Influence of deposition parameters on thin film properties

Role of pyrolysis temperature As already explained above from theoretical models, temperature is a crucial parameter for the spray pyrolysis process. First, the pyrolysis temperature (T_{pyr}) must be set in the correct range to enable the precursor to react as much as possible in CVD conditions. Second, the temperature can be finer tuned to control the film properties, such as growth rate and crystallite size.

Concerning the growth rate, a transition is identified between low deposition temperatures, where the growth rate increases with increased pyrolysis temperature, and high deposition temperatures, where the growth rate stays constant with further increase of the pyrolysis temperature [125]. Briand et al. [136] deposited thin films in the range 460-540°C and observed a transition at a temperature of 500°C. In the study by Sanz Maudes et al. [127] the deposition temperature varied between 300°C and 650°C and the transition temperature was estimated at 515°C. The authors concluded that the film growth was kinetically limited by surface reactions (adsorption/desorption) for low deposition temperatures and it was controlled by mass transfer of the reactants (diffusion) at higher temperatures. In other studies the growth rate keeps increasing at higher temperatures. Sanon et al. [129] observed an exponential increase of the growth rate with increasing temperatures in the range 280-400°C. Korotcenkov et al. [140] reported a transition above 400°C with a lower slope of the growth rate increase with increasing temperature. Therefore, the authors concluded that the kinetic factor went on influencing the growth rate of the film even at higher temperatures for their experimental conditions.

Besides, the substrate temperature has also an influence on the grain size of the SnO₂ films: the crystallite size increases with increasing temperatures. Briand et al. [136] reported a mean grain size of 8-9 nm for deposition at 460-500°C and 14 nm at 540°C. Sanz Maudes et al. [127] observed mean grain size of 24 nm and 32 nm for deposition temperatures of 475°C and 615°C, respectively. Sanon et al. [129] found a linear increase of the crystallite size with the pyrolysis temperature between 300°C (average grain size of 12 nm) and 370°C (average grain size of 55 nm). Korotcenkov et al. [140] reported an average grain size of about 10 nm for deposition temperature of 350°C and 30 nm at 500°C.

From those reports, it is concluded that the temperature is the most influencing parameter in the spray pyrolysis process. The qualitative influence of the deposition temperature on the film properties is understood, however, a quantitative approach is not possible because of the numerous experimental parameters making each spray pyrolysis process unique.

Role of precursor solution SnO₂ thin films have been prepared by spray pyrolysis processes from SnCl₄ dissolved in water or alcohol mostly. Alcoholic solvents are often preferred because their low surface tension and viscosity enables the formation of small droplets and their low boiling point facilitates the vaporization of the droplets [135]. Other solvents, such as butyl acetate [128] or ethyl acetate [141], have also been investigated.

Sears and Gee [128] performed distillation experiments in order to predict, which solvent is most likely to lead to a CVD process. They reported that an aqueous solution of SnCl₄ could not be deposited as a true CVD process, because the droplet was not completely vaporized, so the hydrolysis reaction occurred in the liquid phase before the droplet reached the surface, which led to the deposition of a SnO₂ powder on the substrate. Nonetheless, a semi-CVD process could occur at temperatures above 250°C. The addition of ethanol to the SnCl₄ in water solution enabled a better vaporization of the droplet, though the formation of powder residue was still observed to a small extent. The substitution of water or water-alcohol solvent by non-aqueous solutions such as butyl acetate resulted in the total vaporization of SnCl₄ without powder formation, which was the confirmation for a true CVD process. The authors concluded that a SnO₂ film could be deposited from non-aqueous solutions by a true CVD process.

Additionally to the choice of the solvent, different precursors may be used for the fabrication of SnO₂ thin films by spray pyrolysis. They are listed in Table 4. Most of the precursors are already reported in the reviews by Patil [135] and Perednis et al. [142].

Table 4: Preparation conditions for the deposition of SnO₂ thin films by spray pyrolysis.

Precursor	Solvent	T _{pyr} (°C)	References
SnCl ₄	water-ethanol mix	300-650	[127, 128]
SnCl ₄	water	450	[143]
SnCl ₄	ethanol	250-400	[144, 145]
SnCl ₄	butyl acetate	-	[125, 128]
SnCl ₄ · 5H ₂ O	ethanol	280-440	[144]
SnCl ₄ · 5H ₂ O	water	250-550	[128, 139, 140]
(NH ₄) ₂ SnCl ₆	water	300	[146]
(CH ₃ COO) ₂ SnCl ₂	ethyl acetate	-	[146]
(C ₄ H ₉) ₃ SnOOCCH ₃	ethanol	340-480	[147]
(C ₄ H ₉) ₄ Sn	ethanol	340-480	[148, 149]
(C ₄ H ₉) ₂ Sn(OOCCH ₃) ₂	ethanol	340-480	[148]

The precursor concentration in the sprayed solution must be carefully chosen as a compromise between time of deposition, which influences the substrate cooling, control of the film thickness and growth rate of the film [140]. Moreover, Gourari et al. [131] reported that the grain size of the SnO₂ thin film increased with a higher concentration of the precursor solution.

The ageing of the sprayed solution, from the moment it is prepared until it is sprayed, may play an additional role in the deposition rate of thin films. Korotcenkov et al. [140] investigated that ageing effect and found that the deposition rate of the film was decreased exponentially with the ageing of the precursor solution within 8 hours after the preparation of the solution. This effect abated after 8 hours and the deposition rate was almost the same after 8 hours or 24 hours. The authors assumed that the hydrolysis of the SnCl₄-water solution was responsible for the ageing effect. Therefore, it is advised to let the solution ageing before use, although no other strong influence on the film parameters was reported.

Role of spraying apparatus The increase of the carrier gas pressure results in the decrease of the film thickness, which is probably due to the simultaneous increase of the velocity of the droplets and the decrease of the size of the droplets [140]. The carrier gas pressure also influences the precursor concentration in the droplets.

Sears and Gee [128] reported on the geometry of the spray pyrolysis apparatus. The film deposition occurred from a nozzle placed directly above the substrate, so the spray flow was directed with a 90° angle to the substrate. The authors observed the formation of a powder at the center, where the droplets were forced to impinge the hot surface, but away from the center, where the droplets were not directly in contact with the surface, they noticed the growth of the film. From those considerations, it seems more appropriate to place the nozzle on the side to have a spray flow parallel or with a small angle to the surface.

When looking at the literature, there is no description of a unique spray pyrolysis process. Actually there are about as many set-ups as there are research groups working with spray pyrolysis. Considering the diversity of parameters to fix (temperature, atomizing nozzle, precursor material, solvent and spraying apparatus), there is no quantitative information valid for all spray pyrolysis processes. Each group must analyse and optimize their own process. It is also very complicated to reproduce the same conditions described in the literature because of the little technical information reported. Therefore, much effort has been put in the development of a reproducible spray pyrolysis process, which is presented in the next section. A major goal is to establish this process in cooperation with EV Group (EVG) [150], who is interested in fabricating an industrial tool for spray pyrolysis.

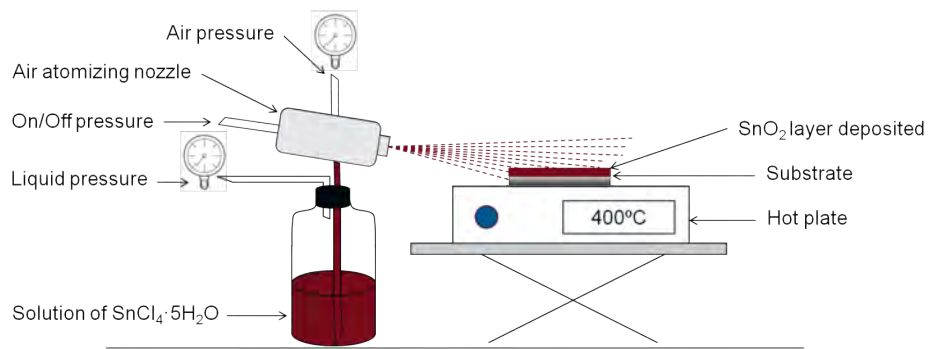
2.1.3 Methods

The apparatus used for the spray pyrolysis is shown in Figure 9. The process takes place in a fume hood to ventilate the corrosive vapours of hydrogen chloride (HCl) formed during the spray pyrolysis reaction (see Equation 5 in 2.1.2). The precursor solution is contained in a glass bottle under pressure. The liquid is atomized by a spray atomizing nozzle and the droplets are transported in a gas flow to the substrate deposited on a hot plate. The nozzle is situated on the side of the hot plate, approximately 5 cm higher than the hot plate and 25 cm away from the substrate. The flow is directed parallel to the surface of the hot plate with a slight inclination down to the hot plate.

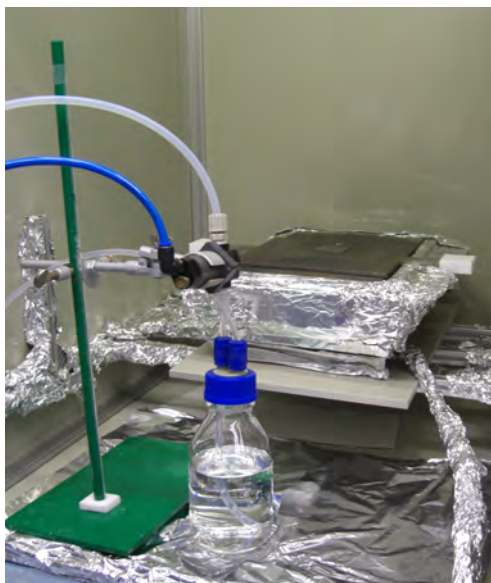
A 0.28 M solution of pentahydrate stannic chloride ($\text{SnCl}_4 \cdot 5\text{H}_2\text{O}$) in ethyl acetate is used as precursor. It is prepared as follows: 50.1 g of the $\text{SnCl}_4 \cdot 5\text{H}_2\text{O}$ powder ($M = 350.6 \text{ g}\cdot\text{mol}^{-1}$) is added in a 500 mL volumetric flask, which is then filled with ethyl acetate until the ring graduation mark in order to dissolve the $\text{SnCl}_4 \cdot 5\text{H}_2\text{O}$ powder. The precursor solution is prepared one day before use to avoid any ageing effects of the solution, as described earlier in 2.1.2.

The atomizing nozzle used is a QuickMist automatic air atomizing nozzle 1/4QMJAU-N SUQF130 from Spraying Systems Co [151]. The nozzle produces a flat spray pattern, so the droplets are mainly dispersed in the lateral direction. The working principle of the nozzle is illustrated in Figure 10. It is based on a pressure-fed liquid system, where the liquid is supplied to the nozzle under pressure. When the needle is retracted, the liquid and compressed carrier gas are mixed internally to produce a completely atomized spray and the nozzle starts spraying. The retraction of the needle is controlled by an internal air cylinder for controlled on-off operation, which interrupts only the liquid portion of the spray. As illustrated in Figure 9a, the pressures applied to the liquid and the carrier gas pressure are precisely controlled by pressure gauges. The pressure applied to the liquid is set to 0.7 bar, for the nitrogen, which is used as carrier gas, the pressure is set to 1.8 bar.

The pyrolysis temperature is 400°C. This temperature has been measured by a thermocouple glued on a silicon chip placed on the hot plate. In order to reach the temperature of 400°C at the surface of the chip, the hot plate is set to a temperature of 455°C at the controller. The hot plate is a model Präzitherm PZ 38-3T, which is produced by Harry Gestigkeit GmbH [153]. The controller is a programmer PR 5-3T. The upper plate consists of titanium, which is known for its excellent resistance to corrosion. Titanium is therefore a material of choice to withstand the formation of HCl vapour as by-product during the pyrolysis reaction (see Equation 5 in 2.1.2). The substrates used for the deposition of the SnO_2 thin films are 2×2 cm



(a)



(b)



(c)

Figure 9: (a) Scheme of the spray pyrolysis process. (b) Image of the spray pyrolysis set-up. (c) Deposition of a SnO_2 thin film by spray pyrolysis on Si substrates placed on a hot plate at 400°C.

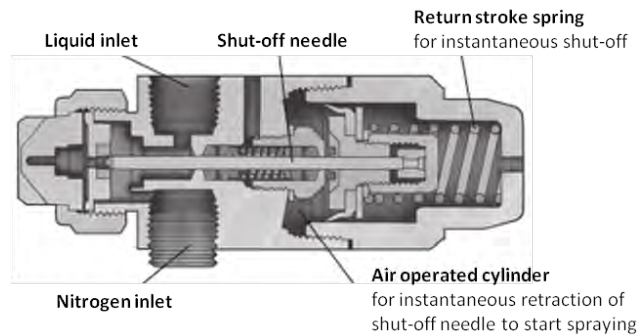


Figure 10: Diagram of the automatic air atomizing nozzle used. Adapted from [152].

sized silicon chips with native oxide (Si), silicon chips with 300 nm thermal oxide on top (SiO_2/Si) or silicon chips with 300 nm thermal oxide (SiO_2/Si) coated with 40 nm copper (Cu) by RF magnetron sputtering.

Thanks to the flat spray pattern of the nozzle, it is possible to process several chips at the same time. Therefore, nine chips are placed in the middle of the hot plate next to each other in a square pattern with three rows of three chips. The simultaneous processing of nine chips is further called a “run”.

One run of spray pyrolysis occurs as follows:

- The substrates are placed on the hot plate for 10 min. This step aims for the homogenisation of the temperature at the surface of the chips. In case of Cu-coated chips, the oxidation of the Cu-layer to cupric oxide (CuO) occurs simultaneously (see 2.1.4).
- The air atomizing nozzle is switched on to spray the $\text{SnCl}_4 \cdot 5\text{H}_2\text{O}$ in ethyl acetate solution. Typically, this step lasts 50 s, which results in the formation of a SnO_2 film with a thickness of about 100 nm. It also goes along with a decrease in the substrate temperature of about 15°C , which can be read on the temperature controller of the hot plate. The spray flow is stopped for 2 min to let the chips recovering the temperature of 400°C . Then the flow is turned on again for 50 s followed by another interruption of 2 min and a last spraying step of 50 s. After 3 successive spraying steps, the thickness of the SnO_2 film obtained is in the range 250-300 nm.
- After the last spraying step, the chips stay on the hot plate 2 min more in order to ventilate the corrosive HCl vapours formed during the spray pyrolysis reaction, before opening the fume hood and removing the samples from the hot plate.

The thickness of the SnO_2 film on the Si chips is measured with an optical interferometer. The film thickness of one chip (2×2 cm) is measured in five

spots and averaged to one value. The average film thickness is calculated over the thickness values of the nine chips of a single run. The succession of several runs processed in a day is further called a “session”. Several sessions are performed over weeks or months.

2.1.4 Results and discussion

Optimization of the spray pyrolysis process

The first step in the optimization of the spray pyrolysis process is to choose the temperature. The development of the spray pyrolysis process aims for the deposition of SnO₂ films used for two applications: (1) as precursor in the SnO₂ nanowire growth, which is of interest in this thesis, and (2) for SnO₂ thin film gas sensors, which is the focus of another R&D work [154]. The pyrolysis temperature was originally adopted for the integration of SnO₂ thin film gas sensors on CMOS chips. The maximum temperature, that the processed CMOS chips can withstand without damages, is 400°C. Therefore, it has been decided to set the process temperature to 400°C also for the deposition of SnO₂ films used as precursor in the SnO₂ nanowire growth and to optimize other process parameters.

Secondly, the size of the atomized droplets is optimized by adjusting the pressure applied to the precursor solution and the carrier gas pressure. The liquid pressure, which has a major influence on the growth rate of the film, is set to 0.7 bar. Low liquid pressures result in low film growth rates, so long spraying times are necessary to obtain the desired thickness. However, long spraying times result in a decrease of the temperature at the surface of the substrate. High liquid pressures increase the deposition rate, which may complicate the precise control of the film thickness. The carrier gas used is nitrogen with a pressure of 1.8 bar. On one hand, increasing the carrier gas pressure results in smaller droplets, but on the other hand, it increases the cooling effect of the flow on the substrate. When both pressure parameters are set, the initial droplet size and velocity are fixed.

Next, the deposition rate of the SnO₂ film is determined. Four substrates are coated with a SnO₂ thin film with different spraying times (without interruption): 15 s, 30 s, 45 s, and 60 s, respectively. The film thickness of each substrate is measured and the results are shown in Figure 11. A linear dependence of the film thickness with the spraying time is observed. Therefore, the desired thickness of the SnO₂ thin film is obtained by controlling the spraying time. The deposition rate, which is defined as the ratio of the film thickness over the spraying time, is newly measured before each spray pyrolysis session and the spraying time is consequently adapted. The average value of the deposition rate is 103 ± 13 nm/min, so the spray pyrolysis process presents a good reproducibility.

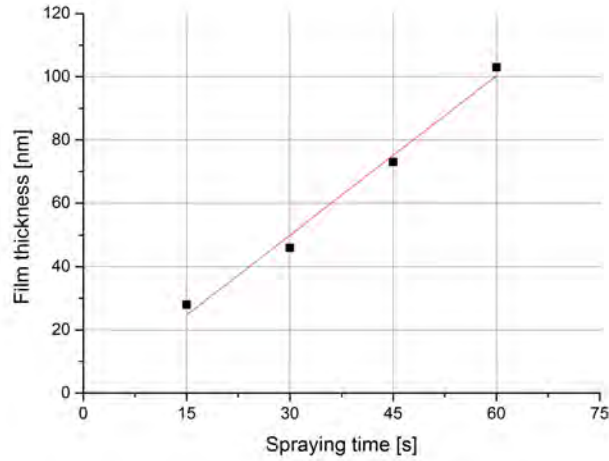


Figure 11: Dependence of the SnO₂ film thickness with the spraying time.

Figure 12 shows a photo of nine substrates after one run of spray pyrolysis. The run consists of three successive spraying steps of 50 s with an interruption of 120 s in between (as described on page 41). A homogeneous colouration over the substrates can be seen, which implies a homogeneous film thickness. The pink line at the edge of the three chips placed on the first row (when considering the flow direction) is characteristic for a locally thicker SnO₂ film. Since the spraying flow is almost parallel to the surface of the substrates, it is assumed that there is a perturbation of the spraying flow while overcoming the height of the first row of chips. Due to this flow perturbation, the vapour is probably locally denser and the film growth faster.

The average and the deviation (minimum-maximum) values of the film thickness are also indicated in Figure 12. The measured values are found in a range of 3-8% around the average value according to the position of the chip, which shows the excellent homogeneity of the film on one chip. The average of the film thickness on all nine chips of a run is 284 nm. The lowest value of the film thickness on all nine chips is 252 nm and the highest is 313 nm. So, the average film thickness on all nine chips is 284 ± 32 nm, which means that the distribution of the values is narrow: $\pm 11\%$.

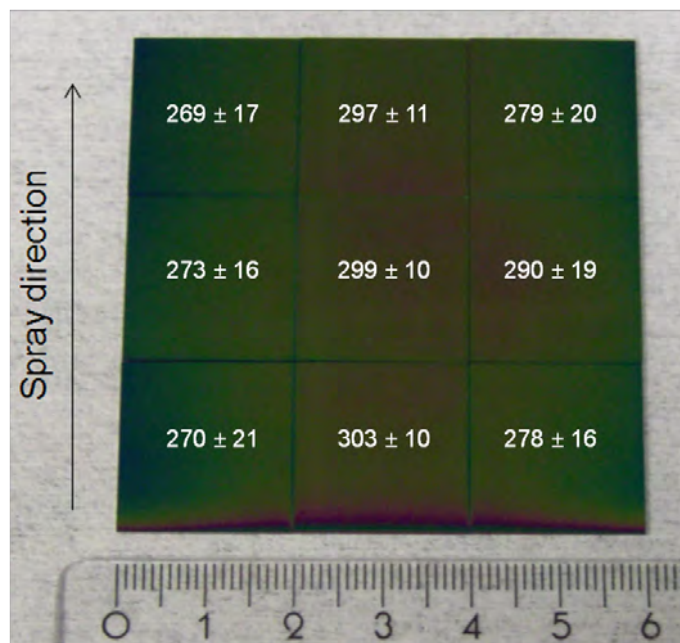


Figure 12: Photo of nine Si chips coated with SnO₂ film after spray pyrolysis and the corresponding film thickness values (in nm).

The optimization of the spray pyrolysis parameters leads to a reproducible process, which enables the deposition of a SnO₂ thin film on a surface area of 36 cm² with a very good homogeneity of the film thickness. However, further improvement could be achieved by more sophisticated machinery with either movable spray head or the employment of several spray heads in parallel, for example.

Characterization of the SnO₂ thin film

Figure 13 shows the X-Ray Diffraction (XRD) pattern of a SnO₂ thin film (thickness about 400 nm) right after deposition by spray pyrolysis (in blue). No diffraction peak can be seen, so the sprayed SnO₂ film presents an amorphous structure. After an annealing step at 400°C in ambient air for 30 min, the structure of the film becomes polycrystalline (black curve). The crystalline phase identified is cassiterite, tetragonal, with the following crystal lattice parameters: $a = b = 4.738\text{\AA}$, $c = 3.188\text{\AA}$, $\alpha = \beta = \gamma = 90^\circ$. This phase is stable with increasing temperatures up to 700°C, which is the maximum temperature achievable with this specific X-Ray diffractometer.

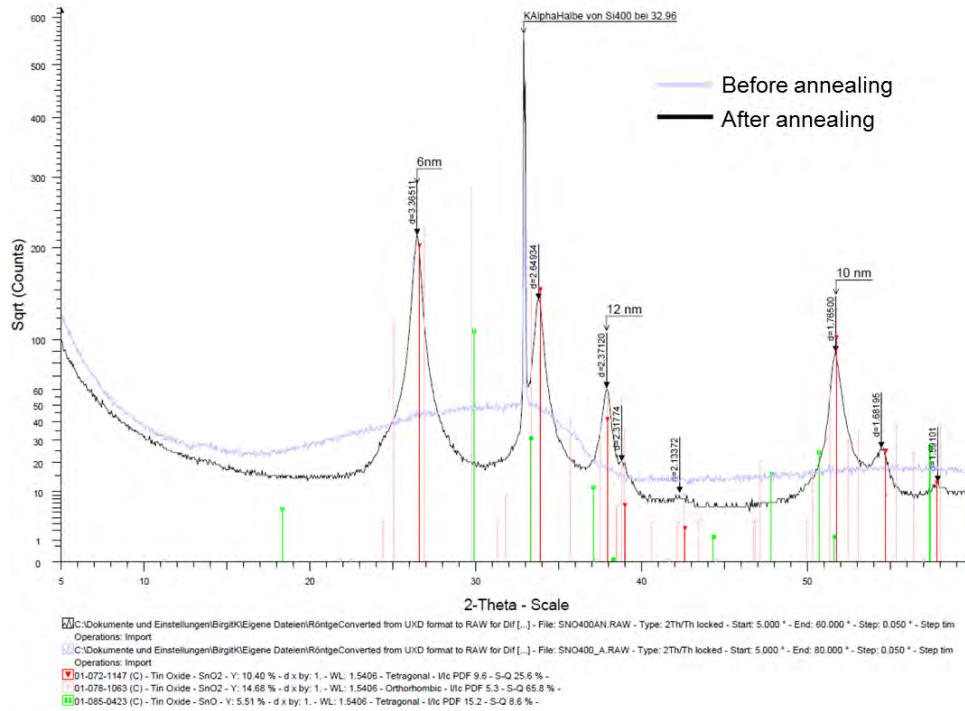


Figure 13: XRD pattern of the SnO₂ film before (in blue) and after (in black) annealing at 400°C for 30 min in ambient air.

The structural changes of the sprayed SnO₂ film are investigated in situ while increasing the temperature up to 700°C. The investigated sample is a substrate coated with a SnO₂ thin film (thickness about 400 nm), which has been previously heated for 13 hours at 350°C for another experimental purpose (not shown here). This annealing step resulted in the transition of the film structure from amorphous to crystalline. The diffraction patterns of the SnO₂ thin film are measured stepwise at temperatures between 350°C and 700°C in ambient air. Each measurement takes about 35 min. The results are shown in Figure 14. The table in the inset indicates the crystallite size, which is calculated from the first peak at about 26 deg using the Scherrer Equation. An increase of the intensity of the first diffraction peak with increasing temperature can be observed, which can be related to the increase of the crystallite size and the decrease of the amorphous part. The first XRD pattern at 350°C shows a crystalline SnO₂ thin film. XRD patterns have been measured (not shown here) after 12 hours at 200°C, and 5 hours at 300°C. The diffraction patterns of the SnO₂ thin film are measured stepwise at temperatures between 350°C and 700°C in ambient air.

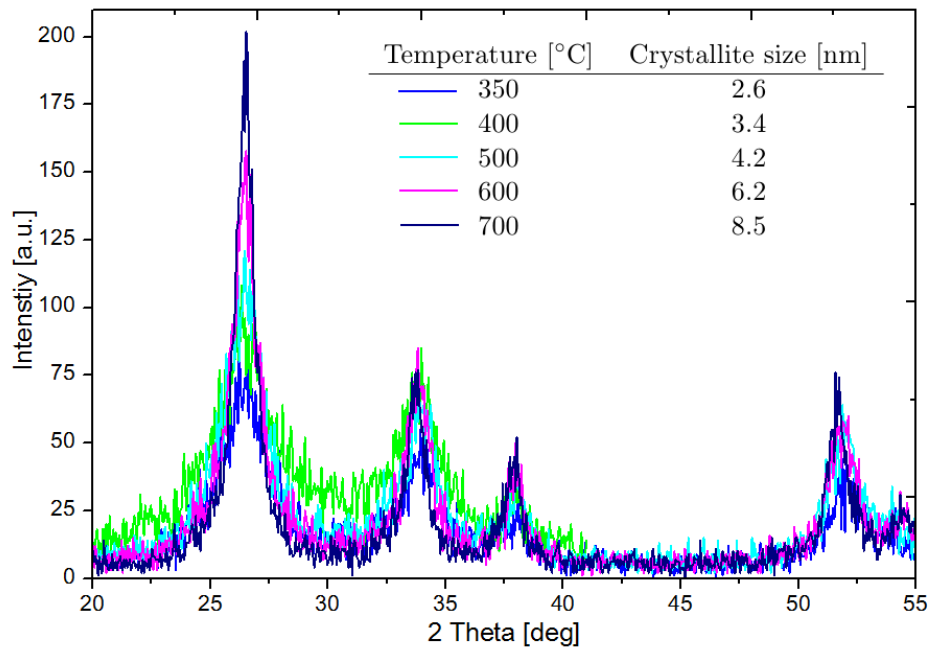


Figure 14: Evolution of the XRD patterns for a SnO₂ thin film (previously heated for 13 hours at 350°C, thickness about 400 nm) with increasing temperature from 350°C to 700°C. Inset: corresponding crystallite size calculated with the Scherrer Equation from the first diffraction peak at about 26 deg.

After spray pyrolysis, the SnO₂ film presents an amorphous structure. An annealing step at 400°C is necessary for the crystallization of the SnO₂ film. As can be seen on Figure 13, the structure of the film becomes polycrystalline after 30 min at 400°C in ambient air. The structure is fixed after this annealing step.

Complementary to the XRD measurements, a cross-section of a SnO₂ thin film deposited on a Si-chip by spray pyrolysis is investigated. The SnO₂ thin film has a thickness of about 60 nm. The sample has been annealed prior to analysis for 30 min at 400°C in ambient air. Figure 15 shows a high resolution transmission electron microscope (TEM) image of the SnO₂ thin film cut by a Focused Ion Beam (FIB) technique. The structure of the SnO₂ thin film is polycrystalline, as already shown with the XRD measurement. In addition, the structure is dense and no pores between the crystallites can be observed inside the film.

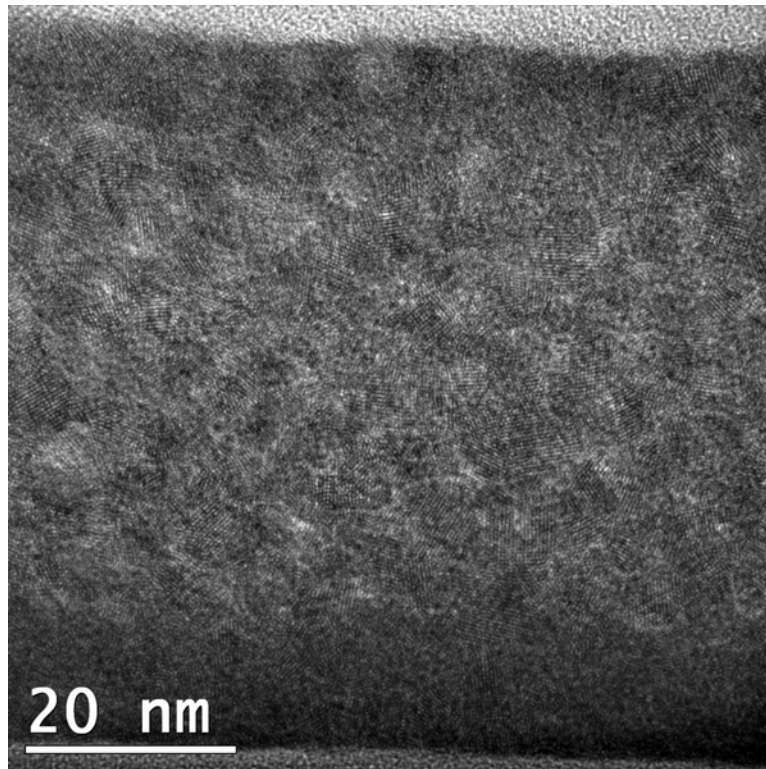


Figure 15: High resolution TEM image showing the cross-section of the non-porous nanocrystalline SnO₂ thin film deposited by spray pyrolysis.

Cu film on SiO₂/Si chip

As already mentioned in 2.1.3, SnO₂ is also deposited by spray pyrolysis on SiO₂/Si chips coated with a Cu thin film (about 40 nm) deposited by RF magnetron sputtering. The first step of the spray pyrolysis process is the heating of the chips on the hot plate at 400°C for a duration of 10 min. Therefore, it is assumed that the Cu film is oxidized. In order to verify this assumption, the Cu thin film on SiO₂/Si chip after this heating process and before the deposition of the SnO₂ thin film by spray pyrolysis is analysed by XRD. Figure 16 shows the XRD pattern of the Cu film after 10 min at 400°C in ambient air. The measurements indicate that the Cu thin film is completely oxidized to CuO after 10 minutes on the hot plate at 400°C. Consequently, it is confirmed that the SnO₂ film obtained by spray pyrolysis is deposited on a CuO thin film on SiO₂/Si chips.

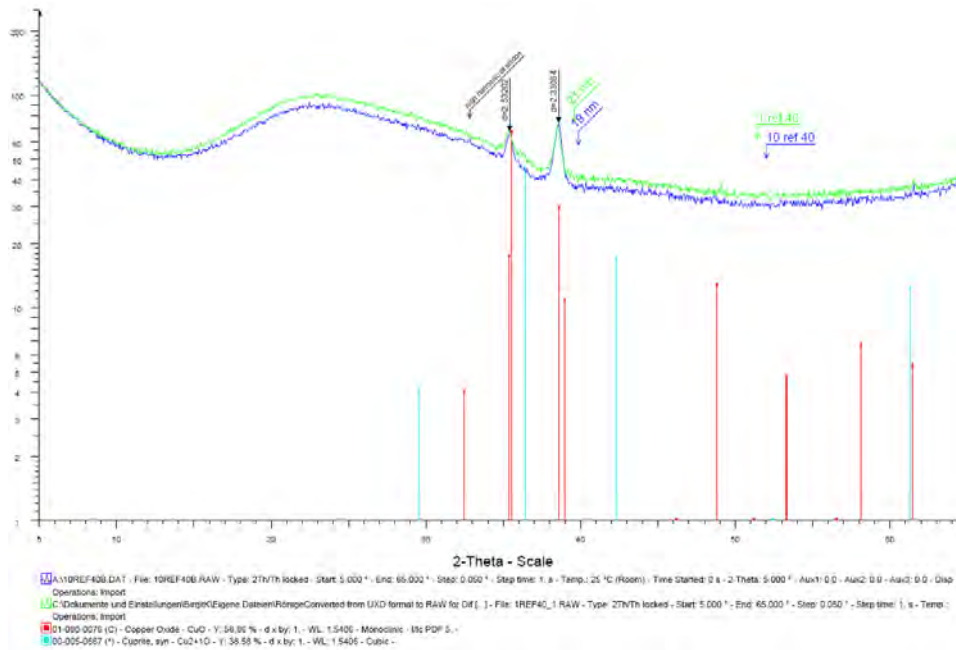


Figure 16: XRD pattern of the oxidized Cu film after 10 min on the hotplate at 400°C.

2.2 Nanowire growth

The preliminary results reported in [155, 156] demonstrated the growth of SnO₂ nanowires at 900°C from a SnO₂ thin film deposited by spray pyrolysis on Cu-coated SiO₂/Si chip. The objective of this study is to optimize the process in terms of reproducibility and to gain a better understanding of the nanowire growth mechanism. Therefore, a series of experiments are conducted with a systematic approach, changing a few parameters one by one.

2.2.1 Methods

The standard nanowire growth process occurs as follows: the sample (described later) is placed on a substrate holder in a tube furnace. The furnace is closed, an argon (Ar) flow (about 1000 sccm) is introduced, and the furnace is switched on. A temperature of 900°C at the substrate holder is reached in 1 hour. The temperature of 900°C is hold for 1.5 hour to enable the growth of SnO₂ nanowires on the substrate. After a total time of 2.5 hours, the furnace is switched off together with the Ar flow. When the temperature in the furnace has decreased below 400°C, the furnace is opened and the sample cools down in the ambient air to about 100°C. Then the sample is removed from the sample holder.

The growth of the SnO₂ nanowires is conducted in a standard tube furnace SR 100-200/12 produced by GERO Hochttemperaturofen GmbH [157]. A continuous Ar flow of about 1000 sccm circulates through the furnace during the nanowire growth. A sample holder, which consists of a steel plate (about 4×5 cm²), is suspended by a steel arm in the middle of the heated zone. A temperature sensor is embedded in the sample holder in order to get more precise information about the temperature of the sample. A scheme of the assembly is depicted in Figure 17.

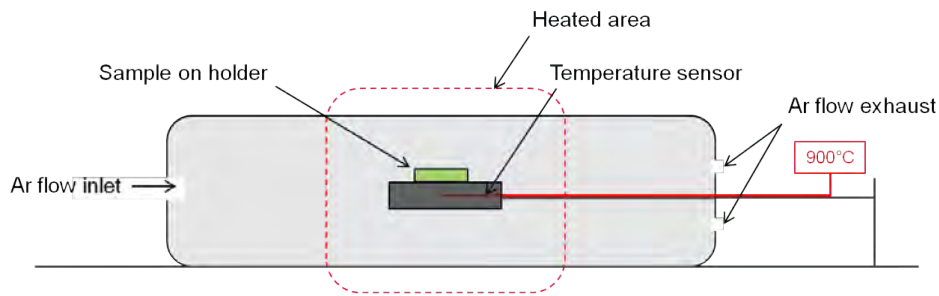


Figure 17: Scheme of the position of the sample in the tube furnace.

The temperature for the nanowire growth is set to 1010°C at the temperature control unit of the furnace power supply, which corresponds to an actual temperature of 900°C at the sample holder (measured with the embedded temperature sensor). The heating and cooling ramp of the sample in the presence of argon flow (about 1000 sccm) is depicted in Figure 18. The heating ramp is fast: the temperature reaches 900°C in 60 min. After the furnace and the argon flow have been switched off (t=150 min), the temperature decreases fast (in 25 minutes) from 900°C down to 700°C. Below 700°C, the cooling rate is rather slow and it takes approximately 110 min until the sample is cooled down to 400°C.

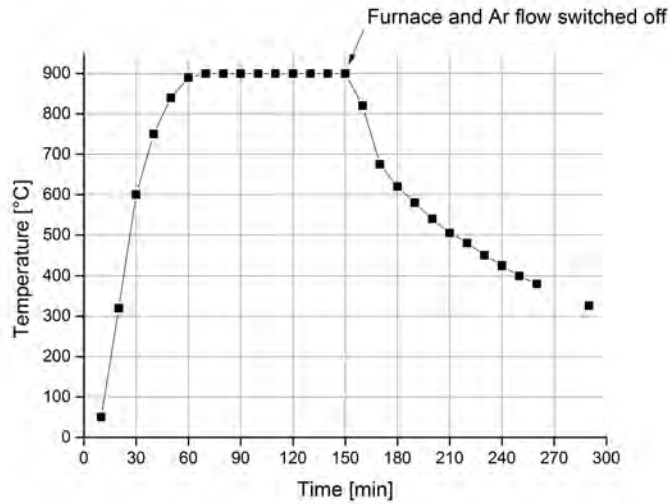


Figure 18: Temperature measured at the substrate holder during the heating process for the nanowire growth.

Figure 19 shows how the samples are mounted in the furnace. Two or three substrates are stacked on top of each other. The bottom substrate is placed directly on the sample holder in the furnace. A middle substrate is optionally deposited on the bottom substrate. Small pieces of SiO_2/Si wafer are as well mounted on the edges of the bottom substrate and act as spacers. Finally, a top substrate is deposited face down on the spacers. The objective of this assembly is to create a confined environment for the growth of SnO_2 nanowires.

The SnO_2 thin film (thickness in the range 250-300 nm) deposited by spray pyrolysis is the precursor material for the SnO_2 nanowire growth. The SnO_2 thin film has been deposited on several substrates (as already mentioned in 2.1.3): silicon chips with native oxide (Si), silicon chips with 300 nm thermal oxide (SiO_2/Si) or silicon chips with 300 nm thermal oxide coated with 40 nm cupric oxide ($\text{CuO}/\text{SiO}_2/\text{Si}$). The influence of the substrate on the nanowire growth is one of the parameters investigated. Additionally, SiO_2/Si substrates are coated with a thin film of Cu (thickness of 40 nm), which is deposited by RF magnetron sputtering. According to the experimental conditions described below, the copper layer may be present in the metallic (Cu) and/or oxidized (CuO) form.

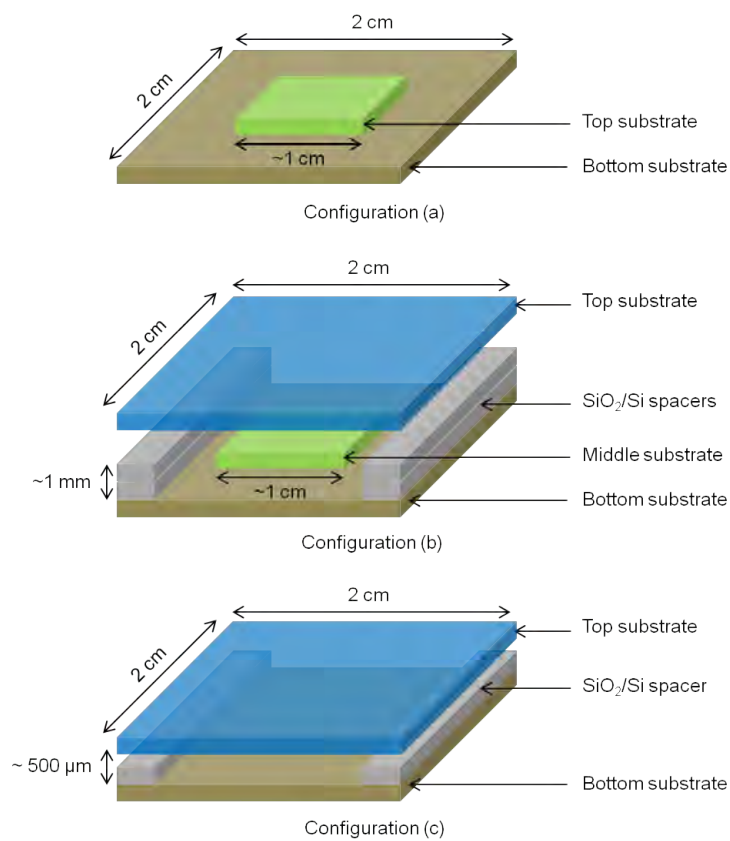


Figure 19: Scheme showing the different configurations how the substrates have been stacked in the furnace for the growth of SnO_2 nanowires: (a) two substrates stacked (used in Experiment 1), (b) confined environment involving three stacked substrates (distance between top and middle substrates about $500 \mu\text{m}$) (used in Experiment 2), (c) confined environment between two stacked substrates (used in Experiments 3-9).

2.2.2 Experimental approach

The starting point to optimize the growth of SnO₂ nanowires is based on the preliminary results reported in [155, 156]. It has been demonstrated that the presence of a metallic intermediate layer (Cu or Au) is required for the growth of SnO₂ nanowires. The first experiments were involving one substrate (SnO₂ thin film deposited by spray pyrolysis on a CuO/SiO₂/Si substrate) placed in the furnace at 900°C for 1.5 hour in argon atmosphere. The results - though not reproducible - showed the growth of few SnO₂ nanowires only on the edges of the samples and sometimes also directly on the steel substrate holder around the substrate. The latter observation led to the assumption that SnO₂ material could be transported through the gas phase and redeposited in the proximity of the sample.

Many experiments have been required in order to optimize the synthesis of SnO₂ nanowires. In this chapter, the key experiments leading to a reproducible process and enabling a better understanding of the nanowire growth mechanism are detailed. Figure 20 shows the configurations of the 9 key experiments.

- In Experiment 1, two samples are stacked, which has for objective to enhance the growth of SnO₂ nanowires on the edges of the top substrate and on the bottom substrate around the top substrate.
- In Experiment 2, the addition of a third substrate on top of the two others aims for the creation of a confined environment. This configuration appears very promising to synthesize SnO₂ nanowires reproducibly.
- Experiment 3 consists in a simplified version of Experiment 2 with only two substrates involved. The results are similar: SnO₂ nanowires grow on the substrate involving the CuO intermediate layer.
- Experiment 4 is another simplification of the system to observe the direct role of Cu (CuO) in the SnO₂ nanowire growth.
- In Experiment 5, the influence of the bottom substrate is studied (SnO₂ layer deposited on SiO₂/Si instead of Si).
- Experiment 6 investigates the possibility to grow SnO₂ nanowires without the presence of Cu (CuO) in the reaction chamber.
- Experiment 7 intends to establish the local growth of SnO₂ nanowires by structuring the Cu (CuO) thin film.
- Experiment 8 is similar to Experiment 4, only the heating process takes place in a forming gas flow instead of an argon gas flow in order to

observe the influence of a reducing atmosphere on the SnO_2 nanowire growth.

- Finally, Experiment 9 considers the catalytic effect of a Au layer replacing the Cu (CuO) layer.

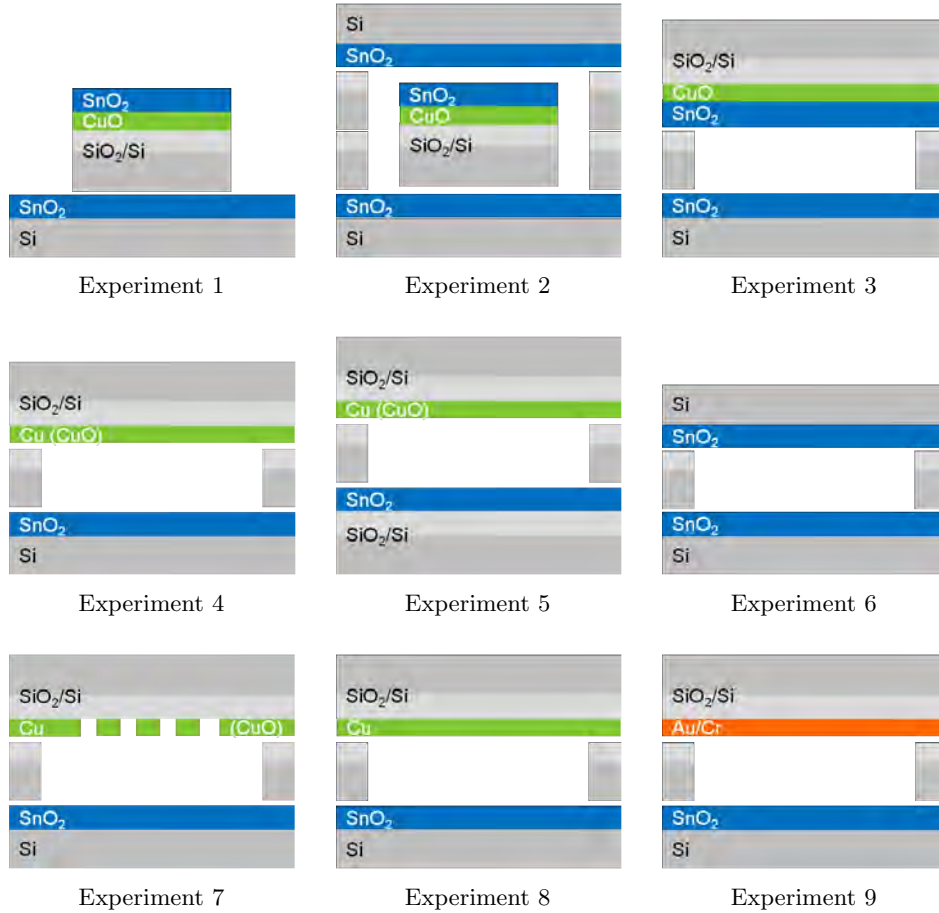


Figure 20: Schemes of the key experiments conducted to optimize the growth of SnO_2 nanowires. The standard experimental conditions are 1.5 hour at 900°C in argon atmosphere. Only for Experiment 8, the argon flow has been replaced by a forming gas flow (95% N_2 + 5% H_2).

2.2.3 Results

Experiment 1

For the first experiment a stack of a $1 \times 1 \text{ cm}^2$ SiO_2/Si substrate coated with 40 nm CuO and 250-300 nm SnO_2 (top substrate) on a $2 \times 2 \text{ cm}^2$ Si substrate coated with SnO_2 (bottom substrate) is introduced in the furnace. The furnace is run to 900°C for 1.5 hours with an Ar flow of 1000 sccm. Figures 21 and 22 show the results of the heating process for the top and bottom substrate, respectively.

Figure 21a shows the surface of the top substrate right after the deposition of the SnO_2 film by spray pyrolysis on a $\text{CuO}/\text{SiO}_2/\text{Si}$ substrate. It is a continuous and relatively smooth layer. After the heating process at 900°C in argon atmosphere (Figure 21b) or in ambient air (Figure 21c), the SnO_2 film becomes polycrystalline. The recrystallisation of the SnO_2 thin film from amorphous to polycrystalline was already discussed in 2.1.4. The crystallite size is in the range 30-200 nm. At the surface of the film heated in argon atmosphere, there is the presence of pores between the crystallites, which is not the case for the film heated in ambient air.

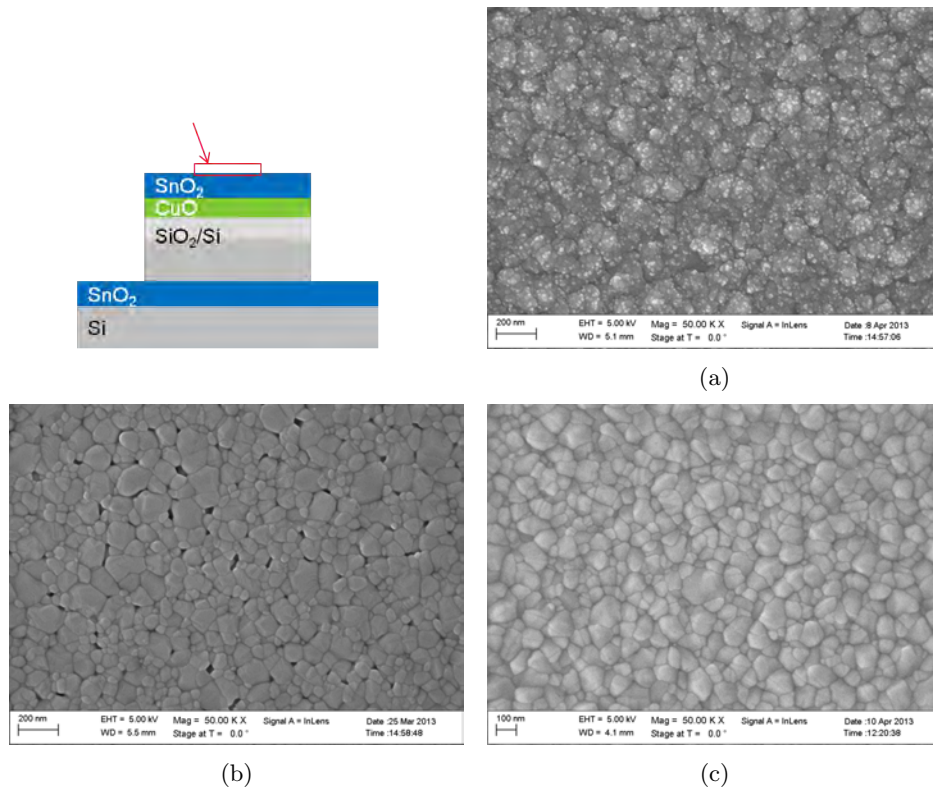


Figure 21: SEM images of the top $\text{SnO}_2/\text{CuO}/\text{SiO}_2/\text{Si}$ substrate of Experiment 1 (a) before the heating process, (b) after the heating process in argon, (c) after the heating process in ambient air.

Figure 22 shows the surface of the bottom substrate after the heating process. A mark left by the SnO₂/CuO/SiO₂/Si substrate, which was placed on top during the heating process, is visible on the SnO₂/Si surface. In the first area (Figure 22a), which was not covered, a dense continuous SnO₂ thin film is observed. The film surface is rougher than the SnO₂ film of the top substrate. Only in a few places, the film bubbles, which results in the film release due to internal mechanical stress. At the edge, where the top chip was deposited, a second zone (Figure 22b) is identified, which is about 40 μm wide. The SnO₂ film is still continuous, though the bubble-shaped delamination increases. The size of the bubbles is smaller than on the open surface. The next zone (Figure 22c) is about 400 μm wide. The SnO₂ film presents open bubbles and cracks. A few dispersed SnO₂ nanowires grow up to 20 μm long. It seems that the nanowires grow from grains of the SnO₂ film, which are mostly located at the edge of a hole. The SnO₂ film gets more and more discontinuous further away below the top chip, and grains are only partly agglomerated, as shown in Figure 22d. In Figures 22e and 22f, the grains are completely dispersed. Additionally, the grain size largely increases from zone (d) to zone (e) and zone (f) with grains up to 1 μm .

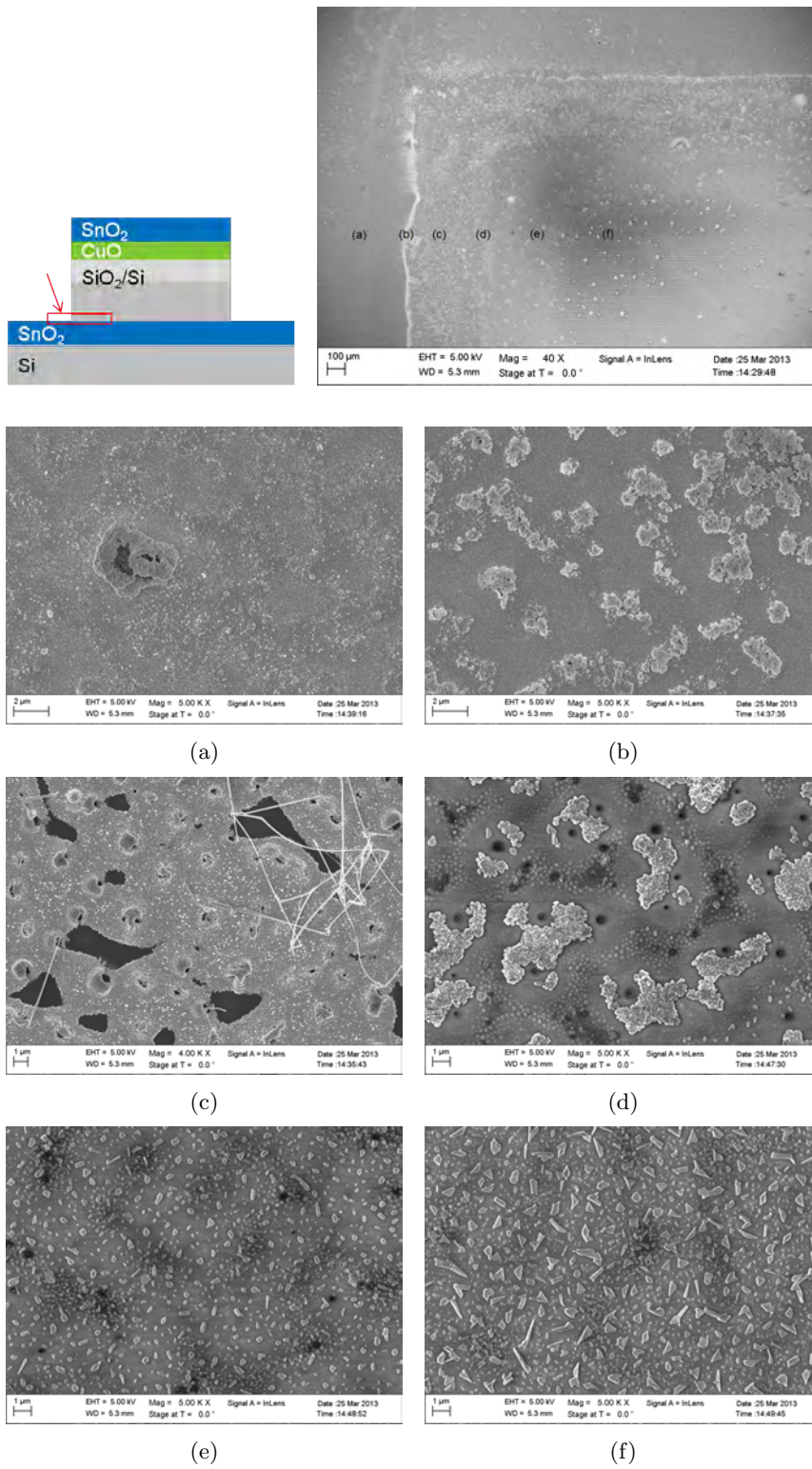
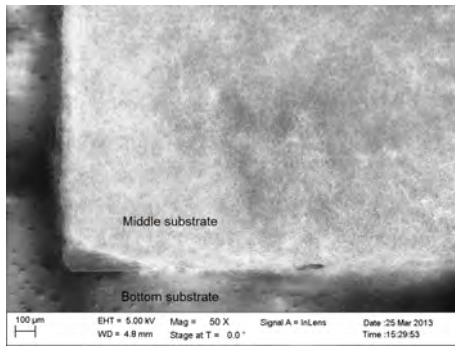


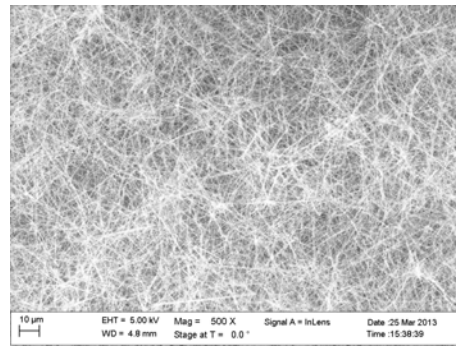
Figure 22: SEM images of the SnO_2/Si bottom substrate of Experiment 1 after the heating process.

Experiment 2

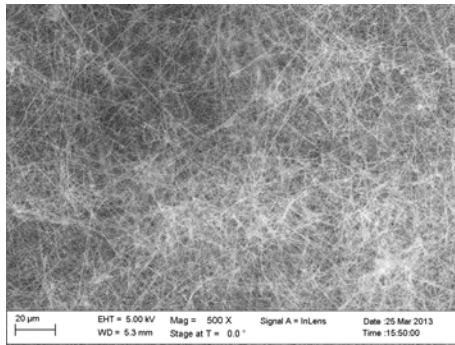
The next step is to employ a more confined environment, where three samples are involved: The bottom and the top substrates are SnO₂-coated Si substrates and the middle substrate is a SnO₂ thin film on a CuO/SiO₂/Si substrate. The results of the heating process are shown in Figure 23. A white wool-like layer covering entirely the middle substrate is observed (Figure 23a). This layer is actually a dense and continuous film of interwoven SnO₂ nanowires, as seen in Figure 23b. The nanowires have diameters in the range 50-300 nm and lengths up to hundreds of micrometers. SnO₂ nanowires also grow on the top substrate, as shown in Figure 23c. The interlacing of SnO₂ nanowires is not as dense and homogeneous as on the middle substrate. Moreover, the growth of SnO₂ nanowires occurs only in the area above the middle substrate and not aside. Finally, Figure 23d shows the bottom substrate at the border with the middle substrate. The growth of SnO₂ nanowires also occurs in the proximity of the middle substrate, but further away only a few dispersed nanowires can be observed.



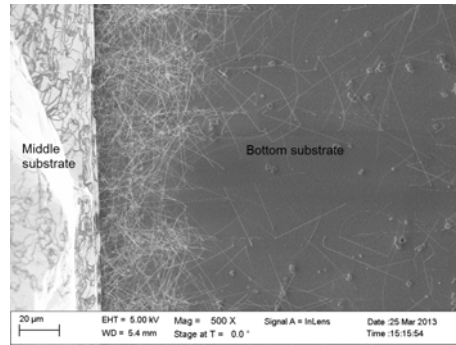
(a)



(b)



(c)



(d)

Figure 23: SEM images of each substrate of the assembly of Experiment 2 after the heating process. (a), (b) Top view of the middle substrate deposited on the bottom substrate. (c) View of the SnO₂ film on the top substrate in the area right above the middle substrate. (d) Top view of the bottom substrate at the border with the middle substrate.

Energy-Dispersive X-ray Spectroscopy (EDS) measurements are performed on the top and middle substrates. The results obtained for the middle substrate (position b in the scheme of Figure 23) are shown in Figure 24. Figures 24a and 24b image the same area of the substrate, but two detectors are used: a backscattered electron detector (BSE) and a secondary electron detector (SE), respectively. The BSE detector enables to image the surface with a contrast depending on the chemical composition: heavy elements appear brighter. In Figure 24a the grains, which appear darker on the image, are composed of Cu, while the other grains (light) are SnO₂. The SE detector delivers information about the topography. Figure 24b shows that the copper oxide grains are deposited on the surface of the SnO₂ film. This is astonishing, because the CuO thin film is an intermediate layer between the SiO₂/Si substrate and the SnO₂ coating on top. This means that Cu or CuO must have diffused through the SnO₂ layer to be present on its surface. Furthermore, facets can be distinguished on the copper oxide grains, so they must have a crystalline structure.

Figure 24c images SnO₂ nanowires grown on the middle substrate. Figure 24d shows the ending of a SnO₂ nanowire, which looks like a droplet, and on top of that droplet a crystalline grain. The square in Figure 24d indicates the position, where the EDS spectrum is measured. The EDS spectrum identifies clearly Cu and a small signal is also due to Sn present in the vicinity (SnO₂ nanowire). A quantitative analysis from this spectrum seems to agree that the grain is composed of CuO. However it appears that the grain is simply deposited on the tip of the nanowire. Another EDS measurement conducted on the droplet shaped ending of the nanowire aside from the CuO grain shows mainly the presence of SnO₂ and a small signal of Cu, which is probably due to the scattering signal from the CuO grain. From those information, it does not seem that the SnO₂ nanowire growth occurs by a vapor-liquid-solid (VLS) growth mechanism, where the tip of the nanowire would be a compound of SnO₂ and CuO.

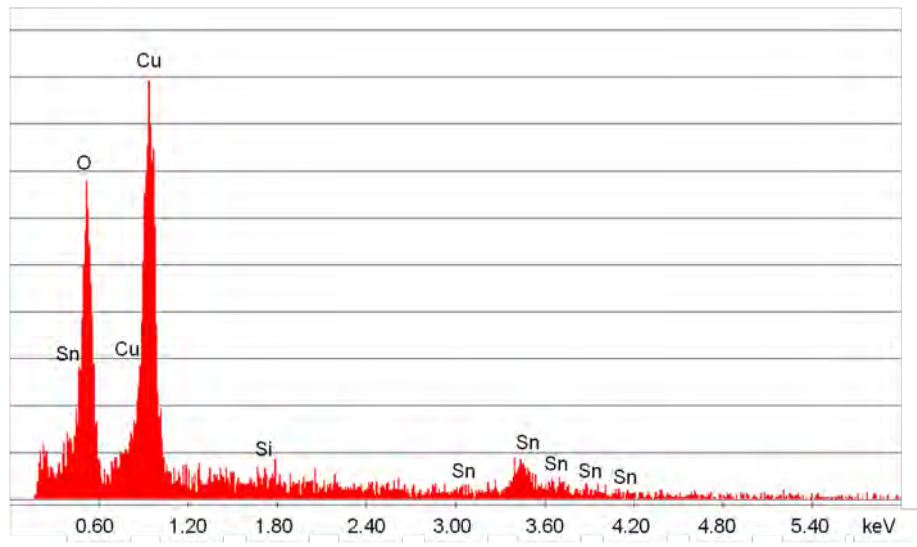
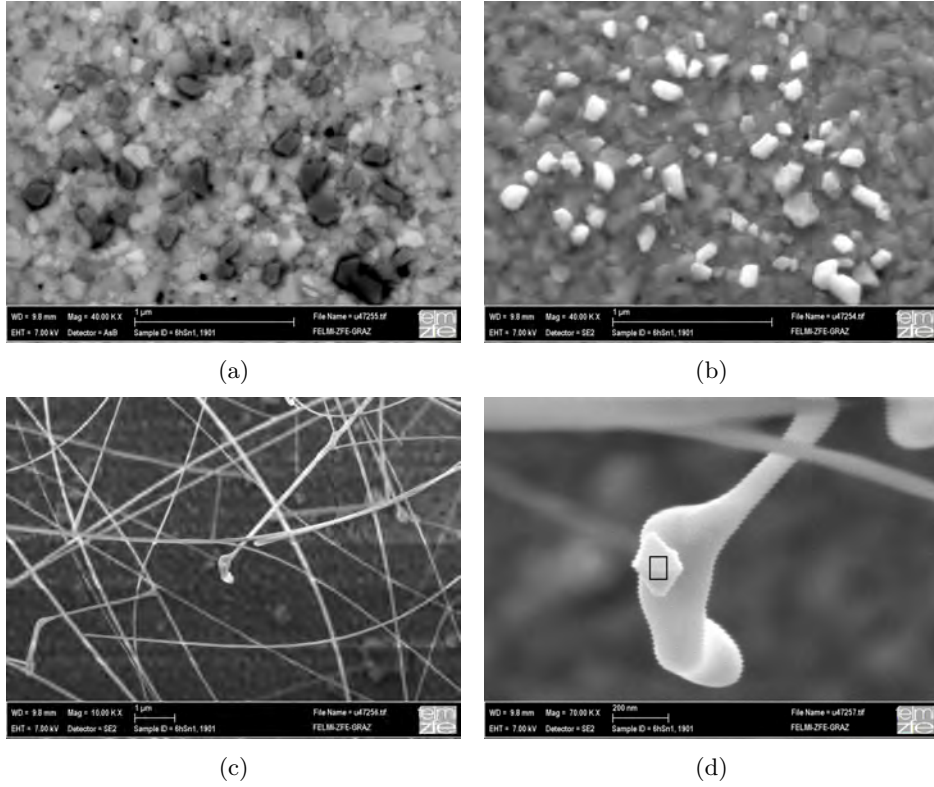
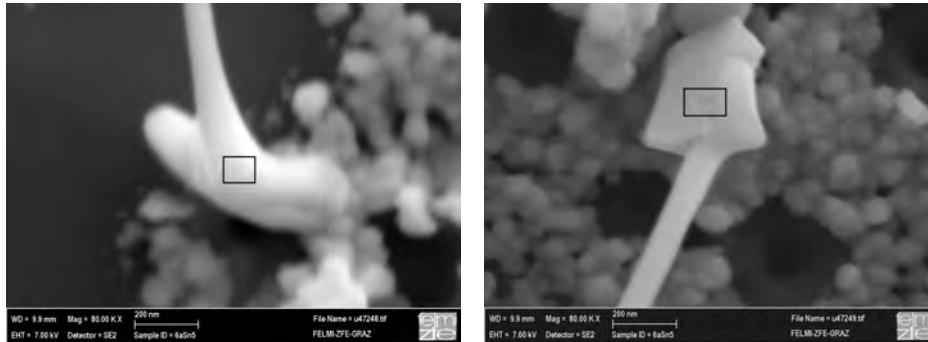


Figure 24: SEM images of the SnO₂ surface of the middle substrate of Experiment 2 after the heating process. (a) Backscattered electron analysis, (b), (c), (d) Secondary electron analysis, and EDS spectrum of the nanowire end.

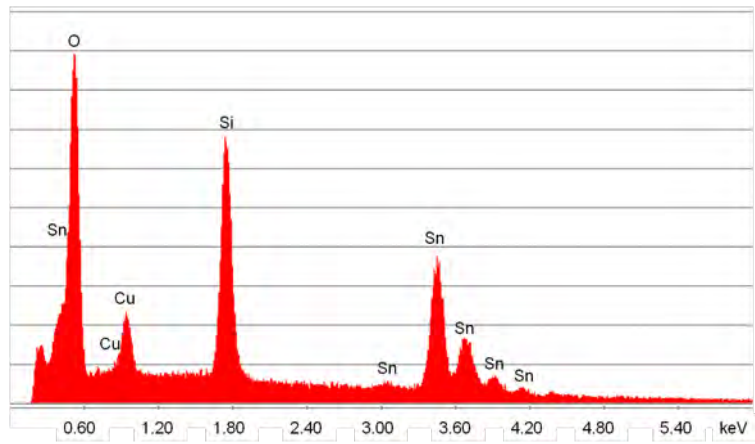
Figure 25 shows the EDS spectra measured at the base of two SnO₂ nanowires grown on the top substrate. The first nanowire imaged in Figure 25a grows from a bean-shaped grain, which does not present any facets characteristic for a crystalline structure. The EDS spectrum in Figure 25c, which is measured in the area indicated by a square, shows the presence of Cu, Si and Sn. The peak corresponding to Si at about 1.70 keV is due to the background signal from the silicon substrate. Other EDS spectra are also measured right and left of the square on both ends of the bean-shaped grain. They do not show any signal corresponding to Cu. This means that the signal due to the presence of Cu in the square area does not come from other CuO grains close by. Moreover, Cu is only locally present in the grain at the base of the nanowire.

The second nanowire shown in Figure 25b grows from a grain, which has facets and seems clearly crystalline. The square indicates the area, where the EDS spectrum is measured. Figure 25d shows the EDS spectrum and a high peak at about 0.9 keV is significant for the presence of Cu. When considering the faceted shape, it is not very surprising that the grain is composed of Cu, because it looks very similar to the CuO grains identified in Figures 24b and 24d. However, the two nanowires analysed here are found on the surface of the top substrate, which is a SnO₂ coated Si substrate, so no Cu is present on the surface before the heating process. This suggests that the CuO crystallites found at the surface of the middle substrate, which must have first diffused through the SnO₂ layer, are transported in the gas phase to be deposited on the top substrate.

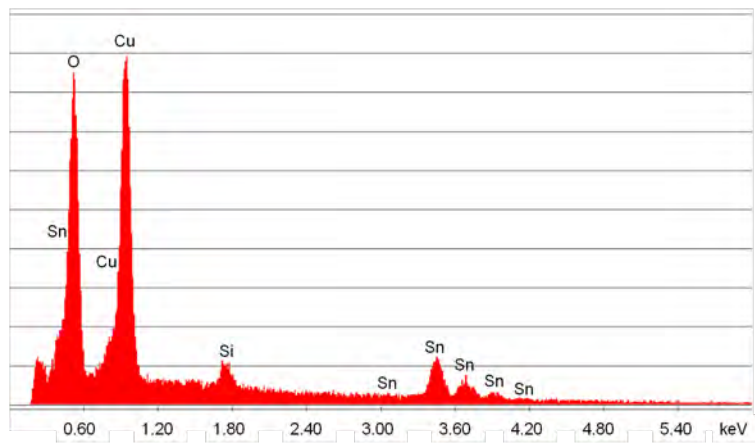


(a)

(b)



(c) EDS spectrum at the nanowire base pictured in (a).



(d) EDS spectrum at the nanowire base pictured in (b).

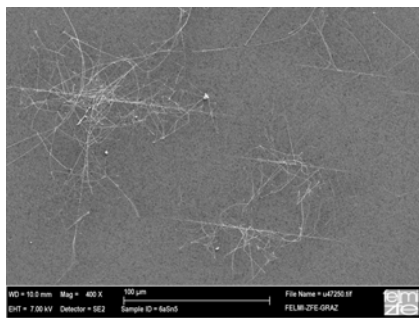
Figure 25: (a), (b) SEM image of a SnO_2 nanowire growing on the top substrate of Experiment 2, (c), (d) Respective EDS spectrum at the nanowire base.

When looking at the surface of the top substrate, some linear cracks in the SnO₂ film can be seen from where nanowires grow, as imaged in Figures 26a and 26b. Those cracks arise along lines that have a specific geometrical orientation: several directions are observed, and all lines are parallel to those directions. The perfect parallelism of the lines according to a few directions lets us presume that it is linked with the crystallographic directions of the Si crystalline substrate. It is assumed that the stress of the SnO₂ film on the Si substrate is very high. It is possible that the strong lattice mismatch between the SnO₂ film and the Si substrate is stronger along specific crystallographic directions of the Si substrate, which would explain the cracks formed along those directions. It is also assumed that there is a strong diffusion of the SnO₂ material into the Si substrate. It could be that the diffusion of SnO₂ is stronger along distinct crystallographic directions of Si. In Figure 26c the SnO₂ film presents many circular holes dispersed randomly on the surface. Additionally, the holes are concentrated along the lines, which actually forms the cracks described above. The holes could be the result of the release of internal stress present in the SnO₂ film. Moreover, there is a concentration of larger grains, which are at the base of the nanowires, along the linear cracks.

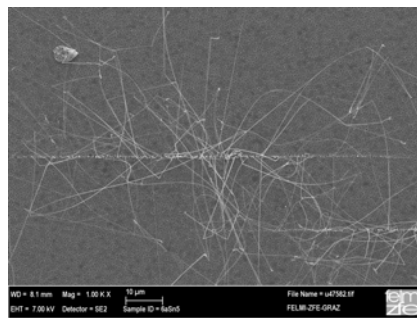
The area represented in Figure 26c is imaged as an elemental mapping of Cu in green (Figures 26d and 26e), Sn in yellow (Figure 26f), O in red (Figure 26g), and Si in blue (Figure 26h). From those images, the following is concluded:

- Cu is present on the top substrate in the form of isolated grains.
- A few larger grains found at the base of some nanowires along the linear crack are also composed of Cu.

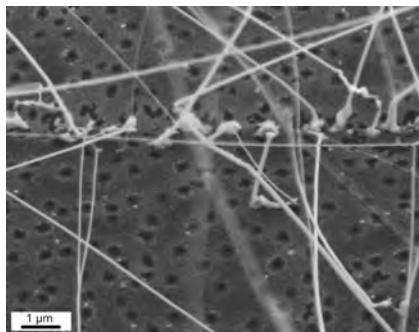
The other larger grains along the crack and at the base of the nanowires are composed of Sn and O, just like the nanowires. The surface of the sample seems to be composed of Sn, O and Si, since it appears with a positive contrast in the corresponding elemental mappings. Sn is present homogeneously on the surface except for the circular holes (approximately 300 nm large) distributed on the surface. Those circular holes appear clearly with a positive contrast in the elemental mapping of Si. Moreover Si is present on the rest of the surface as homogeneously as Sn. This is because the SnO₂ film is not continuous any more. The SnO₂ grains, which constitute the film, are partly dispersed, so the Si surface is visible. Only around the holes, there are more grains of SnO₂, which explains that the signal coming from the Si substrate is smaller and the contrast on the elemental mapping of Si is reduced.



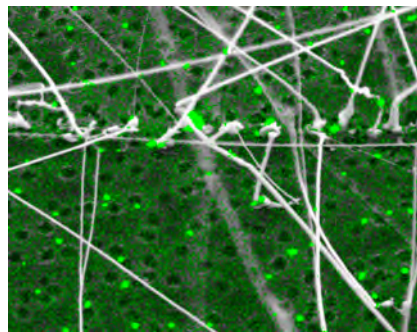
(a)



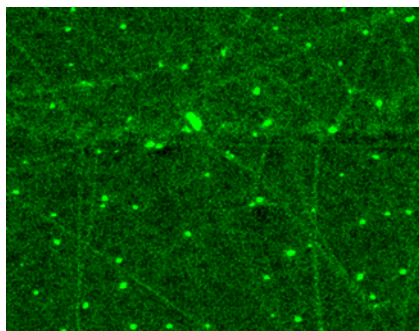
(b)



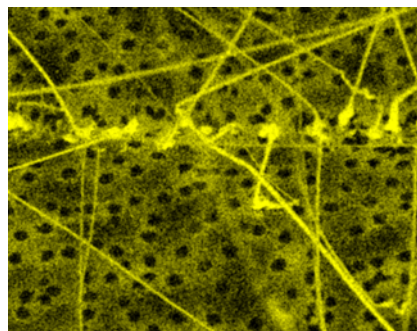
(c)



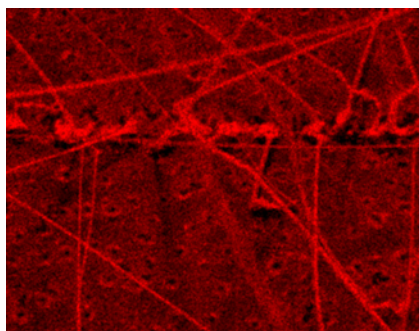
(d)



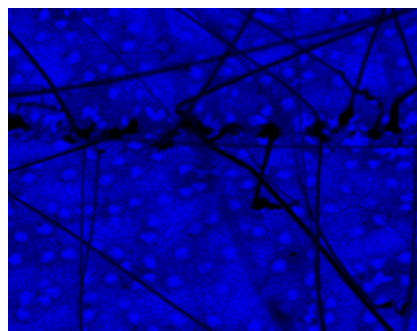
(e) Elemental mapping of Cu.



(f) Elemental mapping of Sn.



(g) Elemental mapping of O.



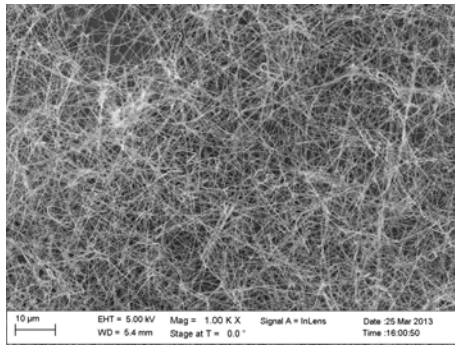
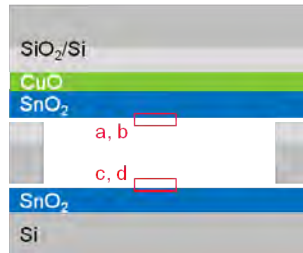
(h) Elemental mapping of Si.

Figure 26: (a-c) SEM images of the top substrate of Experiment 2, (d) Superimposition of the original SEM image (c) and the elemental mapping of Cu, (e-h) Elemental mapping.

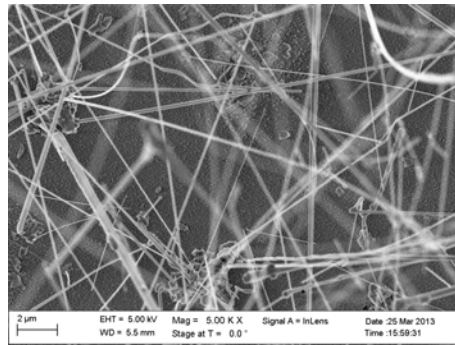
Experiment 3

The results obtained for the nanowire growth in the previous configuration (see Figure 23) are already very satisfying, especially the growth of SnO₂ nanowires on the middle substrate. However, in order to gain a better understanding of the nanowire growth mechanism, further experiments are conducted in a similar confined environment. For Experiment 3, the system is simplified, since only two samples are stacked, as it can be seen in Figure 27. The two samples involved are a SnO₂/CuO/SiO₂/Si top substrate and a SnO₂ layer deposited directly on a silicon chip with a native oxide at the surface (SnO₂/Si) as bottom substrate. The SnO₂ layers of both chips are facing each other. After the heating process, a very dense and homogeneous growth of SnO₂ nanowires is observed on the top substrate (Figure 27a), similar to the growth observed on the middle substrate in Figure 23b. Below the dense layer of interwoven nanowires (Figure 27b), a continuous SnO₂ film with polycrystalline grains is visible as in Figure 21b. Additionally, there are larger grains (300 nm to 1 μm in size) agglomerated together, from which the SnO₂ nanowire growth starts.

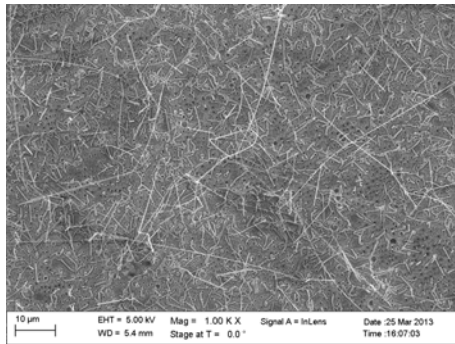
On the SnO₂/Si bottom substrate, there are some nanowires grown on the surface (see Figure 27c), but they do not grow as dense as on the top substrate. Moreover, there are no SnO₂ polycrystalline grains visible on the surface (Figure 27d). It seems that all grains, which have previously constituted the SnO₂ film, have been consumed for the formation of large amorphous or polycrystalline wires (150-500 nm in diameter and up to 5 μm long). Those large wires appear to start growing from a hole in most cases and grow flat on the surface. It is assumed that the smooth surface is composed of SiO₂ with possible Sn atoms diffused inside and the surface visible through the holes is most probably pure SiO₂. The growth of single crystalline nanowires with diameters below 150 nm seemingly starts from the large polycrystalline wires. The single crystalline nanowires grow upwards and are much longer (up to 100 μm).



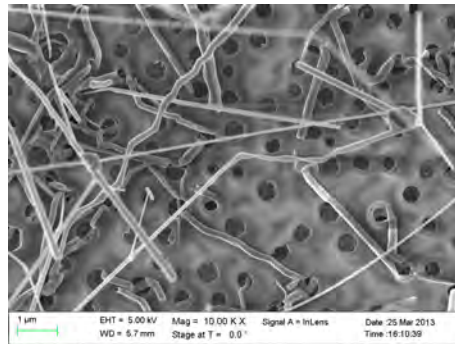
(a)



(b)



(c)

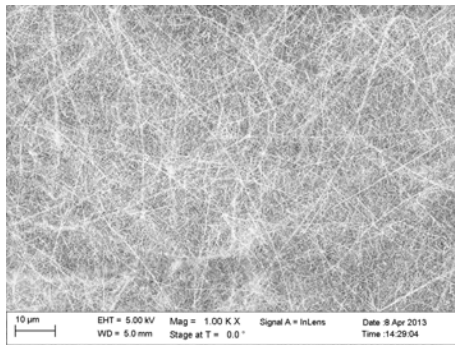
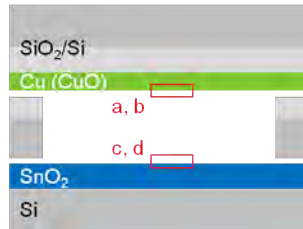


(d)

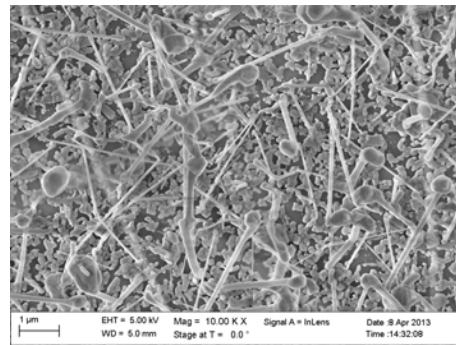
Figure 27: SEM images of the SnO₂ surface after the heating process of Experiment 3 (900°C, 1.5 h, in Ar): (a), (b) top substrate, (c), (d) bottom substrate.

Experiment 4

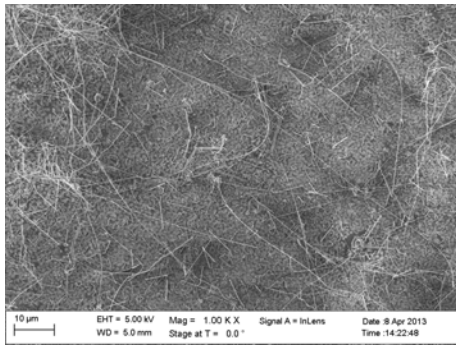
For the following experiments the previous configuration (confined environment between two substrates) is fixed and only the substrates are changed. In Experiment 4, the top substrate is replaced by a SiO_2/Si substrate coated with 40 nm Cu without SnO_2 layer on top, as shown in Figure 28. Since the top substrate did not undergo any heating treatment after deposition of the Cu layer, it is assumed that the Cu thin film is not completely oxidized. However, since it has been stored in ambient atmosphere, it is very likely that the surface of the Cu thin film is oxidized to CuO. Also during the heating process in Ar flow with residual oxygen, it is not clear if copper is present as Cu or CuO. Therefore, it will be further noted Cu (CuO). The precursor material necessary for the SnO_2 nanowire growth is present only on the bottom substrate as a SnO_2 film on a Si substrate. Still, dense interwoven SnO_2 nanowires grow on the top substrate, as shown in Figure 28a. Figure 28b shows the top substrate surface with a higher magnification. It looks like polycrystalline SnO_2 grains are deposited on the SiO_2 surface, which is visible in the background. There are also large polycrystalline wires, from which single crystalline nanowires grow. The further away from the surface, the longer are the single crystalline nanowires, which reach up to hundreds of microns. It is very difficult to interpret if Cu (CuO) is still present at the surface of the top substrate. However, it is assumed that Cu (CuO) is present in the form of the large almost spherical grains, which have diameters between 350 nm and 1 μm . The Cu (CuO) grains seem to be at the base or at the tip of the large polycrystalline wires. Concerning the surface of the bottom substrate (Figures 28c and 28d), it seems identical with the bottom substrate of the previous experiment (Figures 27c and 27d). From that experiment, it is concluded that the SnO_2 material is transported through the gas phase to recrystallize on the top substrate as SnO_2 nanowires. It is suggested that the driving force for the volatility of SnO_2 is related to the reducing effect of the Si substrate on the SnO_2 layer during the heating process. Experiment 5 intends to verify this hypothesis.



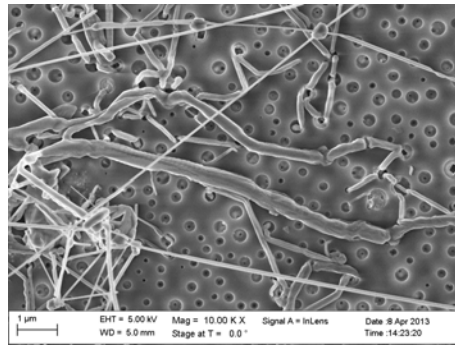
(a)



(b)



(c)

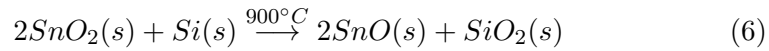


(d)

Figure 28: SEM images of the SnO₂ surface after the heating process of Experiment 4 (900°C, 1.5 h, in Ar): (a), (b) top substrate, (c), (d) bottom substrate.

Experiment 5

In Experiment 5, the SnO₂/Si bottom substrate is replaced by a SnO₂/SiO₂/Si chip, where the 300 nm thermal oxide SiO₂ should act as a barrier against the possible reduction of SnO₂ by Si. Figure 29 shows SEM images of both substrates after the heating process. On the top substrate, which is imaged in Figure 29a, the Cu (CuO) thin film has delaminated and agglomerates (size in the range 1-4 μm) are formed. The SiO₂ surface is visible and no SnO₂ crystallites are located on the surface. The surface of the bottom substrate is shown in Figures 29b and 29c. A few Cu or CuO agglomerates are also present at the surface of the bottom substrate. The SnO₂ film forms a continuous layer of SnO₂ crystallites with some pores between the crystallites very similar to Figure 21b. It appears that the SnO₂ material is intact and has not been transported through the gas phase. This is probably because the thermal oxide (SiO₂) prevents the SnO₂ from being reduced by the Si substrate. Finally, those results support our hypothesis that the reduction of SnO₂ by Si is part of the driving force for the volatility of the SnO₂ material, most likely according to the reactions:



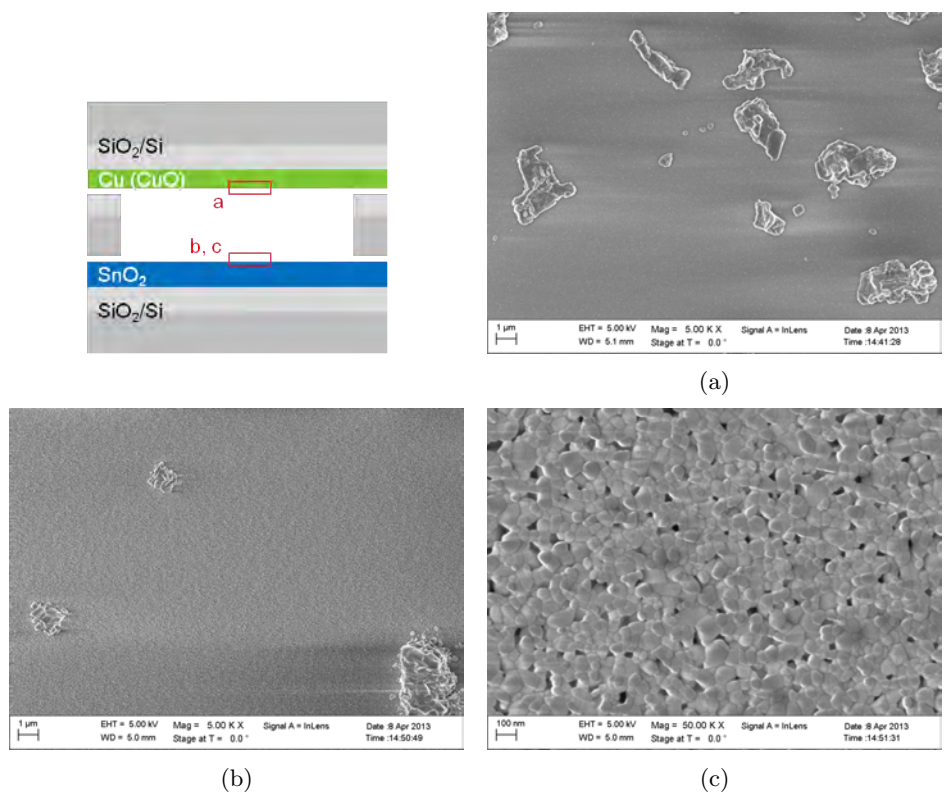


Figure 29: SEM images of the substrates of Experiment 5 after the heating process (900°C, 1.5 h, in Ar): (a) top substrate, (b), (c) bottom substrate.

Experiment 6

In order to gain a better understanding of the role of the Cu (CuO) layer in the nanowire growth, Experiment 6 involves two SnO₂/Si samples facing each other, without any Cu (CuO) layer. The results are shown in Figure 30. The first observation is that no SnO₂ nanowires are found on the top or on the bottom substrate. The surface of both substrates looks alike. Figure 30a shows dispersed agglomerates with a size in the range 5-40 μm. A higher magnification enables the view of SnO₂ crystallites, which build up those agglomerates (Figure 30b). Aside from the agglomerates, SnO₂ crystallites are dispersed on the surface, but no continuous layer is visible. The white spots visible on the surface, which are no SnO₂ grains, may be SnO₂ residue, which has not been transported to the gas phase, or SnO₂, which have diffused into the silicon substrate. The results of this experiment lead us to conclude that the Cu (CuO) layer is necessary for the nanowire growth, though it is uncertain in what extent and if another material, for example Au or Sn, is also appropriate.

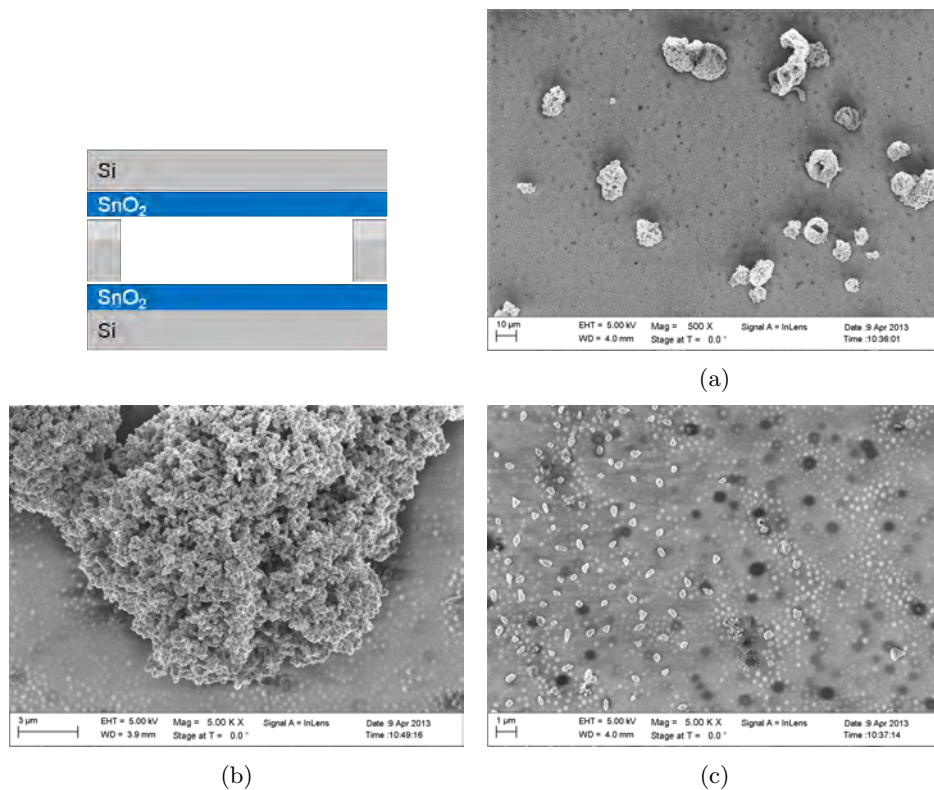


Figure 30: SEM images of the bottom SnO₂/Si surface of Experiment 6 after the heating process (900°C, 1.5 h, in Ar).

Experiment 7

For Experiment 7, the thin film of Cu on a SiO₂/Si substrate is structured by a lithography step followed by Reactive Ion Etching (RIE), so an array of rectangle Cu structures remains. The heating process is conducted with the Cu (CuO) structures on SiO₂/Si as the top substrate. Figure 31 shows SEM images of the surface after the heating process. The rectangular shaped Cu (CuO) structures are visible on Figures 31a and 31b. The SnO₂ nanowires grow exclusively on the Cu (CuO) structures and not on the SiO₂/Si substrate. The nanowires grow long enough to bridge the 100 μm-wide gap between two structures. Figure 31c shows the SiO₂ surface aside from the Cu (CuO) structures, where SnO₂ crystallites are dispersed. Several forms of crystallites can be distinguished. Most are pyramidal with a size of about 500 nm and the sides of the pyramids exhibit facets. Others present an equilateral triangle shape with sides of about 2 μm.

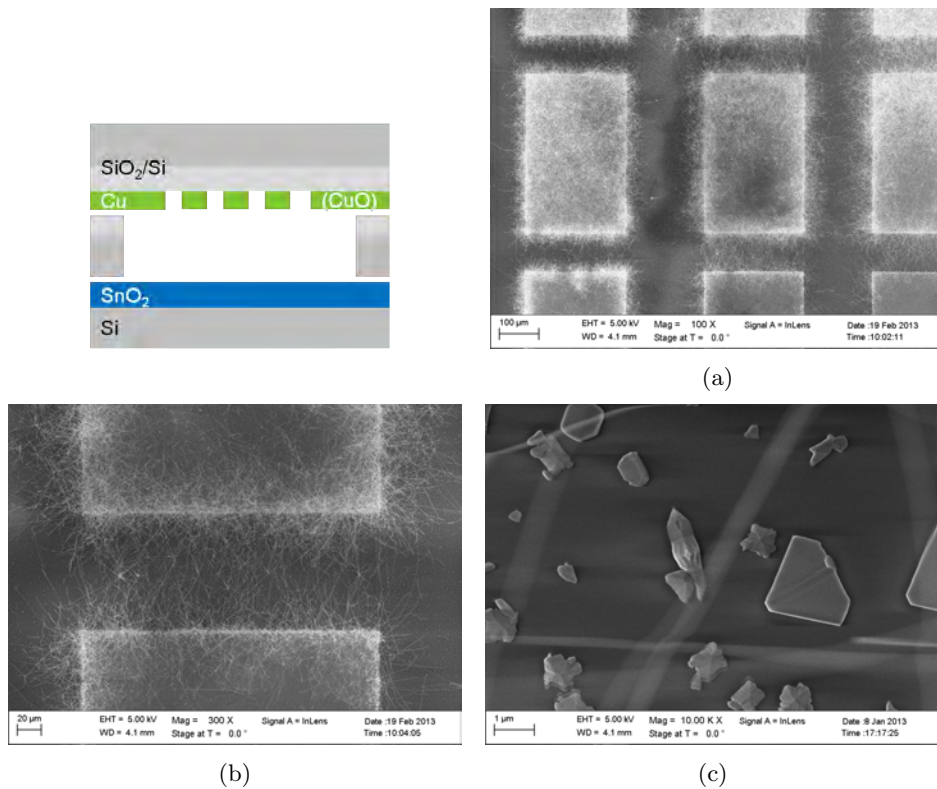


Figure 31: (a), (b) SEM images of the nanowire growth on CuO structures after the heating process of Experiment 7 (900°C, 1.5 h, in Ar), (c) SnO₂ crystallites on the SiO₂ surface aside from the CuO structures.

Experiment 8

As presented before, the reducing effect of the Si substrate on the SnO₂ layer influences the volatility of the SnO₂ material during the heating process. Experiment 8 combines the reducing effect from the Si substrate on the SnO₂ layer and a reducing atmosphere. The argon flow is replaced by a forming gas flow (95% N₂ + 5% H₂). The reducing conditions of the experiment also imply that the copper layer of the top substrate is present as Cu. The results are shown in Figure 32. On the top substrate, the growth of interwoven SnO₂ nanowires is very dense like in the case of a heating process in argon atmosphere. However, the morphology of the nanostructures is different: a large amount of zigzag nanowires and nanobelts is observed (see Figures 32a and 32b). A zigzag nanowire presents two growth directions, which alternate very regularly, typically every 1-2 μm. Moreover, the zigzag nanowires seem to exhibit a square cross-section as visible on Figure 32b.

Figure 32c shows the surface of the top substrate, where SnO₂ crystallites are partly agglomerated with crystalline facets visible. The single crystalline nanowires grow from one of those crystallites present on the top substrate. The heating process conducted in argon atmosphere for the same configuration leads to different observations (Figure 28). The SnO₂ grains present at the surface of the top substrate do not exhibit any crystalline facets and the single crystalline nanowires grow from large polycrystalline wires.

On the surface of the bottom substrate, the Si substrate is not visible, there is still a continuous SnO₂ layer with some cracks (see Figure 32d). The film is much more dense and the SnO₂ grains are not distinct, as if the grains melted together. Additionally, crystallites, which have a pyramidal shape and a size around 300 nm, are dispersed on the surface. The square base of the crystallites could be at the origin of the square cross-section of the zigzag nanowires (Figure 32b).

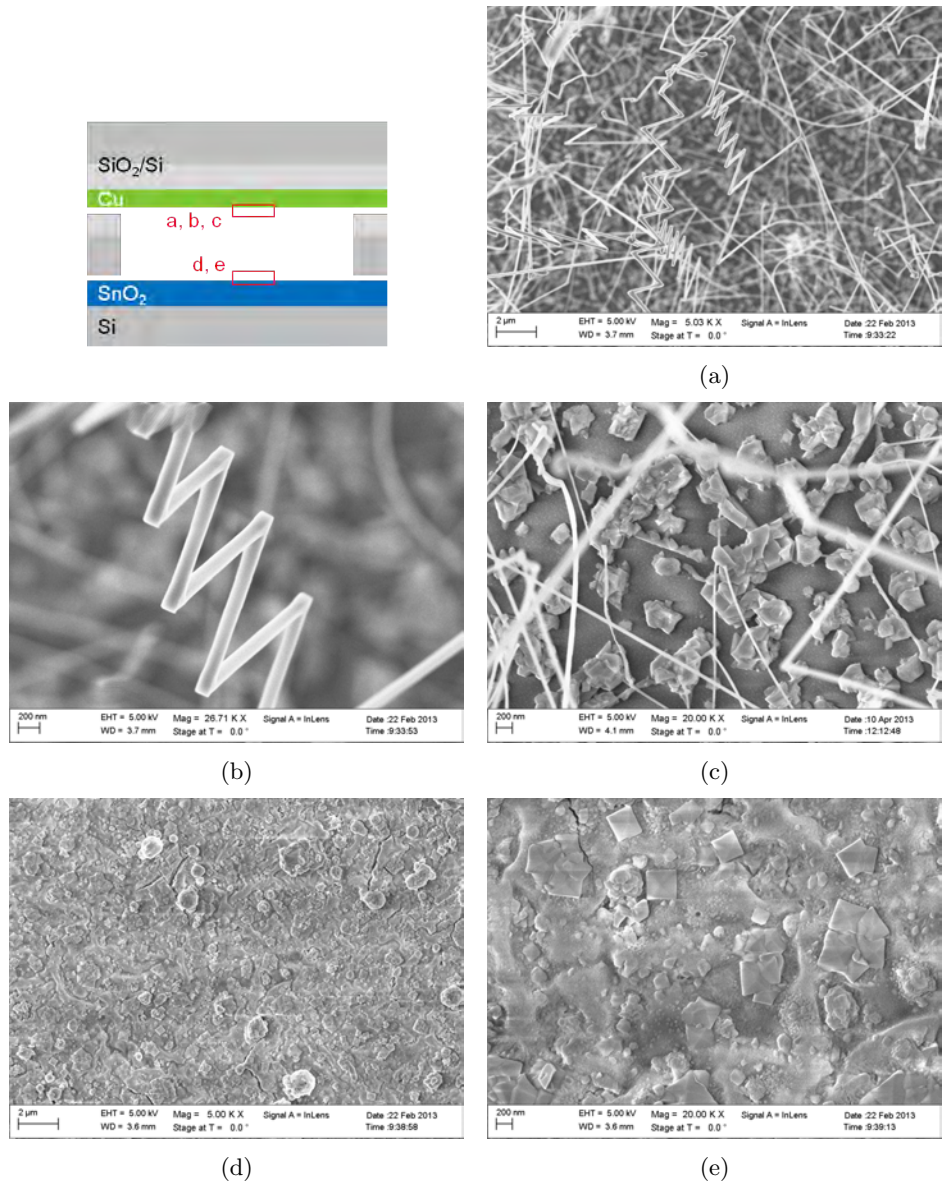


Figure 32: SEM images of the substrates of Experiment 8 after the heating process (900°C, 1.5 h, in 95% N₂ + 5% H₂): (a), (b), (c) top substrate, (d), (e) bottom substrate.

Experiment 9

So far, the importance of Cu (CuO) in the SnO₂ nanowire growth has been pointed out. In the next experiments, the Cu (CuO) coating of the top substrate is replaced by titanium (Ti), tin (Sn) or gold (Au), while the bottom substrate remains a SnO₂/Si substrate. Ti and Sn are deposited on a SiO₂/Si by thermal evaporation with a thickness of 40 nm. For the Au coating, a thin layer of Cr (5 nm) is thermally evaporated on the SiO₂/Si substrate as adhesion layer, followed by the evaporation of 100 nm Au. The parameters of the heating process stays constant: 900°C, 1.5 h, in Ar atmosphere.

On both the Ti as well as the Sn coated top substrate there is no SnO₂ nanowire observed after the heating process. So Ti and Sn are not appropriate to catalyse the SnO₂ nanowire growth. For the top substrate coated with Cr/Au (Experiment 9), the results are shown in Figure 33. A dense layer of interwoven SnO₂ nanowires is observed on the Au surface. The SnO₂ nanowires are as long as grown on Cu (CuO) but their diameters is smaller (30-100 nm). Also there are some droplets visible on Figure 33b, which suggest a Vapor-Liquid-Solution (VLS) reaction.

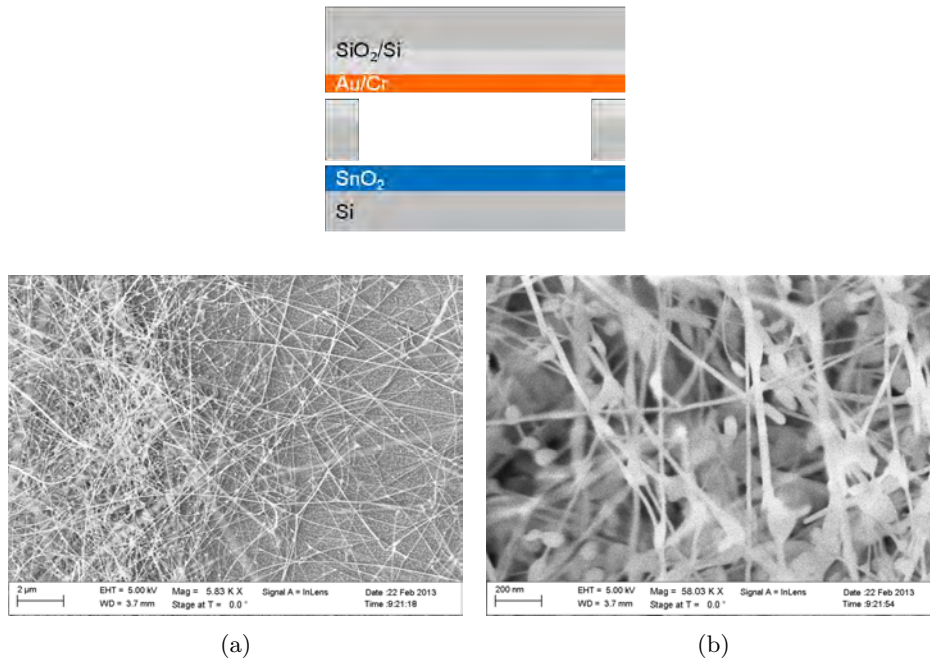








Figure 33: SEM images of the Cr/Au top substrate of Experiment 9 after the heating process (900°C, 1.5 h, in Ar).

Figure 34 sums up the results obtained for Experiments 1-9.

Exp	Sample	Main observations and conclusions
1		<p>Middle substrate: no NW, polycrystalline SnO₂ layer, pores between crystallites</p> <p>Bottom substrate: very few NWs grown in the region covered by the middle chip</p>
2		<p>Top substrate: growth of SnO₂ NWs, CuO crystallites observed at the surface of the SnO₂ layer and at the base of some NWs</p> <p>Middle substrate: dense growth of SnO₂ NWs, CuO crystallites observed on top of the SnO₂ layer</p> <p>Bottom substrate: few NWs grown at the base of the middle substrate</p>
3		<p>Top substrate: dense growth of SnO₂ NWs</p> <p>Bottom substrate: SnO₂ polycrystalline thin film consumed to form large amorphous or polycrystalline wires at the base of few SnO₂ NWs</p>
4		<p>Top substrate: dense growth of SnO₂ NWs, SnO₂ material transported through the gas phase from the bottom substrate to the top substrate</p> <p>Bottom substrate: SnO₂ polycrystalline thin film consumed to form large amorphous or polycrystalline wires at the base of few SnO₂ NWs</p>
5		<p>Top substrate: Cu (CuO) thin film delaminated and formation of agglomerates, no SnO₂ on the substrate</p> <p>Bottom substrate: SnO₂ polycrystalline thin film intact</p>
6		<p>Top substrate: no NW growth, SnO₂ layer delaminated, large agglomerates of SnO₂ crystallites dispersed on the surface</p> <p>Bottom substrate: no NW growth, SnO₂ layer delaminated, large agglomerates of SnO₂ crystallites dispersed on the surface</p>


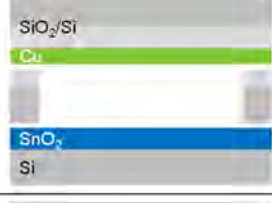

Exp	Sample	Main observations and conclusions
7		<p>Top substrate: dense growth of SnO₂ NWs on the Cu (CuO) structures only</p> <p>Bottom substrate: not observed</p>
8		<p><i>N₂+H₂ atmosphere</i></p> <p>Top substrate: dense growth of SnO₂ NWs, NWs with a zigzag shape and a square cross-section</p> <p>Bottom substrate: continuous SnO₂ layer, SnO₂ crystallites with a pyramidal shape</p>
9		<p>Top substrate: dense growth of SnO₂ NWs (30-100 nm in diameter), droplets observed at the base of NWS suggesting a VLS growth mechanism</p> <p>Bottom substrate: not observed</p>

Figure 34: Summary of the experimented configuration for the optimization of the SnO₂ nanowire growth. All experiments have been conducted at 900°C for 1.5 hours in Ar atmosphere, except Experiment 8 conducted at 900°C for 1.5 hours in forming gas. Experiment 4 is the optimum configuration for the growth of SnO₂ nanowires (framed in red).

2.2.4 Characterization of the SnO₂ nanowires

Morphology

The SnO₂ nanowires synthesized in this thesis are up to hundreds of micrometers long and their diameters range from 50 nm to 400 nm. Figures 35a-35d show SEM images of SnO₂ nanowires synthesized with the optimum configuration identified above in Ar atmosphere. The SnO₂ nanowires grow straight and exhibit a uniform diameter along the growth direction. Figures 35c and 35d focus on the basis of the nanowires. The single crystalline growth of the SnO₂ nanowires seems to start from a larger grain.

Figures 35e and 35f show SnO₂ nanowires, which have also been grown with the optimum configuration but in a reducing atmosphere (95% N₂ + 5% H₂). The as-grown SnO₂ nanostructures are mostly zigzag nanowires and nanobelts, which exhibit two distinct growth directions alternating at regular intervals.

The nanowires have mostly a circular cross-section (see Figure 35g), but some also exhibit a square cross-section as shown in Figure 35h.

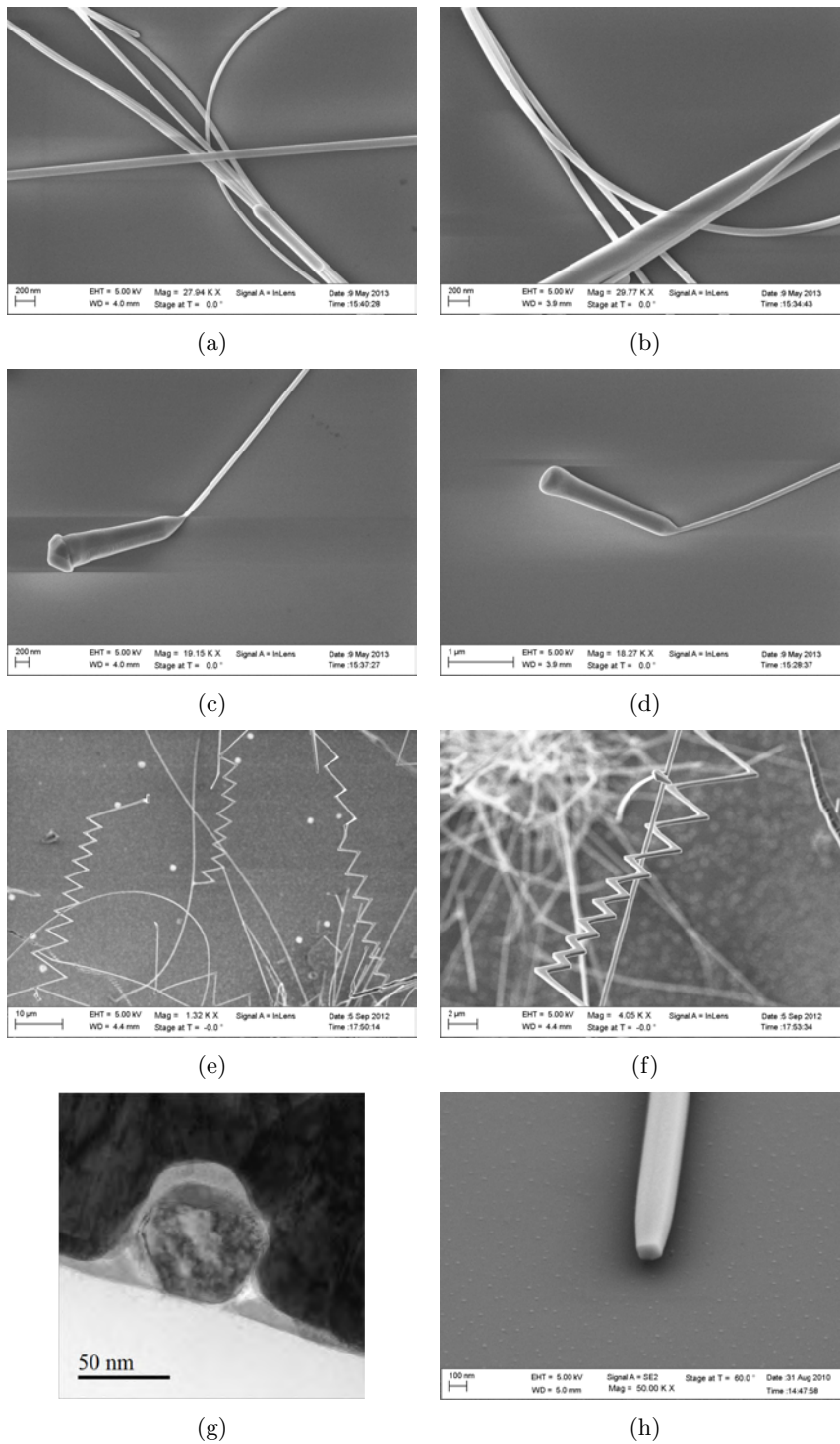


Figure 35: SEM images of SnO₂ nanowires synthesized with the optimum configuration (a-d) in Ar atmosphere and (e-f) in forming gas. (g) TEM image of the cross-section of a SnO₂ nanowire with a circular shape. (h) SEM image of a SnO₂ nanowire exhibiting a square cross-section.

Crystallographic structure

TEM analyses demonstrate that the SnO_2 nanowires are single crystalline. The FFT calculations show that nanowires grow mostly along the crystal growth directions: $[1\ 1\ 1]$, $[1\ 0\ 0]$, $[0\ 1\ 1]$, $[1\ 1\ 0]$ (see Figure 36). For a few nanowires, other crystal growth directions are found: $[8\ 3\ 12]$ and $[4\ 0\ 3]$. Bright field images and electron diffraction patterns were acquired using a Tecnai F20 with a field emission gun (FEG) operating at 200 kV. The microscope has a post column energy filter (Gatan Imaging Filter, GIF) and the images were recorded in zero-loss filtered mode, using a 10 eV wide slit (i.e. elastically scattered electrons only).

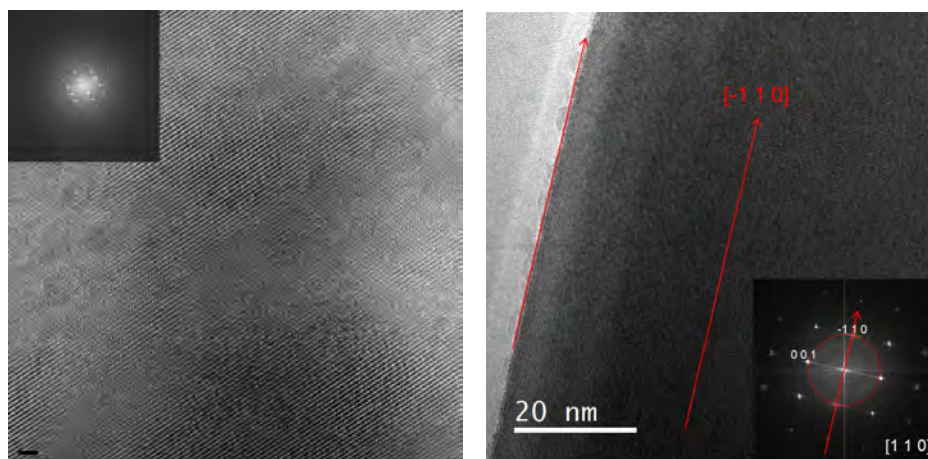


Figure 36: High resolution TEM images and determination of the crystal growth direction.

2.2.5 Discussion

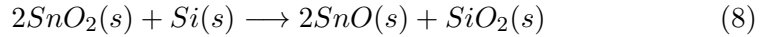
The following conclusions can be drawn from the key experiments presented above:

- For the growth of SnO_2 nanowires, a confined environment (“closed” reaction chamber) is required (Experiments 2-3).
- During the heating phase, the SnO_2 material is transported through the gas phase from the bottom substrate (SnO_2 thin film on Si substrate) to the top substrate (CuO thin film on SiO_2/Si substrate), where it recrystallizes as SnO_2 nanowires (Experiment 4).
- When deposited on SiO_2 , the SnO_2 thin film is not vaporized (Experiment 5). The Si substrate, where the SnO_2 thin film is deposited (Experiment 4), must have a reducing effect on SnO_2 , which probably increases the volatility of SnO_2 and enables its transport through the gas phase.

- Cu or CuO has a catalytic influence on the growth of SnO₂ nanowires. The growth of SnO₂ nanowires is not observed if there is no CuO/Cu present in the reaction chamber (Experiment 6). The growth of SnO₂ nanowires occurs locally, only where CuO/Cu is deposited (Experiment 7).
- In a reducing atmosphere (forming gas), the catalytic layer is Cu and the heating phase results in the growth of zigzag SnO₂ nanowires and nanobelts (Experiment 8).
- Au also plays a catalytic role in the SnO₂ nanowire growth (Experiment 9).

Based on the experimental observations, the following mechanism is proposed to explain the growth of SnO₂ nanowires on CuO/Cu surfaces as conducted in Experiment 4 at 900°C in a constant Ar flow of 1000 sccm:

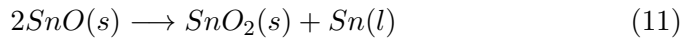
1. The Si substrate reduces the SnO₂ thin film resulting in SnO(s), which is more volatile than SnO₂(s) [52], so most likely SnO(g) is formed according to:



2. SnO(g) is transported through the gas phase and deposited on the CuO/Cu or Au coated substrate forming SnO(s):



3. SnO(s) is unstable at temperatures above 300°C and decomposes to Sn(l) and SnO₂(s) [49] forming the SnO₂ nanowires:



Equation 11 is in disagreement with the Sn-O phase diagrams presented in Figure 6 (Page 22), especially in consideration of the temperatures for the first phase diagram and concerning the products of the SnO(s) dissociation, which are Sn₃O₄(s) and Sn(l) at temperatures above 270°C according to the second phase diagram. However, based on the experimental observations and on the study by Platteeuw [49], this mechanism is plausible.

The catalytic role of the CuO/Cu or Au coated substrate is not completely understood, but it is suggested that CuO/Cu or Au acts as catalyst for the deposition of SnO(g) to SnO(s). Also the growth mechanism of the SnO₂ nanowires is uncertain. A self-catalyst VLS growth mechanism is possible since Sn(l) is formed (Equation 11). However, Figure 25 showed that the grain at the base of a SnO₂ nanowire can be composed of Cu. This result

suggests that the VLS growth mechanism, where the liquid catalyst is a compound of Sn-Cu, Sn-CuO or Sn-Au, is more likely.

A few examples of the use of CuO or Cu₂O for the growth of SnO₂ crystals have been reported. Kunkle et al. [158] reported the growth of single crystals of SnO₂ in a Cu₂O flux. A mixture of SnO₂ and Cu₂O (1:2 volume fraction) has been heated in a Pt-crucible to a temperature of 1250°C during seven days. During the cooling phase, SnO₂ crystals grow in the melt. The SnO₂ crystals as grown have only 0.0021 wt% copper defects identified as CuO and 0.02 wt% silicon defects identified as SiO₂. Colourless SnO₂ crystals have been observed in the melt with a square cross-section of about 1 mm² and lengths of 5-10 mm; rods, platelets and needles have also been observed. It is also possible to initiate SnO₂ crystals from CuO by adding Sn or SnO₂, because CuO decomposes in Cu₂O and O₂ at high temperatures [51].

Fang et al. [159] demonstrated the crucial influence of the substrate for the growth of SnO₂ nanobelts. The growth process is described as follows: Sn powder is placed in an alumina boat covered by a commercial copper foil 5 mm above, and heated at 850°C for 2 h with pure argon at a flow rate of about 200 sccm. SnO₂ zigzag nanobelts are found on the underside of the copper substrate, which faces the reactant, while Cu₂O is identified at the opposite side of the substrate. This result suggests that Sn is oxidized prior to the copper foil by the residual oxygen in the quartz tube. The growth mechanism assumed is a vapor-liquid-solid (VLS) process, where Sn is first vaporized and deposited on the copper substrate before oxidation occurring at the liquid/solid interface. The two main growth directions of the zigzag nanobelts are $[1\ 0\ 1]$ and $[1\ 0\ \bar{1}]$. The authors observed a correlation between the size of the (101) plane of SnO₂ and that of the (100) plane of copper suggesting an epitaxial growth of the SnO₂ nanobelts. Additionally, the use of platinum as substrate covering the crucible results in the growth of straight SnO₂ nanowires with a growth direction vertical to the (332) plane, which could be correlated to the plane (111) of Pt. Wu et al. [160, 161] also observed the formation of zigzag SnO₂ nanobelts when adding CuO to the precursors (SnO₂ and graphite powders), while straight SnO₂ nanowires are obtained without adding CuO powder.

Several authors also report on the importance of confining the reactant vapors between the source material and the substrate in order to grow SnO₂ nanowires. Duan et al. [162, 163] used an iron or copper mesh as substrate for the synthesis of SnO₂ zigzag nanobelts by oxidation of Sn in ambient atmosphere at 900°C. The network also played the role of reactor providing a microenvironment and confining the Sn vapor and the oxygen gas. The authors reported that without the network or outside of it, no zigzag SnO₂ nanobelt was observed.

Huang et al. [164] reported on the role of controlling the reactant vapor concentration in order to tune the morphology of SnO₂ nanostructures. SnO powders were introduced in a crucible covered by multilayer stainless-steel grids and heated to 750-950°C for 1-6 hour. The growth mechanism suggested is a self-catalyst VLS process: SnO decomposes to SnO₂(s) and Sn(l), SnO₂(s) nuclei are formed, Sn(l) is adsorbed on the nuclei and oxidized to SnO₂. The role of the confinement by the grid layers is to tune the concentration of Sn(l) in the as-formed reaction chamber. When confined by thin grids, the concentration of Sn(l) is lower, so the ratio between mass transport and reaction rate is balanced and straight SnO₂ nanobelts are obtained. When confined by thick grids, the concentration of Sn(l) is higher, so the surface reaction rate is increased and the active growth interface is more likely influenced by slight changes of the local conditions (e.g. temperature, partial pressures, supersaturation ratios). These small fluctuations are assumed to be responsible for the change of the preferential growth planes along equivalent directions and the formation of SnO₂ zigzag fibers.

The results reported above are very interesting because they illustrate for the particular case of the formation of SnO₂ zigzag nanobelts the influence of the reactant vapor concentration and of the substrate, which are two parameters playing a crucial role in the synthesis method of SnO₂ nanowires presented in this thesis.

2.3 Summary

The synthesis of SnO₂ nanowires is conducted in two steps. First, a SnO₂ thin film is deposited on a silicon-based substrate by spray pyrolysis. Spray pyrolysis is a CVD process, which is based on the thermal decomposition of a precursor solution directly on the heated substrate. The spray pyrolysis process has been developed to control the most critical parameters (temperature and droplet size) and obtain a reproducible process over time. A very good homogeneity of the film thickness ($\pm 11\%$) on a surface area of 36 cm² has been demonstrated. The SnO₂ thin film deposited by spray pyrolysis is the precursor material for the synthesis of SnO₂ nanowires. The growth of SnO₂ nanowires occurs in the second step, where the SnO₂ thin film is heated in a tube furnace at 900°C in argon atmosphere for 1.5 hour. The optimal configuration for the SnO₂ nanowire growth is a confined environment between two substrates stacked facing each other and separated by spacers. The bottom substrate consists of a SnO₂ thin film (thickness 300 nm) deposited on a silicon substrate with a native oxide (Si). The top substrate is a silicon substrate with a 300 nm thermal oxide on top (SiO₂/Si), which have been coated with 40 nm Cu by sputtering. In that configuration, interwoven SnO₂ nanowires grow on the top substrate and form a dense layer. The mechanism for the nanowire growth is not completely understood. How-

ever, the volatility of the SnO₂ material is triggered by the reduction of the SnO₂ film by the Si substrate. SnO₂ is then transported in the gas phase most probably as SnO and recrystallizes on the Cu-coated substrate. The growth SnO₂ nanowires is also possible on a Au-coated SiO₂/Si substrate. The SnO₂ nanowires are very long (up to hundreds of microns) and have diameters in the range 50-300 nm. They exhibit a single crystalline structure and the main crystal growth directions determined by TEM analysis are [1 1 1], [1 1 0], [0 1 1], [1 0 0].

3 Fabrication of single nanowire gas sensors

3.1 Process flow

As shown in Section 2.2.3, the growth of SnO₂ nanowires has been optimized. SnO₂ nanowires grow particularly dense on CuO coated silicon substrates in the configuration described in Figure 28. SnO₂ recrystallizes on the CuO coated substrate after transport through the gas phase from a SnO₂ film deposited on a Si substrate heated at 900°C in Argon atmosphere. The SnO₂ nanowires used as gas sensors all originate from the top substrate of such a configuration.

The process flow leading to the fabrication of single nanowire sensors is schemed in Figure 37. It starts with the transfer of SnO₂ nanowires from the original growth substrate to a bare SiO₂/Si substrate. The 2×2 cm² original growth chip is cleaved into 8 pieces. One piece is placed in an eppendorf tube with 0.5 mL isopropanol. The sample is ultrasonicated for 30 min, which results in the dispersion of SnO₂ nanowires in the isopropanol solution. The solution is spin-coated on a SiO₂/Si chip for 35 s at 4000 rpm. This step may be repeated several times to reach the desired density of nanowires on the SiO₂/Si chip. The SnO₂ nanowires, which have diameters in the range 50-300 nm and lengths up to 100 μm, are visible with the optical microscope. They are randomly spread on the SiO₂/Si chip.

In order to enable the measurement of resistance change during exposure to target gases, electrodes must be deposited on the SnO₂ nanowire. Lithography techniques are used to pattern a metallic layer and form the contacts on the nanowires. The processing steps are the following: spin-coating of the resist, prebake, exposure, development, deposition of the metallic layer and lift-off. Two different approaches have been investigated to contact the SnO₂ nanowires based on two distinct technologies: optical lithography and electron-beam lithography (e-beam lithography). Optical lithography has been used to process a large number of single nanowire devices in a 2-point configuration, while e-beam lithography, which is a more time-consuming technique, has been used to contact specific nanowires in a 4-point configuration. Optical lithography is a comparable simple technique, while e-beam lithography is much more sophisticated and very time-consuming.

Optical lithography is used to pattern the contacts according to the device design on a photomask. The pattern of the photomask used is shown in Figure 38. Each structure is composed of four large contact pads necessary for bonding. The contact pads are connected to a finer structure composed of four parallel contacts, which are 2 μm wide. The spacing between the contacts 1-2 and 3-4 is 2 μm. The distance between the contacts 2-3 is 2 μm, 5 μm or 10 μm. Ideally, the SnO₂ nanowire lies between the four contacts so a 4-point measurement is possible. However, as already mentioned

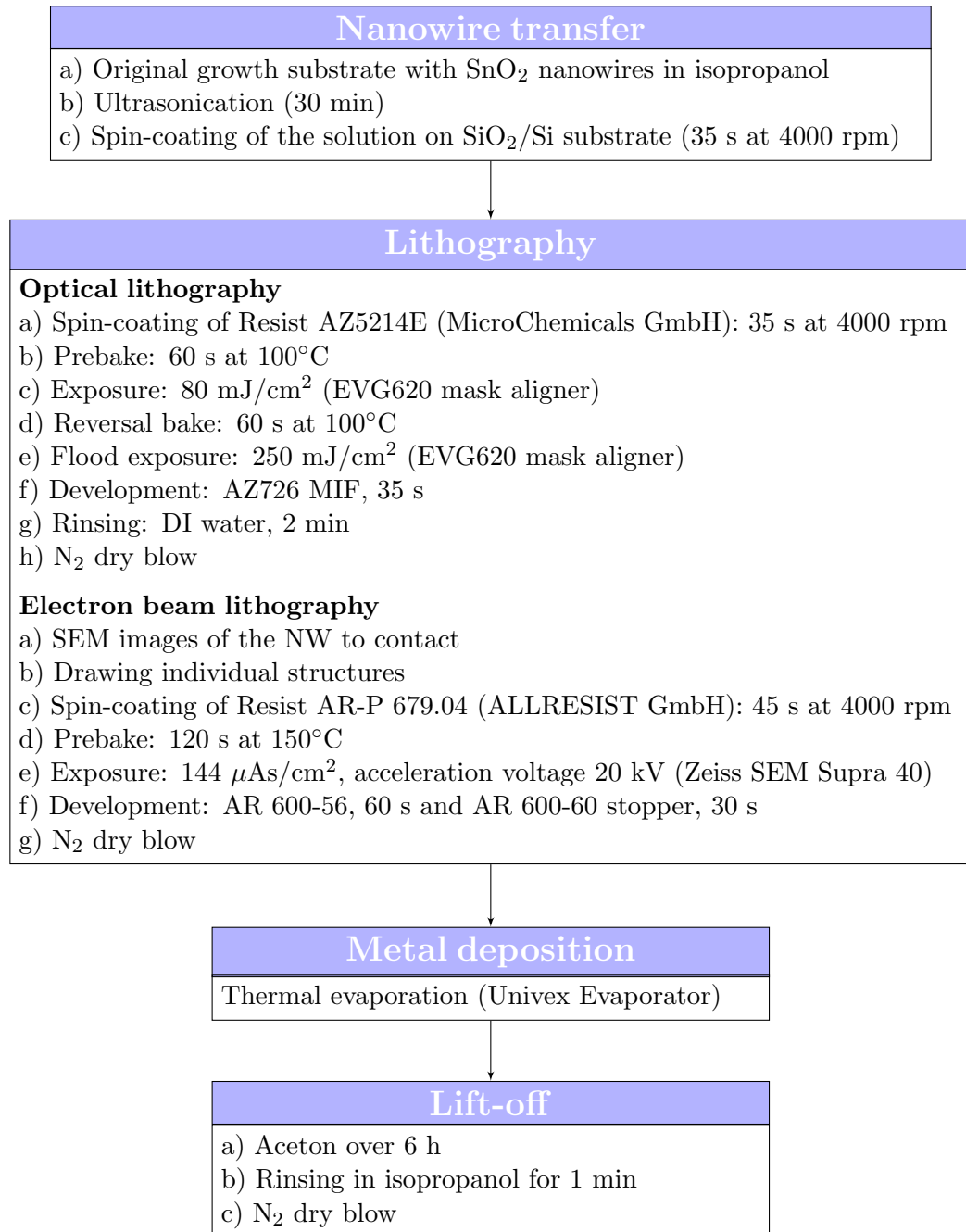


Figure 37: Process flow for the fabrication of SnO₂ nanowire sensors.

above, the SnO_2 nanowires are randomly dispersed on the substrate and even though many nanowires are found between two contacts, few are actually contacted by all the four parallel contacts. After processing, the chip is controlled with the optical microscope and the position of the nanowires between two or more contacts is noted (name of the structure and numbers of the contacts involved). Optical lithography is a simple process appropriate to contact many SnO_2 nanowires at once: as many as hundred nanowires can be contacted in a 2-point configuration on one chip. However, this technique is not suitable for reliable contacting of SnO_2 nanowires in a 4-point configuration, which is the reason why the e-beam lithography process has also been developed.

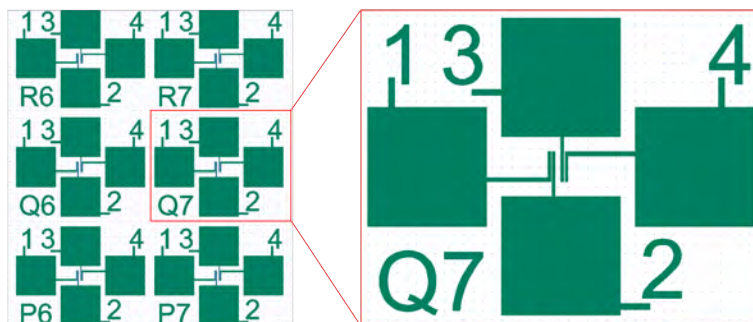


Figure 38: Design of the photomask used to pattern the metal contacts. One structure is composed of four large contact pads (bonding pads) leading to four parallel contacts.

The e-beam lithography technique is a direct writing technique and does not require a photomask. The structures are designed individually for each nanowire, which is of great advantage for contacting SnO_2 nanowires in a 4-point configuration. First the patterning of a metallic layer deposited on a SiO_2/Si substrate by an optical lithography step and a lift-off process provides bonding pads and structures used as alignment marker for the successive e-beam lithography step. The SnO_2 nanowires are dispersed on the chip and SEM images of the nanowires, which are in the area between the pads and thus should be contacted, are taken (Figure 39a). A specific software enables the drawing of the contact structures (Figure 39b). Typically, the width of the contacts is 500 nm and the distance between the contacts varies between 500 nm and 2 μm . The resist is spin-coated on the chip, followed by a prebake step. The chip is then introduced into the SEM for the e-beam exposure. After exposure and development of the structures, the metallic layer (Ti/Au) is thermally evaporated. A final lift-off process results in contacting the nanowire in a 4-point configuration (Figures 39c-39d). Drawing individual structures for each nanowire is an advantage to select the SnO_2 nanowires to contact (possibility to vary the geometry of the

nanowires contacted) and to vary the contact parameters, such as contact width and distance between the contacts, but it is also very time-consuming. Also the time for the e-beam exposure is about 3 minutes per structure, i.e. per nanowire to contact.

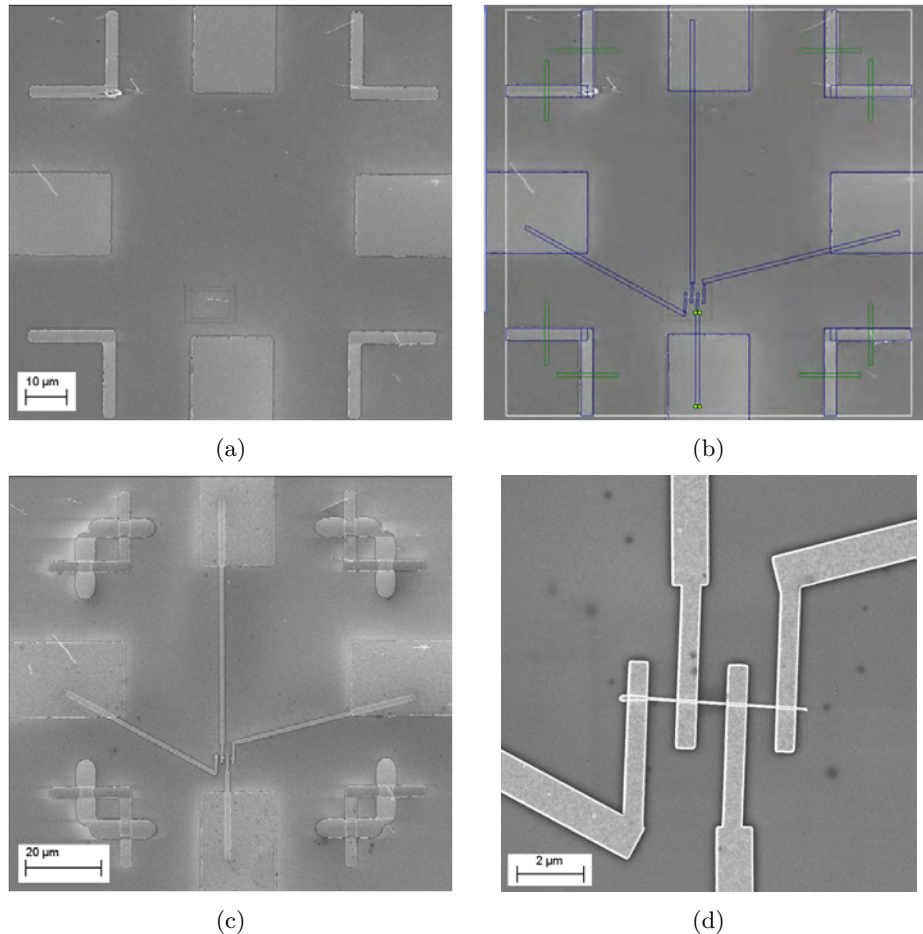


Figure 39: SEM images describing the different steps of the e-beam lithography process. (a) Imaging of the nanowire to contact. (b) Drawing of the pattern from the bonding pads to the nanowire. (c) After e-beam lithography, deposition of the metallic layer and lift-off. (d) Contacts on the SnO₂ nanowire in a 4-point configuration.

3.2 Choice of the metal used for the contacts

The choice of the metal used to establish the electrical contacts on the metal oxide sensors is of utmost importance. The appropriate material and deposition technique must be chosen to obtain ohmic contacts. Commercial sensors (i.e. FIGARO Engineering Inc. and Henan Hanwei Electronics Co.) use Au as electrodes on SnO₂ sensing layers [165, 166]. Platinum

(Pt) is also used as metallization providing good ohmic contacts with SnO₂ [15]. In commercially available conductometric gas sensors, based on thick or thin film technology, the electrical contact area between the electrode and the sensing layer is large (i.e. interdigitated electrodes) and planar, so the contact effects are minimized. The challenge for contacting nanowires is mostly their small dimension and circular geometry, so the established models for electrical contacts on bulk semiconductors may not be applicable [167, 168, 169].

The establishment of ohmic contacts on single SnO₂ nanowire devices is still an issue. Few groups address the problem of non-ohmic contacts, mainly because the studies often focus on the measurement of a network of SnO₂ nanowires and not on single nanowire devices. In the case of a nanowire network, the contact resistance, which is often predominant in the single nanowire devices, is lowered because it is connected to a large number of resistances [53]. In the literature, platinum (Pt) is commonly used as metallic contact on the SnO₂ nanowires [28, 27, 87] and Ti/Au is also reported [97, 170]. The SnO₂ nanowires may also be deposited on top of interdigitated electrodes to build SnO₂ nanowire network devices [30, 57]. More recently, RuO₂ has been investigated to form ohmic contacts with single SnO₂ nanowires [171].

Moreover, the metal chosen may influence the gas response of the sensor. For instance, Barsan et al. [172] reported that a SnO₂ thick film sensor contacted with Pt electrodes exhibited a higher response upon exposure to CO than a similar SnO₂ thick film sensor contacted with Au electrodes. Possible explanations for the enhanced response with Pt electrodes are a catalytic effect at the boundary sensing layer/gas phase/electrodes, a doping of the sensing layer by diffusion of Pt in the electrode region or the formation of an intermediate layer between the sensing layer and the metallic electrode.

In this thesis, different materials have been investigated as metal contact for the SnO₂ nanowires mostly involving gold (Au). Au exhibits good conducting properties, withstands high temperature without oxidizing, its deposition with PVD techniques is simple and it is a suitable material for wire bonding. The challenge lies in its weak adhesion properties on SiO₂/Si substrates. Therefore a thin adhesion layer is necessary. Titanium (Ti) and Chromium (Cr) are known for their good adhesion properties on SiO₂/Si substrates. Therefore, both materials have been tested as intermediate layer between the SnO₂ nanowire and the Au layer. Tin (Sn) has also been tested as intermediate layer in order to investigate if this material enables the fabrication of ohmic contacts with the SnO₂ nanowires. As alternative material to Au, Aluminium (Al) has also been tested.

3.2.1 Methods

The SnO₂ nanowires have been transferred to SiO₂/Si substrates prior to contacting as described in Section 3.1. The metallic layers have been deposited by thermal evaporation. The thickness of the adhesion layer is about 10 nm for Ti and Cr and 20 nm for Sn. On top of the adhesion layer, 150 nm of Au has been deposited. For that study, the patterning of the contact layer has been performed by optical lithography and lift-off processes. Two chips have been processed for each intermediate layer used: Ti-1 and Ti-2 (10 nm Ti/150 nm Au), Cr-1 and Cr-2 (10 nm Cr/150 nm Au), Sn-1 and Sn-2 (20 nm Sn/150 nm Au). On the chips Ti-2, Cr-2 and Sn-2, an oxygen plasma treatment has been conducted after the optical lithography process and before the deposition of the metal layer in order to clean the surface of the SnO₂ nanowires, which will be in contact with the metallization. The different samples investigated are listed in Table 5.

Table 5: List of the samples prepared with different contact materials by optical lithography. The thickness of the layers is indicated in brackets.

Sample	Adhesion layer	Material	Oxygen plasma prior to metal deposition
Al-1	-	Al (100 nm)	-
Al-2	-	Al (100 nm)	yes
Sn-1	Sn (20 nm)	Au (150 nm)	-
Sn-2	Sn (20 nm)	Au (150 nm)	yes
Cr-1	Cr (10 nm)	Au (150 nm)	-
Cr-2	Cr (10 nm)	Au (150 nm)	yes
Ti-1	Ti (10 nm)	Au (150 nm)	-
Ti-2	Ti (10 nm)	Au (150 nm)	yes
Au-1	-	Au (150 nm)	-

In case of Ti or Cr as intermediate adhesive layer between the SnO₂ nanowire and the Au contact, an oxide barrier (TiO_x or CrO_x) might be formed, which is a problem for the desired ohmic contacts. Therefore, in addition, another sample has been prepared without intermediate layer to ensure a direct contact between the Au layer and the SnO₂ nanowire: Au-1. Therefore, a two-step process has been performed. First a metallic layer has been deposited directly on the bare SiO₂/Si chip. This layer consists of an adhesion layer of Ti (5 nm thickness) and a Au layer (25 nm thickness). Successively, the SnO₂ nanowires have been transferred on top of the contacts and a second optical lithography step with the same optical mask aligned on the bottom contacts has been conducted. A second metallic layer of Au (150 nm) has been deposited by thermal evaporation on top of the first metallization

layer. Thus, the nanowires, which bridge two contact pads, are sandwiched between the bottom and the top Au layers, which provides a direct electrical contact between the Au layer and the nanowire.

As comparison, Al has also been tested as contact material without adhesion layer. Al has been thermally evaporated on two chips (Al-1 and Al-2) with a thickness of 100 nm to provide contacts to the SnO₂ nanowires. On the chip Al-2, an oxygen plasma treatment has been conducted after the optical lithography process and before the deposition of the metal layer as cleaning treatment of the SnO₂ nanowire surface.

Table 5 summarizes all samples, which have been investigated. A large number of nanowires is contacted in a 2-point configuration on each sample, so statistical information on the quality of the contacts can be obtained. The I-V characteristics have been measured on a tip probe station with a parameter analyzer (Agilent 4156C [173]) in ambient air. The stage of the tip probe station has been heated up to a temperature of 200°C. The resistance of the measured nanowires has been calculated from the fit of the linear I-V characteristics. Linear I-V characteristics measured in a 2-point configuration means that an ohmic contact is formed. The influence of the oxygen plasma treatment before thermal evaporation of the metal contacts has been investigated, as well as the influence of an annealing step performed on a hot plate in ambient air.

3.2.2 Results

Table 6 sums up the results obtained for the different metal contacts investigated before and after annealing. The number of I-V characteristics, i.e. the number of SnO₂ nanowires, measured on each sample at 200°C before and after annealing is indicated. The percentage of linear I-V characteristics measured is a good information on the quality of the metallic contact with the SnO₂ nanowire. For the samples contacted with an Al layer, the number of devices with linear I-V characteristics is 60% for Al-1 and 30% for Al-2 before annealing. After 5 min annealing at 400°C, no current could be measured while applying a voltage between -10 V and +10 V, which indicates the deterioration of the contacts. For the samples contacted with a Sn/Au layer, the percentage of linear I-V characteristics obtained is very high (in the range of 85-100%) before and after an annealing step of 5 minutes at 400°C. Before annealing, the percentage of linear I-V characteristics on the samples Cr-1 and Cr-2 (Cr/Au contact layer) is 35% and 60%, respectively. After annealing (1 h at 300°C), 70% and 80% of the characteristics measured on Cr-1 and Cr-2, respectively, are linear. For a contact layer composed of Ti/Au, the percentage of linear I-V characteristics is 80% for Ti-1 and 95% for Ti-2, before annealing. After annealing (30 min at 300°C), 85% of the I-V characteristics measured on Ti-1 and Ti-2 are linear. For the sample

contacted only with a Au layer (Au-1), 60% of the I-V characteristics measured are linear before annealing and 85% after annealing (1 h at 300°C).

Table 6: Comparison of the quality of different metallic contacts with SnO₂ nanowires. The I-V characteristics have been measured in a 2-point configuration at 200°C before and after annealing.

Sample	Before annealing		After annealing	
	Number of characteristics measured	Percentage of linear characteristics	Number of characteristics measured	Percentage of linear characteristics
Al-1	17	60%	-	-
Al-2	23	30%	-	-
Sn-1	26	100%	12	100%
Sn-2	30	90%	21	85%
Cr-1	40	35%	39	70%
Cr-2	45	60%	39	80%
Ti-1	170	80%	95	85%
Ti-2	44	95%	132	85%
Au-1	29	60%	22	85%

Figure 40 shows SEM images of a SnO₂ nanowire located on the chip Sn-1 after annealing. The metallic film (20 nm Sn/150 nm Au) is composed of grains up to 100 nm large, which appear to be rather isolated from each other. Interestingly, the metallic layer appears more dense and continuous on the SnO₂ nanowire than on the SiO₂/Si substrate, so the adhesion between the nanowire and the film seems to be satisfying. However, after a few hours at temperatures above 300°C, the deterioration of the contact is observed.

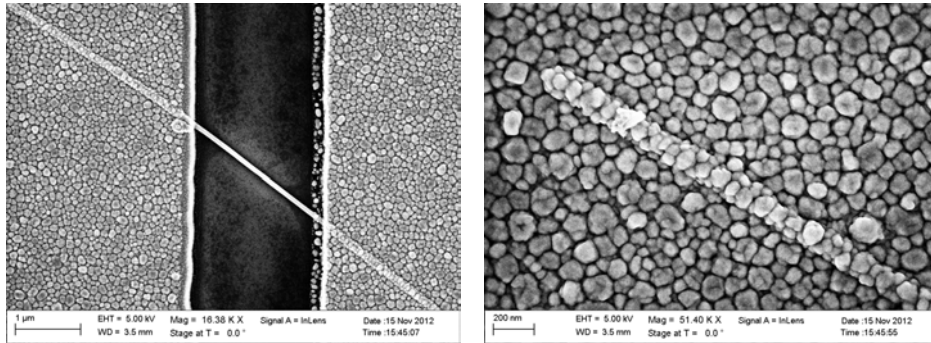


Figure 40: SEM images of a SnO₂ nanowire contacted by a metallic film of Sn/Au after 5 min annealing at 400°C.

Figure 41 shows the SEM image of a SnO₂ nanowire contacted on Ti-1 and the corresponding I-V characteristics measured. At room temperature, the I-V characteristic is not linear. It becomes linear at 200°C and the resistance calculated from the fit of the linear characteristic decreases after an annealing step of 30 minutes at 300°C. This behaviour is rather typical for the nanowires on samples Ti-1 and Ti-2, though the non-linearity of the I-V characteristic at room temperature is not observed for every SnO₂ nanowire, as also reported by Hernandez-Ramirez et al. [28].

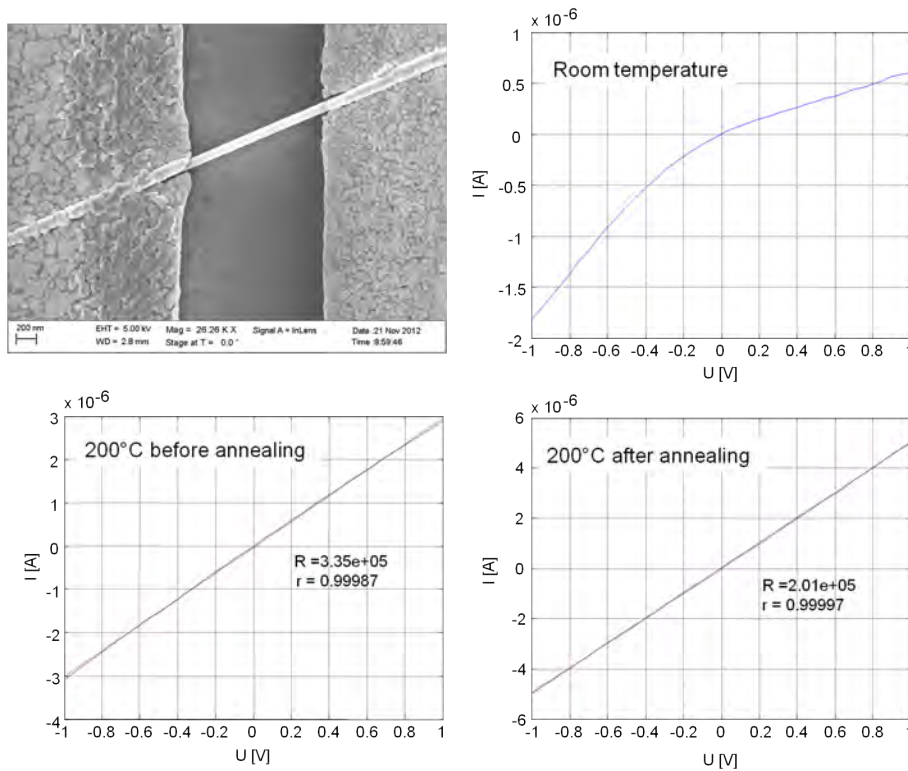


Figure 41: SEM image of a SnO₂ nanowire contacted by a metallic film of Ti/Au and the corresponding I-V characteristics measured at room temperature, at 200°C before annealing and at 200°C after 30 min annealing at 300°C.

Figure 42 shows SEM images of SnO₂ nanowires sandwiched between the two layers of Au after annealing on Au-1. On the left image, the nanowire seems to be well covered by the top Au layer. The top Au layer is structured in large grains but the metal contact should not be hindered. The right image shows a broken nanowire, which partly lifted the top Au layer, so a more precise observation of the coverage of the SnO₂ nanowire by the Au film is possible. It appears that the bottom metallization is not continuous, holes can be seen between the metal grains. This might be due to problems of

adhesion and a thicker bottom layer may be a solution. Moreover, the top Au layer does not cover the SnO₂ nanowire very well from the side: a gap is visible between the nanowire and the Au layer, although this might be caused during the breaking of the nanowire.

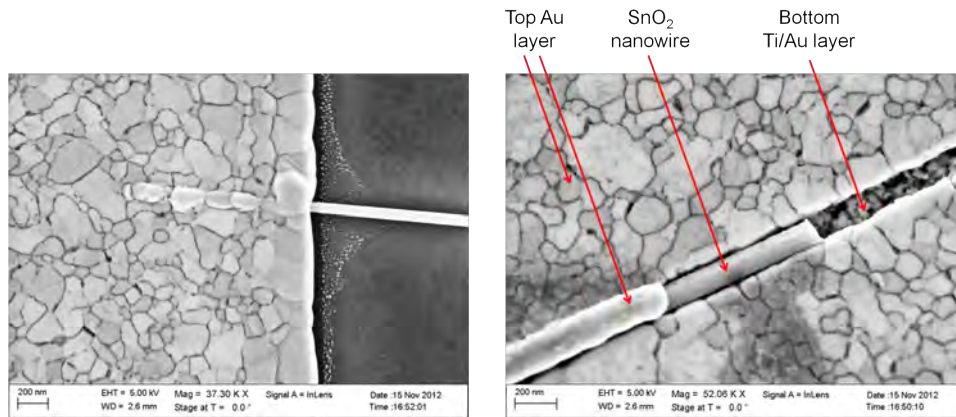


Figure 42: SEM images of a SnO₂ nanowire stacked between two Au layers on Au-1 after 5 min annealing at 400°C.

The distribution of the resistance values measured at 200°C after annealing is shown in Figure 43 for the different metal contacts. Each point represents the resistance of one nanowire with a linear I-V characteristic. The values of resistance are spread over several orders of magnitude. This can be explained by the various geometries of the SnO₂ nanowires measured, which are not taken into account here. After annealing, the resistance values of the nanowires are mostly between 600 MΩ and 2 GΩ for Sn-1 and between 600 MΩ and 15 GΩ for Sn-2. The resistance is in the range 1-15 GΩ for most of the nanowires located on Cr-1 and in the range 5-90 GΩ for most of the nanowires located on Cr-2. For the nanowires contacted with a Ti/Au layer, the resistance values are widely spread over 5 orders of magnitude. They are mostly in the range 200 kΩ - 1 GΩ for Ti-1 and in the range 5 MΩ - 5 GΩ for Ti-2. On the sample Au-1, the values of resistance are mostly between 500 MΩ and 15 GΩ.

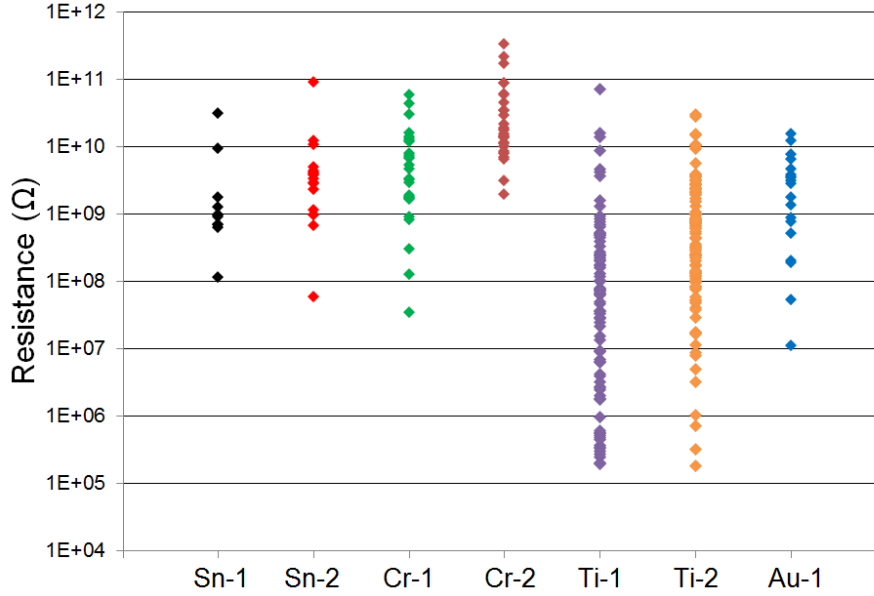


Figure 43: Distribution of resistance values of SnO₂ nanowires measured in a 2-point configuration at 200°C after annealing for different metal contacts. Each point represents the resistance of one nanowire with a linear I-V characteristic.

3.2.3 Discussion

The electron affinity of SnO₂ is 4.5 eV [174]. The work function of the metals used for contacting the SnO₂ nanowires are [175]: 4.50 eV for Cr, 4.33 eV for Ti, 4.42 eV for Sn, 5.1 eV for Au and 4.28 eV for Al (see Figure 44). When a n-type semiconductor and a metal are put in contact, the alignment of the Fermi levels may result in the formation of a Schottky barrier at the interface if the work function of the metal is higher than the electron affinity of the semiconductor. The height of the Schottky barrier Φ_B formed can be calculated according to the Schottky-Mott model as the difference between the work function of the metal Φ_M and the electron affinity of the semiconductor χ_{SC} :

$$\Phi_B = \Phi_M - \chi_{SC} \quad (12)$$

As a consequence, the formation of a Schottky barrier is expected between the SnO₂ nanowire and the Au contact, while the low work function metals - Cr, Ti, Sn and Al - are expected to build ohmic contacts with SnO₂. However, the results show that Au can form ohmic contacts with the SnO₂ nanowires and the use of Cr, Ti, Sn and Al as contact material does not necessarily result in ohmic contacts with the SnO₂ nanowires. This may be related to the formation of surface states due to metal oxidation, surface defects, chemical impurities or organic residue at the SnO₂/metal interface. These surface states created in the band gap of the semiconductor results

in the “pinning” of the Fermi energy level, so the Schottky barrier height becomes independent of the metal work function [176, 177, 178]. Since the oxidation of Cr, Ti and Al is inevitable and the presence of surface defects or organic residues at the SnO₂/metal interface may be different from one nanowire to another, the presence of surface states may be responsible as well for the linear I-V characteristics obtained with Au contacts as for the non linearity of I-V characteristics measured for nanowires contacted with Cr, Ti, Sn and Al.

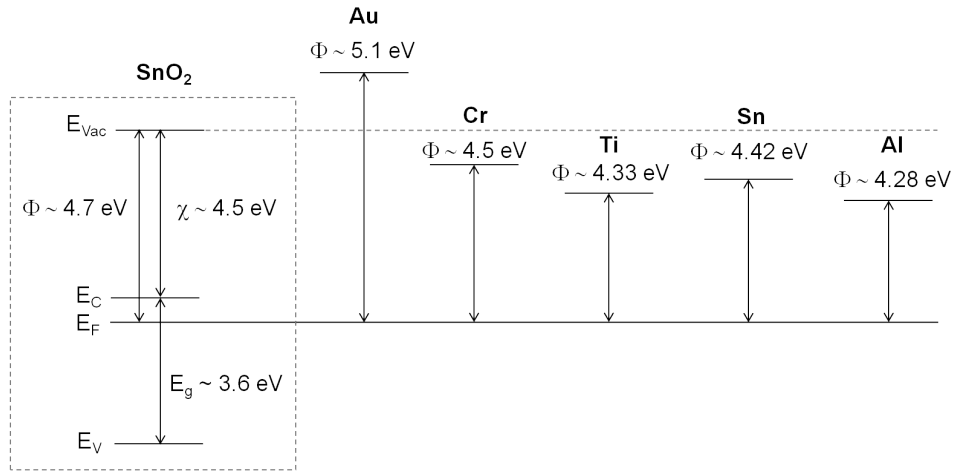


Figure 44: Representation of the work function Φ , the electron affinity χ and the band gap E_g of SnO₂ and comparison with the work function Φ of the metals investigated as contact material.

From the results shown in Table 6, a contact layer composed of Sn/Au seems to be the most promising to establish ohmic contacts with SnO₂ nanowires, followed by Ti/Au, Au and Cr/Au. For the nanowires contacted with Al, no current could be measured when applying a voltage between the two contact pads after an annealing step at 400°C, which indicates that the Al layer has probably been completely oxidized. Further investigations with Au as a protection layer in order to avoid the Al oxidation could be interesting to conduct, as suggested in [179].

The results obtained with the Sn/Au layer seems at first promising because the percentage of linear I-V characteristics is high before and after annealing. The good quality of the contact between the Sn layer and the SnO₂ nanowire might be ensured by the diffusion of oxygen from the SnO₂ nanowire into the Sn layer. The structure of the metal layer on the SiO₂ surface observed in Figure 40 suggests that the Sn layer melts during the annealing step at 400°C. The melting point of Sn is 231.9°C, so this behaviour is expected resulting in the formation of grains. The interest of this experiment lies in the possible formation of a Sn-Au alloy during the cooling down phase (see the

Au-Sn phase diagram in Figure 45), which may withstand temperatures up to 350°C for further gas sensing measurements. However, the deterioration of the contact after a few hours at higher temperature might be an indication that no Sn-Au alloy is formed or that the adhesion properties of the Sn-Au alloy formed is weak on SiO₂, so Sn is not an appropriate adhesion layer for contacting the SnO₂ nanowires.

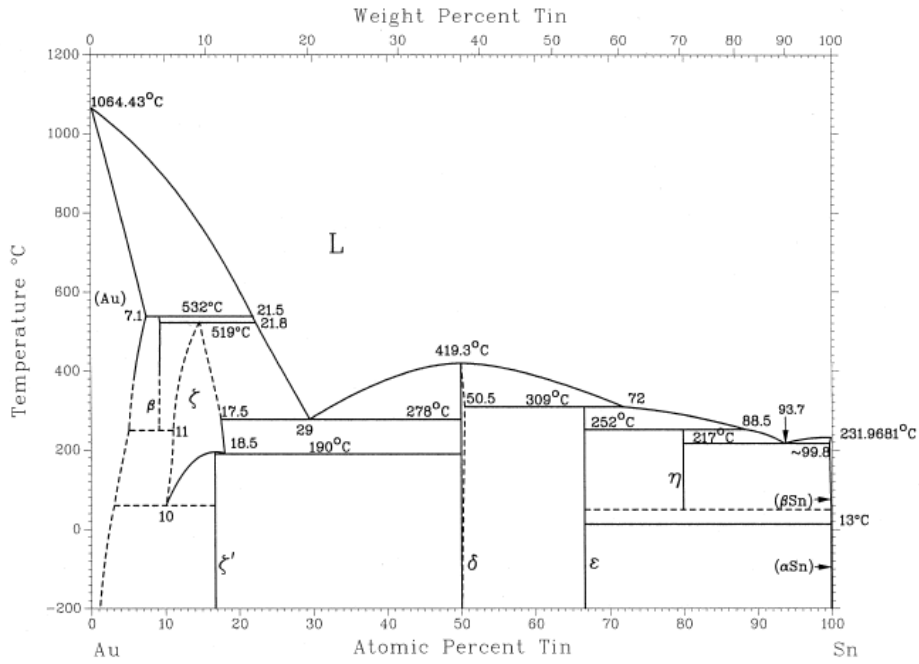


Figure 45: Au-Sn phase diagram from [48].

The use of Cr as an adhesion layer yields a high percentage of linear I-V characteristics especially after annealing, so an improvement of the contact between the nanowire and the metallic layer is observable. However, the resistance values measured at 200°C after annealing are high (in the order of tens of GΩ). As a comparison, the use of Ti as adhesion layer yields a slightly higher percentage of linear I-V characteristics and the resistance values are mostly in the MΩ range at 200°C after annealing. Stern et al. [180] reported on the increase of contact resistivity for GaN nanowires with decreasing carrier density, so the contact resistance increases with the resistance of the nanowires. Therefore, the contact resistance might be lower when using Ti than when using Cr as adhesion layer, which is the reason why Ti has been chosen as adhesion layer to contact SnO₂ nanowires for further gas sensing measurements.

The removal of any adhesion layer by contacting the SnO₂ nanowires directly

stacked between two Au layers (sample Au-1) has also been investigated. An increase of the percentage of linear I-V characteristics is observed after annealing and the average resistance of the nanowires is acceptable although it is higher than for the nanowires contacted with Ti/Au. As shown in Figure 42, the contacts might be improved by depositing a thicker bottom layer. One single nanowire device, which exhibits a resistance in the $M\Omega$ range, is further investigated as gas sensor in the next chapter (sensor A).

The effect of oxygen plasma on the quality of the contacts is not obvious. The objective of using an oxygen plasma is to clean the surface of the SnO_2 nanowires (e.g. removal of resist residue) and to ensure a good contact with the metallic layer. With a Sn adhesion layer, the percentage of linear I-V characteristic is lower for the sample, which has been exposed to oxygen plasma prior to the metal evaporation (Sn-2) and the resistance of the nanowires is slightly higher. The effect of oxygen plasma on the sample Cr-2 results in a higher percentage of the linear I-V characteristics in comparison with the sample Cr-1. However, the resistance after annealing is five times higher for the nanowires on the sample Cr-2 than on the sample Cr-1. After annealing, as many I-V characteristics are linear on Ti-1 and on Ti-2, but the resistance values are higher on Ti-2 than on Ti-1. The higher resistance values on the samples Sn-2, Cr-2 and Ti-2 might be due to the “filling” of some oxygen vacancies during the oxygen plasma treatment resulting in a decrease of the concentration of charge carriers. This might also favour the formation of an oxide barrier (TiO_x , CrO_x) between the metal and the nanowire.

In this study the emphasis has been put on the number of devices measured in order to find out which metal contact is the most likely to establish an ohmic contact with the SnO_2 nanowires and withstand the high temperatures necessary for the gas sensing characterization. This is of primary interest for practical applications. The choice has been made to use the metallization, for which the nanowire resistance measured after annealing is the lowest, because it has been reported that the contact resistance increases with increasing resistivity of the nanowire [171, 180]. Consequently, further investigations have been performed with metal contacts composed of a thin adhesion layer of Ti (10 nm) and a thick layer of Au (150 nm).

The measurement of I-V characteristics of nanowires with the different metallizations in a 4-point configuration would probably clarify the influence of the contact material, the annealing step and the oxygen plasma treatment on the contact resistance and on the resistance of the nanowire itself. This, however, has not been performed because the e-beam lithography process, which is required to contact the nanowires in a 4-point configuration, is extremely time-consuming and would have exceeded the frame of this thesis.

3.3 Electrical characterization of the SnO₂ nanowires

3.3.1 Determination of the contact resistance

The electrical characterization of the SnO₂ nanowire devices consists in determining the contributions of the nanowire itself and of the contact resistance on the total resistance measured in a 2-point configuration. This can be calculated from the comparison between measurements conducted in a 2-point and in a 4-point configuration.

In the 2-point configuration, a voltage V_{2pt} is applied between the two internal electrodes contacting the nanowire and the current I_{2-3} is measured between the same 2 electrodes (see Figure 47a). If the I-V characteristic is linear, the resistance can be calculated by Ohm's law:

$$R_{2pt} = \frac{V_{2pt}}{I_{2-3}} \quad (13)$$

The resistance R_{2pt} is the sum of the resistance of the nanowire itself R_{NW} and of the contact resistance R_C , as illustrated in Figure 46.

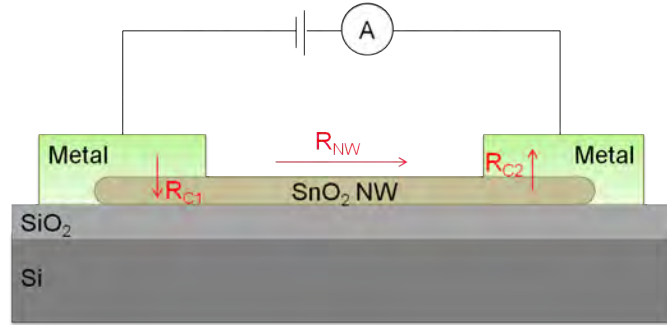


Figure 46: The resistance measured in a 2-point configuration is the sum of the resistance of the nanowire itself R_{NW} and of the contact resistance $R_C = R_{C1} + R_{C2}$ at the interface metal-nanowire.

In the 4-point measurement, a current I_{1-4} is supplied between the external electrodes, while the voltage induced at the internal electrodes V_{4pt} is measured (see Figure 47b). So the resistance is:

$$R_{4pt} = \frac{V_{4pt}}{I_{1-4}} \quad (14)$$

The contact resistance R_C is defined as the difference between the resistance measured between the internal electrodes in a 2-point configuration R_{2pt} and the resistance measured between the internal electrodes in a 4-point configuration R_{4pt} [180]:

$$R_C = R_{2pt} - R_{4pt} \quad (15)$$

The contribution of the contact resistance R_C on the total resistance R_{2pt} can be calculated as a percentage $(\frac{R_C}{R_{2pt}} \times 100)$.

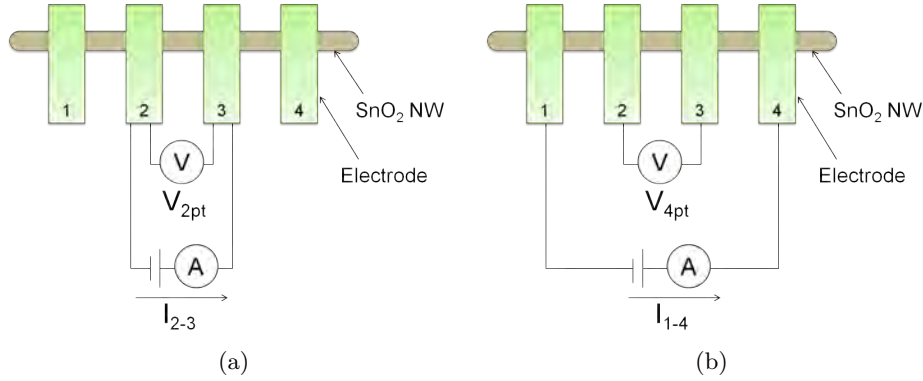


Figure 47: (a) Measurement in a 2-point configuration, (b) Measurement in a 4-point configuration.

Samples have been prepared by e-beam lithography. On the sample Ebeam-1, 23 SnO₂ nanowires have been contacted in a 4-point configuration with a Ti/Au layer (thickness 10/150 nm) patterned by e-beam lithography. The four contacts on one nanowire are about 500 nm wide and separated by a constant distance of about 500 nm.

The nanowires on Ebeam-1 have been first characterized at 200°C after annealing (5 min at 300°C). Only 30% of the I-V characteristics measured in a 2-point configuration between the external contacts are linear after annealing. This result is quite low in comparison with the 85% of linear I-V characteristics measured after annealing on the sample Ti-1 (prepared by optical lithography, results in Table 6). This difference between the samples Ti-1 and Ebeam-1 is probably due to the difference in the lithography processes, which employ different types of resist materials leading to specific residues after resist development. The different exposure techniques (electron beam and UV light) might also induce modifications in the SnO₂ nanowire structure. Actually, modifications of the intrinsic properties of the nanowire due to the electron beam have been reported by Stern et al. [181]. In that study, both optical and e-beam lithography processes were used for the contact patterning on GaN nanowires and the ohmic behaviour of the contacts processed with e-beam lithography was very sensitive to the annealing conditions after processing. The ideal annealing conditions reported were 1 min at 475°C. This is an indication to take into account for future investigations.

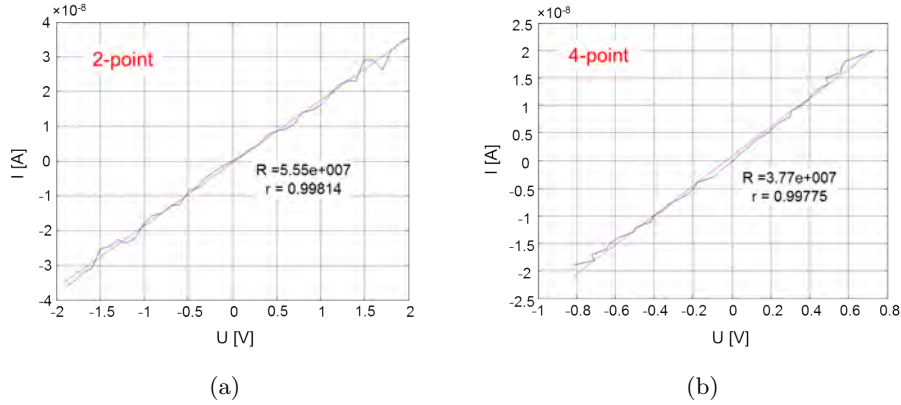


Figure 48: Measurement of a single SnO₂ nanowire on the sample Ebeam-1 (a) in a 2-point configuration between the internal contacts, (b) in a 4-point configuration.

The six SnO₂ nanowires on Ebeam-1 (thereafter named NW-ebeam-1 to NW-ebeam-6), which exhibit linear I-V characteristics in a 2-point configuration at 200°C, have been more extensively investigated. They have been measured successively in a 2-point configuration between the internal contacts and in a 4-point configuration at 200°C. Figure 48 shows a typical result. The resistances R_{2pt} and R_{4pt} , which are calculated from the linear fit of the respective I-V characteristics, are shown in Table 7. R_{2pt} ranges between 30 and 180 M Ω and R_{4pt} between 15 and 90 M Ω . The contact resistance R_C accounts for 30% to 60% of the total resistance R_{2pt} measured in a 2-point configuration.

Table 7: Values of resistance measured on single SnO₂ nanowire devices on the sample Ebeam-1 in a 2-point and in a 4-point configuration at 200°C. The contact resistance R_C and its contribution to the total resistance measured in a 2-point configuration R_{2pt} are calculated. The diameter of the nanowires has been measured from SEM images in order to calculate the conductivity.

Device name	R_{2pt} [M Ω]	R_{4pt} [M Ω]	R_C [M Ω]	R_C/R_{2pt} [%]	Diameter [nm]	Conductivity [S/m]
NW-ebeam-1	180	87	93	52	60	2.0
NW-ebeam-2	56	38	18	33	65	4.0
NW-ebeam-3	112	47	64	58	75	2.4
NW-ebeam-4	97	67	30	31	75	1.7
NW-ebeam-5	42	18	24	57	80	5.6
NW-ebeam-6	30	14	16	54	150	2.0

3.3.2 Measurement of conductivity

A comparison between the conductivity of SnO₂ nanowires located on the sample Ti-1 (prepared by optical lithography, see Table 5) and on the sample Ebeam-1 (prepared by e-beam lithography) is presented.

Assuming that the nanowires have a circular shape, the conductivity σ can be calculated by:

$$\sigma = \frac{1}{R} \times \frac{l}{\pi r^2} \quad (16)$$

where R is the electrical resistance of the nanowire, l and r are the length and the radius of the nanowire, respectively. The geometry of each nanowire has been determined from SEM images. The values of the electrical resistance have been calculated from the linear fit of the I-V characteristics measured at 200°C after annealing at 300°C.

For the sample Ti-1, the geometry of 37 SnO₂ nanowires has been determined. The length of the nanowires is in the range 1.4-5.2 μm and the diameter of the nanowires is in the range 55-200 nm. The corresponding I-V characteristics have been measured in a 2-point configuration at 200°C. The conductivity has been calculated and the values are widely spread over 3 orders of magnitude. From the 37 nanowires:

- 8 nanowires present a conductivity at 200°C in the range 5-10 S/m,
- 15 in the range 20-100 S/m,
- 8 in the range 140-550 S/m,
- 6 in the range 850-2300 S/m.

Those values shall not be considered as absolute values because the resistance used for the calculation come from measurements in a 2-point configuration. As explained in the previous paragraph, the total resistance measured in a 2-point configuration also includes the contact resistance. Consequently, the values of conductivity reported indicate a lower limit of the conductivity of the SnO₂ nanowires on Ti-1.

For the sample Ebeam-1, the I-V characteristics of 6 SnO₂ nanowires (NW-ebeam-1 to NW-ebeam-6) have been measured in a 4-point configuration and their geometry has been determined. The conductivity of the 6 SnO₂ nanowires on Ebeam-1 ranges from 1.5 to 6 S/m at 200°C (see Table 7).

Although the contact resistance is included in the conductivity values calculated for the nanowires on Ti-1, those values are still higher than for the nanowires on Ebeam-1. Consequently, it can be concluded that the conductivity of the SnO₂ nanowires located on Ti-1 is higher than on Ebeam-1.

As a comparison, the values of conductivity for SnO₂ nanowires reported in the literature are 46 S/m [10] and 400-1500 S/m [182] at room temperature. Hernandez-Ramirez et al. [10] also reported conductivity values of 250 S/m and 1295 S/m at 180°C and 240°C, respectively, which is comparable with the values obtained for Ti-1. However, the conductivity of the nanowires on Ebeam-1 is low. The electron beam might be responsible for the low conductivity of the nanowires, since it can modify the intrinsic properties of the nanowire [181].

Another result to discuss is the high difference in the conductivity values (over 3 orders of magnitude) obtained for the nanowires on Ti-1. The contact resistance is probably partly responsible for the differences of conductivity from one nanowire to another. Still the relative difference between the values obtained is large, so it is assumed that the change in conductivity of the nanowire itself is also responsible for the difference measured.

3.4 Investigation of the metal-nanowire interface

In order to understand the discrepancy in the conductivity values presented above for the sample Ti-1 (ranging from 5 to 2300 S/m), the interface nanowire-metal contact is investigated. Therefore, the cross-sections of two nanowires on the sample Ti-1 (Ti/Au metallization patterned by optical lithography) are studied with a transmission electron microscope (TEM). Both nanowires, NW-a and NW-b, present the same geometry, but the resistance of NW-b is 250 times higher than the resistance of NW-a after an annealing step of 30 min at 300°C. Both nanowires are located on the same sample, Ti-1, so the process steps (nanowire transfer, optical lithography, metal deposition, annealing, etc.) are strictly identical. Table 8 lists the main properties of the two nanowires NW-a and NW-b investigated.

Table 8: Properties of the two nanowires investigated by FIB-TEM.

	NW-a	NW-b
Length [μm]	1.8	1.8
Diameter [nm]	70	70
Resistance at 200°C [k Ω]	270	75000
Conductivity at 200°C [S/m]	1730	6
Growth direction	[111]	[100]

Both nanowires, which are covered by the top metallization, have been transversally cut by a Focused Ion Beam (FIB) technique. The two lamellae have been investigated by TEM. Bright field images and electron diffraction patterns were acquired using a Tecnai F20 with a field emission gun (FEG) operating at 200 kV. The microscope has a post column energy fil-

ter (Gatan Imaging Filter, GIF) and the images were recorded in zero-loss filtered mode, using a 10 eV wide slit (i.e. elastically scattered electrons only).

The overview image of the sample NW-a is shown in Figure 49. The cross-section image shows the SnO₂ nanowire located on the SiO₂/Si substrate and the top metallization (10 nm Ti/150 nm Au). The metallic layer follows the topography induced by the nanowire. The Au layer is composed of large crystalline grains. The Ti layer is partly crystalline (visible on enlarged pictures, not shown here).

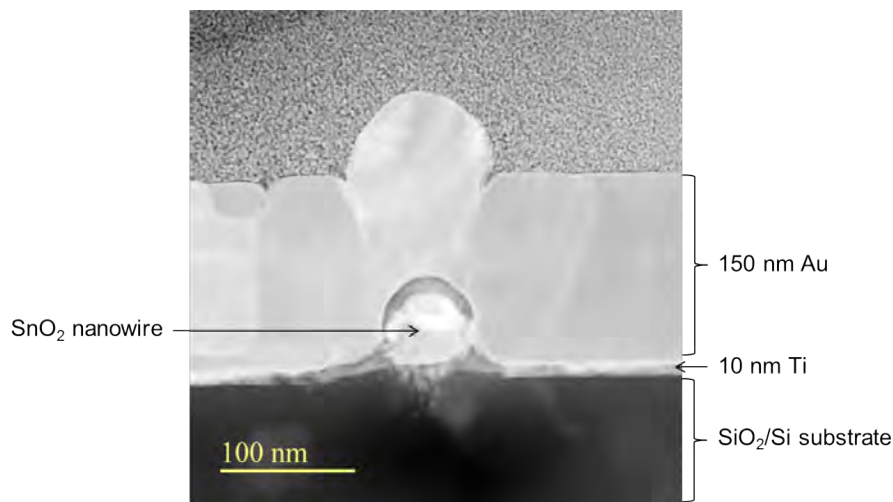


Figure 49: TEM image of a cross-section of the NW-a. The SnO₂ nanowire is deposited on a SiO₂/Si substrate. A thin layer of Ti has been deposited by thermal evaporation as adhesion layer, followed by a thicker layer of Au to establish the electrical contact with the SnO₂ nanowire.

Electron energy loss spectroscopy (EELS) has been performed on the sample NW-a in order to check the chemical composition. The spectra are not shown here, but the results are discussed. The positions, where the spectra have been measured, are indicated on the high-angle annular dark-field (HAADF) image of Figure 50a. The EELS spectra confirm the presence of Sn in the positions A and B. The presence of Sn is also observed in position F below the nanowire in the SiO₂ layer, which suggests that Sn or SnO₂ has diffused into the SiO₂. It is not clear if the diffusion of Sn into the SiO₂ occurs naturally or if it is induced by the focused ion beam during the preparation of the sample. The samples have been annealed at 300°C for 30 min prior to the TEM investigations, which might also be responsible for this diffusion process. However, this phenomenon is also observed on the sample NW-b, as illustrated by the elemental mapping in Figure 50b. Ti has been identified in the positions C, D and E, which suggests that Ti diffuses into the Au

layer at the grain boundaries. The analysis does not enable to conclude on the possible presence of TiO_2 at the interface Ti/SnO_2 , which could be responsible for high contact resistance.

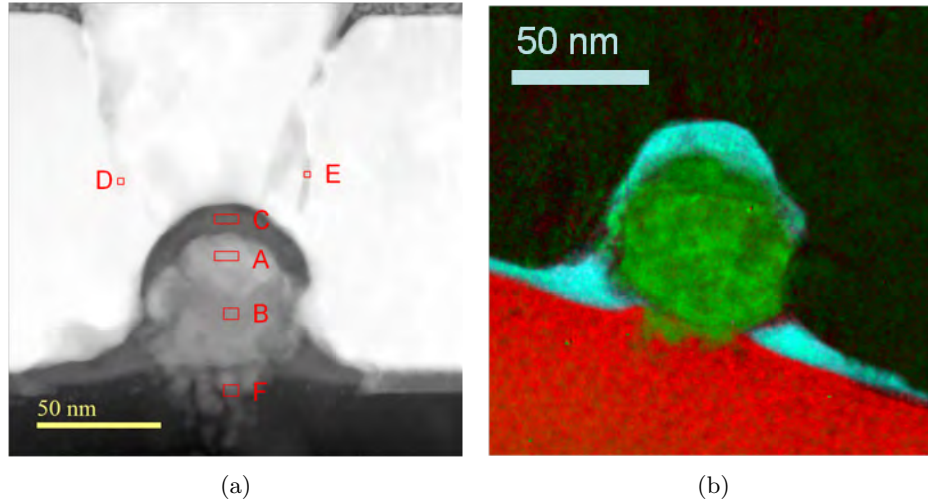
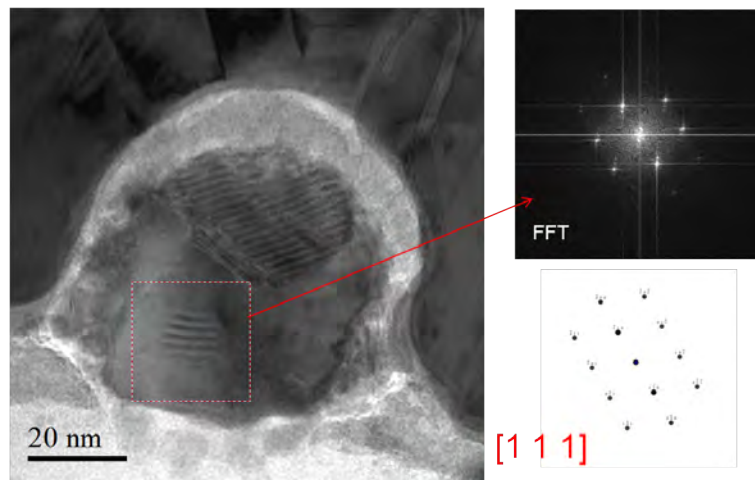


Figure 50: (a) HAADF image of NW-a. The positions A to F indicate the location where the EELS spectra have been measured. (b) Elemental mapping of NW-b: SnO_2 is represented in green, Ti in blue and SiO_x in red.

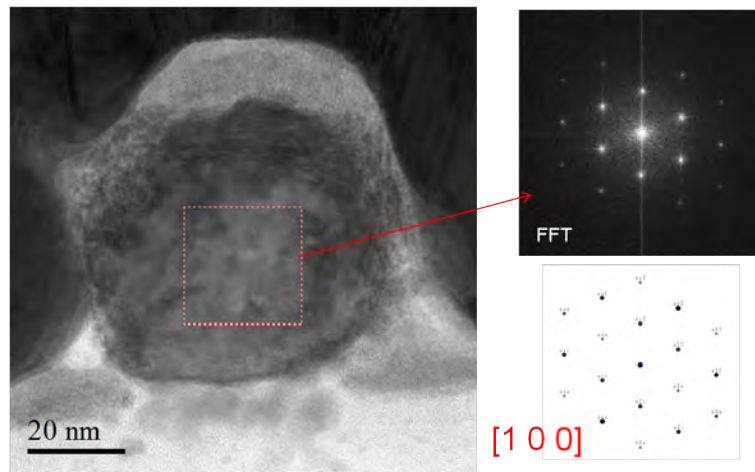
Figure 51 shows high resolution images of the samples NW-a and NW-b. The SnO_2 nanowires are both single crystalline. The crystal orientation of the nanowires could be determined by analysing the diffraction patterns. The direction of the crystal growth is $[111]$ for NW-a and $[100]$ for NW-b. The growth direction $[111]$ has already been identified as one of the common growth directions for the SnO_2 nanowires synthesized in this study, while the growth direction $[100]$ has not been previously observed.

Since no distinction in the composition at the interface is observed for the two samples, it is suggested that the crystal orientation of the nanowire has an important role in the difference in conductivity. The nanowire grown along the direction $[111]$ has a higher conductivity than the nanowire grown along the direction $[100]$. A possible explanation is that one of the two lattices presents more oxygen vacancies, which would be responsible for a higher conductivity. Another parameter to consider is the electron density along the two directions, which may influence the overall conductivity.

This experiment lays the basis for further investigations. A more extensive electrical characterization of the nanowires prior to the TEM observation - including the distinction between resistance of the nanowire and contact resistance - and a theoretical study of the different crystal lattices should help to draw conclusions.



(a) NW-a



(b) NW-b

Figure 51: TEM images of the SnO₂ nanowires covered by a Ti/Au metallic layer on a SiO₂/Si substrate. The analysis of the diffraction patterns measured in the indicated areas gives information on the crystal orientation of the nanowires. The direction of the crystal growth is [111] for NW-a and [100] for NW-b.

3.5 Summary

In this section, the fabrication process of single SnO₂ nanowire devices has been presented. After synthesis, the SnO₂ nanowires are dispersed in an isopropanol solution and transferred onto a SiO₂/Si substrate by spin-coating. Metallic contacts are patterned on top of the SnO₂ nanowires by a lithography step and a lift-off process. Optical lithography has been used to contact a large number of individual SnO₂ nanowires in a 2-point configuration on the same chip. E-beam lithography has enabled the contact of a few indi-

vidual SnO₂ nanowires in a 4-point configuration in order to determine the contact resistance and the conductivity of the SnO₂ nanowires.

The challenge is to establish ohmic contacts with single SnO₂ nanowires. Therefore, different materials have been deposited on the SnO₂ nanowires: Al, Ti/Au, Cr/Au, Sn/Au and Au. The percentage of linear I-V characteristics measured at 200°C in a 2-point configuration before and after an annealing step for 5-30 min at 300-400°C as well as the values of the resistance measured have been compared. The Al contacts did not withstand the high temperature of annealing most probably because of the oxidation of the Al layer. Sn/Au yielded the highest percentage of linear I-V characteristics, but the contacts deteriorated after a few hours at high temperatures. The results obtained with Cr/Au and Ti/Au were similar, but the values of resistance measured after annealing were lower for the SnO₂ nanowires contacted with a Ti/Au layer. The direct contact of Au on SnO₂ nanowires resulted also in a high percentage of linear I-V characteristics and acceptable values of resistance. As contact resistance has been reported to decrease with increasing SnO₂ nanowire conductivity [180], Ti/Au has been selected to contact the SnO₂ nanowires for further investigations. The effect of an oxygen plasma treatment after the lithography step and before the metal deposition has been investigated on some samples. The objective of the oxygen plasma is to clean the surface of the SnO₂ nanowires and ensure a better contact between the metallic layer and the SnO₂ nanowire. The effect of oxygen plasma on the contact quality (for Cr/Au and Ti/Au) is not conclusive, so the samples further investigated did not undergo this treatment. It has to be pointed out that these statistical investigations have been extremely time-consuming both from sample processing as well as from electrical characterization. However, this study is of high value for optimizing nanowire-based gas sensors.

SnO₂ nanowires contacted with a Ti/Au metallic layer patterned by e-beam lithography have been electrically characterized. Successive 2-point and 4-point measurements revealed the relatively high values of the contact resistance at 200°C, which contributes for 30-60% of the resistance of the SnO₂ nanowires when measured in a 2-point configuration. The conductivity of the SnO₂ nanowires contacted in a 4-point configuration on the sample processed with e-beam lithography is in the range 1.5-6 S/m. For the SnO₂ nanowires contacted in a 2-point configuration on the sample processed with optical lithography, the conductivity is higher but the values calculated are much more dispersed: in the range 5-2300 S/m. The interface between the Ti/Au contact and the SnO₂ nanowire has been investigated for two nanowires, which present conductivity values of 7 S/m and 1530 S/m. Therefore, a lamella of the nanowires covered by the Ti/Au layer has been transversally cut by a FIB technique and investigated by TEM measurements. The interface metal-nanowire seems to be very similar for

both nanowires. Both nanowires are single crystalline but a difference in their crystalline orientation is observed. For the nanowire with the large conductivity, the crystal growth is oriented in the crystalline direction [111]. For the nanowire with the lower conductivity value, the crystal growth is oriented in the direction [100].

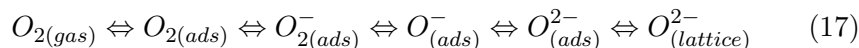
4 Characterization of gas sensing properties

4.1 Reaction mechanism of gas species on SnO₂ surfaces

The understanding of the reactions between gas molecules and the surface of the SnO₂ nanowires is crucial for the reliable detection of specific target gas species. In the literature, the ionosorption model (see Section 1.2) is largely accepted.

4.1.1 O₂

The ionosorption of oxygen at the surface of SnO₂ results in the formation of surface states, which may trap electrons from the conduction band, thus resulting in the decrease of the conductivity. Since O₂ is a strong electron acceptor, it can be reduced at the SnO₂ surface in several species [25, 183]:



It is very complex to experimentally analyse, which oxygen species predominate at the SnO₂ surface, due to the background of lattice oxygen. Assumptions are made that molecular adsorption predominates on stoichiometric surfaces of n-type semiconductors, while dissociative adsorption is promoted by the presence of oxygen vacancies [183]. Furthermore, it is generally accepted that the nature of the ionosorbed oxygen species at the surface of SnO₂ depends on the adsorption temperature:

- Below 150°C, the molecular form O₂⁻ predominates.
- Above 150°C, the atomic form (O⁻, O²⁻) predominates.

This transition temperature of 150°C was observed by Chang [184] for the ionosorption of oxygen on SnO₂ powders as a result of electron paramagnetic resonance (EPR) measurements. Moreover, it could be correlated to an anomalous temperature dependence found for the conductance of a SnO₂ thin film. Below 160°C the thin film conductance increased with increasing temperature, which is expected for a thermal excitation of charge carriers in a semiconductor. This increase of conductance with increasing temperature (up to 160°C) has also been explained by the decrease of chemisorbed O₂⁻ species present at the SnO₂ surface with increasing temperature (due to the partial desorption of O₂⁻ species and the consequent release of the trapped electrons in the conduction band of SnO₂). Above 160°C the sample conductance decreased with increasing temperature. This was interpreted in terms of conversion of chemisorbed O₂⁻ into O⁻ (and O²⁻ with further increase of

temperature) and thus additional transfer of electrons from the conduction band of SnO₂ to the ionosorbed oxygen.

As already explained in the description of the ionosorption model, the electrical conductivity of SnO₂ is influenced only by ionosorbed species: O₂⁻, O⁻, O²⁻. Besides, oxygen may also chemisorb at the surface of SnO₂ as non charged molecular species: O_{2(ads)}. Those non charged oxygen species do not influence the SnO₂ conductivity, so they cannot be detected by resistance measurements. Nevertheless, those non charged species undergo a local charge transfer, which influences the electron affinity of the SnO₂ surface and changes in electron affinity are measurable by work function changes. By combining conductivity measurements and work function changes, Sahn et al. [185] showed that only ionic species are adsorbed at the SnO₂ surface at 400°C, while non charged oxygen species, which decreases the electron affinity of SnO₂, are adsorbed at the SnO₂ surface at 200°C.

Yamazoe et al. [43] conducted temperature programmed desorption (TPD) studies of oxygen from SnO₂ powders under various conditions. The results depend on the adsorption temperature. A low temperature oxygen desorption peak around 100°C, which was ascribed to O₂⁻, was only observed for oxygen adsorption below 150°C and cooling to room temperature (RT) in the oxygen atmosphere. A second oxygen desorption peak, which was assigned to O⁻ and/or O²⁻, was observed at about 500°C if oxygen was adsorbed at 400°C. Kawabe et al. [186] conducted X-ray photoelectron spectroscopy (XPS) to study the oxygen species adsorbed onto Ar-ion etched reduced SnO₂ surface from room temperature up to 200°C. The adsorbed oxygen species were identified as: O₂²⁻ adsorbed at room temperature, O₂⁻ adsorbed at 100°C, and O⁻ adsorbed at 200°C.

This model is widely accepted in the literature [43, 37, 25]. However, Gurlo [42] reviewed the reported results, which identified oxygen species adsorbed at the SnO₂ surface by spectroscopic analyses (temperature programmed desorption (TPD), electron paramagnetic resonance (EPR), infrared spectroscopy (IR)), and emphasized that “neither the superoxide ion O₂⁻, nor charged atomic oxygen O⁻, nor peroxide ions O₂²⁻ have been observed on SnO₂ under the real working conditions of sensors”. He conceded that superoxide ion O₂⁻ has been observed, however, only after low temperature adsorption (below 150°C) and on reduced SnO₂, which are not the working conditions of the gas sensors.

Hernandez-Ramirez et al. [28] measured the response of single SnO₂ nanowire sensors upon introduction of oxygen in a nitrogen atmosphere. The results show that the adsorption of oxygen species at the surface of the SnO₂ nanowire is a slower process than the desorption of those oxygen species. After almost 3 hours at 295°C in synthetic air, the nanowire surface has not reached the steady state yet. On the contrary, back in nitrogen atmosphere

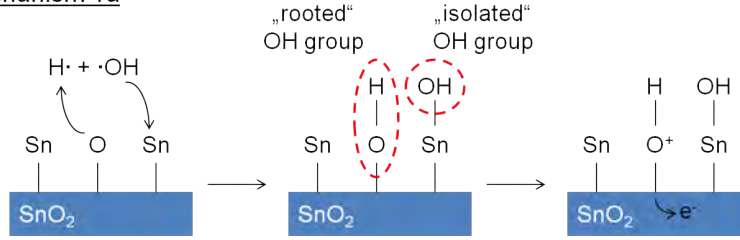
the nanowire reaches a steady state with a time constant of about 10 min. Moreover, the sensor response to the change of atmosphere between nitrogen and synthetic air is higher for nanowires with smaller diameters. This result gives support to the model, which assumes the existence of a space charge zone created by the adsorbed oxygen, thus limiting the central area of the nanowire for electrical transportation.

4.1.2 H₂O

The presence of water vapour in the atmosphere (humidity) plays a crucial role in the detection of other gas species, because water adsorbs at the SnO₂ surface. Below 200°C, water is observed as molecular species, which may be physisorbed at the SnO₂ surface or adsorbed by hydrogen bonding on oxygen species (lattice or ionosorbed oxygen). At temperatures above 200°C, the dissociation of the water molecule at the SnO₂ surface occurs and chemisorbed hydroxyl groups are present at the SnO₂ surface, as shown by IR and TPD measurements [187, 188, 43, 189]. The formation of hydroxyl groups is due to an acid/base reaction: OH⁻ groups chemisorb on Sn lattice atoms (Lewis acid site) leaving H⁺ reacting with lattice or ionosorbed oxygen [172]. The surface Sn-OH groups are stable up to 500°C [190].

The adsorption of water at the surface of SnO₂ results in an increase in the conductivity of SnO₂. This phenomenon is reversible upon water desorption. More precisely, Yamazoe et al. [43] reported that the change in conductivity is due to chemisorbed hydroxyl groups, while the adsorption of molecular water does not influence the SnO₂ conductivity. The change of SnO₂ conductivity in the presence of water has been often experimentally observed, e.g. [190]. However, the charge transfer mechanism at the origin of the conductivity change is not exactly known. Two mechanisms have been suggested by Heiland and Kohl [191] and are illustrated in Figure 52.

Mechanism 1a



Mechanism 1b

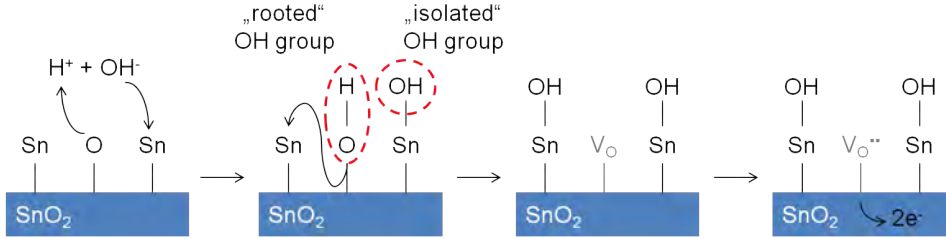
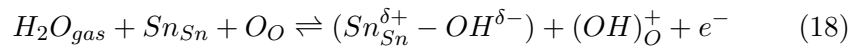
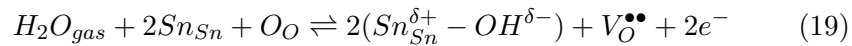


Figure 52: Schematic representation of the adsorption mechanisms of water on SnO_2 surfaces suggested in [191].

The mechanism 1a relies on the homolytic dissociation of the water molecule followed by the chemisorption of the OH group on a Sn site ($\text{Sn}_{\text{Sn}}^{\delta+} - \text{OH}^{\delta-}$), referred to as the “isolated” group, and the reaction of the neutral H with a lattice oxygen O_O to form a “rooted” group $(\text{OH})_O$. The rooted OH group has a lower electron affinity than the lattice oxygen, which fixed two electrons prior to the reaction with H. Therefore, the rooted OH group may be ionized $(\text{OH})_O^+$ and release one electron to the conduction band. This first mechanism can be written as the following reaction:



The mechanism 1b suggests a heterolytic dissociation of the water molecule. The as-formed hydroxyl group reacts with a Sn atom ($\text{Sn}_{\text{Sn}}^{\delta+} - \text{OH}^{\delta-}$). The proton reacts with a lattice oxygen to form a rooted hydroxyl group. Subsequently, this rooted hydroxyl group binds to a Sn atom, becoming an isolated hydroxyl group and generating an oxygen vacancy V_O . This oxygen vacancy may be ionized and releases two electrons into the conduction band. The overall equation is:



The results of work function measurements conducted on SnO_2 thick films in the presence of CO and humidity led Barsan et al. [35] to suggest that the mechanism 1a is the correct one to describe the water adsorption on SnO_2 .

The previous mechanisms consider the direct adsorption of water molecules on the SnO₂ surface. However, the influence of the ionosorbed oxygen present at the surface of the SnO₂ should also be considered. Caldararu et al. [189] assumed that water molecules stabilize surface anionic vacancies and block those oxygen adsorption sites. Similarly, Morrison et al. [192] suggested that water molecules physisorb on the H⁺ and OH⁻ surface groups, thus “neutralizing any apparent charged sites” and hindering the ionosorption of oxygen species on the SnO₂ surface. Another effect is the displacement of pre-adsorbed oxygen by water adsorption suggested by Henrich and Cox [183]. In any of these mechanisms, the particular state of the surface has a major role since steps and surface defects, such as in-plane oxygen vacancies, promote the dissociative adsorption up to a certain concentration [183, 193].

In the study by Hernandez-Ramirez et al. [28], it has been shown that the interaction of water molecules with a single SnO₂ nanowire (chemisorption of hydroxyl groups) in synthetic air is a faster process than the desorption of those water species. The influence of water on the resistance change of the SnO₂ nanowire is four times higher in synthetic air than in nitrogen, which reveals the role played by the availability of oxygen. Moreover, there is a maximum of resistance change upon exposure to humidity in synthetic air at 300°C, which surprisingly agrees with the temperature range in which the O⁻ concentration is dominant at the surface of SnO₂. During the humidity pulse in synthetic air, the observed resistance drift has been attributed to a reorganization of the species on the nanowire surface. The drift slope increases as the measurement temperature increases, pointing out that it corresponds to an activated process. Moreover, the reorganization of the species on the surface seems to correspond to a non-reversible process, since the base line after the humidity pulse is slightly shifted from its initial level before applying the humid synthetic air pulse. No resistance drift is observed during the humidity pulse applied in nitrogen.

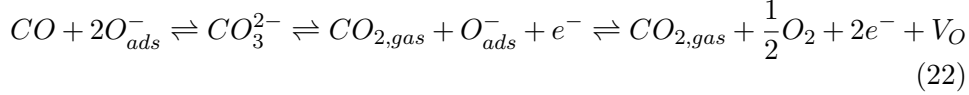
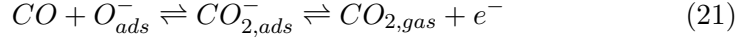
4.1.3 CO

The different reaction mechanisms possible between the CO molecules and the SnO₂ surface in various environments are discussed. In the absence of oxygen, the CO molecule adsorb directly on lattice oxygen acting as an electron donor and forming CO⁺ groups present at the surface (Equation 20) [194]:



At ambient oxygen concentrations, the direct adsorption is hindered and the only reaction partner considered is the ionosorbed oxygen species (O⁻), leading to the formation of CO₂ and the release of electrons in the conduction

band. Carboxylate and bidentate carbonate are formed as intermediate species according to the Equations 21 and 22, respectively [188, 194, 195]:



In the presence of humidity, CO reacts in parallel with ionosorbed oxygen (Equations 21 and 22) and with hydroxylate groups as illustrated in Figure 53. The reaction of CO with the oxygen of an isolated hydroxyl group results in the formation of a CO₂ gas molecule, while the freed hydrogen atom reacts with a lattice oxygen and form a rooted hydroxyl group. This rooted hydroxyl group may become ionized, so electrons are released in the conduction band of the SnO₂ nanowire. Work function measurements suggest a dominant reaction of CO with hydroxyl groups for low CO concentrations and a dominant reaction of CO with ionosorbed oxygen for high CO concentrations [35]. This transition is observed around 10-20 ppm CO.

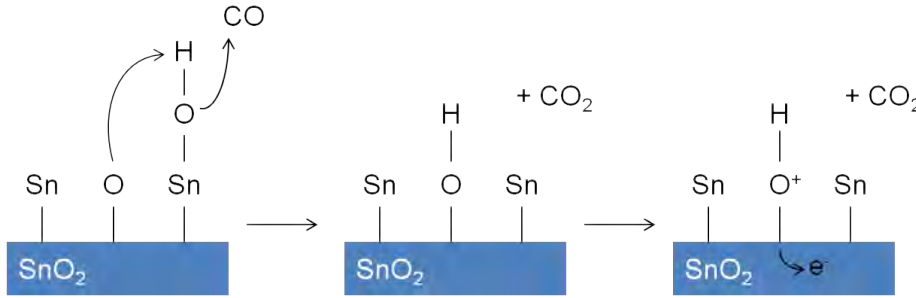
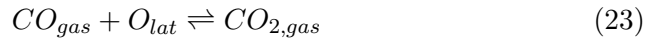


Figure 53: Schematic representation of the adsorption mechanism of CO in the presence of water on SnO₂ surfaces as suggested in [35].

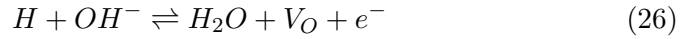
Kohl [195] compared the reaction mechanism at the surface of a SnO₂ single crystal (101) and of a polycrystalline thin film. The direct reaction of CO with lattice oxygen according to Equation 23 is considered:



The desorbing species after reaction with CO were recorded by thermal desorption spectroscopy. The investigation led to the conclusion that CO desorbs from (101) surfaces mainly as CO and only little CO₂ is formed after the reaction of CO with a lattice oxygen at temperature up to 530°C. On polycrystalline surfaces CO₂ is the main desorbing species with a maximum at about 140°C. This study suggests that the reaction mechanisms are different on single crystalline (101) surfaces and on polycrystalline thin films.

4.1.4 H₂

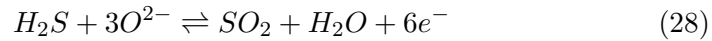
The sensitivity of SnO₂ gas sensors for the detection of hydrogen is particularly high. However, the properties of the H₂ molecule (non-polar, very low polarisability, very weak donor or acceptor properties, strong H-H bond) suggest that the molecular adsorption results in a weak physisorption and the dissociation requires highly reactive oxide surfaces [183]. Nevertheless, the change in conductivity of the SnO₂ gas sensors indicates that the dissociation of H₂ occurs at the surface of SnO₂, which is probably enhanced by the presence of oxygen vacancies. The following reaction mechanisms have been reported [195, 183, 196]:



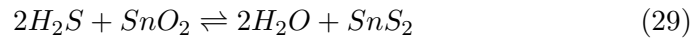
The reaction of H atoms with the lattice oxygen or with ionosorbed oxygen species on SnO₂ surfaces results in the formation of hydroxyl groups or water molecules accompanied by the release of electrons in the conduction band.

4.1.5 H₂S

Hydrogen sulfide (H₂S) may react with ionosorbed oxygen species at the SnO₂ surface. This reaction results in the release of electrons in the conduction band and a decrease of the SnO₂ resistance [197], according to:



Moreover, at high temperatures sulfur deposition may occur most probably by replacement of oxygen [183]:



SnS₂ has a better conductivity than the metal oxide SnO₂ [197]. However, the resistance change measured by the SnO₂ gas sensors upon exposure to H₂S is completely reversible, so it is suggested that sulfur does not diffuse deep into the SnO₂ bulk. Spectroscopic studies of the adsorption of H₂S on SnO₂ surfaces have not been found in the literature. This is probably due to the high reactivity of H₂S with metals, which makes it inappropriate for analysis in UHV systems [183].

4.2 Methods

4.2.1 Gas measurement setup

After the processing of the metal contacts on the SnO_2 nanowires (process flow described in Section 3.1), the sensor chip is cleaved to a size of about 0.5 cm^2 and glued next to a thermocouple (10×2 PT 6.8-0.4, Delta-R GmbH) on top of two discrete microheaters (4×1 Pt100B, Delta-R GmbH) (Figure 54a). The wires of the microheaters and of the thermocouple are soldered to a ceramic carrier (Figure 54b). The soldering of the wires ensures the mechanical stability of the suspended sensor chip. The objective of this configuration is the thermal isolation of the ceramic carrier from the sensor chip, which is heated up to 350°C during gas sensing measurements. Finally, Au wires are bonded from the sensor chip to the ceramic carrier. The ceramic carrier is plugged in the gas measurement chamber for gas sensing tests (Figure 54c).

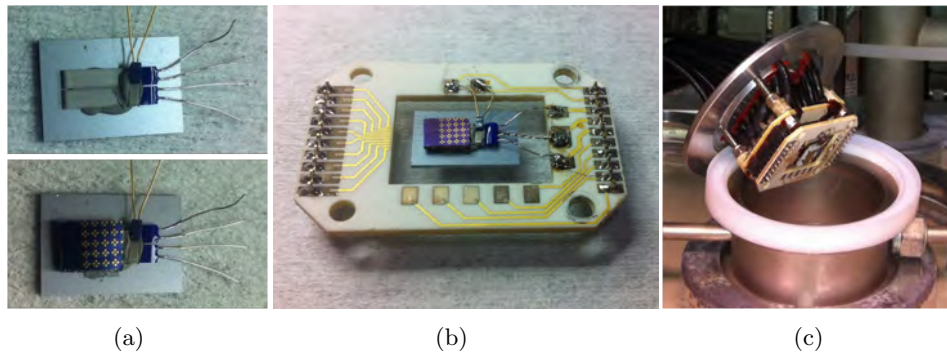


Figure 54: Mounting of the sensor chip for gas sensing measurements. (a) The sensor chip is glued next to a thermocouple on top of two microheaters. (b) The wires of the microheaters and of the thermocouple are soldered to a ceramic carrier and Au wires are bonded from the sensor chip to the ceramic carrier. (c) The ceramic carrier is plugged in the gas measurement chamber for gas sensing tests.

The gas sensing measurements occur in an automated setup, which is schemed in Figure 55. Mass Flow Controllers (MFC) from the company Bronkhorst High-Tech BV [198] enable to control the flow of gas, which is introduced into the gas measurement chamber. The flow of carrier gas is split into two lines each controlled by a MFC: the first line leads directly to the gas measurement chamber, while the second line directs the carrier gas through a water recipient. According to the amount of flow, which goes through the water recipient, the carrier gas is more or less charged with humidity. It is possible to direct the flow of carrier gas entirely into the “dry” line, so no extra humidity is introduced into the gas measurement chamber. Both lines meet again before introduction into the gas measurement chamber, where

the relative humidity and the temperature of the carrier gas (room temperature) are measured by a commercial sensor (KOBOLD Messring GmbH, type AFK-E [199]). The carrier gas is either nitrogen (N_2) or synthetic air (80% N_2 + 20% O_2). Nitrogen is pure at 99.999% and contains less than 3 ppm O_2 and 5 ppm H_2O [200]. Therefore, when measuring the sensors in a nitrogen flow without adding humidity, the conditions will thereafter be considered “inert” and “dry”. Likewise, the concentration of water in the synthetic air mixture is less than 2 ppm [201], which is why the gas measurements in synthetic air will be considered to occur in “dry” conditions. The flow of test gas (CO , H_2 or H_2S) is also controlled by a MFC. The carrier gas and the test gas are mixed in the gas measurement chamber. The total gas flow (carrier gas flow + test gas flow) introduced into the gas measurement chamber is always kept constant to 1000 sccm. The flow of test gas accounts for less than 10% of the total flow, so the relative humidity measured by the KOBOLD sensor for the carrier gas is still relevant. Finally, the gas flows through an exhaust when exiting the gas measurement chamber.

In order to measure the electrical signal of the single nanowire devices, three Source Measure Units (SMU) from Keithley [202] are used to measure up to three nanowire devices on the same chip in parallel. A constant current is forced to flow through the nanowire and the voltage is measured. A current source (Keithley 6221) connected to the microheaters enables the heating of the sensor chip. The resistance of the thermocouple is measured by a multimeter (Agilent Technologies 34401A [203]) to control the temperature. A picture of the setup is shown in Figure 56.

Some artefacts in the sensor resistance are sometimes observed during the first seconds, when the test gas is introduced in the gas measurement chamber (see for instance Figure 65). These artefacts might be due to the simultaneous reaction of several test gas species on the nanowire surface. In order to characterize the response of a sensor to several gas species, the sensor is successively exposed to the corresponding gas species. However, there is only one gas pipe common for all test gas species (CO , H_2 , ...). Therefore, it is possible that small quantities of other test gas species, which have been previously investigated, are also introduced in the gas measurement chamber together with the main test gas species to detect. These possible cross-reactions might be responsible for the observed artefacts.

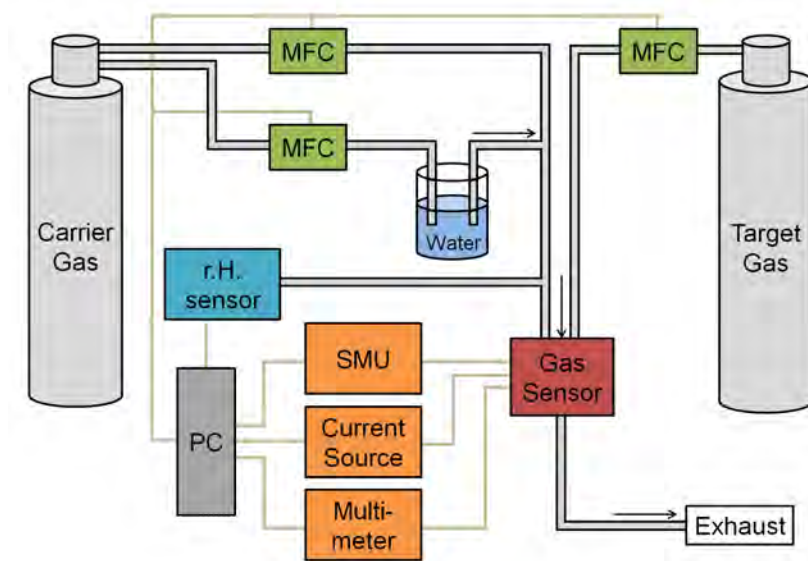


Figure 55: Scheme of the gas measurement setup.



Figure 56: Picture of the gas measurement setup.

4.2.2 Analysis of the data

The response S of the n-type nanowire sensor upon exposure to a defined concentration of a reducing target gas is calculated as the relative difference between the resistance value in the background gas R_{air} , measured before the target gas pulse, and the minimum resistance value measured during the target gas pulse R_{gas} , expressed in percentage.

$$S = \frac{R_{air} - R_{gas}}{R_{air}} \times 100 \quad (30)$$

The response time t_{resp} is defined as the time necessary to reach 90% of the difference between the resistance in the background gas and the resistance in the test gas related to the baseline value in the background gas (see Figure 57). The recovery time t_{recov} is defined as the time necessary for the resistance to reach the threshold value of 10% below the initial resistance.

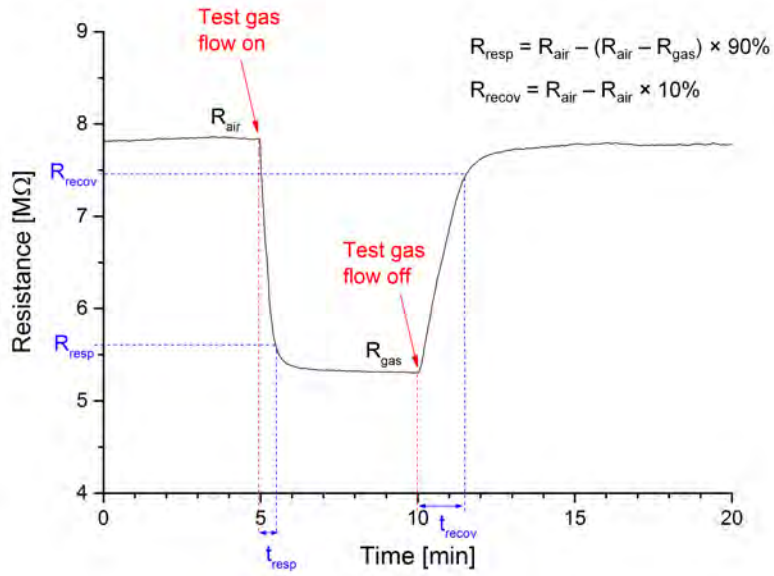


Figure 57: Definition of the response and recovery times.

4.2.3 Description of the nanowire sensors

Numerous nanowire devices have been fabricated as described in detail in Section 3. Out from all these devices, the gas sensors listed in Table 9 have been fully characterized in the gas measurement setup. The six single nanowire sensors are located on four samples (A, B, C and D). Each sample has been processed individually and the main difference between the four samples relies on the process followed for depositing the metal contacts.

The nanowires B1 and B2, on one hand, and C1 and C2, on the other hand, are located on samples B and C, respectively. Consequently, the gas sensing measurements delivered by those nanowire sensors (B1/B2 and C1/C2) are particularly interesting to compare, because they are identical from the processing point of view.

Table 9: Characteristics of the single SnO₂ nanowire sensors. l and d are the length and diameter of the nanowire, respectively.

Sensor	l (μm)	d (nm)	Configuration	Lithography	Metallization
A	53	300	2-point	optical	Au sputtered
B1	2	60	2-point	optical	Ti/Au evaporated
B2	2	100	2-point	optical	Ti/Au evaporated
C1	0.5	90	4-point	e-beam	Ti/Au evaporated
C2	0.5	70	4-point	e-beam	Ti/Au evaporated
D	1	65	4-point	e-beam	Ti/Au sputtered

The nanowire measured on the sample A is sandwiched between two Au layers, as described in Section 3.2.1 for the sample Au-1. For the sample A, the upper Au layer has been deposited by RF-magnetron sputtering. The nanowire has only two contact pads, so only a measurement in a 2 point configuration is possible. The length of the nanowire between the two contact pads is approximately 53 μm and its diameter is about 300 nm, so it is a relatively thick nanowire. For the samples B, C and D, the metallic contacts are composed of a Ti/Au layer (10 nm Ti/150 nm Au). The samples B and D have been processed with optical lithography as described for the sample Ti-1, only the deposition method used for sample B is thermal evaporation, while the metallic contacts have been deposited by RF-magnetron sputtering for sample D. The different deposition technologies have been employed in order to optimize lift-off behaviour as well as uniform coating of the nanowires. The sample C has been processed with e-beam lithography and the metallic contacts have been deposited by thermal evaporation, as described in Section 3.3.1 for the sample Ebeam-1.

The single SnO₂ nanowire sensors have been measured in the presence of various concentrations of CO, H₂ and H₂S in different background atmospheres (nitrogen or synthetic air, with or without humidity). Table 10 summarizes for each target gas the main experimental conditions and the corresponding sensors investigated. Due to the duration of the measurements conducted (7-12 hours in average), the focus has been put on showing the influence of the measurement conditions (e.g. humidity, temperature, test gas concentration, etc.) on the nanowire sensor response rather than repeating similar

measurements for each sensor. Thus, each gas sensing measurement aims to show the particular influence of one parameter. This focus on qualitative results rather than on a quantitative comparison of the sensors can also be explained by the inherent difference in the geometry of each single nanowire sensor, as shown in Table 9.

Table 10: Summary of experimental conditions for the detection of CO, H₂ and H₂S with the corresponding sensors investigated.

Target gas	Carrier gas	Concentration range	Relative humidity	Temperature range	Sensor investigated
CO	N ₂ /SA	10-100 ppm	0-35%	250-350°C	A, B1, C1, C2
H ₂	SA	1-90 ppm	0-50%	150-350°C	B1, B2, D
H ₂ S	SA	0.1-1 ppm	0-65%	300-350°C	A, D

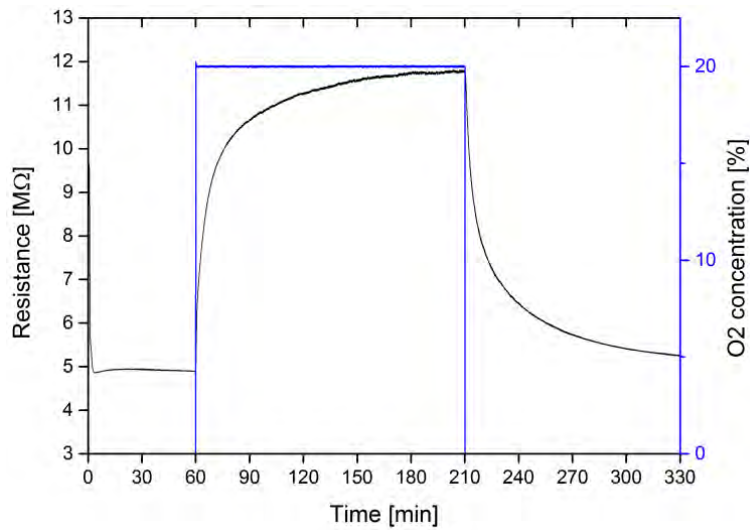
4.3 Results

The study of the gas sensing performance of single SnO₂ nanowire sensors starts with variations of the background atmosphere. These investigations are of high importance in order to understand the basic influence of the environment on the electrical resistance of the SnO₂ nanowire. Then, the sensors are measured in more complex environments with the addition of reducing test gases: CO, H₂, H₂S.

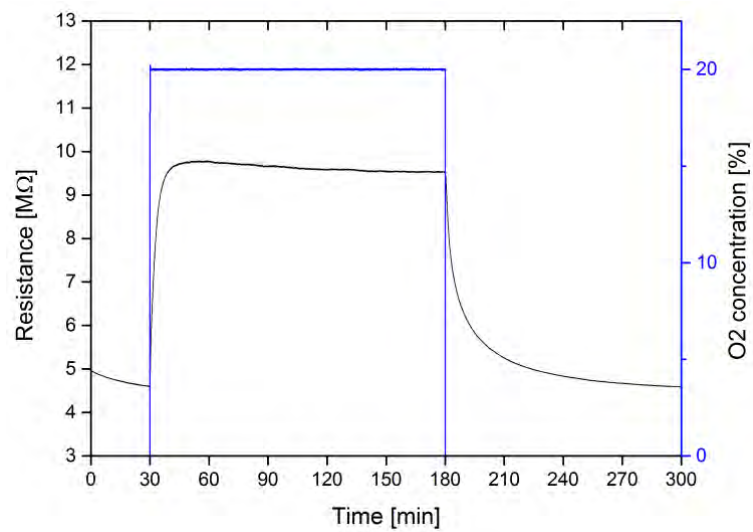
4.3.1 Response to oxygen and water molecules

Figure 58 shows the resistance of the single SnO₂ nanowire sensor A in a background flow of dry and humid nitrogen with a gas pulse of oxygen at an operating temperature of 300°C. Oxygen is introduced with a concentration of 20% in order to simulate the conditions of dry synthetic air, which is the usual background gas for testing the gas sensors. The nanowire resistance has been measured for 30-60 min in nitrogen, 2.5 hours in “synthetic air” (80% N₂, 20% O₂) and 2 hours in nitrogen. This sequence has been repeated two times: once in a dry flow of nitrogen (Figure 58a) and the second time in a flow of nitrogen with a relative humidity of 35% (Figure 58b). The objective of this measurement is to link the change of resistance of the SnO₂ nanowire with the adsorption and desorption reactions of oxygen on the nanowire surface and to understand the influence of humidity on these adsorption/desorption processes.

In dry conditions (Figure 58a), the value of the nanowire resistance in nitrogen at 300°C is 4.9 MΩ. The introduction of oxygen in the gas measurement chamber results in an increase of the electrical resistance. The resistance reaches a plateau at 11.8 MΩ, which corresponds to an increase by about 140%, with a time constant of 50 min (response time). When the oxygen flow is switched off, the nanowire resistance decreases slowly towards its initial value. After 2 hours, the resistance reached is 5.2 MΩ. Since this value is already within a 10% range above the initial resistance, the recovery time can be calculated, though the sensor still did not completely recover. The recovery time is about 90 min. In nitrogen atmosphere with a relative humidity of 35% (Figure 58b), the value of the nanowire resistance at 300°C is 4.6 MΩ. As well as in dry conditions, the introduction of oxygen results in an increase of the electrical resistance. The resistance reaches a plateau at 9.5 MΩ, which corresponds to an increase by about 110%, with a time constant of 5 min (response time). When the oxygen flow is turned off, the nanowire resistance recovers its initial value with a recovery time of 40 min.



(a)



(b)

Figure 58: Change of resistance of sensor A upon exposure to 20% oxygen in a nitrogen atmosphere at an operating temperature of 300°C (a) in dry conditions, (b) at a relative humidity of 35%.

4.3.2 Response to CO

Figure 59 shows the change of resistance of the nanowire sensor A upon exposure to different concentrations of CO in various background atmospheres. The background atmosphere is either dry nitrogen ($N_2 + 0\%$ rH), humid nitrogen ($N_2 + 35\%$ rH), dry synthetic air (SA + 0% rH), or humid synthetic air (SA + 35% rH). The nanowire resistance is first measured in the background atmosphere for 1 hour before the introduction of CO pulses. Afterwards, CO is introduced into the gas measurement chamber for 5 minutes, then the CO flow is switched off for 10 minutes. This sequence is repeated two times for each concentration (10 ppm, 30 ppm, 50 ppm, 70 ppm and 90 ppm), so a total of 10 CO pulses. The sensor is operated at a constant temperature of 350°C . In order to compare the responses of the nanowire sensor to CO in the different background atmospheres, the resistance has been normalized to the resistance measured after 60 min immediately before the CO pulse sequence is started.

The resistance of the SnO_2 nanowire decreases in the presence of CO in the background atmosphere (response) and increases again to the initial resistance value when the flow of CO is switched off (recovery). The change of resistance increases with increasing CO concentrations. In nitrogen, the resistance changes slowly upon exposure to CO and the steady state is not yet reached after 5 minutes of CO exposure and 10 minutes of recovery. Besides, the resistance change induced by the first CO pulse is different: an increase of resistance is observed before the resistance starts decreasing as expected. This fast and short increase of resistance might be due to a rest of oxygen in the gas line. A drift of the resistance baseline is observed over time in all background atmospheres, though the drift is the largest in dry synthetic air. In synthetic air, the steady state is rapidly achieved within 1 to 2 minutes. In the presence of CO in humid synthetic air, the resistance change can be decomposed in two parts: first a fast and large decrease, then a slight increase. A similar but inverse behaviour can be observed during the recovery phase: first the resistance increases fast, then a slight decrease of resistance occurs.

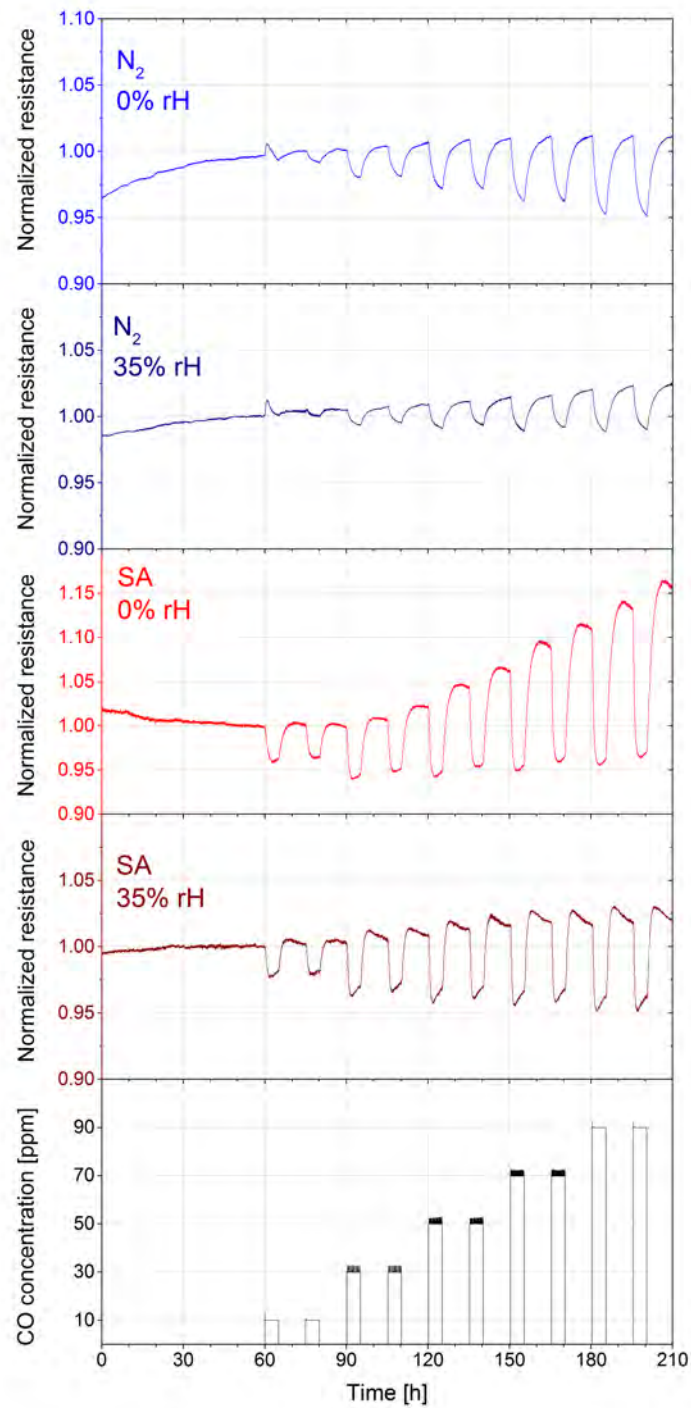


Figure 59: Change of resistance of sensor A at 350°C upon exposure to 10-90 ppm CO in a background atmosphere of dry nitrogen (blue), humid nitrogen (dark blue), dry synthetic air (red), and humid synthetic air (brown).

Figure 60 shows the response of sensor A upon exposure to CO in various background atmospheres. The response for each CO pulse has been calculated from the data presented above (Figure 59) and the average between the two values obtained for the same CO concentration is represented. The following results are obtained:

- The response of the nanowire sensor increases with increasing CO concentrations in the range 10-90 ppm.
- The response to CO is higher in synthetic air than in nitrogen.
- The response to CO is roughly two times higher in dry than in humid synthetic air.

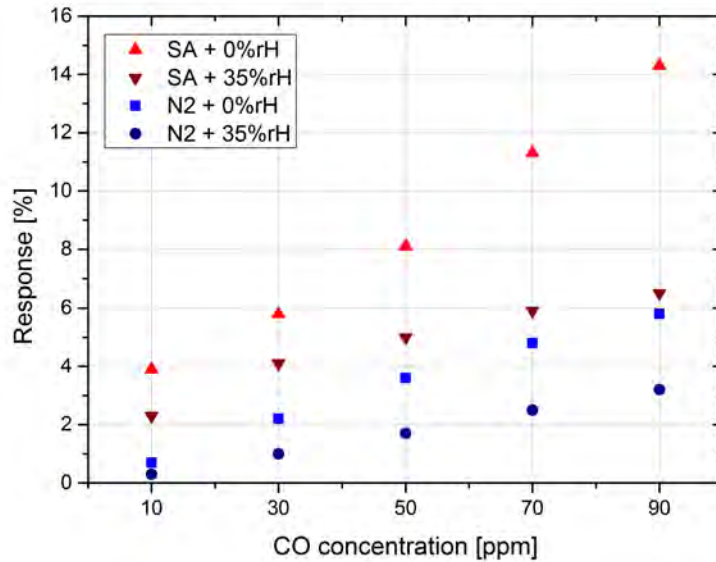


Figure 60: Response of sensor A to increasing concentrations of CO at 350°C in dry synthetic air (red triangles), synthetic air with 35% relative humidity (brown inverted triangles), dry nitrogen (blue squares), and nitrogen with 35% relative humidity (dark blue circles).

Figure 61 shows the response of sensor A to 50 ppm CO in dry nitrogen at 250°C, 300°C and 350°C. For each temperature, the nanowire resistance is measured for 1-1.5 hour in dry nitrogen in order to enable its stabilization after the change of temperature. Afterwards, CO with a concentration of 50 ppm is introduced into the gas measurement chamber two times for 15 minutes each followed by a recovery period of 15 minutes. The measurement is repeated two times (Measurement 1 and Measurement 2) in order to study the repeatability of the sensor response.

Measurement 1 and Measurement 2 show very similar results. There is a small offset of the resistance, but the overall behaviour of the resistance upon changes of temperature and exposure to CO are the same. As already observed in other experiments above, the nanowire resistance is decreased in the presence of CO. At 250°C, the response to CO as well as the recovery in dry nitrogen are very slow and the steady state is not reached after 15 minutes. At 300°C, the resistance changes induced by the CO pulses are already faster than at 250°C, even though the steady state is not reached either. At 350°C, the response to the presence of CO is even faster than at 300°C. The steady state is reached for both response and recovery phases. The results demonstrate the good repeatability of gas sensing measurements.

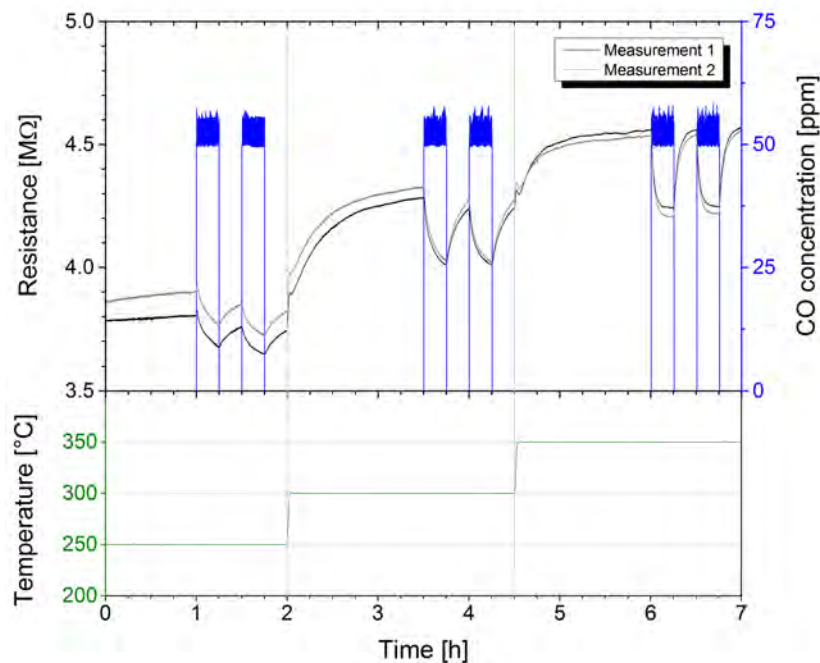
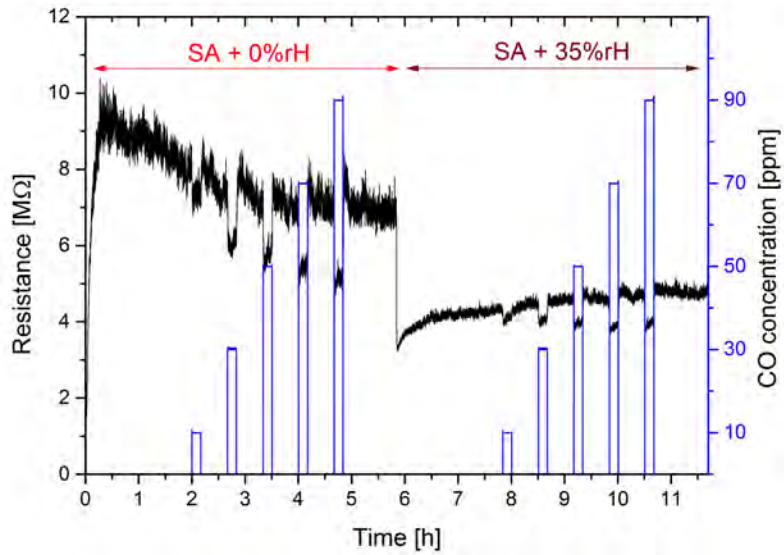
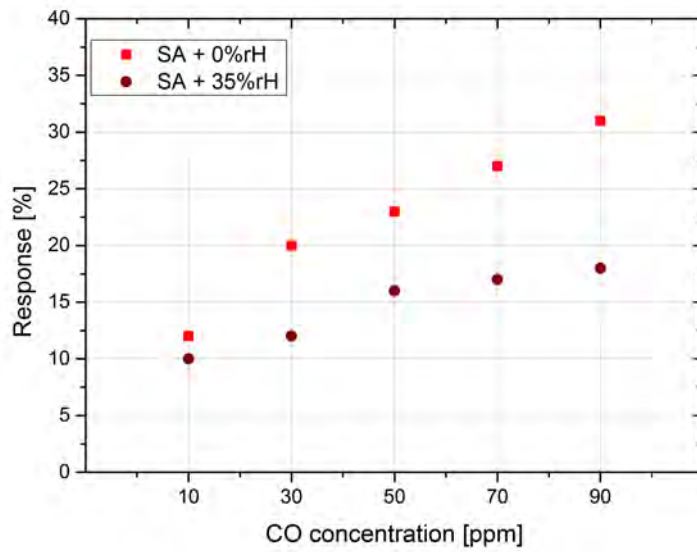


Figure 61: Change of resistance of sensor A upon exposure to 50 ppm CO in dry nitrogen at 250°C, 300°C, and 350°C. The measurement has been repeated two times: Measurement 1 (black) and Measurement 2 (dark grey).

Figure 62 presents the results of the single SnO₂ nanowire sensor B1 upon exposure to increasing concentrations of CO in the range 10-90 ppm at 300°C. The change of resistance induced by the introduction of CO is measured successively in dry synthetic air and in humid synthetic air (35% relative humidity), as shown in Figure 62a. The noise of the measured resistance is increased in comparison with the sensor A (Figure 59), but the signal is still well measurable. The baseline resistance is lower in the presence of humidity (about 5 MΩ) than in dry synthetic air (about 7.2 MΩ). The resistance drift is also reduced in the presence of humidity. The sensor response to CO, which has been calculated for each CO concentration in both dry and humid synthetic air, is plotted in Figure 62b. The sensor response is higher in dry synthetic air (12-31%) than in humid synthetic air (10-18%). The higher response in dry atmosphere over humid atmosphere has already been observed for sensor A (Figure 60). In the presence of humidity, the response for CO concentrations of 50 ppm, 70 ppm and 90 ppm is almost the same: 16%, 17% and 18%, respectively, which indicates that the sensor signal saturates at CO concentrations above 50 ppm. On the contrary, the response for increasing CO concentrations in the same range (10-90 ppm) is continuously increased in dry synthetic air.



(a)



(b)

Figure 62: (a) Change of resistance of sensor B1 upon exposure to increasing concentrations of CO in the range 10-90 ppm successively in dry synthetic air and in humid synthetic air (35% relative humidity) at 300°C. (b) Response of the sensor to the different concentrations of CO in dry synthetic air (red squares) and in humid synthetic air (brown circles).

For the next measurement, the response of the sensors C1 and C2 to CO are compared. Both nanowire sensors are located on the same chip, which means that the process steps leading to their fabrication are strictly identical. Another consequence is that the sensors C1 and C2 can be measured at the same time in parallel in the gas measurement chamber. Moreover, since the contacts (in a 4 point configuration) are spaced by a distance of 500 nm in both cases, the geometry of both sensors differs only by the diameter of the nanowires: 90 nm for C1 and 70 nm for C2. So the difference of response between the two sensors shall directly reflect the influence of the nanowire diameter.

Figure 63 shows the resistance change of the sensors C1 and C2 upon exposure to 90 ppm CO in dry synthetic air (red) and in dry nitrogen (blue) at 200°C, 250°C and 300°C in a logarithmic scale. The baseline resistance of the sensors C1 and C2 is strongly influenced by the background atmosphere. In nitrogen the resistance of C1 and C2 is in the range 1-10 MΩ, while in synthetic air the resistance varies between 100 MΩ and 1 GΩ. At 200°C, the sensors C1 and C2 are not able to detect 90 ppm CO in dry nitrogen. At 250°C and 300°C, the response is visible, but very slow in comparison to the one in dry synthetic air. In dry synthetic air, the response time decreases with increasing temperature and it is below 1 minute at 300°C. Also the response is increased for both C1 and C2 by increasing the temperature in both dry atmospheres, i.e. nitrogen and synthetic air.

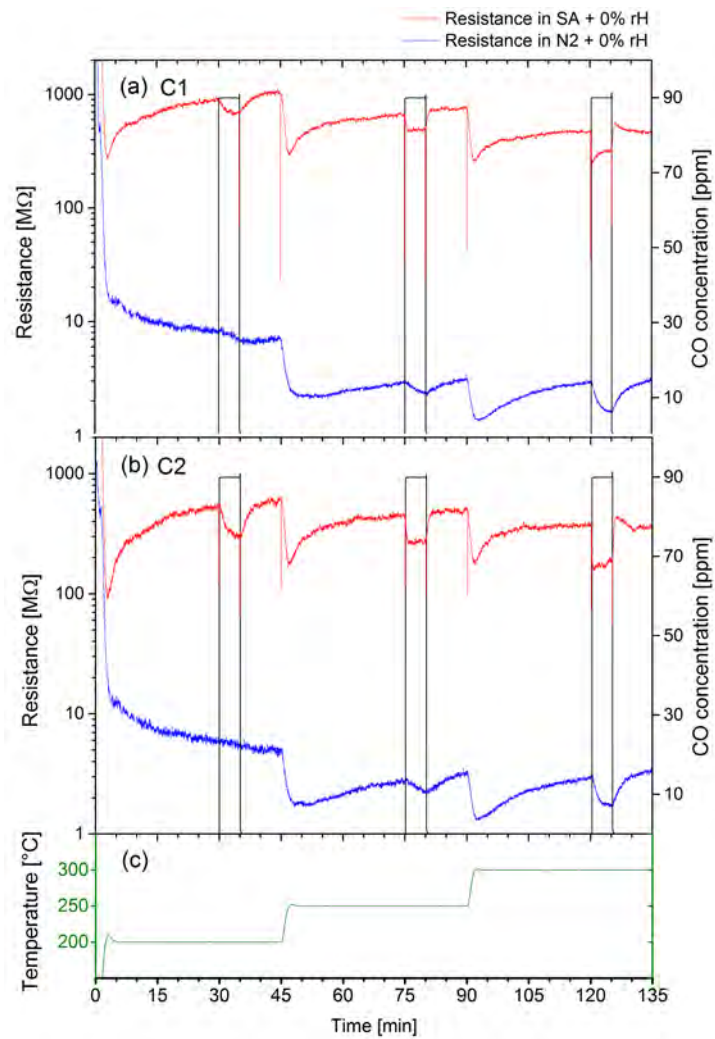


Figure 63: Change of resistance of two single SnO₂ nanowire sensors upon exposure to 90 ppm CO in dry synthetic air (red) and in dry nitrogen (blue) for increasing temperatures in the range 200-300°C. (a) Resistance of C1, (b) Resistance of C2, (c) Temperature profile. Both sensors are measured at the same time in parallel in the gas measurement chamber.

Figure 64 summarizes the responses obtained by the sensors C1 and C2 upon exposure to 90 ppm CO in dry nitrogen (top) and in dry synthetic air (bottom) at 250°C and 300°C, as presented above in Figure 63. An interesting difference between the measurements in nitrogen and in synthetic air is that the responses of both sensors to 90 ppm CO are almost the same when measured in nitrogen, while they are clearly distinct when measured in synthetic air. In nitrogen, the response of C1 and C2 at 250°C is in the range 20-22% and at 300°C it is 43-46%. In synthetic air, the response of C1 is 27% at 250°C and 46% at 300°C. The response of C2 in synthetic air is 42% at 250°C and 54% at 300°C. So a higher response to 90 ppm CO in synthetic air is obtained for the sensor C2, which is the thinner nanowire (70 nm diameter). Besides, the response of the sensor C1 in synthetic air is comparable to the response measured in nitrogen. This result is astonishing because the response in synthetic air is expected to be higher than the response in nitrogen, as already observed for the sensor A in Figure 60.

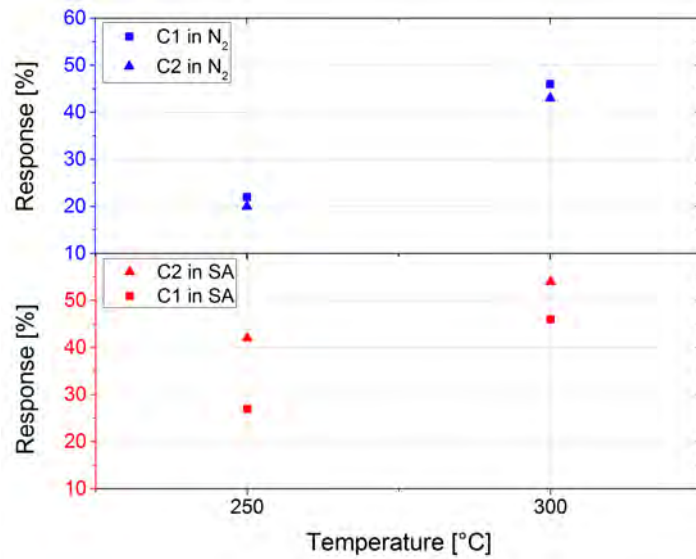


Figure 64: Comparison of the response to 90 ppm CO in dry nitrogen (top) and in dry synthetic air (bottom) of the sensors C1 (squares) and C2 (triangles) at 250°C and 300°C.

4.3.3 Response to H₂

Three sensors have been tested for the detection of H₂: the sensors D, B1 and B2. First the results of the sensor D measured in a 4 point configuration upon exposure to 20 ppm H₂ in dry synthetic air at 250°C, 300°C and 350°C are shown in Figure 65. Before the introduction of H₂, the nanowire resistance is measured for 30 minutes in the background atmosphere at the desired operating temperature. Then three pulses of H₂ flow are introduced into the gas measurement chamber for a duration of 15 minutes. After each pulse, the H₂ flow is interrupted for 15 minutes in order to enable the recovery of the sensor. The last recovery step lasts 30 minutes. This sequence is repeated at each operating temperature.

The exposure of the sensor D to 20 ppm H₂ in dry synthetic air results in a decrease of the resistance. The sensor response reaches 36%, 49% and 66% at 250°C, 300°C and 350°C, respectively. The response and recovery are very fast for each three temperature steps: below 2 min. The baseline resistance of the nanowire sensor is very stable at 250°C, while a slight drift towards lower resistance values is observed at 300°C and 350°C. Interestingly, the resistance of the nanowire in the presence of H₂ stays constant even with increasing temperatures and do not drift even at 300°C and 350°C. The increasing sensor response for increasing operating temperatures is obviously caused by the increase of the resistance baseline in dry synthetic air with increasing temperatures.

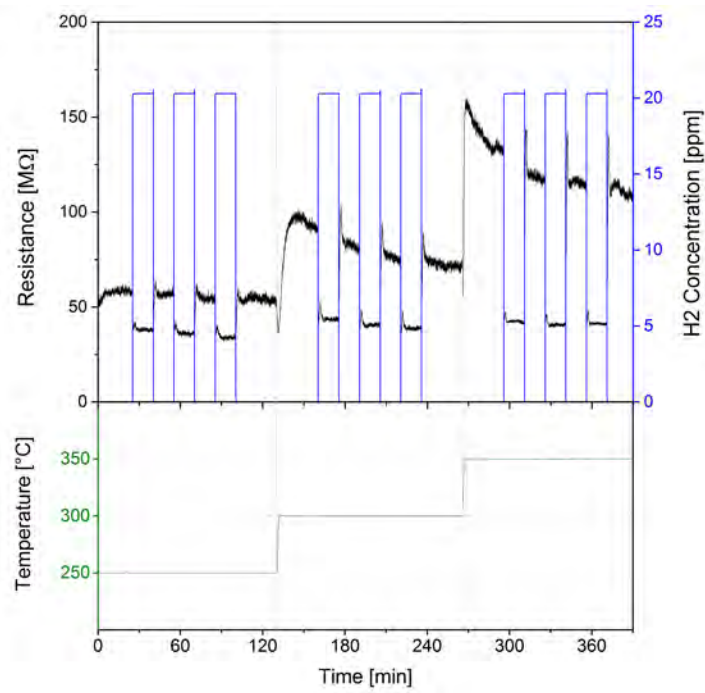


Figure 65: Change of resistance of the single SnO₂ nanowire sensor D measured in a 4 point configuration upon exposure to 20 ppm H₂ in dry synthetic air for increasing temperatures in the range 250-350°C.

Figure 66 shows the response for the sensor D (measured in a 4 point configuration) upon exposure to increasing concentrations of H₂ in the range 1-20 ppm in dry synthetic air at 250°C, 300°C and 350°C and in humid synthetic air (50% rH) at 250°C. The detection of 1 ppm H₂ is possible from a temperature of 300°C and above. The highest responses are obtained at 350°C: 26% for 1 ppm, 61% for 10 ppm and 75% for 20 ppm H₂. With a resistance change of 26% at 350°C upon exposure to 1 ppm H₂, it is likely that the sensor is able to detect even smaller concentrations of H₂ in the ppb range. At 250°C, the response is 43% for 10 ppm H₂ and 54% for 20 ppm H₂ in dry synthetic air. It decreases to 23% and 33% for 10 ppm and 20 ppm H₂, respectively, in the presence of humidity. Still the sensor presents a good response upon exposure to 10 ppm H₂ in humid synthetic air.

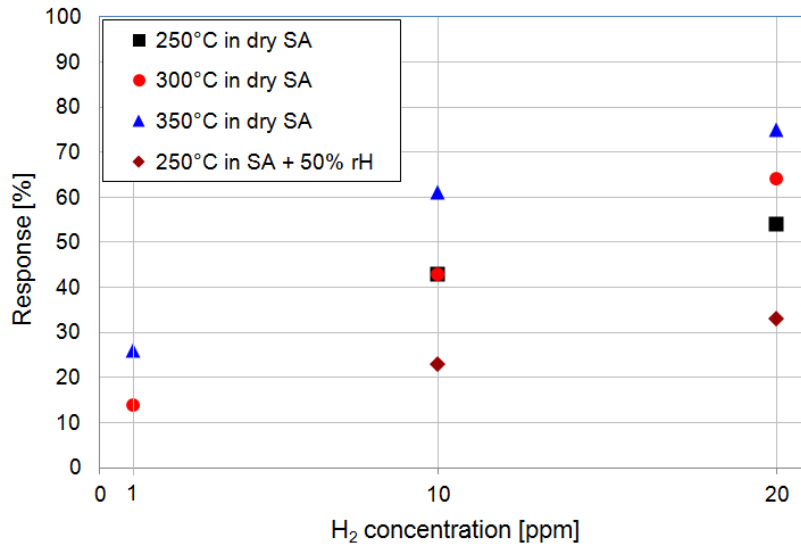


Figure 66: Comparison of the response of sensor D to increasing concentrations of H₂ in the range 1-20 ppm in dry synthetic air at 250°C (black squares), at 300°C (red circles), at 350°C (blue triangles) and in humid synthetic air at 250°C (brown diamonds).

Figure 67 is another measurement of the sensor D upon exposure to 10 ppm H_2 at $150^\circ C$ in a background atmosphere of synthetic air with 50% relative humidity. The sensor response is calculated (average over the three pulses) and a resistance change of 22% is obtained, which is comparable with the measurement at $250^\circ C$. At $150^\circ C$, the response and recovery times are in the range 2-3 min and 4-5 min, respectively. This result is important for practical applications. The sensor exhibits a good response in the presence of humidity and the temperature can be lowered from $250^\circ C$ to $150^\circ C$ for the same efficiency.

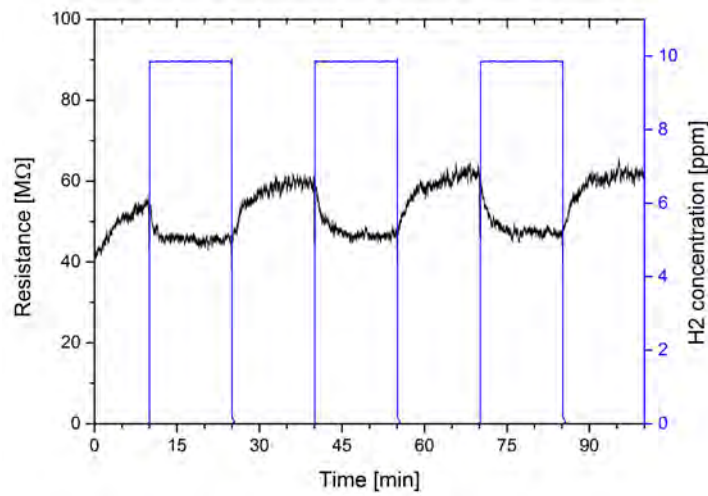


Figure 67: Change of resistance of sensor D upon exposure to 10 ppm H_2 in synthetic air with 50% relative humidity at $150^\circ C$.

The single nanowire sensors B1 and B2 have also been measured in the presence of H₂ in dry and humid synthetic air. Figure 68 shows the change of resistance of the sensor B1 upon exposure to increasing concentrations of H₂ in the range 10-90 ppm at 300°C. The background atmosphere is dry synthetic air at the beginning of the measurement and changes after 3.5 hours to synthetic air with a relative humidity of 40%. The H₂ pulses last 5 minutes and the interruptions between 2 pulses 10 minutes. The same measurement has also been conducted at the same time in parallel for the sensor B2 (not shown here). The resistance baseline of the sensor B1 is decreased by the introduction of humidity in synthetic air. A slight drift of the resistance is observed in both environments. The response to H₂ is higher in dry synthetic air than in the presence of humidity. The response is increased upon exposure to increasing concentrations of H₂ in the range 10-90 ppm. The response and recovery times are less than one minute both in dry and in humid synthetic air.

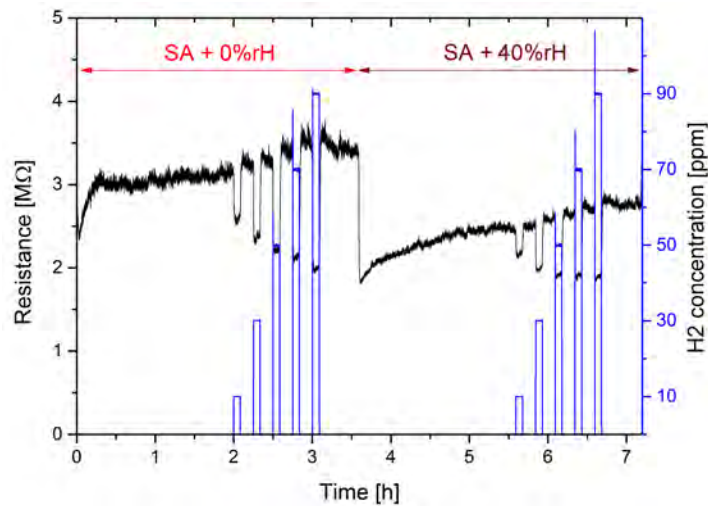


Figure 68: Change of resistance of sensor B1 upon exposure to increasing concentrations of H₂ in the range 10-90 ppm in dry synthetic air (0-3.5 h) and in humid synthetic air (3.5-7 h) at 300°C.

Figure 69 summarizes the responses measured for the sensors B1 and B2 upon increasing concentrations of H_2 in the range 10-90 ppm at 300°C . Figures 69a and 69b demonstrate the better performance of both nanowire sensors in dry synthetic air. Besides, an important feature for practical applications is the distribution of the response values over the range of concentrations. In dry synthetic air, the values of the sensor response B1 increase from 20% to 45% for increasing concentrations of H_2 in the range 10-90 ppm. So a quantitative measurement of the concentration of H_2 detected should be possible. In the presence of humidity, the responses of the sensor B1 to H_2 concentrations in the lower concentration range 10-50 ppm also increase with increasing concentration. In the concentration range 50-90 ppm the response values (between 27% and 32%) do not clearly increase with the concentration.

For the sensor B2, the saturation effect of the response upon increasing concentrations of H_2 is already visible in dry synthetic air for concentrations of 50 ppm and above. In humid synthetic air, the effect is even more pronounced. The responses range between 12% and 21% over the whole H_2 concentration range 10-90 ppm, so the sensor will not deliver any reliable information about the H_2 concentration detected even in the lower concentration range. Figures 69c and 69d directly compare the response of the sensors B1 and B2 in dry synthetic air and in humid synthetic air, respectively. The response of both sensors are quite comparable although the better performance of the sensor B1 over B2 is highlighted. Again the nanowire sensor with a smaller diameter (60 nm for B1) exhibits a higher response than the thicker nanowire (100 nm for B2).

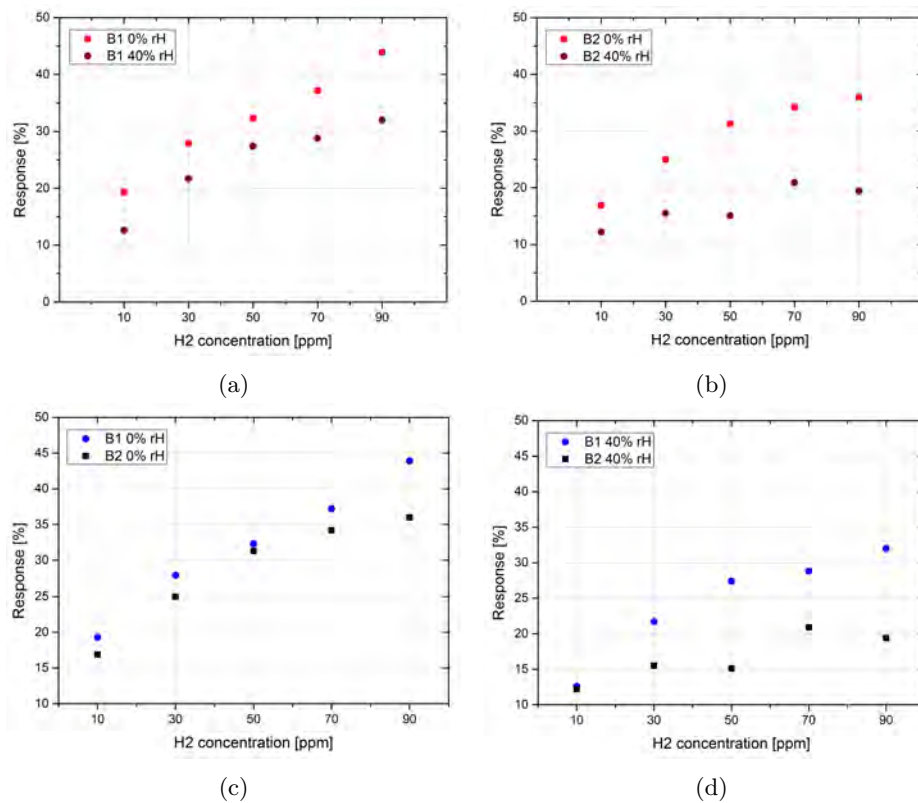


Figure 69: Comparison of the response of the sensors B1 and B2 upon increasing concentrations of H₂ in the range 10-90 ppm in dry or humid synthetic air at 300°C. (a) Sensor B1 in dry (red squares) and humid (brown circles) synthetic air. (b) Sensor B2 in dry (red squares) and humid (brown circles) synthetic air. (c) Comparison of the sensor responses B1 (blue circles) and B2 (black squares) in dry synthetic air. (d) Comparison of the sensor responses B1 (blue circles) and B2 (black squares) in humid synthetic air.

4.3.4 Response to H₂S

The resistance change of the sensor A has been measured at 350°C upon exposure to increasing concentrations of H₂S between 100 ppb and 1 ppm in synthetic air with different humidity level: 0%, 35% and 65% relative humidity. The results are shown in Figure 70. The sensor is measured for 30 minutes in the background atmosphere. The first pulse of H₂S flow is introduced in the gas measurement chamber for 5 minutes followed by an interruption of 10 minutes. Two H₂S pulses are introduced for each concentration: 100 ppb, 500 ppb and 1 ppm.

H₂S induces a high resistance change of the nanowire sensor. Even for concentrations as low as 100 ppb, the signal is clearly detectable. In dry synthetic air, the response and recovery are slower than in humid synthetic air. It seems that the resistance does not recover completely after exposure of H₂S in dry synthetic air, at least within 10 minutes. In synthetic air with a relative humidity of 35% and 65%, the sensor recovers within 10 minutes, though the resistance after the H₂S exposure is slightly higher than before the H₂S pulses.

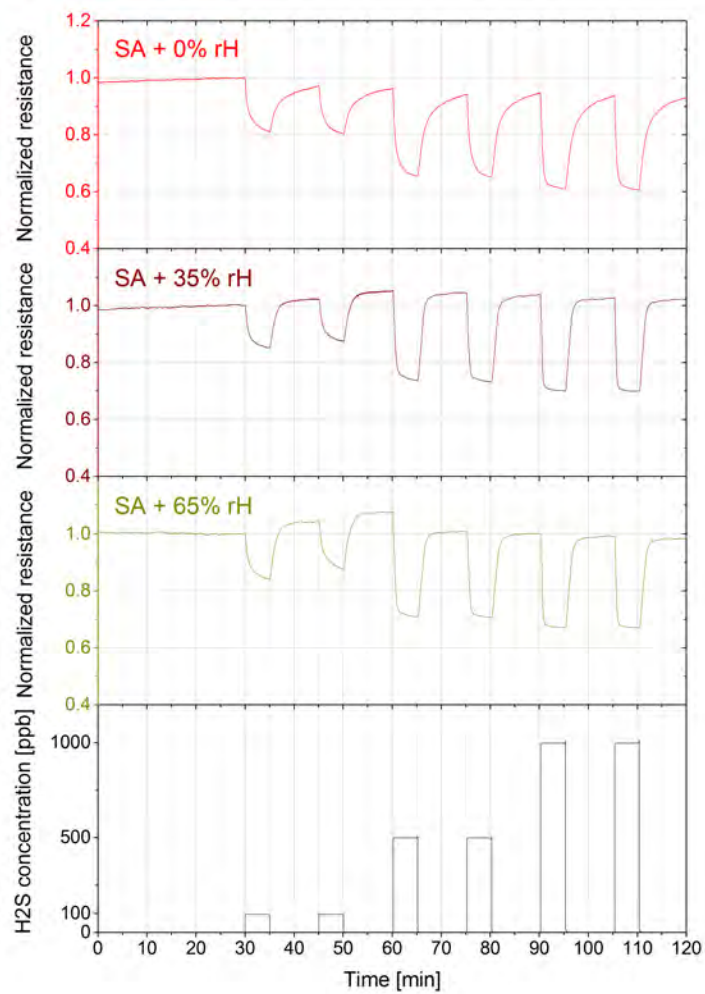


Figure 70: Change of resistance of sensor A at 350°C upon exposure to increasing concentrations of H₂S in the range 100-1000 ppb in synthetic air with different relative humidity level: 0% (top), 35% (middle) and 65% (bottom). The resistance has been normalized.

The sensing performances of sensor A to H₂S exposure are summed up in Figure 71. The humidity level does not influence the sensor response, which is surprising because the effect of humidity is strong on the response to CO and H₂, as shown above. The resistance change due to the introduction of 100 ppb H₂S is about 15%. The response is increased to 30-35% for an exposure to 500 ppb H₂S and the same response is obtained for 1 ppm H₂S. The nanowire sensor A exhibits a high sensitivity to very low concentrations of H₂S, but the sensor response saturates for concentrations of 500 ppb and above.

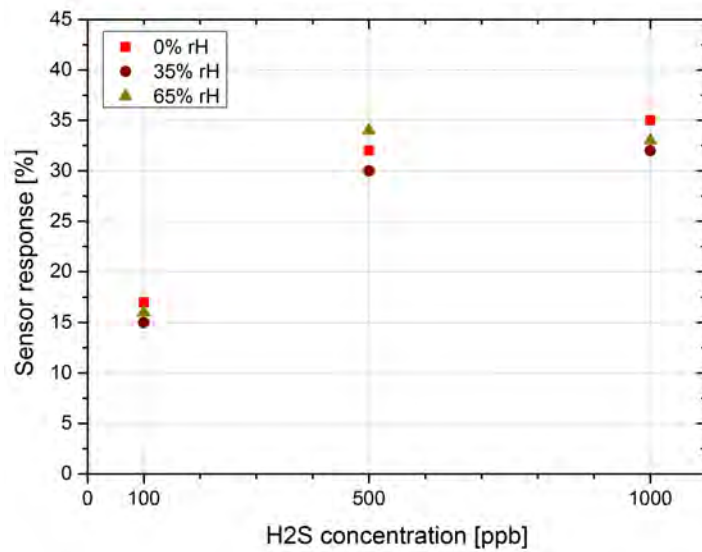


Figure 71: Comparison of the response of sensor A upon exposure to increasing concentrations of H₂S in the range 100-1000 ppb in synthetic air with different relative humidity level: 0% (red squares), 35% (brown circles) and 65% (green triangles) at 350°C.

The sensor D has also been exposed to H₂S and the results are shown in Figure 72. The resistance change upon exposure to 1 ppm H₂S has been measured at 300°C in dry synthetic air. The H₂S pulse has been repeated three times for 15 minutes with 15 minutes interruptions. The resistance is decreased in the presence of H₂S by a factor 100. This is the largest response measured in this thesis. The response and recovery times of the sensor are quite fast: in the order of 2 and 6 minutes, respectively. The response is reproducible and the recovery of the baseline resistance is very good.

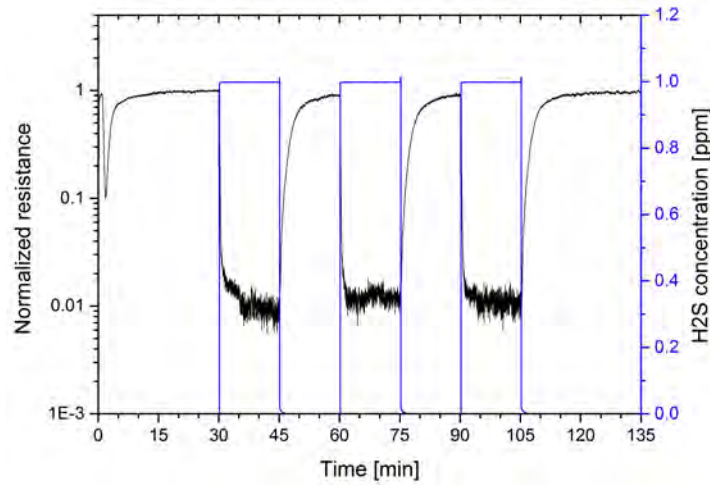


Figure 72: Change of resistance of sensor D upon exposure to 1 ppm H₂S in dry synthetic air at 300°C. Notice that the resistance has been normalized and the axis has a logarithmic scale.

4.4 Discussion

Table 11 compares gas sensing responses obtained for the different nanowire sensors upon exposure to CO, H₂ and H₂S in dry synthetic air at 300°C or at 350°C. As reminded in the table, there are some differences in the processing and in the measurement conditions of the six sensors. The sensors have either been processed by optical lithography and measured in a 2-point configuration or by e-beam lithography and measured in a 4-point configuration. The method used for the deposition of the contacts has also been varied (thermal evaporation or sputtering) in order to optimize lift-off behaviour and to ensure a uniform coating of the nanowires. As explained earlier, the focus has been put on obtaining qualitative information regarding different measurement conditions rather than on making a quantitative comparison of the nanowire sensors. However, it is very satisfying to observe similar responses for the sensors B1 and B2 upon exposure to H₂ and for the sensors C1 and C2 upon exposure to CO, because both B1/B2 and C1/C2 sensors have been processed and measured simultaneously. The difference measured between the responses B1 and B2, on one hand, and C1 and C2, on the other hand, is discussed later considering the difference in the nanowire diameters. Also, the responses for each gas individually are different for each sensor, but the change in nanowire resistance is always clearly measurable.

Table 11: Comparable gas sensor responses for the different nanowire sensors upon exposure to CO, H₂ and H₂S in dry synthetic air at 300°C, except for sensor A, which has been operated at 350°C. l and d are the length and diameter of the nanowire, respectively. The process conditions indicate if the sensor has been measured in a 2-point or 4-point configuration, which lithography process has been used (optical or e-beam) and how contacts have been deposited (evaporation or sputtering).

Sensor	l (μm)	d (nm)	Process conditions	CO 90 ppm	H ₂ 10 ppm	H ₂ S 1 ppm
A	53	300	2-pt, optical, sputt	14%	-	35%
B1	2	60	2-pt, optical, evap	31%	19%	-
B2	2	100	2-pt, optical, evap	-	17%	-
C1	0.5	90	4-pt, e-beam, evap	46%	-	-
C2	0.5	70	4-pt, e-beam, evap	54%	-	-
D	1	65	4-pt, e-beam, sputt	-	43%	99%

4.4.1 Influence of the background atmosphere

The first step is the measurement of a single nanowire in an inert background atmosphere (nitrogen) and the influence of the introduction of oxygen. As shown in Figure 58, the introduction of oxygen results in the increase of the nanowire resistance. According to the gas sensor principle presented in Section 1.2, this increase of resistance upon exposure to oxygen is due to the transfer of electrons from the conduction band of the SnO₂ nanowire to the oxygen species during their ionosorption as O⁻ species at the surface of the nanowire and the formation of a depletion layer, which reduces the conduction channel. The resistance saturates in the presence of oxygen, which means that the adsorption reaction of O₂ species at the surface of the nanowire reaches a steady state. When the oxygen flow is turned off, the resistance is decreased due to the desorption reaction of oxygen species from the nanowire surface, which induces the release of electrons in the conduction band of the SnO₂ nanowire.

The analysis of the response and recovery times (50 min and 90 min, respectively) suggests a faster adsorption than desorption of oxygen at the surface of the SnO₂ nanowire in dry atmosphere. Hernandez-Ramirez et al. [28] reported a different behaviour: a slower process of the adsorption of oxygen species at the surface of the SnO₂ nanowire than the desorption of those oxygen species. This result has been obtained by measuring the AC impedance of a single nanowire (diameter of 70 nm) in a changing atmosphere from nitrogen to synthetic air and back to nitrogen. After 3 hours at nearly 300°C in synthetic air, the nanowire surface has not reached the steady state yet. On the contrary, back in nitrogen atmosphere the nanowire reaches a steady state with a time constant of about 10 min.

The relative difference between the resistance values in dry nitrogen (4.9 M Ω) and in humid nitrogen (4.6 M Ω) is quite small (6%). Since the change of resistance is assumed to be directly correlated with the surface reactions, the previous observation suggests that only few water molecules react with lattice sites of the SnO₂ nanowire. In comparison, the relative difference between the resistance values in dry synthetic air (11.8 M Ω) and in humid synthetic air (9.5 M Ω) is three times higher (19%), which suggests that the effect of water molecules is larger in synthetic air than in nitrogen. Hernandez-Ramirez et al. [28] observed an influence of water on the resistance change of the SnO₂ nanowire four times higher in synthetic air than in nitrogen. The difference lies in the presence of ionosorbed oxygen at the surface of the nanowire in synthetic air. The water molecules seem to react preferably with ionosorbed oxygen than with lattice sites.

Also, the response to oxygen is lower in humid atmosphere (110%) in comparison with dry conditions (140%), so the number of ionosorbed oxygen species at the surface of the nanowire must be lower in humid atmosphere than in dry atmosphere. There are several possible explanations reported in the literature:

- Caldararu et al. [189] suggested that the presence of hydroxyl groups at the surface of SnO₂ limits the adsorption of oxygen up to 320-340°C.
- Morrison [192] assumed that the dipoles of physisorbed water molecules would line up to neutralize any apparent charges of the ionosorbed oxygen species and result in their desorption.
- The reaction mechanism for water suggests that the water molecules react with the ionosorbed oxygen resulting in their desorption and in the subsequent release of the previously trapped electrons into the conduction band.

Humidity also influences the kinetics of the adsorption and desorption reactions of oxygen species. Two effects are observed:

- The adsorption process of oxygen is about eight times faster than the desorption process in humid atmosphere, while in dry atmosphere the adsorption process is only two times faster than the desorption.
- The steady state for the adsorption of oxygen at the surface of the nanowire in humid conditions is reached about ten times faster than in dry conditions.

The first observation might be explained by the stabilization of the ionosorbed oxygen at the surface of the nanowire by water molecules through hydrogen bonds, which may delay the desorption of the oxygen species. The second

effect, i.e. the faster adsorption of oxygen on SnO_2 in the presence of humidity, might be due to the polarization of the SnO_2 surface by water molecules, which may be already partly adsorbed and result in the enhanced kinetics for the ionosorption of oxygen.

The fact that the resistance of the nanowire sensor increases in the presence of oxygen in a nitrogen background supports the principle based on the ionosorption of oxygen at the surface of the SnO_2 nanowire. Also the observed decrease of the nanowire resistance in the presence of CO , H_2 and H_2S is in good agreement with the results reported in the literature and with the gas sensing principle applied to reducing gas species, which are assumed to react with the ionosorbed oxygen. During the desorption process, the electrons, which were trapped at the surface state created by the ionosorbed oxygen, are released into the conduction band, thus decreasing the electrical resistance of the nanowire.

In the literature, the suggested mechanism for the detection of CO in nitrogen is the direct adsorption of CO at the SnO_2 surface acting as an electron donor, thus releasing electrons into the conduction band of SnO_2 (see Section 4.1.3). In the presence of a large amount of oxygen (ambient oxygen concentration as in synthetic air), the only reaction path considered is the reaction of CO with the ionosorbed oxygen.

The response of the nanowire sensors A, C1 and C2 have been measured upon exposure to CO in dry nitrogen and in dry synthetic air. The first remark is that the sensor response is higher in synthetic air than in nitrogen (see Figures 60 and 64). Only for the sensor C1 similar responses in both environments have been observed. Schmid et al. [204] stated that a larger electrical effect is produced by the direct adsorption of CO at the SnO_2 surface in the absence of O_2 than by the reaction of CO with the ionosorbed oxygen in the presence of O_2 . This statement goes along with their observation that the response to CO in pure nitrogen is higher than in nitrogen + 2% O_2 in dry conditions, though it is in contradiction with the results obtained in the present thesis. The sensing material used in the study by Schmid et al. is a polycrystalline thick film, which surely presents different properties than the single crystalline nanowire measured here. It is possible that the direct reaction of CO on SnO_2 is enhanced by the presence of defects at the surface of the polycrystalline film, such as grain boundaries, but it does not seem to be the dominant reaction in this study. It is suggested that the resistance change is dominated by the reaction of CO with the ionosorbed oxygen, which would explain why the response measured on the nanowire is higher in dry synthetic air than in dry nitrogen.

Besides, a drift of the resistance baseline is observed in dry and humid nitrogen and in dry and humid synthetic air, though the drift is the largest in dry synthetic air. In the literature, the drift in resistance of the SnO_2 gas

sensors is a well known issue and is often related to the oxygen transport into the bulk material. As reported by Kamp et al. [205], the conductivity of SnO₂ is affected by: (1) a change in the concentration of oxygen vacancies due to surface reactions involving a charge transfer and to oxygen diffusion into the bulk material, and (2) a redistribution of the oxygen vacancies in the space charge layer driven by the electric field formed upon the ionosorption of gas molecules at the surface of the metal oxide.

4.4.2 Influence of humidity

The response of the nanowire sensor A has been more extensively measured upon exposure to CO in humid nitrogen and in humid synthetic air. It is observed that humidity lowers the response to CO in both nitrogen and synthetic air (Figure 60). Still the response in humid synthetic air is slightly higher than the response in dry nitrogen. Sensor B1 has also been measured upon exposure to CO in dry and in humid synthetic air. As observed for sensor A, the response of sensor B1 to CO is decreased in the presence of humidity (Figure 62b). As discussed above, the results suggest that more ionosorbed oxygen species are present at the surface of the SnO₂ nanowire in dry synthetic air than in humid synthetic air. Consequently, there are more adsorption sites for the CO molecules in a dry atmosphere, which would explain the higher response measured in dry synthetic air than in humid synthetic air. Those results might also be explained by cross-reactivity effects between the CO and H₂O molecules for the same adsorption sites. This hypothesis has been reported by Hernandez-Ramirez et al. [206], who measured a single SnO₂ nanowire sensor in dry synthetic air at 265°C upon exposure to successive pulses of CO, relative humidity and a combination of CO and relative humidity. The results show that the response to a mixed CO/H₂O pulse is not the sum of the responses obtained for the same concentrations of gas species introduced separately, so they concluded that complex cross-reactivity effects between CO and humidity must be responsible.

Barsan et al. [35] studied the adsorption of CO on SnO₂ thick film sensor doped with 0.2% wt of Pd in the presence of humidity. They observed an increased response to CO with increasing humidity from 0% to 50% relative humidity. In order to understand this phenomenon, they conducted catalytic conversion measurements and reported a decreased CO consumption with increasing humidity, which is surprising because since a higher sensor response has been obtained for higher humidity concentration, an increase of the CO consumption with increasing humidity is expected. Complementary investigations on different sensor parts enabled the clarification of that aspect. The only effect of the sensitive layer showed a strong CO consumption but no measurable dependence on humidity, while the Pt electrodes and heater parts show a significant CO consumption, which decreases with in-

creasing humidity. So the influence of humidity is not related to the sensing material alone but to a combination of the substrate and the electrode-sensing material.

The decrease of the sensor response in the presence of humidity has also been observed during the detection of H_2 with sensor D (Figure 66) and sensors B1 and B2 (Figure 69). Only for the detection of H_2S , no difference in the response of the nanowire sensor has been observed in dry or humid synthetic air (Figure 71).

4.4.3 Influence of the operating temperature

The increase of temperature results in an increased response. This has been illustrated for the detection of CO with the sensors C1 and C2 (Figure 63) and for the detection of H_2 with sensor D (Figure 65 and 66). In the case of CO detection with the sensors C1 and C2 (Figure 63), the influence of the temperature on the adsorption and desorption rates is also visible: the response and recovery times are lowered (faster processes) for increasing operating temperatures. These results illustrate the influence of the temperature on the kinetics of the reactions between the gas phase and the SnO_2 nanowire.

4.4.4 Influence of the size of the nanowire

The diameter of the nanowire is assumed to influence the sensor response. As reported by Hernandez-Ramirez et al. [28], the response of a single SnO_2 nanowire based sensor upon exposure to CO (concentration range: 20-1000 ppm) in synthetic air is higher for a nanowire with a smaller diameter (comparison between two nanowires 25 nm and 70 nm in diameter). This behaviour has also been observed in this thesis for the sensors C1 (90 nm in diameter) and C2 (70 nm in diameter) upon exposure to 90 ppm CO in dry synthetic air. The response of sensor C2 is higher than the response of sensor C1: the difference between both responses is 20% at 250°C and 10% at 300°C (Figure 64). Interestingly, the responses obtained for both sensors for the same CO concentration in dry nitrogen are practically the same. The following discussion and the schemes of Figure 74 intend to explain those results.

Barsan et al. [37] reported values of the Debye length for SnO_2 single crystals ranging from 129 nm to 11 nm for increasing temperatures between 130°C and 430°C in the presence of oxygen (see Figure 73). The extrapolation of those values results in a Debye length of 40 nm at 250°C and 27 nm at 300°C. The width of the depletion layer due to the ionosorption of oxygen is in the order of the Debye length [53]. Assuming that those values also apply to single crystalline SnO_2 nanowires, it means that the nanowire C2 is

completely depleted of electrons in synthetic air at 250°C, while the nanowire C1 is only partly depleted. When CO is introduced in the gas measurement chamber, the reaction of CO with ionosorbed oxygen results in the release of electrons in the conduction band of the SnO₂ nanowire. Consequently, the nanowire C2 becomes partly depleted and the width of the depletion layer of the nanowire C1 is decreased. The width of the depletion layer, which is induced by the surface reactions between the SnO₂ nanowire and the test gas, is constant for nanowires with different diameters when exposed to similar environments (temperature and gas concentration), because it is not related to the radial dimensions of the nanowire [40]. Consequently, reducing the radial dimension of the nanowire leads to a higher change in width of the depletion layer relatively to the radius of the nanowire, which explains the higher response of sensor C2 to CO in synthetic air at 250°C. At 300°C, the depletion layer is higher for the nanowire C2 than for the nanowire C1. When CO is introduced, the width of the depletion layer increases likewise for both nanowires, only the effect is higher for the nanowire C2 than for the nanowire C1. This explains the higher response of C2 to CO in synthetic air at 300°C and the smaller difference between both responses in comparison with the results at 250°C. Moreover, due to the increase of temperature more CO molecules react with the ionosorbed species, so more electrons are released into the conduction band and the decrease of the width of the depletion layer is higher at 300°C than at 250°C, which explains the higher resistance change measured.

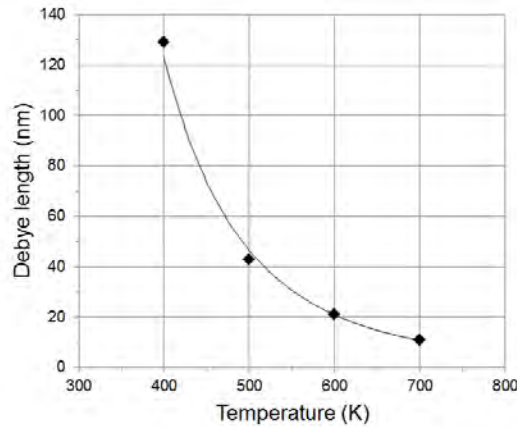


Figure 73: Dependence of the Debye length with the temperature for SnO₂ single crystals (values reported in [37]).

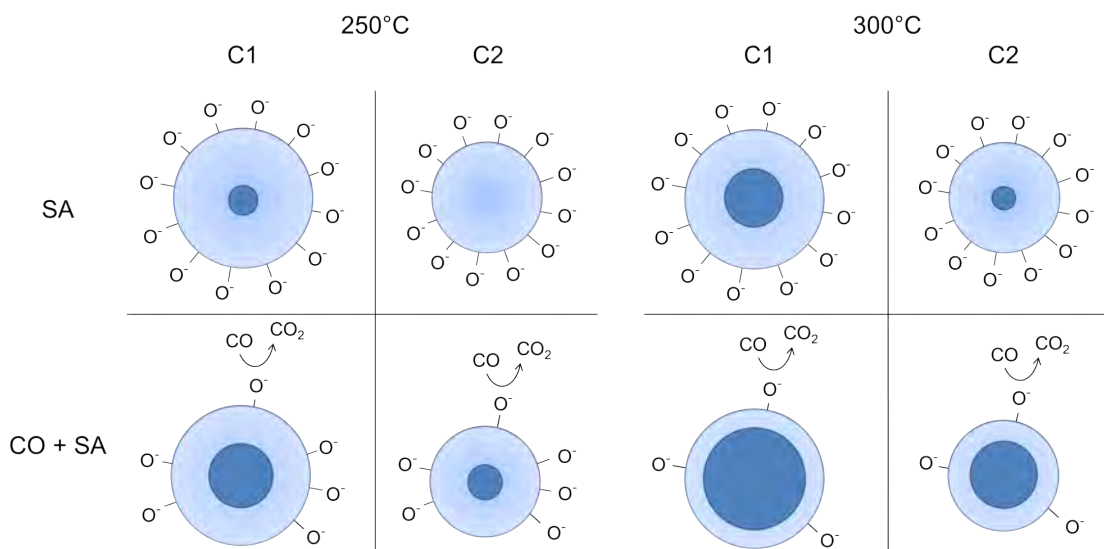


Figure 74: Effect of the surface reactions on the width of the depletion layer of the SnO_2 nanowire. The depletion layer is represented in light blue and the conduction channel in dark blue. At 250°C in synthetic air, the nanowire C1 is partly depleted and the nanowire C2 is completely depleted. In the presence of CO, the ionosorbed oxygen species O^- are consumed, leading to the release of electrons in the conduction band, thus decreasing the width of the depletion layer. At 300°C , both nanowires are partly depleted in synthetic air. Due to the increase of temperature, more CO molecules react with the ionosorbed species, so the effect on the width of the depletion layer is higher than at 250°C , which explains the higher resistance change measured.

In nitrogen, there is no ionosorbed oxygen at the surface of the SnO_2 nanowire, therefore there is no depletion layer. In the presence of CO, the CO molecules react directly on lattice sites and act as electron donors, so electrons are released in the conduction band of the nanowire, hence the decrease of resistance measured. In that case, the resistance change is simply due to the increase of concentration of the charge carriers into the nanowire. It is supposed that the number of CO molecules reacting with the SnO_2 lattice is the same on both nanowires C1 and C2, therefore the same number of electrons is released in the nanowires, which explains the similar responses obtained in nitrogen at 250°C and at 300°C . Moreover, it seems that the direct adsorption of CO at the surface of the nanowire is enhanced with increasing temperature from 250°C to 300°C , because the response measured is higher at 250°C than at 300°C .

The increased response for a nanowire with a smaller diameter has also been observed for the detection of 10-90 ppm H_2 with sensors B1 (60 nm in diameter) and B2 (100 nm in diameter) at 300°C in humid synthetic air (Figure 69d).

4.4.5 Influence of the concentration of the test gas

The response of the nanowire sensor increases with increasing concentrations of the test gas to detect. This result has been shown for the detection of CO with sensor A (Figure 60) and sensor B1 (Figure 62b), for the detection of H₂ with sensor D (Figure 66) and sensors B1 and B2 (Figure 69) and for the detection of H₂S with sensor A (Figure 71). However, a saturation effect of the sensor may occur for higher concentrations of test gas. In that case, the increase of the concentration of the test gas will not result in an increase of the sensor response anymore. The saturation of the sensor response depends on the test gas, on the background atmosphere and on the diameter of the nanowire.

For the detection of CO, the saturation of the sensor B1 starts with a concentration of 50 ppm in humid synthetic air. In dry synthetic air, however, no saturation effect is visible in the range 10-90 ppm CO. The sensor A does not present any saturation effect in the range 10-90 ppm CO in dry synthetic air nor in humid synthetic air, though the increase of response with increasing CO concentration is higher (higher slope) in dry synthetic air than in humid synthetic air (Figure 60). Both sensors have very different geometries: sensor A (53 μm in length and 300 nm in diameter) and sensor B1 (2 μm in length and 60 nm in diameter). A possible explanation for the saturation of sensor B1 in humid synthetic air is the small surface area available at the surface of the nanowire for the CO molecules to react.

For the detection of H₂, a saturation of the sensor response is observed from a concentration of 50 ppm on for the sensor B1 in humid synthetic air, for the sensor B2 in dry synthetic air (Figure 69). The response of the sensor B1 does not saturate in the range 10-90 ppm H₂ in dry synthetic air. For the sensor B2 in humid synthetic air, the saturation of the effect is visible for concentrations of H₂ above 10 ppm. By comparing the results for the sensors B1 and B2, it appears that the nanowire with larger diameter (B2) saturates for lower concentrations of H₂ than the nanowire with the smaller diameter (B1). This behaviour contradicts the hypothesis that the surface area plays a role in the saturation of the sensor response.

For the detection of H₂S, the saturation starts with a very low concentration of 500 ppb for the sensor A in dry and humid air (Figure 71). The saturation of the SnO₂ nanowire sensor caused by exposure to very low H₂S concentrations might be related to the deposition of sulfur on the SnO₂ surface (formation of SnS₂ described in Section 4.1.5), which may act as a passivation layer and hinder further reactions of H₂S on SnO₂.

4.4.6 Long-term stability

The long-term stability of the sensors has not been the focus of this thesis. Nevertheless, the total duration of measurement of each sensor (i.e. the total time, for which a current is applied and the voltage is measured at temperatures above 200°C), as well as the time period over which those measurements were conducted, are summarized in Table 12. Sensor A has been measured over one year during about 460 hours (i.e. 19 days). Each measurement lasts 16 hours in average. The longest measurement had a duration of 72 hours. Sensors B1 and D have been measured over nearly two months during a total of about 70 hours each, while sensors C1 and C2 have been measured over two weeks for a total of 100 hours. Sensor B2 has been measured for about 40 hours, but it was not possible to measure the sensor further because of a degradation of the contacts. The contacts of sensor D were also damaged with the time, which is most probably due to diffusion processes at the high operating temperatures. The nanowire sensor A presents the most stable signal over time.

All these measurements were performed in “DC-conditions”. Assuming test procedures employed by very specific sensor companies, where pulsed measurements are employed, the total measurement times might be extrapolated. Considering pulsed measurements alternating 500 ms of measurement and 10 s of pause, a total measurement time of 70 hours would mean a lifetime of 61 days in pulsed operation conditions. For the sensor A, which has been measured for 460 hours, the operation in pulsed conditions would mean a lifetime of 400 days.

Table 12: Duration and time period of operation of the nanowire sensors.

Sensor	Total duration of operation	Time period of the measurements
A	460 h	1 year
B1 and B2	70 h	2 months
C1 and C2	100 h	2 weeks
D	70 h	2 months

4.5 Summary

Six SnO₂ single nanowire sensors have been measured in various gaseous atmospheres. Tables 13 and 14 sum up the main results obtained for the detection of O₂, CO, H₂ and H₂S in various atmospheres and for different operating temperatures.

The first measurements investigate the influence of oxygen and humidity

Table 13: Summary of the gas sensing results of the nanowire sensors - Part 1.

Sensor	Carrier gas	Test gas	Concentration range	r.H.	Temperature	Response	Main results
A	N ₂	O ₂	20%	0%	300°C	140%	Desorption process of oxygen gas species on the SnO ₂ surface slower than the adsorption process; Faster interaction in humid than in dry conditions; Higher resistance change in dry than in humid conditions
A	N ₂	O ₂	20%	35%	300°C	110%	
A	N ₂	CO	10-90 ppm	0%	350°C	0-6%	Increased response of the nanowire sensor with increasing CO concentrations in the range 10-90 ppm; Higher response to CO in SA than in N ₂ ; Response to CO roughly two times higher in dry than in humid conditions
A	N ₂	CO	10-90 ppm	35%	350°C	0-4%	
A	SA	CO	10-90 ppm	0%	350°C	4-14%	
A	SA	CO	10-90 ppm	35%	350°C	2-7%	
B1	SA	CO	10-90 ppm	0%	300°C	13-31%	Higher response in dry SA than in humid SA;
B1	SA	CO	10-90 ppm	35%	300°C	10-18%	Saturation of the sensor response in humid SA for concentrations above 50 ppm
C1	N ₂	CO	90 ppm	0%	250-300°C	22-43%	Slower reaction process of CO with the SnO ₂ nanowire in N ₂ than in SA; C1: same response in N ₂ and in SA; C2: higher response in SA than in N ₂ ; In N ₂ , same response for C2 and C1; In SA, higher response of C2 (70 nm in diameter) in comparison with C1 (90 nm in diameter)
C1	SA	CO	90 ppm	0%	250-300°C	27-46%	
C2	N ₂	CO	90 ppm	0%	250-300°C	20-46%	
C2	SA	CO	90 ppm	0%	250-300°C	42-54%	

Table 14: Summary of the gas sensing results of the nanowire sensors - Part 2.

Sensor	Carrier gas	Test gas	Concentration range	r.H.	Temperature	Response	Main results
D	SA	H ₂	1-20 ppm	0%	350°C	25-75%	Detection of 1 ppm H ₂ possible with 25% response at 350°C; Decrease of the response in humid SA by a factor 2 in comparison with dry SA; Good response for 10 ppm H ₂ exposure at 150°C in humid SA
D	SA	H ₂	10 ppm	0%	250°C	43%	
D	SA	H ₂	10 ppm	50%	250°C	23%	
D	SA	H ₂	10 ppm	50%	150°C	22%	
B1	SA	H ₂	10-90 ppm	0%	300°C	20-45%	Higher response in dry SA than in humid SA; Higher response of B1 (60 nm in diameter) in comparison with B2 (100 nm in diameter); B1: Saturation of the sensor response in humid SA for concentrations above 50 ppm; B2: Saturation of the sensor response in dry SA for concentrations above 50 ppm and in humid SA
B1	SA	H ₂	10-90 ppm	40%	300°C	12-32%	
B2	SA	H ₂	10-90 ppm	0%	300°C	17-36%	
B2	SA	H ₂	10-90 ppm	40%	300°C	12-21%	
A	SA	H ₂ S	100 ppb	0-65%	350°C	15-17%	Detection of concentrations of H ₂ S as low as 100 ppb in dry and humid SA with 15% response at 350°C; No influence of the humidity level on the response of the sensor; Saturation of the response for concentrations above 500 ppb
A	SA	H ₂ S	500 ppb	0-65%	350°C	30-34%	
A	SA	H ₂ S	1 ppm	0-65%	350°C	32-35%	
D	SA	H ₂ S	1 ppm	0%	300°C	99%	Decrease of resistance by a factor 100 upon exposure to 1 ppm H ₂ S in dry SA at 300°C

on the nanowire sensor. The results support the ionosorption model described in the literature. The following conclusions have been drawn from the measurements and the discussion:

- The adsorption rate of oxygen on the SnO₂ nanowire surface in dry atmosphere is higher than the desorption rate.
- The water molecules react preferably with ionosorbed oxygen than with lattice sites.
- The number of ionosorbed oxygen species is higher in dry than in humid atmosphere.

Four sensors have been measured in the presence of CO in various background atmospheres. The best response to 90 ppm CO in dry synthetic air has been obtained with the sensors C1 (46%) and C2 (54%) at 300°C. CO could be detected in the range 10-90 ppm by sensor B1 in humid synthetic air (35% relative humidity) at 300°C with a response of 10-18%. The responses measured with sensor A were smaller due to the large diameter of the nanowire (about 300 nm). Nevertheless, interesting conclusions were drawn from the measurements of sensor A for CO concentrations in the range 10-90 ppm in nitrogen and synthetic air, in dry and humid conditions. It has been established that the response to CO is higher in the presence of oxygen than in nitrogen, which means that the reaction of CO with ionosorbed oxygen has a higher reaction rate than the reaction of CO with lattice oxygen. Also, the response to CO is lower in humid atmosphere than in dry atmosphere, which is probably due to the competition between CO and H₂O molecules for occupying the adsorption sites.

Three sensors have been measured in the presence of H₂ in a background of dry or humid synthetic air: D, B1, and B2. Sensor D demonstrated particularly good responses in the presence of humidity at low temperature, i.e. 150°C, for a concentration of 10 ppm H₂. The influence of the temperature on the sensor response was discussed and the best performance has been measured at 350°C for 20 ppm H₂ in dry synthetic air. Sensors B1 and B2 were measured over a large range of H₂ concentrations at 300°C. A saturation effect of the response at higher H₂ concentration is especially visible in the presence of humidity. The sensor B1 exhibits a better performance for the detection of H₂. The comparison of the response of the three sensors is possible for a H₂ concentration of 10 ppm and a temperature of 300°C. For those parameters and in dry synthetic air, the response measured for the sensor D was 43%, for the sensor B1 19% and for the sensor B2 17%. In humid synthetic air, the response is 23% for the sensor D, 13% for the sensor B1 and 12% for the sensor B2. The better performance of the sensor D over the sensors B1 and B2 is obvious, though the reason is not clear.

Two sensors have been measured in the presence of H₂S in synthetic air. The sensing results obtained for H₂S are very good. Sensor A exhibits a resistance change of 15% to concentrations of H₂S as low as 100 ppb in synthetic air at 350°C. However, the sensor response saturates for concentrations of 500 ppb H₂S and above. Another important feature is that the sensor response is not influenced by the level of humidity, which is very good for practical applications. The sensor D presents a very high response to 1 ppm H₂S with a resistance change of two orders of magnitude in dry synthetic air at 300°C.

The following assumptions made in the literature concerning the sensing mechanism of metal oxide gas sensors have been verified:

- The presence of humidity lowers the response of the sensor to reducing gas species.
- The reactions occurring at the surface of SnO₂ nanowires with gaseous molecules are activated processes requiring high operating temperatures (generally above 200°C).
- The response to a test gas is higher when the sensor uses a nanowire with a smaller diameter.

5 Towards stable, selective and CMOS integrated SnO₂ nanowire sensors

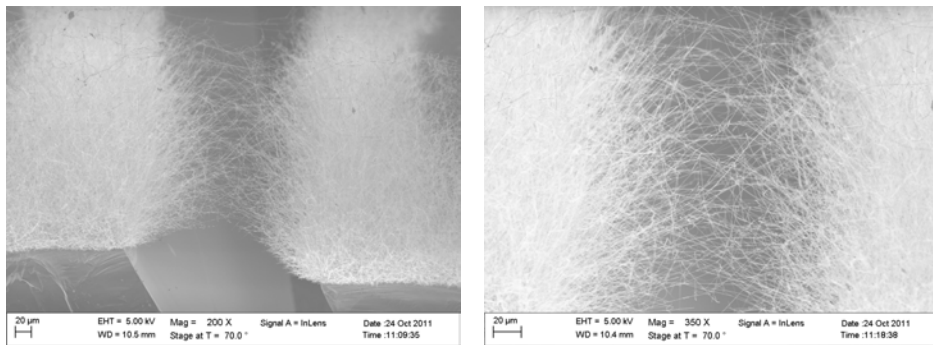
This section presents briefly a few complimentary experiments conducted in order to improve key features of SnO₂ nanowire gas sensors for a future possible commercialization. Stability of nanowire sensors is a crucial issue and the most reliable devices so far have been realized based on nanowire networks. Metal oxide gas sensors are known for their high sensitivity to a broad range of gas species. However, this advantage may become a weakness in terms of selectivity. Therefore, the functionalization of metal oxides with metallic nanoparticles has gained interest. Another concern is the miniaturization of the devices and the decrease of their power consumption. Both issues may be solved by the integration of gas sensors with CMOS technology.

5.1 Towards stable nanowire sensors: the nanowire network configuration

The fabrication of single nanowire devices is necessary for a fundamental understanding of the gas sensing mechanisms at the surface of SnO₂ single crystals. The previous sections have shown the challenges to build stable devices, especially the processing of metallic contacts ensuring an ohmic electrical contact with the single nanowire. For commercial purposes, the fabrication of devices based on networks of nanowires presents several advantages especially concerning the stability.

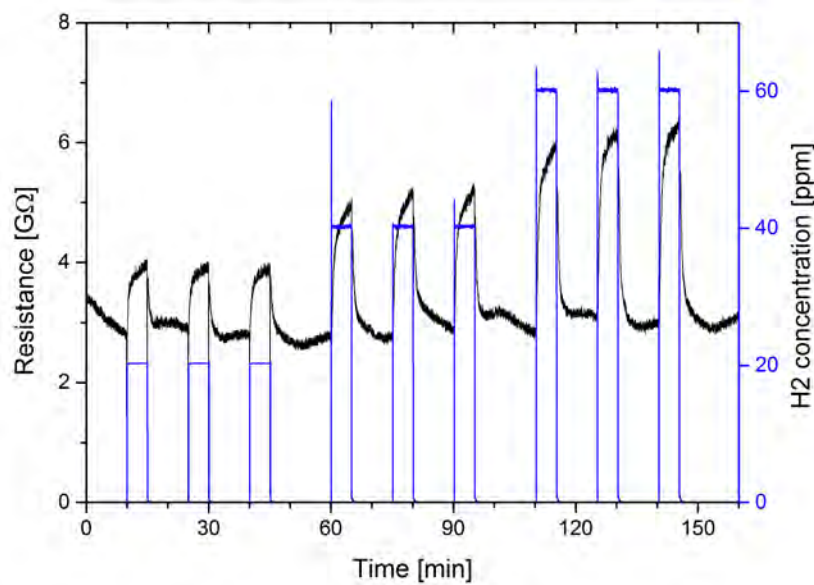
Figures 75a and 75b show the SnO₂ nanowire network, which has been grown with a similar technique developed in Section 2. Two SiO₂/Si substrates coated with a thin intermediate layer of Cu and a SnO₂ thin film are carefully glued on a substrate base separated by a gap of about 200 μm . After the heating process in Ar atmosphere at 900°C for 1.5 hour, ultralong SnO₂ nanowires are observed growing from one substrate to the other, bridging the gap between the two wafer pieces. An electrical contact is established between the two substrates, so the gas sensing properties of the SnO₂ nanowire network can be measured. The results for the detection of 20-60 ppm H₂ in humid synthetic air (60% relative humidity) at room temperature are shown in Figure 75c. In the presence of 20 ppm, 40 ppm and 60 ppm H₂, the resistance measured is changed by 30%, 45% and 50%, respectively. It is remarkable that such high responses are measured at room temperature. For single nanowire devices, no resistance change has been measured upon exposure to similar concentrations of H₂ at room temperature. The response observed for the nanowire network might be explained by the self-heating effect of the nanowires due to the current forced through the network. Also, the nanowire network is suspended between the

two substrates, so each nanowire is completely surrounded by the ambient gas molecules. Curiously, the resistance is increased in the presence of H_2 , which is the opposite behaviour compared to single nanowire devices. The reason for the inverted signal is not clear. Since the temperature at the surface of the SnO_2 nanowires is not known, it is very difficult to understand the reactions responsible for the resistance change especially in the presence of humidity.



(a)

(b)



(c)

Figure 75: (a) and (b) SEM images of the SnO_2 nanowire network grown between two substrates separated by a distance of about $200 \mu m$. (c) Detection of 20-60 ppm H_2 in humid synthetic air (60% rH) at room temperature.

5.2 Towards selective nanowire sensors: functionalization of SnO₂ nanowires with metallic nanoparticles

In this work, the sensitivity of the SnO₂ nanowire sensors upon exposure to CO, H₂ and H₂S has been demonstrated. However, selectivity is an issue, which has not been addressed. Research groups in the gas sensing field invest much effort into building sensor arrays with different metal oxide materials or into the functionalization of the sensors with metallic nanoparticles in order to differentiate the gas species.

The joint work of AIT and the University of Freiburg in Germany in the framework of the “NanoSmart” project aimed at the functionalization of SnO₂ thin films and single SnO₂ nanowire devices with metallic and bimetallic nanoparticles. The results of the influence of the nanoparticles on the response to 50 ppm CO in humid synthetic air (35% relative humidity) at 300°C are shown in Figure 76. The response for a bare SnO₂ nanowire is 16% (response reported in Figure 62). With the presence of Pd nanoparticles at the surface of the SnO₂ nanowire, the response reaches 50%. The influence of Au nanoparticles is even higher with a response of 70%. The functionalization of the SnO₂ nanowire with bimetallic nanoparticles of Pd_{0.7}Au_{0.3} results in a response of 40%. The nanoparticles act as catalyst for the chemical reactions between the gas molecules and the surface of the SnO₂ nanowires.

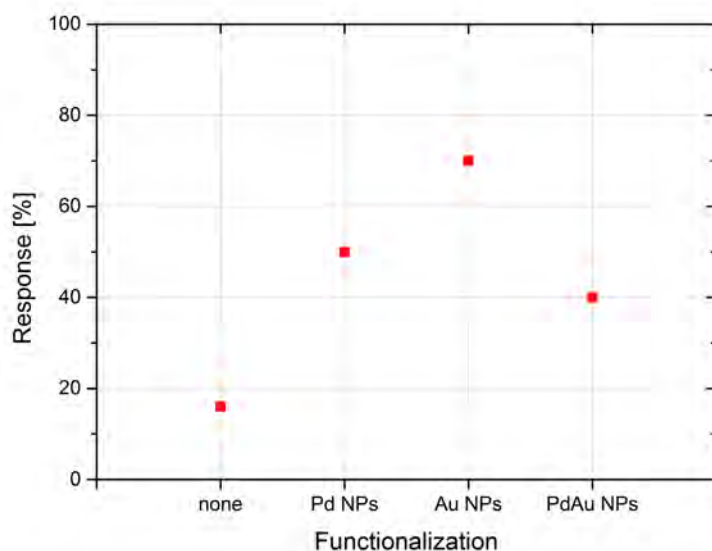
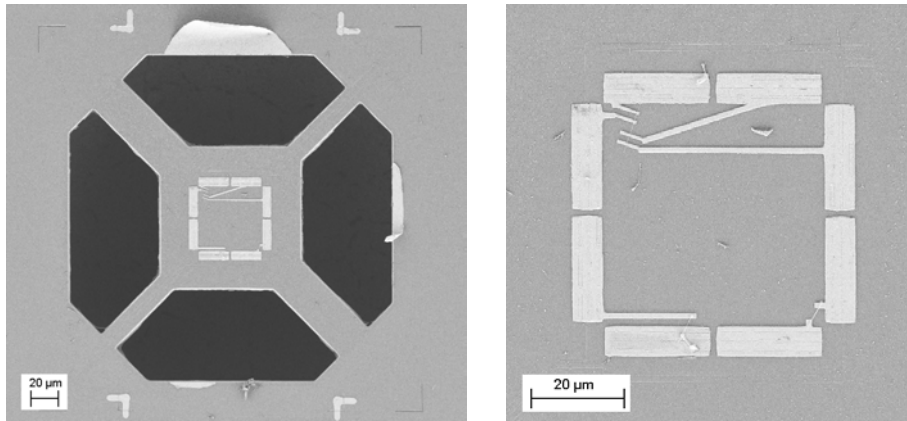


Figure 76: Comparison of the response of single SnO₂ nanowires functionalized with metallic nanoparticles to 50 ppm CO in dry synthetic air at 300°C.

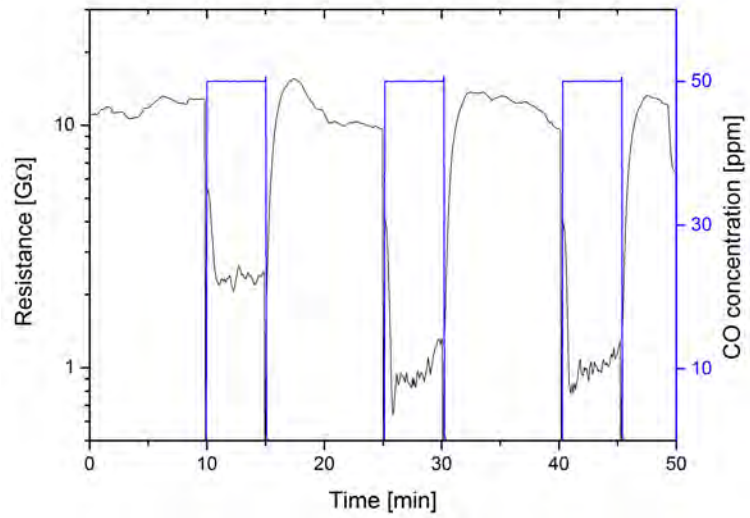
5.3 Towards CMOS integrated nanowire sensors: processing of nanowire sensor on a microhotplate

The miniaturization of the available commercial gas sensors and their integration with CMOS technology in order to produce gas sensors for the mass consumer market is a main industrial challenge. In order to reduce the power consumption, the use of microhotplates, which enables the local heating of the sensing area, spreads out. In the framework of the COCOA project (CATRENE platform), a microhotplate has been designed in a joint work between AIT and FOTEC Forschungs- und Technologietransfer GmbH. The production has been conducted by ams AG. Figure 77a shows an overview of the fully released $100\ \mu\text{m} \times 100\ \mu\text{m}$ plate connected to the rest of the silicon chip by 4 suspension arms. An e-beam lithography process has been developed to contact single SnO_2 nanowires directly on the microhotplate, as shown in Figure 77b. The response of a SnO_2 nanowire to 90 ppm CO in dry synthetic air at about 365°C is reported in Figure 77c. The resistance change measured is 80% for the first pulse and 90% for the next two pulses. Those results demonstrate the successful integration of single SnO_2 nanowire gas sensor on CMOS processed microhotplates.



(a)

(b)



(c)

Figure 77: (a) SEM image of the fully released microhotplate connected to the rest of the silicon chip by 4 suspension arms. (b) SEM image of the SnO₂ nanowires contacted by e-beam lithography. (c) Response of a single SnO₂ nanowire to 50 ppm CO in dry synthetic air with the microhotplate operated at about 365°C.

Conclusion and outlook

Technological improvements on gas sensors regarding the sensing performances, the miniaturization and the reduction of the power consumption of the devices will enable their commercialization on the consumer market for diverse applications including personal safety and environmental monitoring. The issues of miniaturization and reduction of the power consumption are currently investigated via integration of metal oxide films with CMOS technology. Concerning improvements of the gas sensing performances, the scientific community is currently exploring the capabilities of metal oxide nanowires. The final objective will probably involve the integration of metal oxide nanowires with CMOS technology to combine the advantages of both technologies and produce smart gas sensors for daily-life applications.

The objective of this thesis is the fabrication of SnO₂ nanowire gas sensors. The related technological challenges are addressed and the feasibility of the integration of SnO₂ nanowire sensors on CMOS processed chips is shortly discussed as outlook. The focus is set on the detection of three gas species: carbon monoxide (CO), hydrogen (H₂) and hydrogen sulfide (H₂S). The detection of CO and H₂S, which are toxic gases with permissible exposure limit (PEL) of 35 ppm and 10 ppm, respectively, is used for safety devices. H₂ is an explosive gas with a lower explosive level (LEL) of 4%, but the detection of lower concentrations of H₂ is necessary for leak detection from hydrogen-powered cars and fueling stations.

The sensing principle of SnO₂ nanowire gas sensors is mainly described in the literature by the ionosorption model. The term ionosorption refers to the chemisorption of gas species on the surface of the SnO₂ nanowire combined with a charge transfer occurring between the adsorbate and the SnO₂ nanowire. The ionosorbed molecules at the surface of the SnO₂ nanowire create a space charge layer near the surface resulting in a band bending effect and induce changes in the electrical conductivity of the nanowire. Ionosorption is an activated process requiring high temperatures. In ambient atmosphere at temperatures above 150°C, oxygen species ionosorb on the SnO₂ surface as O₂⁻ or O⁻, so electrons from the conduction band of the SnO₂ nanowire are trapped. The gas species to detect (e.g. CO, H₂) react with the ionosorbed oxygen and electrons are released back into the conduction band of the SnO₂ nanowire, so the electrical resistance is decreased.

The synthesis of SnO₂ nanowires by vapor phase growth takes place in a furnace at 900°C in argon atmosphere on a CuO/Cu or Au coated substrate, which is stacked face down with a distance of about 500 μm above the bottom Si substrate coated with a SnO₂ thin film deposited by spray pyrolysis. The growth mechanism proposed involves the reducing effect of the bottom Si substrate on the SnO₂ thin film resulting in the formation of gaseous SnO, which is transported through the gas phase and recrystallizes as SnO₂

nanowires on the CuO/Cu or Au surface of the top substrate. Though the catalytic effect of Au on the growth of SnO₂ nanowires is often reported in the literature, only few studies have reported the catalytic role of CuO or Cu₂O for the growth of SnO₂ zigzag nanobelts. SnO₂ zigzag nanowires have also been successfully synthesized in this thesis on a Cu coated substrate in reducing conditions, where the argon flow has been replaced by a forming gas (95% N₂ + 5% H₂) flow.

This synthesis method is not quite as straightforward as other growth methods based on thermal evaporation reported in the literature, because the starting material is a SnO₂ thin film deposited by spray pyrolysis, while other methods start from commercially available powders of Sn, SnO or SnO₂. However, thanks to the effort made for the development of a reproducible spray pyrolysis process, this additional step is simple and fast. Moreover, since the process parameters have been optimized to deposit a SnO₂ thin film at a temperature of 400°C, spray pyrolysis enables the direct integration of a SnO₂ thin film sensor on a CMOS processed chip [7, 208]. The other parameters of the nanowire growth process (temperature and time) are similar to the ones reported in the literature. Besides, it has been shown that the local growth of SnO₂ nanowires can be controlled by the patterning of the CuO/Cu film. This property may be used to grow a network of SnO₂ nanowires between two CuO/Cu structures for the on-chip fabrication of a sensor. This fabrication method has already been reported in the case of a nanowire growth catalyzed by Au [209].

For the fabrication of single nanowire gas sensors, the SnO₂ nanowires are transferred from the growth substrate to a bare SiO₂/Si substrate by dispersion in isopropanol using ultrasonication and spin-coating of the solution. The nanowires are statistically dispersed on the surface. After a lithography step, the metallic contacts are deposited by thermal evaporation on top of the nanowires and a final lift-off process results in the patterning of the contacts. Two processes have been developed: the optical lithography and the electron-beam lithography.

The technological challenges for the fabrication of single nanowire sensors include the establishment of ohmic contacts. Therefore, several materials (Al, Sn/Au, Cr/Au, Ti/Au and Au) have been investigated as metal contact and the optical lithography process has been used in order to contact a large number of individual SnO₂ nanowires in a 2-point configuration on the same chip, so statistical results can be obtained. The I-V characteristics of single nanowires have been measured at 200°C before and after annealing and the percentage of linear I-V has been calculated. It has been shown that Al contacts are damaged after an annealing step at 400°C for 5 minutes. This is most probably due to the oxidation of the Al layer. The highest ratio of ohmic contacts is obtained with Sn/Au. However, the contacts degrade after only a few hours at temperatures above 300°C. This degradation has

been attributed to the formation of rather isolated grains in the contact layer probably caused by the melting of the Sn layer. In comparison, the Au, Cr/Au and Ti/Au contacts are more stable at high temperature. Cr/Au yields a slightly lower ratio of linear I-V characteristics than Au and Ti/Au. Although the values of the nanowire resistance measured with Ti/Au are widely distributed (100 kOhm - 10 GOhm), lower values are obtained than with Au and Cr/Au (mostly in the range 10 MOhm - 10 GOhm). Since it has been reported in the literature that the contact resistance increases with increasing values of the nanowire resistance [180], it is assumed that the contact resistance is lowered by contacting the nanowires with Ti/Au, so this material has been further used for contacting the nanowires. However, the contact resistance could not be measured and compared for the different samples because the nanowires were contacted in a 2-point configuration.

The development of the electron-beam lithography process has enabled to contact a few individual SnO₂ nanowires with Ti/Au in a 4-point configuration, so the contact resistance and the conductivity of the SnO₂ nanowires have been calculated. It results that when measuring SnO₂ nanowires in a 2-point configuration at 200°C, 30% to 60% of the resistance measured comes from the contact resistance and the rest from the nanowire itself. Those values are high and emphasize the importance of measuring nanowires in a 4-point configuration.

By comparing both lithography processes, it can be pointed out that the ratio of ohmic devices is much higher on the sample processed with optical lithography (80%) than on the sample processed with e-beam lithography (30%). This suggests that the e-beam lithography process can be improved. Particularly the annealing conditions of the metal contact post processing shall be further investigated. Besides, the conductivity of the SnO₂ nanowire is smaller on the sample processed with e-beam lithography. This difference may be explained by the influence of the electron beam on the intrinsic properties of the SnO₂ nanowires as suggested in [181].

The sensing performances of six single SnO₂ nanowire sensors have been investigated for the detection of CO, H₂ and H₂S in different concentration ranges at temperatures between 150°C and 350°C in humid or in dry conditions. CO has been detected in the range 10-90 ppm at 300°C with a response of 13-31% in dry synthetic air and 10-18% in humid synthetic air. The best results obtained for the detection of 10-90 ppm H₂ are 20-45% in dry synthetic air and 13-32% in humid synthetic air at 300°C. The response of the nanowire sensors saturates for concentrations of CO and H₂ above 50 ppm in humid synthetic air. For the detection of 10 ppm H₂ in humid synthetic air, the operating temperature has been reduced from 250°C to 150°C without altering the sensor response. The nanowire sensors are highly sensitive to H₂S. A response of 15% has been measured for a H₂S concentration as low as 100 ppb. Moreover, the sensor response to H₂S is not influenced by

changes of humidity, which is of great advantage for practical applications.

A single nanowire sensor has been extensively measured in the presence of CO, in nitrogen and in synthetic air, in dry and in humid conditions in order to better understand the reactions taking place at the SnO₂ nanowire surface. It results that the reaction of CO with ionosorbed oxygen has a higher reaction rate than the reaction of CO with lattice oxygen. Besides, the response to CO in humid atmosphere is lower than in dry atmosphere. This is probably due to the competition between CO and H₂O molecules for occupying the adsorption sites. This result can also be related to the number of ionosorbed oxygen species, which is lower in humid atmosphere than in dry atmosphere. The measured response to CO of two nanowire sensors located on the same sample is higher for the nanowire sensor with a smaller diameter. The use of nanowires with diameters smaller or of the order of the depletion layer is known to improve the sensor sensitivity.

A nanowire sensor based on a suspended network of SnO₂ nanowires between two substrates has also been fabricated. The nanowire network sensor exhibits responses in the range 30%-50% for the detection of 20-60 ppm H₂ in humid synthetic air at room temperature. Since, no resistance change has been measured upon exposure to similar concentrations of H₂ at room temperature for single nanowire devices, it is assumed that the nanowires of the network are heated by self-heating effect due to the current forced through the network. The higher sensitivity of the nanowire network is also probably related to its unique configuration, where the suspended nanowires are completely surrounded by the ambient gas molecules. Besides, an inverted signal (increase of resistance) has been measured with the nanowire network sensor upon exposure to H₂. Since the temperature at the surface of the SnO₂ nanowires is not known, it is very difficult to understand the reactions responsible for the increase of resistance measured additionally in the presence of humidity. However, this configuration is very promising and shall be further investigated.

In order to address the issue of selectivity of the SnO₂ nanowire gas sensors, the joint work of AIT and the University of Freiburg in Germany in the frame of the "NanoSmart" project aimed at the functionalization of SnO₂ thin films and single SnO₂ nanowire devices with metallic and bimetallic nanoparticles, which act as catalyst for the chemical reactions between the gas molecules and the surface of the SnO₂ nanowires. The results show higher responses for the functionalized nanowire sensors than for the bare nanowire sensor upon exposure to 50 ppm CO in humid synthetic air at 300°C. The catalytic effect of Au nanoparticles for the detection of CO is higher than the one of Pd and PdAu nanoparticles. It is concluded that the sensitivity of the SnO₂ nanowire sensors can be increased by the functionalization with metallic nanoparticles. Further measurements shall be conducted with other target gas species to study the cross-sensitivity of the

functionalized nanowire sensors in order to conclude if the metallic nanoparticles contribute to the selective detection of a certain gas.

In the framework of the COCOA project (CATRENE platform), a microhotplate has been designed in a joint work between AIT and FOTEC Forschungs- und Technologietransfer GmbH in order to reduce the power consumption of the devices. The production has been conducted by ams AG. An e-beam lithography process has been developed to contact single SnO₂ nanowires directly on the microhotplate (100 μm × 100 μm). Afterwards, the microhotplate has been fully released connected to the rest of the silicon chip by 4 suspension arms. The response of a single SnO₂ nanowire sensor to 90 ppm CO in dry synthetic air at about 365°C is 80-90%. This integration solution requires an e-beam lithography process to be sure to obtain a single SnO₂ nanowire contacted on the microhotplate. An optical lithography process using a photomask with a defined geometry may also be used to contact statistically distributed nanowires on the microhotplate. In that case, it is best to increase the density of nanowires dispersed on the chip and to use interdigitated electrodes to contact at least one nanowire on the microhotplate.

In this thesis, the conditions for the growth of SnO₂ nanowires have been optimized, the fabrication process of single SnO₂ nanowire sensors has been developed, the influence of the contact material on the ohmic behavior of the contacts has been investigated, the electrical characterization of the nanowires has been realized and the gas sensing properties of the single SnO₂ nanowire sensors have been characterized upon exposure to CO, H₂ and H₂S. Preliminary results of nanowire sensors based on a suspended network of SnO₂ nanowires and on single nanowire sensors functionalized with metallic nanoparticles have also been presented. Finally, the integration of a single SnO₂ nanowire gas sensor on a suspended microhotplate processed with CMOS technology has been successfully demonstrated and discussed as outlook. This last result is a first step towards the integration of SnO₂ nanowire gas sensors with CMOS technology, which will potentially result in the realization of smart gas sensors implemented in personal computers and smart phones for daily-life applications.

Glossary

AAO	Anodic Aluminium Oxide
ALD	Atomic Layer Deposition
BSE	Backscattered Electron Detector
CMOS	Complementary Metal-Oxide-Semiconductor
CNT	Carbon Nanotube
CVD	Chemical Vapour Deposition
EDS	Energy-Dispersive X-ray Spectroscopy
EELS	Electron Energy Loss Spectroscopy
EPR	Electron Paramagnetic Resonance
FFT	Fast Fourier Transform
FIB	Focused Ion Beam
HAADF	High-Angle Annular Dark-Field
HVAC	Heating, Ventilation and Air Conditioning
IR	Infrared Spectroscopy
ITO	Indium Doped Tin Oxide
LEL	Lower Explosive Limit
MFC	Mass Flow Controller
NW	Nanowire
PAN	Polyacrylonitrile
PEALD	Plasma-Enhanced Atomic Layer Deposition
PEL	Permissible Exposure Limit
PLD	Pulsed Laser Deposition
PVD	Physical Vapour Deposition
rH	Relative Humidity
RF	Radio Frequency
RIE	Reactive Ion Etching
RT	Room Temperature
SE	Secondary Electron Detector
SEM	Scanning Electronic Microscope
SMU	Source Measure Unit
TCO	Transparent Conducting Oxide
TEM	Transmission Electronic Microscope
TPD	Temperature Programmed Desorption
UHV	Ultra High Vacuum
VLS	Vapor Liquid Solid growth
VOC	Volatile Organic Compound
VS	Vapor Solid growth
XPS	X-Ray Photoelectron Spectroscopy
XRD	X-Ray Diffraction
YSZ	Yttria-Stabilized Zirconia

References

- [1] S. T. Omaye, “Metabolic modulation of carbon monoxide toxicity,” *Toxicology*, vol. 180, no. 2, pp. 139–150, 2002.
- [2] M. Mysen, S. Berntsen, P. Nafstad, and P. G. Schild, “Occupancy density and benefits of demand-controlled ventilation in Norwegian primary schools,” *Energy and Buildings*, vol. 37, pp. 1234–1240, Dec. 2005.
- [3] J. W. Gardner, P. K. Guha, F. Udrea, and J. A. Covington, “CMOS Interfacing for Integrated Gas Sensors : A Review,” *IEEE Sensors Journal*, vol. 10, no. 12, pp. 1833–1848, 2010.
- [4] P. Yang, R. Yan, and M. Fardy, “Semiconductor nanowire: what’s next?,” *Nano letters*, vol. 10, pp. 1529–36, May 2010.
- [5] N. S. Ramgir, Y. Yang, and M. Zacharias, “Nanowire-based sensors,” *Small*, vol. 6, pp. 1705–22, Aug. 2010.
- [6] X. Chen, C. K. Wong, C. a. Yuan, and G. Zhang, “Nanowire-based gas sensors,” *Sensors and Actuators B: Chemical*, vol. 177, pp. 178–195, Feb. 2013.
- [7] Y. Cui, Q. Wei, H. Park, and C. M. Lieber, “Nanowire nanosensors for highly sensitive and selective detection of biological and chemical species,” *Science*, vol. 293, pp. 1289–92, Aug. 2001.
- [8] A. Kolmakov and M. Moskovits, “Chemical Sensing and Catalysis By One-Dimensional Metal-Oxide Nanostructures,” *Annual Review of Materials Research*, vol. 34, pp. 151–180, Aug. 2004.
- [9] V. Sysoev, T. Schneider, J. Goschnick, I. Kiselev, W. Habicht, H. Hahn, E. Strelcov, and a. Kolmakov, “Percolating SnO₂ nanowire network as a stable gas sensor: Direct comparison of long-term performance versus SnO₂ nanoparticle films,” *Sensors and Actuators B: Chemical*, vol. 139, pp. 699–703, June 2009.
- [10] F. Hernandez-Ramirez, a. Tarancon, O. Casals, E. Pellicer, J. Rodriguez, a. Romano-Rodriguez, J. Morante, S. Barth, and S. Mathur, “Electrical properties of individual tin oxide nanowires contacted to platinum electrodes,” *Physical Review B*, vol. 76, p. 085429, Aug. 2007.
- [11] S. Santra, S. Z. Ali, P. K. Guha, P. Hiralal, H. E. Unalan, S. H. Dalal, J. a. Covington, W. I. Milne, J. W. Gardner, F. Udrea, M. Pardo, and G. Sberveglieri, “CMOS Alcohol Sensor Employing ZnO Nanowire Sensing Films,” in *AIP Conference Proceedings*, pp. 119–122, Aip, 2009.

- [12] S. Steinhauer, E. Brunet, T. Maier, G. Mutinati, A. Köck, O. Freudenberg, C. Gspan, W. Grogger, A. Neuhold, and R. Resel, “Gas sensing properties of novel CuO nanowire devices,” *Sensors and Actuators B: Chemical*, vol. 187, pp. 50–57, Oct. 2013.
- [13] T. Seiyama, A. Kato, K. Fujiishi, and M. Nagatani, “A new detector for gaseous components using semiconductive thin films,” *Analytical Chemistry*, vol. 34, pp. 1502–1503, 1962.
- [14] FIGARO Engineering Inc., “History of the company.” <http://www.figaro.co.jp/en/company/history.html>. [Jan. 30, 2014].
- [15] E. Comini, G. Faglia, and G. Sberveglieri, eds., *Solid State Gas Sensing*. Springer, 2009.
- [16] D. K. Aswal and S. K. Gupta, eds., *Science and Technology of Chemiresistor Gas Sensors*. Nova Science Publishers, 2007.
- [17] X. Liu, S. Cheng, H. Liu, S. Hu, D. Zhang, and H. Ning, “A survey on gas sensing technology,” *Sensors*, vol. 12, pp. 9635–65, Jan. 2012.
- [18] G. Korotcenkov, S. D. Han, and J. R. Stetter, “Review of electrochemical hydrogen sensors,” *Chemical reviews*, vol. 109, pp. 1402–33, Mar. 2009.
- [19] C. Hagleitner, D. Lange, A. Hierlemann, O. Brand, and H. Baltes, “CMOS Single-Chip Gas Detection System Comprising Capacitive, Calorimetric and Mass-Sensitive Microsensors,” *IEEE Journal of Solid-State Circuits*, vol. 37, no. 12, pp. 1867–1878, 2002.
- [20] J. Kong, N. R. Franklin, C. Zhou, M. G. Chapline, S. Peng, K. Cho, and H. Dai, “Nanotube Molecular Wires as Chemical Sensors,” *Science*, vol. 287, pp. 622–625, Jan. 2000.
- [21] K. H. An, S. Y. Jeong, H. R. Hwang, and Y. H. Lee, “Enhanced Sensitivity of a Gas Sensor Incorporating Single-Walled Carbon Nanotube-Polypyrrole Nanocomposites,” *Advanced Materials*, vol. 16, pp. 1005–1009, June 2004.
- [22] F. Schedin, a. K. Geim, S. V. Morozov, E. W. Hill, P. Blake, M. I. Katsnelson, and K. S. Novoselov, “Detection of individual gas molecules adsorbed on graphene,” *Nature materials*, vol. 6, pp. 652–655, Sept. 2007.
- [23] H. Y. Jeong, D.-S. Lee, H. K. Choi, D. H. Lee, J.-E. Kim, J. Y. Lee, W. J. Lee, S. O. Kim, and S.-Y. Choi, “Flexible room-temperature NO₂ gas sensors based on carbon nanotubes/reduced graphene hybrid films,” *Applied Physics Letters*, vol. 96, p. 213105, 2010.

- [24] H. J. Yoon, D. H. Jun, J. H. Yang, Z. Zhou, S. S. Yang, and M. M.-C. Cheng, "Carbon dioxide gas sensor using a graphene sheet," *Sensors and Actuators B: Chemical*, vol. 157, pp. 310–313, Sept. 2011.
- [25] M. Batzill and U. Diebold, "The surface and materials science of tin oxide," *Progress in Surface Science*, vol. 79, no. 2-4, pp. 47–154, 2005.
- [26] E. Strelcov, S. Dmitriev, B. Button, J. Cothren, V. Sysoev, and A. Kolmakov, "Evidence of the self-heating effect on surface reactivity and gas sensing of metal oxide nanowire chemiresistors.," *Nanotechnology*, vol. 19, p. 355502, Sept. 2008.
- [27] D. C. Meier, S. Semancik, B. Button, E. Strelcov, and A. Kolmakov, "Coupling nanowire chemiresistors with MEMS microhotplate gas sensing platforms," *Applied Physics Letters*, vol. 91, no. 6, p. 063118, 2007.
- [28] F. Hernandez Ramirez, A. Tarancon, O. Casals, J. Arbiol, A. Romano Rodriguez, and J. Morante, "High response and stability in CO and humidity measures using a single SnO₂ nanowire," *Sensors and Actuators B: Chemical*, vol. 121, pp. 3–17, Jan. 2007.
- [29] L. Qian, K. Wang, Y. Li, H. Fang, Q. Lu, and X. Ma, "CO sensor based on Au-decorated SnO₂ nanobelt," *Materials Chemistry and Physics*, vol. 100, pp. 82–84, Nov. 2006.
- [30] E. Comini, G. Faglia, G. Sberveglieri, Z. Pan, and Z. L. Wang, "Stable and highly sensitive gas sensors based on semiconducting oxide nanobelts," *Applied Physics Letters*, vol. 81, no. 10, p. 1869, 2002.
- [31] E. Comini, G. Faglia, G. Sberveglieri, D. Calestani, L. Zanotti, and M. Zha, "Tin oxide nanobelts electrical and sensing properties," *Sensors and Actuators B: Chemical*, vol. 111-112, pp. 2–6, Nov. 2005.
- [32] K.-Y. Dong, J.-K. Choi, I.-S. Hwang, J.-W. Lee, B. H. Kang, D.-J. Ham, J.-H. Lee, and B.-K. Ju, "Enhanced H₂S sensing characteristics of Pt doped SnO₂ nanofibers sensors with micro heater," *Sensors and Actuators B: Chemical*, vol. 157, pp. 154–161, Sept. 2011.
- [33] Z. Ying, Q. Wan, Z. T. Song, and S. L. Feng, "SnO₂ nanowhiskers and their ethanol sensing characteristics," *Nanotechnology*, vol. 15, pp. 1682–1684, Nov. 2004.
- [34] G. Sberveglieri, C. Baratto, E. Comini, G. Faglia, M. Ferroni, a. Ponzoni, and a. Vomiero, "Synthesis and characterization of semiconducting nanowires for gas sensing," *Sensors and Actuators B: Chemical*, vol. 121, pp. 208–213, Jan. 2007.

- [35] N. Barsan and U. Weimar, “Understanding the fundamental principles of metal oxide based gas sensors; the example of CO sensing with SnO₂ sensors in the presence of humidity,” *Journal of Physics: Condensed Matter*, vol. 15, pp. 813–839, 2003.
- [36] A. Gurlo, “Insights into the Mechanism of Gas Sensor Operation,” in *Metal Oxide Nanomaterials for Chemical Sensors* (M. A. Carpenter, A. Kolmakov, and S. Mathur, eds.), Springer, integrated ed., 2013.
- [37] N. Barsan and U. D. O. Weimar, “Conduction Model of Metal Oxide Gas Sensors,” *Journal of Electroceramics*, vol. 7, pp. 143–167, 2001.
- [38] A. Gurlo, N. Barsan, and U. Weimar, “Gas sensors based on semiconducting metal oxides,” in *Metal Oxides Chemistry and Applications* (J. L. G. Fierro, ed.), pp. 683–738, Taylor & Francis Group, 2006.
- [39] H. Ogawa, “Hall measurement studies and an electrical conduction model of tin oxide ultrafine particle films,” *Journal of Applied Physics*, vol. 53, no. 6, p. 4448, 1982.
- [40] M. Tonezzer and N. Hieu, “Size-dependent response of single-nanowire gas sensors,” *Sensors and Actuators B: Chemical*, vol. 163, pp. 146–152, Mar. 2012.
- [41] S. I. Rembeza, E. S. Rembeza, T. V. Svistova, and O. I. Borsiakova, “Electrical Resistivity and Gas Response Mechanisms of Nanocrystalline SnO₂ Films in a Wide Temperature Range,” *Physica Status Solidi (A)*, vol. 179, no. 1, pp. 147–152, 2000.
- [42] A. Gurlo, “Interplay between O₂ and SnO₂: oxygen ionosorption and spectroscopic evidence for adsorbed oxygen,” *ChemPhysChem*, vol. 7, pp. 2041–52, Oct. 2006.
- [43] N. Yamazoe, J. Fuchigami, M. Kishikawa, and T. Seiyama, “Interactions of tin oxide surface with O₂, H₂O and H₂,” *Surface Science*, vol. 86, pp. 335–344, 1979.
- [44] T. G. G. Maffei, G. T. Owen, M. W. Penny, T. K. H. Starke, S. A. Clark, H. Ferkel, and S. P. Wilks, “Nano-crystalline SnO₂ gas sensor response to O₂ and CH₄ at elevated temperature investigated by XPS,” *Surface Science*, vol. 520, pp. 29–34, 2002.
- [45] S. Samson, “Defect structure and electronic donor levels in stannic oxide crystals,” *Journal of Applied Physics*, vol. 44, no. 10, p. 4618, 1973.
- [46] Y. Li-Zi, S. Zhi-Tong, and W. Chan-Zheng, “A thermodynamic study of tin oxides by coulometric titration,” *Journal of Solid State Chemistry*, vol. 113, pp. 221–224, 1994.

- [47] J. Maier and W. Göpel, “Investigations of the Bulk Defect Chemistry of Polycrystalline Tin(IV) Oxide,” *Journal of Solid State Chemistry*, vol. 72, pp. 293–302, 1988.
- [48] ASM International, *ASM Handbook Volume 3: Alloy Phase Diagrams*. ASM International, 1992.
- [49] J. C. Platteeuw and G. Meyer, “The system tin + oxygen,” *Transactions of the Faraday Society*, vol. 52, pp. 1066–1073, 1956.
- [50] F. Lawson, “Tin Oxide - Sn_3O_4 ,” *Nature*, vol. 215, p. 955, 1967.
- [51] L. Gmelin, *Gmelin Handbuch der anorganischen Chemie. Band 46=Sn, Zinn, Teil C1: Verbindungen mit Wasserstoff, Sauerstoff, Stickstoff und Halogenen*. verlag che ed., 1972.
- [52] M. O. Orlandi, E. R. Leite, R. Aguiar, J. Bettini, and E. Longo, “Growth of SnO nanobelts and dendrites by a self-catalytic VLS process,” *The journal of physical chemistry B*, vol. 110, pp. 6621–5, Apr. 2006.
- [53] E. Comini, C. Baratto, G. Faglia, M. Ferroni, a. Vomiero, and G. Sberveglieri, “Quasi-one dimensional metal oxide semiconductors: Preparation, characterization and application as chemical sensors,” *Progress in Materials Science*, vol. 54, pp. 1–67, Jan. 2009.
- [54] A. Wolfsteller, N. Geyer, T.-K. Nguyen-Duc, P. Das Kanungo, N. Zakharov, M. Reiche, W. Erfurth, H. Blumtritt, S. Kalem, P. Werner, and U. Gösele, “Comparison of the top-down and bottom-up approach to fabricate nanowire-based silicon/germanium heterostructures,” *Thin Solid Films*, vol. 518, pp. 2555–2561, Feb. 2010.
- [55] X.-L. Han, G. Larrieu, E. Dubois, and F. Cristiano, “Carrier injection at silicide/silicon interfaces in nanowire based-nanocontacts,” *Surface Science*, vol. 606, pp. 836–839, May 2012.
- [56] Y. Sun, R. a. Graff, M. S. Strano, and J. a. Rogers, “Top-down fabrication of semiconductor nanowires with alternating structures along their longitudinal and transverse axes,” *Small*, vol. 1, pp. 1052–7, Nov. 2005.
- [57] N. V. Hieu, L. T. N. Loan, N. D. Khoang, N. T. Minh, D. T. Viet, D. C. Minh, T. Trung, and N. D. Chien, “A facile thermal evaporation route for large-area synthesis of tin oxide nanowires: Characterizations and their use for liquid petroleum gas sensor,” *Current Applied Physics*, vol. 10, pp. 636–641, Mar. 2010.

- [58] L. Tien, S. Pearton, D. Norton, and F. Ren, "Synthesis and characterization of single crystalline SnO₂ nanorods by high-pressure pulsed laser deposition," *Applied Physics A*, vol. 91, pp. 29–32, Jan. 2008.
- [59] T. Yanagida, A. Marcu, H. Matsui, K. Nagashima, K. Oka, K. Yokota, M. Taniguchi, and T. Kawai, "Enhancement of Oxide VLS Growth by Carbon on Substrate Surface," *Journal of Physical Chemistry C*, vol. 112, pp. 18923–18926, Nov. 2008.
- [60] A. Klamchuen, T. Yanagida, M. Kanai, K. Nagashima, K. Oka, T. Kawai, M. Suzuki, Y. Hidaka, and S. Kai, "Impurity induced periodic mesostructures in Sb-doped SnO₂ nanowires," *Journal of Crystal Growth*, vol. 312, pp. 3251–3256, Oct. 2010.
- [61] A. Klamchuen, T. Yanagida, M. Kanai, K. Nagashima, K. Oka, S. Seki, M. Suzuki, Y. Hidaka, S. Kai, and T. Kawai, "Dopant homogeneity and transport properties of impurity-doped oxide nanowires," *Applied Physics Letters*, vol. 98, no. 5, p. 053107, 2011.
- [62] S. Mathur, S. Barth, H. Shen, J.-C. Pyun, and U. Werner, "Size-dependent photoconductance in SnO₂ nanowires," *Small*, vol. 1, pp. 713–7, July 2005.
- [63] R. Müller, F. Hernandez-Ramirez, H. Shen, H. Du, W. Mader, and S. Mathur, "Influence of Precursor Chemistry on Morphology and Composition of CVD-Grown SnO₂ Nanowires," *Chemistry of Materials*, vol. 24, pp. 4028–4035, 2012.
- [64] S. Gubbala, V. Chakrapani, V. Kumar, and M. K. Sunkara, "Band-Edge Engineered Hybrid Structures for Dye-Sensitized Solar Cells Based on SnO₂ Nanowires," *Advanced Functional Materials*, vol. 18, pp. 2411–2418, Aug. 2008.
- [65] Y. Shen, T. Yamazaki, Z. Liu, D. Meng, T. Kikuta, N. Nakatani, M. Saito, and M. Mori, "Microstructure and H₂ gas sensing properties of undoped and Pd-doped SnO₂ nanowires," *Sensors and Actuators B: Chemical*, vol. 135, pp. 524–529, Jan. 2009.
- [66] S.-W. Choi, S.-H. Jung, and S. S. Kim, "Significant enhancement of the NO₂ sensing capability in networked SnO₂ nanowires by Au nanoparticles synthesized via γ -ray radiolysis," *Journal of hazardous materials*, vol. 193, pp. 243–8, Oct. 2011.
- [67] L. Li, J. Huang, T. Wang, H. Zhang, Y. Liu, and J. Li, "An excellent enzyme biosensor based on Sb-doped SnO₂ nanowires," *Biosensors & bioelectronics*, vol. 25, pp. 2436–41, July 2010.

- [68] S. H. Luo, Q. Wan, W. L. Liu, M. Zhang, Z. F. Di, S. Y. Wang, Z. T. Song, C. L. Lin, and J. Y. Dai, "Vacuum electron field emission from SnO₂ nanowhiskers synthesized by thermal evaporation," *Nanotechnology*, vol. 15, pp. 1424–1427, Nov. 2004.
- [69] Q. Wan, E. Dattoli, and W. Lu, "Doping-dependent electrical characteristics of SnO₂ nanowires.," *Small*, vol. 4, pp. 451–4, Apr. 2008.
- [70] J. H. He, T. H. Wu, C. L. Hsin, K. M. Li, L. J. Chen, Y. L. Chueh, L. J. Chou, and Z. L. Wang, "Beaklike SnO₂ nanorods with strong photoluminescent and field-emission properties.," *Small*, vol. 2, pp. 116–20, Jan. 2006.
- [71] J.-M. Wu, "Characterizing and comparing the cathodoluminescence and field emission properties of Sb doped SnO₂ and SnO₂ nanowires," *Thin Solid Films*, vol. 517, pp. 1289–1293, Dec. 2008.
- [72] J. Yoon, K. W. Min, J. Kim, G. T. Kim, and J. S. Ha, "p-n heterojunction diode arrays of p-type single walled carbon nanotubes and aligned n-type SnO₂ nanowires.," *Nanotechnology*, vol. 23, p. 265301, July 2012.
- [73] I.-S. Hwang, Y.-S. Kim, S.-J. Kim, B.-K. Ju, and J.-H. Lee, "A facile fabrication of semiconductor nanowires gas sensor using PDMS patterning and solution deposition," *Sensors and Actuators B: Chemical*, vol. 136, pp. 224–229, Feb. 2009.
- [74] L. V. Thong, N. D. Hoa, D. T. T. Le, D. T. Viet, P. D. Tam, A.-T. Le, and N. V. Hieu, "On-chip fabrication of SnO₂-nanowire gas sensor: The effect of growth time on sensor performance," *Sensors and Actuators B: Chemical*, vol. 146, pp. 361–367, Apr. 2010.
- [75] V. Kumar, S. Sen, K. Muthe, N. Gaur, S. Gupta, and J. Yakhmi, "Copper doped SnO₂ nanowires as highly sensitive H₂S gas sensor," *Sensors and Actuators B: Chemical*, vol. 138, pp. 587–590, May 2009.
- [76] S. Sun, G. Meng, Y. Wang, T. Gao, M. Zhang, Y. Tian, X. Peng, and L. Zhang, "Large-scale synthesis of SnO₂ nanobelts," *Applied Physics A: Materials Science & Processing*, vol. 76, pp. 287–289, Feb. 2003.
- [77] Y. Chen, X. Cui, K. Zhang, D. Pan, S. Zhang, B. Wang, and J. Hou, "Bulk-quantity synthesis and self-catalytic VLS growth of SnO₂ nanowires by lower-temperature evaporation," *Chemical Physics Letters*, vol. 369, pp. 16–20, Feb. 2003.
- [78] Y. Lilach, J.-P. Zhang, M. Moskovits, and A. Kolmakov, "Encoding morphology in oxide nanostructures during their growth.," *Nano letters*, vol. 5, pp. 2019–22, Oct. 2005.

- [79] Z. W. Pan, Z. R. Dai, and Z. L. Wang, "Nanobelts of Semiconducting Oxides," *Science*, vol. 291, pp. 1947–1949, 2001.
- [80] L. V. Thong, L. T. N. Loan, and N. Van Hieu, "Comparative study of gas sensor performance of SnO₂ nanowires and their hierarchical nanostructures," *Sensors and Actuators B: Chemical*, vol. 150, pp. 112–119, Sept. 2010.
- [81] Z. R. Dai, J. L. Gole, J. D. Stout, and Z. L. Wang, "Tin Oxide Nanowires, Nanoribbons, and Nanotubes," *The Journal of Physical Chemistry B*, vol. 106, pp. 1274–1279, Feb. 2002.
- [82] M.-S. Park, G.-X. Wang, Y.-M. Kang, D. Wexler, S.-X. Dou, and H.-K. Liu, "Preparation and Electrochemical Properties of SnO₂ Nanowires for Application in Lithium-Ion Batteries," *Angewandte Chemie*, vol. 119, pp. 764–767, Jan. 2007.
- [83] A. Kar, M. a. Stroschio, M. Dutta, J. Kumari, and M. Meyyappan, "Growth and properties of tin oxide nanowires and the effect of annealing conditions," *Semiconductor Science and Technology*, vol. 25, p. 024012, Feb. 2010.
- [84] J.-S. Lee, S.-K. Sim, B. Min, K. Cho, S. W. Kim, and S. Kim, "Structural and optoelectronic properties of SnO₂ nanowires synthesized from ball-milled SnO₂ powders," *Journal of Crystal Growth*, vol. 267, pp. 145–149, June 2004.
- [85] P. Li, M. Lei, X. Wang, and W. Tang, "Large-scale SnO₂ nanowires synthesized by direct sublimation method and their enhanced dielectric responses," *Materials Letters*, vol. 63, pp. 357–359, Feb. 2009.
- [86] N. V. Hieu, H.-R. Kim, B.-K. Ju, and J.-H. Lee, "Enhanced performance of SnO₂ nanowires ethanol sensor by functionalizing with La₂O₃," *Sensors and Actuators B: Chemical*, vol. 133, pp. 228–234, July 2008.
- [87] A. Fort, M. Mugnaini, S. Rocchi, V. Vignoli, E. Comini, G. Faglia, and A. Ponzoni, "Metal-oxide nanowire sensors for CO detection: Characterization and modeling," *Sensors and Actuators B: Chemical*, vol. 148, pp. 283–291, June 2010.
- [88] J. Wang, D. Liu, X. Yan, H. Yuan, L. Ci, Z. Zhou, Y. Gao, L. Song, L. Liu, W. Zhou, G. Wang, and S. Xie, "Growth of SnO₂ nanowires with uniform branched structures," *Solid State Communications*, vol. 130, pp. 89–94, Apr. 2004.

- [89] B. Wang, L. F. Zhu, Y. H. Yang, N. S. Xu, and G. W. Yang, "Fabrication of a SnO₂ Nanowire Gas Sensor and Sensor Performance for Hydrogen," *Journal of Physical Chemistry C*, vol. 112, no. 17, pp. 6643–6647, 2008.
- [90] J. Yan, A. Sumboja, E. Khoo, and P. S. Lee, "V₂O₅ loaded on SnO₂ nanowires for high-rate Li ion batteries.," *Advanced materials*, vol. 23, pp. 746–50, Feb. 2011.
- [91] R. S. Wagner and W. C. Ellis, "Vapor-Liquid-Solid Mechanism of Single Crystal Growth," *Applied Physics Letters*, vol. 4, no. 5, p. 89, 1964.
- [92] Y. Wu and P. Yang, "Direct Observation of Vapor-Liquid-Solid Nanowire Growth," *Journal of American Chemical Society*, vol. 123, no. 13, pp. 3165–3166, 2001.
- [93] M. S. Moreno, R. C. Mercader, and A. G. Bibiloni, "Study of intermediate oxides in SnO thermal decomposition," *Journal of Physics: Condensed Matter*, vol. 4, pp. 351–355, 1992.
- [94] J. Huang, N. Matsunaga, K. Shimano, N. Yamazoe, and T. Kunitake, "Nanotubular SnO₂ Templated by Cellulose Fibers: Synthesis and Gas Sensing," *Chemistry of Materials*, vol. 17, no. 13, pp. 3513–3518, 2005.
- [95] W. Zhu, W. Wang, H. Xu, and J. Shi, "Fabrication of ordered SnO₂ nanotube arrays via a template route," *Materials Chemistry and Physics*, vol. 99, pp. 127–130, 2006.
- [96] Y. Wang, J. Y. Lee, and H. C. Zeng, "Polycrystalline SnO₂ Nanotubes Prepared via Infiltration Casting of Nanocrystallites and Their Electrochemical Application," *Chemistry of Materials*, vol. 17, no. 15, pp. 3899–3903, 2005.
- [97] A. Kolmakov, Y. Zhang, G. Cheng, and M. Moskovits, "Detection of CO and O₂ Using Tin Oxide Nanowire Sensors," *Advanced Materials*, vol. 15, pp. 997–1000, June 2003.
- [98] N. Wang, X. Cao, and L. Guo, "Facile One-Pot Solution Phase Synthesis of SnO₂ Nanotubes," *Journal of Physical Chemistry C*, vol. 112, no. 33, pp. 12616–12622, 2008.
- [99] Y. Wang, X. Jiang, and Y. Xia, "A solution-phase, precursor route to polycrystalline SnO₂ nanowires that can be used for gas sensing under ambient conditions.," *Journal of the American Chemical Society*, vol. 125, pp. 16176–7, Dec. 2003.

- [100] C. Ye, X. Fang, Y. Wang, T. Xie, A. Zhao, and L. Zhang, "Novel Synthesis of Tin Dioxide Nanoribbons via a Mild Solution Approach," *Chemistry Letters*, vol. 33, no. 1, pp. 54–55, 2004.
- [101] B. Cheng, J. M. Russell, W. Shi, L. Zhang, and E. T. Samulski, "Large-Scale, solution-phase growth of single-crystalline SnO₂ nanorods.," *Journal of the American Chemical Society*, vol. 126, pp. 5972–3, May 2004.
- [102] L. Vayssieres and M. Graetzel, "Highly Ordered SnO₂ Nanorod Arrays from Controlled Aqueous Growth," *Angewandte Chemie*, vol. 116, pp. 3752–3756, July 2004.
- [103] S. Shi, Y. Liu, Y. Chen, J. Zhang, Y. Wang, and T. Wang, "Ultrahigh ethanol response of SnO₂ nanorods at low working temperature arising from La₂O₃ loading," *Sensors and Actuators B: Chemical*, vol. 140, pp. 426–431, July 2009.
- [104] G. Xi and J. Ye, "Ultrathin SnO₂ nanorods: template- and surfactant-free solution phase synthesis, growth mechanism, optical, gas-sensing, and surface adsorption properties.," *Inorganic chemistry*, vol. 49, pp. 2302–9, Mar. 2010.
- [105] L. Qin, J. Xu, X. Dong, Q. Pan, Z. Cheng, Q. Xiang, and F. Li, "The template-free synthesis of square-shaped SnO₂ nanowires: the temperature effect and acetone gas sensors.," *Nanotechnology*, vol. 19, p. 185705, May 2008.
- [106] O. Lupan, L. Chow, G. Chai, a. Schulte, S. Park, and H. Heinrich, "A rapid hydrothermal synthesis of rutile SnO₂ nanowires," *Materials Science and Engineering: B*, vol. 157, pp. 101–104, Feb. 2009.
- [107] D.-F. Zhang, L.-D. Sun, J.-L. Yin, and C.-H. Yan, "Low-Temperature Fabrication of Highly Crystalline SnO₂ Nanorods," *Advanced Materials*, vol. 15, pp. 1022–1025, June 2003.
- [108] D. Li, J. T. McCann, Y. Xia, and M. Marquez, "Electrospinning: A Simple and Versatile Technique for Producing Ceramic Nanofibers and Nanotubes," *Journal of the American Ceramic Society*, vol. 89, pp. 1861–1869, June 2006.
- [109] D.-J. Yang, I. Kamienchick, D. Y. Youn, A. Rothschild, and I.-D. Kim, "Ultrasensitive and Highly Selective Gas Sensors Based on Electrospun SnO₂ Nanofibers Modified by Pd Loading," *Advanced Functional Materials*, vol. 20, pp. 4258–4264, Dec. 2010.

- [110] Q. Qi, T. Zhang, L. Liu, and X. Zheng, "Synthesis and toluene sensing properties of SnO₂ nanofibers," *Sensors and Actuators B: Chemical*, vol. 137, pp. 471–475, Apr. 2009.
- [111] J.-K. Choi, I.-S. Hwang, S.-J. Kim, J.-S. Park, S.-S. Park, U. Jeong, Y. C. Kang, and J.-H. Lee, "Design of selective gas sensors using electrospun Pd-doped SnO₂ hollow nanofibers," *Sensors and Actuators B: Chemical*, vol. 150, pp. 191–199, Sept. 2010.
- [112] W.-S. Kim, B.-S. Lee, D.-H. Kim, H.-C. Kim, W.-R. Yu, and S.-H. Hong, "SnO₂ nanotubes fabricated using electrospinning and atomic layer deposition and their gas sensing performance," *Nanotechnology*, vol. 21, p. 245605, June 2010.
- [113] Y. Liu, C. Zheng, W. Wang, C. Yin, and G. Wang, "Synthesis and Characterization of Rutile SnO₂ Nanorods," *Advanced Materials*, vol. 13, no. 24, pp. 1883–1887, 2001.
- [114] W. Wang, C. Xu, X. Wang, Y. Liu, Y. Zhan, C. Zheng, F. Song, and G. Wang, "Preparation of SnO₂ nanorods by annealing SnO₂ powder in NaCl flux," *Journal of Materials Chemistry*, vol. 12, pp. 1922–1925, May 2002.
- [115] C. Xu, X. Zhao, S. Liu, and G. Wang, "Large-scale synthesis of rutile SnO₂ nanorods," *Solid State Communications*, vol. 125, pp. 301–304, 2003.
- [116] Y. Wang and J. Y. Lee, "Molten Salt Synthesis of Tin Oxide Nanorods: Morphological and Electrochemical Features," *The Journal of Physical Chemistry B*, vol. 108, pp. 17832–17837, Nov. 2004.
- [117] D. Wang, X. Chu, and M. Gong, "Gas-sensing properties of sensors based on single-crystalline SnO₂ nanorods prepared by a simple molten-salt method," *Sensors and Actuators B: Chemical*, vol. 117, pp. 183–187, Sept. 2006.
- [118] R. Chamberlin and J. S. Skarman, "Chemical spray deposition process for inorganic films," *Journal of the Electrochemical Society*, vol. 113, no. 1, pp. 86–89, 1966.
- [119] E. Benamar, M. Rami, C. Messaoudi, D. Sayah, and a. Ennaoui, "Structural, optical and electrical properties of indium tin oxide thin films prepared by spray pyrolysis," *Solar Energy Materials and Solar Cells*, vol. 56, pp. 125–139, Jan. 1999.
- [120] P. S. Patil, S. B. Nikam, and L. D. Kadam, "Influence of substrate temperature on properties of sprayed WO₃ thin films," *Materials Chemistry and Physics*, vol. 69, pp. 77–83, 2001.

- [121] M. D. Blesic, Z. V. Saponjic, J. M. Nedeljkovic, and D. P. Uskokovic, "TiO₂ films prepared by ultrasonic spray pyrolysis of nanosize precursor," *Materials Letters*, vol. 54, pp. 298–302, 2002.
- [122] R. Todorovska, N. Petrova, and D. Todorovsky, "Spray pyrolysis deposition of YSZ and YSZ-Pt composite films," *Applied Surface Science*, vol. 252, pp. 1266–1275, Dec. 2005.
- [123] D. Perednis, O. Wilhelm, S. Pratsinis, and L. Gauckler, "Morphology and deposition of thin yttria-stabilized zirconia films using spray pyrolysis," *Thin Solid Films*, vol. 474, pp. 84–95, Mar. 2005.
- [124] F. Paraguay, W. L. Estrada, D. R. N. Acosta, E. Andrade, and M. Miki-yoshida, "Growth, structure and optical characterization of high quality ZnO thin films obtained by spray pyrolysis," *Thin Solid Films*, vol. 350, pp. 192–202, 1999.
- [125] W. Siefert, "Properties of thin In₂O₃ and SnO₂ films prepared by corona spray pyrolysis and a discussion of the spray pyrolysis process," *Thin Solid Films*, vol. 121, pp. 275–282, 1984.
- [126] G. Korotcenkov, "In₂O₃ films deposited by spray pyrolysis: gas response to reducing (CO, H₂) gases," *Sensors and Actuators B: Chemical*, vol. 98, pp. 122–129, Mar. 2004.
- [127] J. Sanz Maudes and T. Rodriguez, "Sprayed SnO₂ films: growth mechanism and film structure characterization," *Thin Solid Films*, vol. 69, pp. 183–189, 1980.
- [128] W. M. Sears and M. A. Gee, "Mechanics of film formation during the spray pyrolysis of tin oxide," *Thin Solid Films*, vol. 165, pp. 265–277, 1988.
- [129] G. Sanon, R. Rup, and A. Mansingh, "Growth and characterization of tin oxide films prepared by chemical vapour deposition," *Thin Solid Films*, vol. 190, pp. 287–301, 1990.
- [130] L. Bruno, C. Pijolat, and R. Lalauze, "Tin dioxide thin-film gas sensor prepared by chemical vapour deposition - Influence of grain size and thickness on the electrical properties," *Sensors and Actuators B: Chemical*, vol. 18-19, pp. 195–199, 1994.
- [131] H. Gourari, M. Lumbreras, R. Van Landschoot, and J. Schoonman, "Elaboration and characterization of SnO₂ - Mn₂O₃ thin layers prepared by electrostatic spray deposition," *Sensors and Actuators B: Chemical*, vol. 47, pp. 189–193, 1998.

- [132] G. S. Korotchenkov, S. V. Dmitriev, and V. I. Brynzari, "Processes development for low cost and low power consuming SnO₂ thin film gas sensors (TFGS)," *Sensors and Actuators B: Chemical*, vol. 54, pp. 202–209, 1999.
- [133] A. Nakaruk and C. C. Sorrell, "Conceptual model for spray pyrolysis mechanism: fabrication and annealing of titania thin films," *Journal of Coatings Technology and Research*, vol. 7, pp. 665–676, May 2010.
- [134] A. R. Barron, "Chemical Vapor Deposition," 2009.
- [135] P. S. Patil, "Versatility of chemical spray pyrolysis technique," *Materials Chemistry and Physics*, vol. 59, pp. 185–198, June 1999.
- [136] D. Briand, M. Labeau, J. F. Currie, and G. Delabouglise, "Pd-doped SnO₂ thin films deposited by assisted ultrasonic spraying CVD for gas sensing : selectivity and effect of annealing," *Sensors and Actuators B: Chemical*, vol. 48, pp. 395–402, 1998.
- [137] C. H. Chen, A. A. J. Buysman, E. M. Kelder, and J. Schoonman, "Fabrication of LiCoO₂ thin film cathodes for rechargeable lithium battery by electrostatic spray pyrolysis," *Solid State Ionics*, vol. 80, pp. 1–4, 1995.
- [138] J. C. Vigié and J. Spitz, "Chemical Vapor Deposition at Low Temperatures," *Journal of Electrochemical Society*, vol. 122, pp. 585–588, 1975.
- [139] V. Brinzari, G. Korotcenkov, V. Golovanov, J. Schwank, V. Lantto, and S. Saukko, "Morphological rank of nano-scale tin dioxide films deposited by spray pyrolysis from SnCl₄ · 5 H₂O water solution," *Thin Solid Films*, vol. 408, pp. 51–58, 2002.
- [140] G. Korotcenkov, V. Brinzari, J. Schwank, M. Dibattista, and A. Vasiliev, "Peculiarities of SnO₂ thin film deposition by spray pyrolysis for gas sensor application," *Sensors and Actuators B: Chemical*, vol. 77, pp. 244–252, 2001.
- [141] A. Tischner, T. Maier, C. Stepper, and A. Köck, "Ultrathin SnO₂ gas sensors fabricated by spray pyrolysis for the detection of humidity and carbon monoxide," *Sensors and Actuators B: Chemical*, vol. 134, pp. 796–802, Sept. 2008.
- [142] D. Perednis and L. J. Gauckler, "Thin Film Deposition Using Spray Pyrolysis," *Journal of Electroceramics*, vol. 14, pp. 103–111, Mar. 2005.

- [143] M. Fujimoto, T. Urano, S. Murai, and Y. Nishi, "Microstructure and X-Ray Study of Preferentially Oriented SnO₂ Thin Film Prepared by Pyrohydrolytic Decomposition," *Japanese Journal of Applied Physics*, vol. 28, no. 12, p. 2587, 1989.
- [144] V. Vasu and A. Subrahmanyam, "Physical properties of sprayed SnO₂ films," *Thin Solid Films*, vol. 202, pp. 283–288, 1991.
- [145] M. Miki-Yoshida and E. Andrade, "Growth and structure of tin dioxide thin films obtained by an improved spray pyrohydrolysis technique," *Thin Solid Films*, vol. 224, pp. 87–96, 1993.
- [146] H. Pink, L. Treitinger, and L. Vite, "Preparation of Fast Detecting SnO₂ Gas Sensors," *Japanese Journal of Applied Science*, vol. 19, no. 3, p. 513, 1980.
- [147] I. Yagi, K. Kakizawa, K. Murakami, and S. Kaneko, "Preferred Orientation of SnO₂ Thin Films Grown from Tri-n-Butyltin Acetate by Spray Pyrolysis Technique," *Journal of the Ceramic Society of Japan*, vol. 102, pp. 296–298, 1994.
- [148] K. Murakami, I. Yagi, and S. Kaneko, "Oriented Growth of Tin Oxide Thin Films on Glass Substrates by Spray Pyrolysis of Organotin Compounds," *Journal of the American Ceramic Society*, vol. 79, no. 10, pp. 2557–262, 1996.
- [149] M. Okuya, S. Kaneko, K. Hiroshima, I. Yagi, and K. Murakami, "Low temperature deposition of SnO₂ thin films as transparent electrodes by spray pyrolysis of tetrabutyltin(IV)," *Journal of the European Ceramic Society*, vol. 21, pp. 2099–2102, 2001.
- [150] EV Group (EVG), "Homepage." <http://www.evgroup.com/en/about/>. [Apr. 26, 2013].
- [151] Spraying Systems Co., "Homepage." <http://www.spray.com/>. [Apr. 26, 2013].
- [152] Spraying Systems Co., "Section G: Automatic Spray Nozzles." http://www.spray.com/cat70m/cat70mpdf/ssco.cat70m_g.pdf. [Feb. 21, 2013].
- [153] Harry Gestigkeit GmbH, "High Temperature Titan Hotplate Prazitherm." <http://www.gestigkeit.de/14/english/Products.html>. [Apr. 26, 2013].
- [154] G. C. Mutinati, *3D-CMOS Integrable Gas Sensor Device Based on Nanocrystalline Tin Dioxide Films*. PhD thesis, Vienna University of Technology, 2013.

- [155] A. Köck, A. Tischner, T. Maier, M. Kast, C. Edtmaier, C. Gspan, and G. Kothleitner, “Atmospheric pressure fabrication of SnO₂-nanowires for highly sensitive CO and CH₄ detection,” *Sensors and Actuators B: Chemical*, vol. 138, pp. 160–167, Apr. 2009.
- [156] A. Zima, *Development of highly sensitive nano-gassensors based on nanocrystalline tin dioxide thin films and single-crystalline tin dioxide nanowires*. PhD thesis, Vienna University of Technology, 2009.
- [157] GERO Hochtemperaturofen GmbH Co. KG, “Standard Tube Furnace up to 1200°C.” <http://www.gero-gmbh.de/pdfs/rohroefen/gero-rohrofen-sr.pdf>. [Mar. 18, 2013].
- [158] H. F. Kunkle and E. E. Kohnke, “Flux Growth of Stannic Oxide Crystals,” *Journal of Applied Physics*, vol. 36, no. 4, p. 1489, 1965.
- [159] Z. Fang, K. Tang, J. Shen, G. Shen, and Q. Yang, “Epitaxy of Single-Crystalline Zigzag Tin Dioxide Nanobelts,” *Crystal Growth & Design*, vol. 7, pp. 2254–2257, Nov. 2007.
- [160] J. Wu, K. Yu, L. Li, J. Xu, D. Shang, Y. Xu, and Z. Zhu, “Controlable synthesis and field emission properties of SnO₂ zigzag nanobelts,” *Journal of Physics D: Applied Physics*, vol. 41, p. 185302, Sept. 2008.
- [161] L. Li, K. Yu, J. Wu, Y. Wang, and Z. Zhu, “Structure and humidity sensing properties of SnO₂ zigzag belts,” *Crystal Research and Technology*, vol. 45, pp. 539–544, May 2010.
- [162] J. Duan, S. Yang, H. Liu, J. Gong, H. Huang, X. Zhao, R. Zhang, and Y. Du, “Single crystal SnO₂ zigzag nanobelts,” *Journal of the American Chemical Society*, vol. 127, pp. 6180–6181, May 2005.
- [163] J. Duan, J. Gong, H. Huang, X. Zhao, G. Cheng, Z.-Z. Yu, and S. Yang, “Multiform structures of SnO₂ nanobelts,” *Nanotechnology*, vol. 18, p. 055607, Feb. 2007.
- [164] L. Huang, L. Pu, Y. Shi, R. Zhang, B. Gu, Y. Du, and S. Wright, “Controlled growth of well-faceted zigzag tin oxide mesostructures,” *Applied Physics Letters*, vol. 87, no. 16, p. 163124, 2005.
- [165] FIGARO Engineering Inc., “Data sheet TGS 2444 for the detection of Ammonia.” http://www.figaro.co.jp/en/product/docs/tgs2444_product_infomation_rev02.pdf. [Oct. 24, 2013].
- [166] Henan Hanwei Electronics CO. LTD, “Technical data MQ-7 gas sensor.” <https://www.sparkfun.com/datasheets/Sensors/Biometric/MQ-7.pdf>. [Jan. 24, 2014].

- [167] F. Léonard and a. Talin, “Size-Dependent Effects on Electrical Contacts to Nanotubes and Nanowires,” *Physical Review Letters*, vol. 97, p. 026804, July 2006.
- [168] F. Léonard and a. A. Talin, “Electrical contacts to one- and two-dimensional nanomaterials.,” *Nature nanotechnology*, vol. 6, pp. 773–83, Dec. 2011.
- [169] H. Park, R. Beresford, R. Ha, H.-J. Choi, H. Shin, and J. Xu, “Evaluation of metal-nanowire electrical contacts by measuring contact end resistance.,” *Nanotechnology*, vol. 23, p. 245201, July 2012.
- [170] V. V. Sysoev, B. K. Button, K. Wepsiec, S. Dmitriev, and A. Kolmakov, “Toward the nanoscopic ”electronic nose”: hydrogen vs carbon monoxide discrimination with an array of individual metal oxide nano- and mesowire sensors.,” *Nano letters*, vol. 6, pp. 1584–8, Aug. 2006.
- [171] Y. Cheng, R. Yang, J.-P. Zheng, Z. L. Wang, and P. Xiong, “Characterizing individual SnO₂ nanobelt field-effect transistors and their intrinsic responses to hydrogen and ambient gases,” *Materials Chemistry and Physics*, vol. 137, pp. 372–380, Nov. 2012.
- [172] N. Barsan, M. Schweizer-berberich, and W. Gopel, “Fundamental and practical aspects in the design of nanoscaled SnO₂ gas sensors: a status report,” *Fresenius’ Journal of Analytical Chemistry*, vol. 365, no. 4, pp. 287–304, 1999.
- [173] Agilent Technologies Inc., “Precision Semiconductor Parameter Analyzer.” <http://www.home.agilent.com/en/pd-153517-pn-4156C/precision-semiconductor-parameter-analyzer>. [Oct. 24, 2013].
- [174] A. Serventi, D. Rickerby, M. Horrillo, and R. Saint-Jacques, “Transmission electron microscopy investigation of the effect of deposition conditions and a platinum layer in gas-sensitive r.f.-sputtered SnO₂ films,” *Thin Solid Films*, vol. 445, pp. 38–47, Nov. 2003.
- [175] H. B. Michaelson, “The work function of the elements and its periodicity,” *Journal of Applied Physics*, vol. 48, no. 11, p. 4729, 1977.
- [176] C. Mead, “Metal-semiconductor surface barriers,” *Solid-State Electronics*, vol. 9, pp. 1023–1033, Nov. 1966.
- [177] W. E. Spicer, P. W. Chye, P. R. Skeath, C. Y. Su, and I. Lindau, “New and unified model for Schottky barrier and III-V insulator interface states formation,” *Journal of Vacuum Science and Technology*, vol. 16, p. 1422, Sept. 1979.

- [178] L. J. Brillson, “The structure and properties of metal-semiconductor interfaces,” *Surface Science Reports*, vol. 2, pp. 123–326, 1982.
- [179] L. J. Brillson and Y. Lu, “ZnO Schottky barriers and Ohmic contacts,” *Journal of Applied Physics*, vol. 109, no. 12, p. 121301, 2011.
- [180] E. Stern, G. Cheng, M. P. Young, and M. a. Reed, “Specific contact resistivity of nanowire devices,” *Applied Physics Letters*, vol. 88, no. 5, p. 053106, 2006.
- [181] E. Stern, G. Cheng, J. F. Klemic, E. Broomfield, D. Turner-Evans, C. Li, C. Zhou, and M. a. Reed, “Methods for fabricating Ohmic contacts to nanowires and nanotubes,” *Journal of Vacuum Science & Technology B: Microelectronics and Nanometer Structures*, vol. 24, no. 1, p. 231, 2006.
- [182] M. S. Arnold, P. Avouris, Z. W. Pan, and Z. L. Wang, “Field-Effect Transistors Based on Single Semiconducting Oxide Nanobelts,” *The Journal of Physical Chemistry B*, vol. 107, pp. 659–663, Jan. 2003.
- [183] V. E. Henrich and P. A. Cox, *The Surface Science of Metal Oxides*. cambridge ed., 1994.
- [184] S. Chang, “Oxygen chemisorption on tin oxide: Correlation between electrical conductivity and EPR measurements,” *Journal of Vacuum Science and Technology*, vol. 17, p. 366, Jan. 1980.
- [185] T. Sahm, A. Gurlo, N. Bârsan, and U. Weimar, “Basics of oxygen and SnO₂ interaction; work function change and conductivity measurements,” *Sensors and Actuators B: Chemical*, vol. 118, pp. 78–83, Oct. 2006.
- [186] T. Kawabe, S. Shimomura, T. Karasuda, K. Tabata, E. Suzuki, and Y. Yamaguchi, “Photoemission study of dissociatively adsorbed methane on a pre-oxidized SnO₂ thin film,” *Surface Science*, vol. 448, pp. 101–107, 2000.
- [187] E. W. Thornton and P. G. Harrison, “Tin oxide surfaces. Part 1. - Surface hydroxyl groups and the chemisorption of carbon dioxide and carbon monoxide on tin(IV) oxide,” *Journal of the Chemical Society, Faraday Transactions 2, Molecular and Chemical Physics*, vol. 71, pp. 461–472, 1975.
- [188] S. Emiroglu, N. Barsan, U. Weimar, and V. Hoffmann, “In situ diffuse reflectance infrared spectroscopy study of CO adsorption on SnO₂,” *Thin Solid Films*, vol. 391, pp. 176–185, 2001.

- [189] M. Caldararu, D. Sprinceana, V. T. Popa, and N. I. Ionescu, "Surface dynamics in tin dioxide-containing catalysts II. Competition between water and oxygen adsorption on polycrystalline tin dioxide," *Sensors and Actuators B: Chemical*, vol. 30, no. 1, pp. 35–41, 1996.
- [190] J. F. McAleer, P. T. Moseley, J. O. W. Norris, D. E. Williams, and B. C. Tofield, "Tin dioxide gas sensors. Part 1: Aspects of the surface chemistry revealed by electrical conductance variations," *Journal of Chemical Society, Faraday Transactions*, vol. 1, no. 83, pp. 1323–1346, 1987.
- [191] G. Heiland and D. Kohl, *Chemical Sensor Technology vol. 1*. Tokyo: Kodansha, 1988.
- [192] S. R. Morrison, "Semiconductor gas sensors," *Sensors and Actuators*, vol. 2, pp. 329–341, 1982.
- [193] V. A. Gercher and D. F. Cox, "Water adsorption on stoichiometric and defective SnO₂ (110) surfaces," *Surface Science*, vol. 322, pp. 177–184, 1995.
- [194] S. Hahn, N. Bârsan, U. Weimar, S. Ejakov, J. Visser, and R. Soltis, "CO sensing with SnO₂ thick film sensors: role of oxygen and water vapour," *Thin Solid Films*, vol. 436, pp. 17–24, July 2003.
- [195] D. Kohl, "Surface processes in the detection of reducing gases with SnO₂-based devices," *Sensors and Actuators*, vol. 18, no. 1, pp. 71–113, 1989.
- [196] V. Malyshev and A. V. Pislyakov, "Investigation of gas-sensitivity of sensor structures to hydrogen in a wide range of temperature, concentration and humidity of gas medium," *Sensors and Actuators B: Chemical*, vol. 134, pp. 913–921, Sept. 2008.
- [197] V. Malyshev and A. Pislyakov, "SnO₂-based thick-film-resistive sensor for H₂S detection in the concentration range of 1-10 mg.m⁻³," *Sensors and Actuators B: Chemical*, vol. 47, pp. 181–188, 1998.
- [198] Bronkhorst High-Tech BV, "Mass flow meters & controllers for gas." http://www.bronkhorst.com/en/products/gas_flow_meters_and_controllers/. [Oct. 24, 2013].
- [199] Kobold Messring GmbH, "Humidity/Temperature Measuring Instrument." http://www.sensor.si/data/pdf_kobold/A2/a2gb_afk-e.pdf. [Oct. 24, 2013].
- [200] Linde Gas GmbH, "Produktdatenblatt Stickstoff 5.0." http://produkte.linde-gas.at/datenblatt/stickstoff_5.0.pdf. [Feb. 11, 2014].

- [201] Linde Gas GmbH, “Produktdatenblatt Synthetische Luft KW-frei.” http://produkte.linde-gas.at/datenblatt/n2o2_kw-frei_0,20_o2_n2.pdf. [Feb. 11, 2014].
- [202] Keithley Instruments Inc., “Homepage.” <http://www.keithley.com/>. [Oct. 24, 2013].
- [203] Agilent Technologies Inc., “Multimeter Data Sheet.” <http://cp.literature.agilent.com/litweb/pdf/5968-0162EN.pdf>. [Oct. 24, 2013].
- [204] W. Schmid, N. Bârsan, and U. Weimar, “Sensing of hydrocarbons and CO in low oxygen conditions with tin dioxide sensors: possible conversion paths,” *Sensors and Actuators B: Chemical*, vol. 103, pp. 362–368, Sept. 2004.
- [205] B. Kamp, R. Merkle, R. Lauck, and J. Maier, “Chemical diffusion of oxygen in tin dioxide: Effects of dopants and oxygen partial pressure,” *Journal of Solid State Chemistry*, vol. 178, pp. 3027–3039, Oct. 2005.
- [206] F. Hernandez-Ramirez, S. Barth, a. Tarancon, O. Casals, E. Pellicer, J. Rodriguez, a. Romano-Rodriguez, J. R. Morante, and S. Mathur, “Water vapor detection with individual tin oxide nanowires,” *Nanotechnology*, vol. 18, p. 424016, Oct. 2007.
- [207] G. Mutinati, E. Brunet, S. Steinhauer, A. Köck, J. Teva, J. Kraft, J. Siegert, F. Schrank, and E. Bertagnolli, “CMOS-integrable Ultrathin SnO₂ Layer for Smart Gas Sensor Devices,” *Procedia Engineering*, vol. 47, pp. 490–493, Jan. 2012.
- [208] L. Filipovic, S. Selberherr, G. Mutinati, E. Brunet, S. Steinhauer, A. Köck, J. Teva, J. Kraft, J. Siegert, F. Schrank, C. Gspan, and W. Grogger, “Modeling the Growth of Tin Dioxide using Spray Pyrolysis Deposition for Gas Sensor Applications,” *IEEE Transactions on Semiconductor Manufacturing*, vol. PP, no. 99, pp. 1–1, 2014.
- [209] S.-W. Choi, S.-H. Jung, and S. S. Kim, “Functionalization of selectively grown networked SnO₂ nanowires with Pd nanodots by γ -ray radiolysis,” *Nanotechnology*, vol. 22, p. 225501, June 2011.

List of Figures

1	Schematic representation of a conductometric gas sensor . . .	11
2	Schematic representation of the band bending effect caused by the ionosorption of oxygen at the surface of an n-type semiconductor	16
3	Schematic representation of the gas sensing principle of SnO ₂ gas sensors according to the ionosorption model	17
4	Schematic representation of the gas sensing principle of SnO ₂ gas sensors according to the reduction-reoxidation model . . .	18
5	Crystal structure of the rutile SnO ₂	20
6	Sn-O phase diagrams	22
7	Schematic representation of the spray pyrolysis principle . . .	32
8	Mechanism of precursor decomposition depending on the substrate temperature and the initial droplet size	34
9	Description of the apparatus used for the spray pyrolysis process	40
10	Diagram of the automatic air atomizing nozzle	41
11	Dependence of the SnO ₂ film thickness with the spraying time.	43
12	Image showing the homogeneity of the spray pyrolysis process on nine chips	44
13	XRD pattern of the SnO ₂ thin film deposited by spray pyrolysis before and after annealing	45
14	XRD patterns measured between 350°C and 700°C for a SnO ₂ thin film deposited by spray pyrolysis	46
15	TEM image of the SnO ₂ thin film deposited by spray pyrolysis	47
16	XRD pattern of the oxidized Cu film after 10 min on the hotplate at 400°C.	48
17	Scheme of the position of the sample in the tube furnace. . .	49
18	Temperature measured at the substrate holder during the heating process for the nanowire growth.	50
19	Scheme showing the different assemblies of substrates for the growth of SnO ₂ nanowires	51
20	Schemes of the key experiments conducted to optimize the growth of SnO ₂ nanowires	53
21	SEM images of the top substrate before and after Experiment 1	54
22	SEM images of the SnO ₂ /Si bottom substrate of Experiment 1 after the heating process.	56

23	SEM images of each substrate of the assembly of Experiment 2 after the heating process	58
24	SEM images of the SnO ₂ surface of the middle substrate of Experiment 2 after the heating process	60
25	SEM image and respective EDS spectrum at the base of the nanowire	62
26	Elemental mapping of SnO ₂ nanowires grown on the top substrate of Experiment 2	64
27	SEM images of the SnO ₂ surface after the heating process of Experiment 3	66
28	SEM images of the SnO ₂ surface after the heating process of Experiment 4	68
29	SEM images of the substrates of Experiment 5 after the heating process	70
30	SEM images of the bottom SnO ₂ /Si surface of Experiment 6 after the heating process	71
31	SEM images of the nanowire growth on CuO structures after the heating process of Experiment 7	72
32	SEM images of the substrates of Experiment 8 after the heating process	74
33	SEM images of the Cr/Au top substrate of Experiment 9 after the heating process	75
34	Summary of the experimented configuration for the optimization of the SnO ₂ nanowire growth	77
35	SEM images showing the morphology of the SnO ₂ nanowires synthesized	78
36	High resolution TEM images and determination of the crystal growth direction.	79
37	Process flow for the fabrication of SnO ₂ nanowire sensors. . .	85
38	Photomask used to pattern the metal contacts	86
39	Description of the e-beam lithography process	87
40	SEM images of a SnO ₂ nanowire contacted with Sn/Au . . .	91
41	SEM images of a SnO ₂ nanowire contacted with Ti/Au and the corresponding I-V characteristics	92
42	SEM images of a SnO ₂ nanowire stacked between two Au layers	93
43	Comparison of the resistance values of SnO ₂ nanowires contacted with different metallic layers	94

44	Comparison of the metal work functions with the SnO ₂ electron affinity	95
45	Au-Sn phase diagram	96
46	Representation of the contact resistance in a 2-point measurement	98
47	Definition of 2-point and 4-point measurements	99
48	Comparison of I-V characteristics measured in a 2-point and in a 4-point configuration.	100
49	TEM image showing the cross-section of a SnO ₂ nanowire covered by a Ti/Au layer	103
50	Comparison of the interface metal-nanowire for two nanowires	104
51	Determination of the crystal orientation of two nanowires by diffraction	105
52	Schematic representation of the adsorption mechanisms of water on SnO ₂ surfaces	111
53	Schematic representation of the adsorption mechanism of CO in the presence of water on SnO ₂ surfaces	113
54	Mounting of the sensor chip for gas sensing measurements . .	115
55	Scheme of the gas measurement setup	117
56	Picture of the gas measurement setup	117
57	Definition of the response and recovery times.	118
58	Detection of O ₂ in dry and humid N ₂ atmosphere	122
59	Detection of CO in N ₂ and SA and influence of humidity . . .	124
60	Response of sensor A to CO in N ₂ and SA and influence of humidity	125
61	Repeatability of the detection of CO in N ₂	126
62	Response of sensor B1 to CO in SA	128
63	Detection of CO in SA and N ₂ by sensors C1 and C2	130
64	Response of sensors C1 and C2 to CO in SA and N ₂	131
65	Detection of H ₂ in SA by sensor D	133
66	Response of sensor D to increasing H ₂ concentrations in SA .	134
67	Detection of H ₂ in SA at 150°C in the presence of humidity by sensor D	135
68	Detection of increasing concentrations of H ₂ in SA by sensor B1	136

69	Response of sensors B1 and B2 to H ₂ in SA and influence of humidity	138
70	Detection of H ₂ S in SA and influence of humidity	140
71	Response of sensor A to H ₂ S in SA	141
72	Detection of H ₂ S in SA by sensor D	142
73	Dependence of the Debye length with the temperature for SnO ₂	148
74	Effect of the surface reactions on the width of the depletion layer of the SnO ₂ nanowire	149
75	Network of SnO ₂ nanowires for room temperature detection of H ₂	157
76	Effect of nanoparticles on the response to CO	158
77	Single SnO ₂ nanowire integrated on a CMOS processed microhotplate	160

List of Tables

1	Applications and corresponding target species of gas sensors.	10
2	Summary of the gas species detected by SnO ₂ nanowire and nanobelt sensors.	14
3	Synthesis conditions reported in the literature for the growth of SnO ₂ nanowires by thermal evaporation.	26
4	Preparation conditions for the deposition of SnO ₂ thin films by spray pyrolysis.	37
5	List of the samples prepared with different contact materials by optical lithography.	89
6	Comparison of the quality of different metallic contacts with SnO ₂ nanowires.	91
7	Contact resistance and conductivity of single nanowire devices	100
8	Properties of the two nanowires investigated by FIB-TEM. . .	102
9	Characteristics of the single SnO ₂ nanowire sensors	119
10	Summary of experimental conditions for the detection of CO, H ₂ and H ₂ S with the corresponding sensors investigated. . . .	120
11	Comparable gas sensor responses for the different nanowire sensors	143
12	Duration and time period of operation of the nanowire sensors.	151
13	Summary of the gas sensing results of the nanowire sensors - Part 1.	152
14	Summary of the gas sensing results of the nanowire sensors - Part 2.	153

List of own publications

Journal Papers

- [1] E. Brunet, T. Maier, G. Mutinati, S. Steinhauer, A. Köck, C. Gspan, and W. Grogger, "Comparison of the gas sensing performance of SnO₂ thin film and SnO₂ nanowire sensors," *Sensors and Actuators B: Chemical*, vol. 165, pp. 110–118, Apr. 2012.
- [2] L. Filipovic, S. Selberherr, G. Mutinati, E. Brunet, S. Steinhauer, A. Köck, J. Teva, J. Kraft, J. Siegert, F. Schrank, C. Gspan, and W. Grogger, "Modeling the Growth of Tin Dioxide using Spray Pyrolysis Deposition for Gas Sensor Applications," *IEEE Transactions on Semiconductor Manufacturing*, vol. PP, no. 99, pp. 1–1, 2014.
- [3] C. Griessler, E. Brunet, T. Maier, S. Steinhauer, A. Köck, T. Jordi, F. Schrank, and M. Schrems, "Tin oxide nanosensors for highly sensitive toxic gas detection and their 3D system integration," *Microelectronic Engineering*, vol. 88, pp. 1779–1781, Aug. 2011.
- [4] S. Steinhauer, E. Brunet, T. Maier, G. Mutinati, and A. Köck, "Suspended CuO nanowires for ppb level H₂S sensing in dry and humid atmosphere," *Sensors and Actuators B: Chemical*, vol. 186, pp. 550–556, Sept. 2013.
- [5] S. Steinhauer, E. Brunet, T. Maier, G. Mutinati, A. Köck, O. Freudenberg, C. Gspan, W. Grogger, A. Neuhold, and R. Resel, "Gas sensing properties of novel CuO nanowire devices," *Sensors and Actuators B: Chemical*, vol. 187, pp. 50–57, Oct. 2013.
- [6] G. Tulzer, S. Baumgartner, E. Brunet, G. C. Mutinati, S. Steinhauer, A. Köck, P. E. Barbano, and C. Heitzinger, "Kinetic parameter estimation and fluctuation analysis of CO at SnO₂ single nanowires," *Nanotechnology*, vol. 24, p. 315501, Aug. 2013.

Book Chapter

- [1] E. Brunet, G. C. Mutinati, S. Steinhauer, and A. Köck, "Oxide Ultrathin Films in Sensor Applications," in *Oxide Ultrathin Films: Science and Technology* (G. Pacchioni and S. Valeri, eds.), pp. 239–264, Wiley-VCH, 2011.

Conference Contributions

- [1] E. Brunet, C. Griessler, T. Maier, G. C. Mutinati, S. Steinhauer, and A. Köck, “Tin Oxide Nanowire Sensors for Highly Sensitive Detection of Toxic Gases,” in *Nanotech Conference & Expo 2011*, (Boston, US), pp. 306–309, 2011.
- [2] E. Brunet, T. Maier, G. C. Mutinati, S. Steinhauer, and A. Köck, “Network of SnO₂ nanowires for increased gas sensing performance,” in *IMCS 2012 - The 14th International Meeting on Chemical Sensors*, (Nuremberg, Germany), pp. 1538–1541, 2012.
- [3] E. Brunet, G. C. Mutinati, S. Steinhauer, and A. Köck, “Gas sensor device based on a SnO₂ nanowire network for increased sensing performances,” in *Nanotech Conference & Expo 2012*, (Santa Clara, US), pp. 102–105, 2012.
- [4] L. Filipovic, S. Selberherr, G. Mutinati, E. Brunet, S. Steinhauer, A. Köck, J. Kraft, F. Schrank, C. Gspan, and W. Grogger, “Modeling Spray Pyrolysis Deposition,” in *Proceedings of the World Congress on Engineering 2013 Vol II*, (London, U.K.), pp. 987–992, 2013.
- [5] L. Filipovic, S. Selberherr, G. C. Mutinati, E. Brunet, S. Steinhauer, A. Köck, J. Teva, J. Kraft, F. Schrank, C. Gspan, and W. Grogger, “Modeling the Growth of Thin SnO₂ Films using Spray Pyrolysis Deposition,” in *SISPAD 2013, International Conference on Simulation of Semiconductor Processes and Devices*, (Glasgow, Scotland, U.K.), pp. 208–211, 2013.
- [6] A. Köck, E. Brunet, O. Freudenberg, C. Gamauf, J. Kraft, G. C. Mutinati, T. Maier, A. Nemecek, F. Schrank, M. Schrems, M. Siegele, J. Siegert, S. Steinhauer, and J. Teva, “Metal oxide nanowire gas sensors for indoor and outdoor environmental monitoring,” in *Proceedings SPIE 8725, Micro- and Nanotechnology Sensors, Systems, and Applications V*, (Baltimore, Maryland, USA), p. 87250L, 2013.
- [7] G. Mutinati, E. Brunet, S. Steinhauer, A. Köck, J. Teva, J. Kraft, J. Siegert, F. Schrank, and E. Bertagnoli, “CMOS-integrable Ultrathin SnO₂ Layer for Smart Gas Sensor Devices,” in *Procedia Engineering, 26th European Conference on Solid-State Transducers, EUROSENSOR 2012*, vol. 47, (Kraków, Poland), pp. 490–493, Jan. 2012.
- [8] G. C. Mutinati, E. Brunet, T. Maier, S. Steinhauer, and A. Köck, “Gas sensors based on silicon chip-to-chip synthesis of tin oxide nanowires,” in *ESSDERC 2011 - 41st European Solid State Device Research Conference*, (Helsinki, Finland), pp. 319–322, 2011.

- [9] C. Schmidt, F. Altmann, G. Mutinati, E. Brunet, S. Steinhauer, A. Köck, H. Kruschke, J. Teva, J. Kraft, J. Siegert, F. Schrank, M. Siegele, C. Gamauf, and A. Nemecek, “Thermal investigations on CMOS integrated micro-hot-plates using IR Thermography,” in *ISTFA. Conference proceedings from the 38th International Symposium for Testing and Failure Analysis*, (Phoenix, Arizona, USA), pp. 592–595, 2012.
- [10] S. Steinhauer, E. Brunet, T. Maier, G. Mutinati, A. Köck, and O. Freudenberg, “Single Suspended CuO Nanowire for Conductometric Gas Sensing,” in *Procedia Engineering, 26th European Conference on Solid-State Transducers, EUROSENSOR 2012*, vol. 47, (Kraków, Poland), pp. 17–20, Elsevier B.V., Jan. 2012.
- [11] S. Steinhauer, E. Brunet, T. Maier, G. Mutinati, A. Köck, W.-D. Schubert, C. Edtmaier, C. Gspan, and W. Grogger, “Synthesis of High-Aspect-Ratio CuO Nanowires for Conductometric Gas Sensing,” in *Procedia Engineering, EuroensorsXXV*, vol. 25, (Athens, Greece), pp. 1477–1480, Elsevier B.V., Jan. 2011.
- [12] S. Steinhauer, E. Brunet, T. Maier, G. C. Mutinati, and A. Köck, “CuO nanowire gas sensors for CO detection in humid atmosphere,” in *Solid-State Sensors, Actuators and Microsystems (TRANSDUCERS & EUROSENSORS XXVII)*, no. June, (Barcelona, Spain), pp. 1095–1098, 2013.
- [13] S. Steinhauer, E. Brunet, T. Maier, G. C. Mutinati, and A. Köck, “On-Chip Synthesis of CuO Nanowires,” in *Conference on Nanotechnology (IEEE-NANO)*, pp. 1–4, 2012.
- [14] G. Tulzer, S. Baumgartner, E. Brunet, S. Steinhauer, G. C. Mutinati, A. Köck, and C. Heitzinger, “Modeling H₂ Adsorption Processes at SnO₂ Nanowire Surfaces. Parameter Estimation and Simulation.,” in *BIODEVICES, Proceedings of the International Conference on Biomedical Electronics and Devices*, (Barcelona, Spain), pp. 265–268, 2013.

Curriculum Vitae

Personal Data

Name	Elise Brunet
Date of birth	July, 8th 1986
Place of birth	Issy-les-Moulineaux, France
Nationality	French

Education

05/2010- Present	Vienna University of Technology PhD program at the Faculty of Technical Chemistry
09/2007- 09/2009	University Paris Diderot - Paris 7 Master in Material Science “Surfaces, Thin Films and Nanotechnology”
09/2004- 06/2007	University Paris Diderot - Paris 7 Bachelor in Chemistry

Career

05/2010- 10/2013	AIT Austrian Institute of Technology GmbH, Vienna, Austria Research fellow
02/2009- 08/2009	OMV AG, Vienna, Austria Internship: Study of the adhesion properties of bitumen with aggregates in asphalt mixes
03/2008- 08/2008	Siemens AG, Munich, Germany Internship: Optimization of the fabrication process of PZT piezoelectric ceramics
04/2007- 06/2007	University CUVI Vigo, Spain Internship: Study of the reaction between silver nanoparticles and nitric oxide